UNIVERSITY OF OKLAHOMA

GRADUATE COLLEGE

SYNTHESIS AND REDOX BEHAVIOR OF RUTHENIUM NITROSYL PORPHYRIN COMPLEXES

A DISSERTATION

SUBMITTED TO THE GRADUATE FACULTY

in partial fulfillment of the requirements for the

Degree of

DOCTOR OF PHILOSOPHY

By

JEREMY R. ZINK
Norman, Oklahoma
2022

SYNTHESIS AND REDOX BEHAVIOR OF RUTHENIUM NITROSYL PORPHYRIN COMPLEXES

A DISSERTATION APPROVED FOR THE
DEPARTMENT OF CHEMISTRY AND BIOCHEMISTRY

BY THE COMMITTEE CONSISTING OF

Dr. George B. Richter-Addo, Chair

Dr. Ann H. West

Dr. Wai Tak Yip

Dr. Bayram Saparov

Dr. Mark A. Nanny

© Copyright by JEREMY R. ZINK 2022
All Rights Reserved.

Acknowledgments

First, I would like to express my immense gratitude to my research advisor and committee chair, Dr. George B. Richter-Addo. Your insight and unwavering support had an indelible impact on my professional and personal development. I feel extremely fortunate for the experience afforded by the Richter-Addo research group and the OU Graduate College.

I would also like to thank my advisory committee members: Drs. Ann H. West, Wai Tak Yip, Bayram Saparov and Mark A. Nanny for the guidance throughout my graduate studies. Their advice has been vital in the completion of my dissertation and has provided a broader perspective to this work.

My sincere thanks to the Richter-Addo research group members, past and present; especially (i) Dr. Erwin G. Abucayon for training me on many of the lab instrumentation and synthesis techniques, (ii) Drs. Jun (Eva) Yi, Myron W. Jones, Dennis Awasabisah and Adam J. Warhausen for their advice regarding the dissertation writing process and preparation for conferences, and (iii) Dr. Bing Wang, Dr. Samantha M. Powell, Dr. Viridiana E. Herrera, James Herndon, Megan Ayala, Mike Gorbet, Jennifer Londono-Salazar, Brad Ross and Tsitsi Kapfunde for the stimulating conversations in and outside of the lab.

I would like to extend my appreciation to our research collaborator and my former research advisor at SIUE, Dr. Michael J. Shaw, for his critical insights in the electrochemical and spectroelectrochemical results obtained in this work. I am deeply indebted to the research support staff of the OU Department of Chemistry and Biochemistry: Dr. Douglas R. Powell for his assistance with all the X-ray crystallographic work; Dr. Susan L. Nimmo for training me on various nuclei NMR spectroscopy and low temperature experiments; Dr. Steve Foster for his efforts with mass

spectrometry; Erin Mayberry for all the glass-blowing work, along with Carl Van Buskirk and Jeff Jackson in the electronic shop for all their help.

We are very grateful for the financial support provided by the University of Oklahoma and National Science Foundation (NSF). This work and the completion of my dissertation would not have been possible without this funding.

Lastly, I would like to thank my friends and family for all of their love and support throughout my educational pursuits. To my parents (Beth and Robert Zink) and brother (Jacob Zink), your help and encouragement means more than I will ever be able to truly express. Also, I am sincerely grateful to my closest friends Dave Wilson and Tim Morgan, and their amazing families.

Table of Contents

List of Tables

List of Figures

Abstract

This dissertation details the synthesis, characterization, and redox behavior of various six-coordinate ruthenium nitrosyl porphyrin complexes. The primary focus of this work is centered on factors that impact the redox behavior and the reactivity of these previously unreported compounds.

Chapter 1 introduces, in a broader sense, the interactions of nitric oxide with heme proteins and the utilization of synthesized metalloporphyrins as models. Specifically, this dissertation focuses on employing ruthenium as the metal center, and I place my work in context of related adducts from previous research by former group members and others.

Chapter 2 describes the preparation of aryloxide complexes (por)Ru(NO)(OAr_{xH}) (por = OEP and T(*p*-OMe)PP; x = 0, 1, 2) from the alcohol exchange reaction of the corresponding (por)Ru(NO)(OR) precursors with the appropriate phenol reagent containing an increasing number of internal hydrogen bonds. These nitrosyl aryloxide complexes were characterized by X-ray crystallography, and IR and ^{1}H NMR spectroscopy. The IR spectra exhibit higher ν_{NO} frequencies in compounds possessing more internal hydrogen bonds, a result of diminished π-backdonation to the Ru-NO fragment. Similarly, crystal structures of the OEP and T(*p*-OMe)PP complexes display a trend of increasing Ru-O bond lengths with increasing intramolecular hydrogen bonds. This is also reflected in the redox behavior of these (por)Ru(NO)(OAr_{xH}) complexes, which have been examined by cyclic voltammetry and IR-spectroelectrochemistry, showing the first oxidation occurs at an increasingly positive potential with more intramolecular hydrogen bonds present. The subsequent chemical process for the 0- and 1-H compounds become more reversible at scan rates above 200 mV/s while the 2-H complexes displayed

chemically irreversible oxidations. An aryloxide ligand-centered oxidation and dissociation was confirmed via chemical oxidation of (OEP)Ru(NO)(OAr_{2H}) with $AgPF_6$ and supported by DFT calculations for the frontier molecular orbitals of these (porphine)Ru(NO)(OAr_{xH}) complexes.

Chapter 3 details the synthesis and reactivity of several ruthenium nitroxyl (HNO) porphyrin complexes. The preparation of these (por)Ru(HNO)(L_{Im}) (por = TPP, T(*p*-OMe)PP, T(*p*-Cl)PP; L_{Im} = 1-MeIm, -EtIm and –PhIm) compounds were achieved following hydride attack on the corresponding [(por)Ru(NO)(L_{Im})]BF_4 precursors with $NaBH_4$. Unlike the Fe-HNO analogues, the decomposition of the Ru-HNO complexes appear to undergo hydride loss. The IR spectra of the solid samples displayed ν_{NO} bands at significantly lower frequencies (1372-1381 cm^{-1}) than the reported value for free HNO (1500 cm^{-1}) and the experimentally obtained nitrosonium compounds (1862-1869 cm^{-1}). ^1H NMR spectral data of the target nitroxyl complexes demonstrated δ_{HNO} peaks in a similar range to previously reported heme-HNO models but are significantly different from non-heme group 7-9 transition metal complexes. Reactions with the known HNO trap PPh_3 resulted in the generation of the corresponding O=PPh_3 and HN=PPh_3 adducts, confirming the presence of coordinated HNO. Reactions utilizing carbon monoxide and nitric oxide gas both yielded N_2O, although through slightly different mechanisms. A similar approach was performed with PhNO but did not produce N_2O and is believed to be the result of an alternative reaction mechanism involving an as yet unidentified intermediate. The separate reactivity studies employing 1,3-cyclohexadiene and HS-$C(CH_3)_3$ showed no evidence for direct interaction with the Ru-HNO fragment, but instead displayed the presence of the decomposition product.

Chapter 4 highlights the preparation and redox behavior of monometallic and dimetallic complexes of ruthenium nitrosyl porphyrins containing carboxylate and bridging dicarboxylate

axial ligands. IR data of the monometallic acid and ester compounds revealed a shift of the ν_{NO} to lower frequencies with increasing alkyl chain length of the axial ligand due to increased electron density being donated to the Ru-NO fragment. The dimetallic derivatives display an opposing trend as a result of weak electronic communication between the porphyrin macrocycles in close proximity. The redox behavior of these monometallic ester and dimetallic complexes were investigated by cyclic voltammetry and IR-spectroelectrochemistry, which revealed the more electron donating components (e.g., T(*p*-OMe)PP > TPP and $C_6 > C_2$) yielded slightly lower oxidation and higher reduction potentials. A porphyrin-centered first oxidation and first reduction that led to slow dissociation of the carboxylate ligand was confirmed via chemical redox reagents (e.g., $AgPF_6$ and Cp^*_2Co) with $TRuC_2RuT$ and was supported by frontier molecular orbitals analyses of the model (porphine)Ru(NO)(OC(=O)$(CH_2)_2$C(=O)OMe) complex. The dimetallic derivatives undergo a similar mechanism exhibiting two sequential 1-electron transfers that form a mixed valence state enroute to its final dicationic product, as demonstrated by the large peak potential differences and increased current.

Chapter 1: Introduction

1.1. Introduction

The simple diatomic molecule nitric oxide (NO) has received increased interest over the last three decades in light of its vital role in biologically relevant processes such as cardiovascular regulation, immune response, and neurotransmission.[1-8] A significant number of studies in this field have been dedicated to the interactions of NO with the metal centers present in heme containing proteins. One such example is the extensively studied cascade reaction resulting in smooth muscle relaxation initiated through NO binding to the hemoprotein soluble guanylate cyclase (sGC).[9,10] Production of mammalian NO is carried out by the enzyme NO synthase, which utilizes its heme active site to convert L-arginine in the presence of oxygen and NADPH to free NO with citrulline as a byproduct. (Figure 1.1).[11,12] Along with its critical involvement in certain physiological functions, NO has a crucial part in the natural flow of nitrogen through various ecosystems commonly referred to as the global nitrogen cycle. Specifically, in the denitrification process where nitrite (NO_2^-) is reduced to NO prior to being converted into nitrous oxide (N_2O) via detoxification by specific types of bacteria and fungi.[13,14] NO has also been shown to form outside of living organisms in high energy systems such as lightning strikes and combustion engines.[15-17]

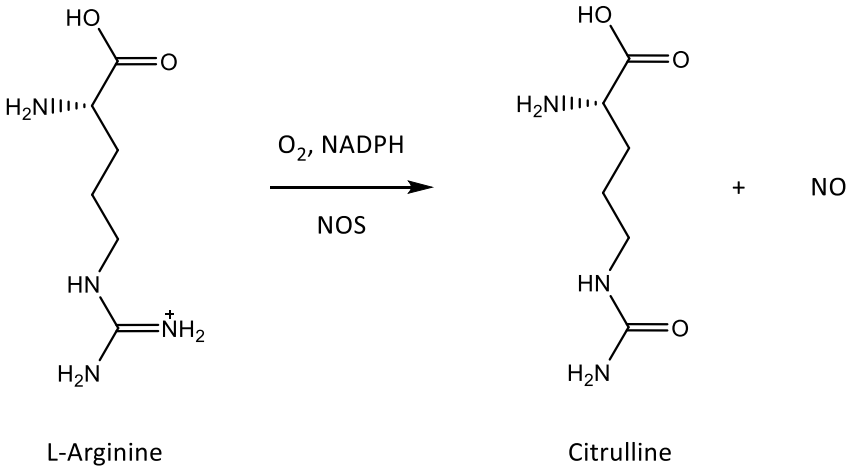

Figure 1.1 Depiction of L-arginine transformation into free NO and citrulline by NO synthase.

Iron protoporphyrin IX (Fe-PPIX), commonly known as heme *b* (Figure 1.2 left), plays an important role in the oxygen transport proteins hemoglobin (Hb) and myoglobin (Mb). This cofactor commonly exhibits coordination at the Fe center on the proximal side to an evolutionarily conserved histidine (e.g., Hb and Mb), cysteine (e.g., cytochrome P450 and NO synthase), or in some cases a tyrosine (e.g., catalase) residue.[18]

Biosynthesis of the heme moiety is a complex multistep mechanism that involves several enzymes.[19] With this in mind it is unsurprising that the direct synthesis of an exact mimic is difficult accomplish in a laboratory setting. However, there are many alternatives available to bioionorganic chemists that have served as models over the years which also allow for tunability in certain aspects including metal center identity and porphyrin macrocycle substituents. Due to the complexity of the Fe containing systems, such as their propensity to exhibit multiple spin states, low spin second and third row transition metal analogues are common substitutes. The work in this dissertation focuses on Ru complexes with various functionalization taking place at the *meso* and *β* positions on the porphyrin macrocycle (Figure 1.2 right).

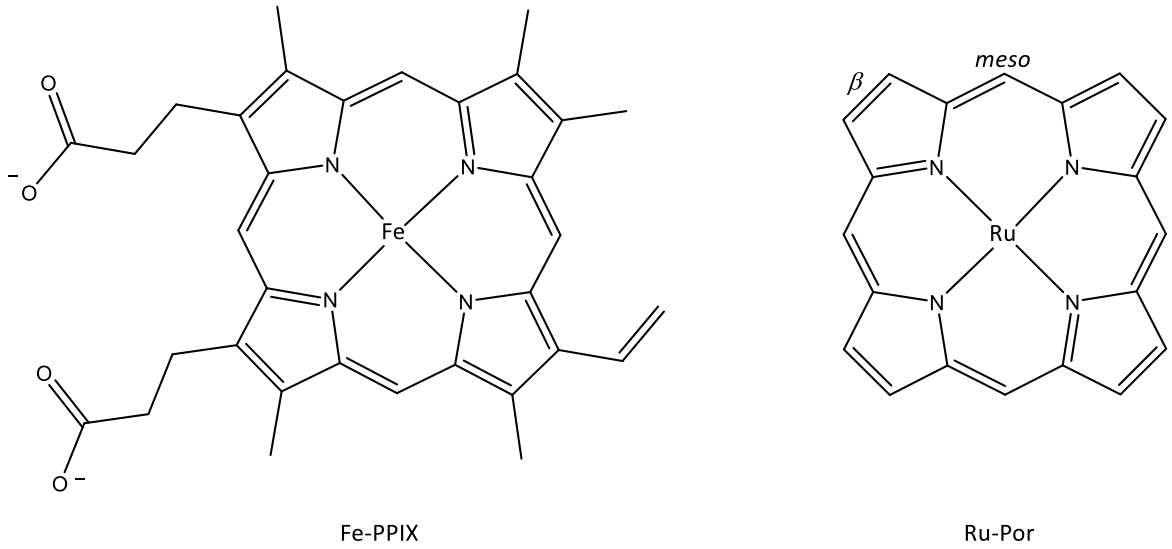

Fe-PPIX Ru-Por

Figure 1.2 Structure of heme *b* (left) and a synthetic Ru-heme model (right) with common substitution sites labelled.

Cyclic voltammetry (CV) is a powerful electroanalytical technique commonly used by our group and others as a means to probe the redox behavior of heme model compounds. This method is particularly useful in determining the presence of redox active sites in a molecular species and possible chemical reactions initiated via heterogenous electron transfer (i.e., through an electrode) without the need of chemical reagents. Another significant advantage to utilizing CV is the ability to distinguish between different processes by comparing the magnitude of energy required as well as aid in mechanistic elucidation of chemical reactions that take place in nature.[20]

Although there are several benefits to CV, it is limited in not being able to provide definitive structural information (i.e., site of electron transfer and chemical change). To remedy this, it is common to couple data obtained from CV with spectroelectrochemistry, which combines electrochemistry and various forms of spectroscopy (e.g., IR, UV-vis, Raman, EPR, NMR), for a more complete analysis. The technique we use most often is IR-

spectroelectrochemistry, specifically a fiber-optic setup that utilizes the reflective surface of the working electrode to examine the bulk analyte solution.[21] As mentioned previously, the primary focus of our group centers around heme-NO models, that conveniently display characteristic features in the mid-IR range. By measuring IR data prior to and following an applied potential the shift or disappearance of these features in a difference spectrum can be used to delineate the site and structural change following a specific redox event. Information collected from these methods for synthetic models offer greater insight into the chemistry involved in certain biological functions.

In six-coordinate nitrosyl metalloporphyrins several factors can influence the redox behavior such as macrocycle type, metal center and oxidation state, axial ligand identity, and environment/second coordination sphere (Figure 1.3). By altering one, or several, of these aspects knowledge can be extracted regarding the impact individual components has on the intrinsic properties of the complex.

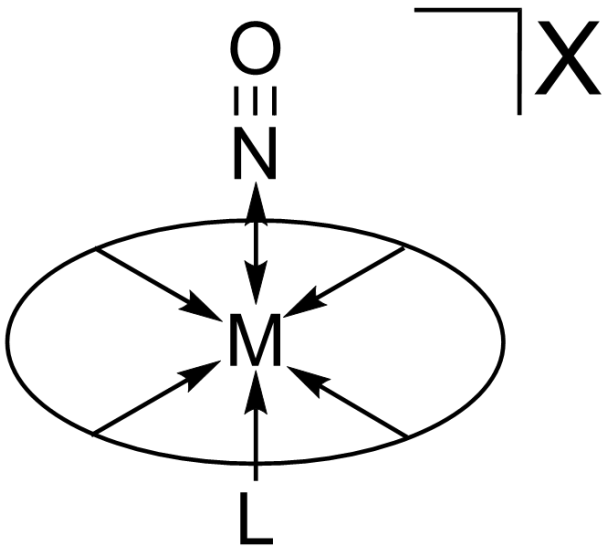

Figure 1.3 Illustration of a heme-NO and contributing factors to its redox behavior.

1.2. My Dissertation Research

My research focuses primarily on the redox behavior of NO-bound synthetic heme models. In particular, examining ruthenium complexes and the influence that certain components, such as axial ligand, porphyrin identity and external chemical reagents, have on the fundamental electronic properties of these model compounds.

Chapter 2 revisits the previous work of former group member Adam Warhausen that sought to clarify the role of internal hydrogen bonding and the ancillary effect it has on the redox behavior in certain hemoproteins.[22-25] This was accomplished through a comprehensive study that consists of the spectral properties, structural information and electrochemical data for the *in situ* analysis of an expanded set of (por)Ru(NO(OAr_{xH}) (por = OEP and T(*p*-OMe)PP; x = 0, 1, 2) complexes. The low spin nature of these ruthenium(II) complexes allowed for not only characterization by ^{1}H NMR spectroscopy but also restricted access to multiple spin states, commonly observed in the unstable iron analogues, that would otherwise have complicated the overarching goal of this work. Thus, the preparation, characterization and anodic investigation of these ruthenium nitrosyl porphyrin compounds possessing intramolecular hydrogen bonds forms the basis for my first project.

The second project of my dissertation expands upon research initiated by another former group member, Jonghyuk Lee, which targets the isolation of synthetic heme-HNO model compounds that utilize ruthenium porphyrins containing imidazole derivatives as histidine mimics.[26] Although studies of more biologically relevant HNO systems modelling these active intermediates in crucial biological processes have been published, the reactivity of nitroxyl complexes remains largely under-reported.[27-33] Due to the instability of these iron analogues,

second row transition metal complexes of HNO are attractive substitutes. The synthesis and spectroscopic details of various (por)Ru(HNO)(L_{Im}) (por = TPP, T(*p*-OMe)PP, T(*p*-Cl)PP; L_{Im} = 1-methylimidazole, 1- ethylimidazole, 1-phenylimidazole) compounds; as well as the interactions of the representative sample (TPP)Ru(HNO)(1-MeIm) with triphenylphosphine, carbon monoxide, nitric oxide, nitrosobenzene, 1,3-cyclohexadiene and ^{t}BuSH are the subjects of Chapter 3 in my dissertation.

In the final part of my work (Chapter 4) a series of monometallic and dimetallic nitrosyl carboxylate complexes are prepared in order to investigate the impact chain length has on the electronic communication in these metalloporphyrin compounds. To achieve this, the synthesized (por)M(NO)(OC(=O)$(CH_2)_n$C(=O)OR) and (por)M(NO)(OC(=O)$(CH_2)_n$C(=O)O)M′(NO)(por) (por = TPP, T(*p*-OMe)PP, OEP; M, M′ = Ru, Os; n = 2, 4, 6; R = H, Me) complexes were spectroscopically characterized and the redox behavior investigated. Related monometallic carboxylate[34,35] and dimetallic μ-dithiolate[36,37] derivatives of ruthenium heme models have been reported previously by our group; however, there are currently no reports for the systems described herein. Utilization of the monocarboxylate ester analogues serve as a comparison to delineate electron transfer mechanisms of potential 2-electron redox events (i.e., sequential vs concerted) for the dimetallic species via electrochemical and spectroelectrochemical techniques.

1.3. References

1. Ignarro, L. J.; Adams, J. B.; Horwitz, P. M.; Wood, K. S. *J. Biol. Chem.* **1986**, *261*, 1997-5002.

2. Radomski, M. W.; Palmer, R. M. J.; Moncada, S. *Proc. Natl. Acad. Sci. USA*. **1990**, *87*, 5193-5197.

3. Radomski, M. W.; Palmer, R. M. J.; Moncada, S. *Proc. Natl. Acad. Sci. USA*. **1990**,

87, 3547-3551.

4. Nathan, C. *Fed. Am. Soc. Exp. Biol.* **1992**, *6*, 3051-3064.

5. Garg, U. C.; Hassid, A. *J. Clin. Invest.* **1989**, *83*, 1774-1777.

6. Butler, A. R.; Williams, D. L. H. *Chem. Soc. Rev.* **1993**, *22*, 233-241.

7. Culotta, E.; Koshland, D. E. *Science* **1992**, *258*, 1862-1865.

8. Averill, B. A. *Chem. Rev.* **1996**, *96*, 2951-2964.

9. Stone, J. R.; Marletta, M. A. *Biochem.* **1994**, *33*, 5636-5640.

10. Bellamy, T. C.; Wood, J.; Garthwaite, J. *Proc. Natl. Acad. Sci. USA.* **2002**, *99*, 507-510.

11. Marletta, M. A. *J. Biol. Chem.* **1993**, *268*, 12231-12234.

12. Derbyshire, E. R. and Marletta, M. A. *Annu. Rev. Biochem.* **2012**, *81*, 533-559.

13. Copeland, D. M.; Soares, A. S.; West, A. H.; Richter-Addo, G. B. *J. Inorg. Biochem*. **2006**, *100*, 1413–1425.

14. Fowler, D.; Steadman, C. E.; Stevenson, D.; Coyle, M.; Rees, R. M.; Skiba, U. M.; Sutton, M. A.; Cape, J. N.; Dore, A. J.; Vieno, M.; Simpson, D.; Zaehle, S.; Stocker, B. D.; Rinaldi, M.; Facchini, M. C.; Flechard, C. R.; Nemitz, E.; Twigg, M.; Erisman, J. W.; Butterbach-Bahl, K.; Galloway, J. N. *Atmos. Chem. Phys*. **2015**, *15*, 13849–13893.

15. Hill, R. D. *Geophys. Res. Lett.* **1979**, *6*, 945-947.

16. Hill, R. D.; Rahmim, I.; Rinker, R. G. *Ind. Eng. Chem. Res.* **1988**, *27*, 1264-1269.

17. Schulz, Christof; Yip, Brandon; Sick, Volker; Wolfrum, Juergen *Chem. Phys. Lett.* **1995**, *242*, 259-264.

18. Poulos, T. L. *Chem. Rev.* **2014**, *114*, 3919-3962.

19. Layer, G.; Reichelt, J.; Jahn, D.; Heinz, D. W. *Protein Science.* **2010**, *19*, 1137—1161.

20. Elgrishi, N.; Rountree, K. J.; McCarthy, B. D.; Rountree, E. S.; Eisenhart, T. T.; Dempsey, J. L. *J. Chem. Educ*. **2018**, *95*, 197-206.

21. Shaw, M. J.; Henson, R. L.; Houk, S. E.; Westhoff, J. W.; Jones, M. W.; Richter-Addo, G. B. *J. Electroanal. Chem*. **2002**, *534*, 47-53.

22. Reid, T. J.; Murthy, M. R. N.; Sicignano, A.; Tanaka, N.; Musick, W. D. L.; Rossmann, M. G. *Proc. Natl. Acad. Sci*. **1981**, *78*, 4767–4771.

23. Ko, T. P.; Day, J.; Malkin, A. J.; McPherson, A. *Acta Cryst*. **1999**, *D55*, 1383–1394.

24. Murshudov, G. N.; Grebenko, A. I.; Brannigan, J. A.; Antson, A. A.; Barynin, V.; Dodson, G. G.; Dauter, Z.; Wilson, K. S.; Melik-Adamyan, W. R. *Acta Cryst*. **2002**, *D58*, 1972–1982.

25. Warhausen, A. J. Ph.D. Dissertation, University of Oklahoma, 2011.

26. Lee, J.; Richter-Addo, G. B. *J. Inorg. Biochem.* **2004**, *98*, 1247-1250.

27. Einsle, O.; Messerschmidt, A.; Huber, R.; Kroneck, P. M. H.; Neese, F. *J. Am. Chem. Soc*. **2002**, *124*, 11737-11745.

28. Bykov, D.; Neese, F. *Inorg. Chem*. **2015**, *54*, 9303-9316.

29. Daiber, A.; Shoun, H.; Ullrich, V. *J. Inorg. Biochem*. **2005**, *99*, 185-193.

30. Nomura, T.; Kimura, T.; Kanematsu, T.; Yamada, D.; Yamashita, K.; Hirata, K.; Ueno, G.; Murakami, H.; Hisano, T.; Yamagiwa, R.; Takeda, H.; Gopalasingam, C.; Kousaka, R.; Yanagisawa, S.; Shoji, O.; Kumasaka, T.; Yamamoto, M.; Takano, Y.; Sugimoto, H.; Tosha, T.; Kubo, M.; Shiro, Y. *Proc. Natl. Acad. Soc.* **2021**, *118*, 1-5.

31. Sulc, F.; Fleischer, E.; Farmer, P .J.; Ma, D.; La Mar, G. N. *J. Biol. Inorg. Chem*. **2003**, *8*, 348–352.

32. Abucayon, E. G.; Khade, R. L.; Zhang, Y.; Richter-Addo, G. B. *J. Am. Chem. Soc*. **2016**, *38*, 104-107.

33. Abucayon, E. G.; Khade, R. L.; Powell, D. R.; Shaw, M. J.; Zhang, Y.; Richter-Addo, G. B. *Dalton Trans.* **2016**, *45*, 18259-18266.

34. Awasabisah, D.; Xu, N.; Sharmah Gutman, K. P.; Powell, D. R.; Shaw, M. J.; Richter-Addo, G. B. *Eur. J. Inorg.* **2016**, *19*, 509-518.

35. Awasabisah, D.; Xu, N.; Sharmah Gautam, K. P.; Powell, D. R.; Shaw, M. J.; Richter-Addo, G. B. *Dalton Trans*. **2013**, *42*, 8537-8540.

36. Lee, J.; Yi, G.-B.; Khan, M. A.; Richter-Addo, G. B. *Inorg. Chem*. **1999**, *38*, 4578-4584.

37. Cheng, L.; Chen, L.; Chung, H.-S.; Khan, M. A.; Richter-Addo, G. B. *Organometallics.* **1998**, *17*, 3853-3864.

Chapter 2: Preparation and electrochemical investigation of nitrosyl ruthenium porphyrins coordinated to aryloxides containing internal H-bonds

2.1. Introduction

The proximal tyrosinate ligand in heme catalase displays H-bonding interactions with a nearby Arg residue (Figure 2.1).[1-3] Such H-bonding interactions with the proximal ligands of heme proteins are not uncommon, and these "secondary" interactions help modulate the electron-donating properties of the proximal ligands and hence the redox behaviors of the heme cofactors. Classic examples include studies of these effects in cysteinate-ligated hemes (e.g., cytochrome P450[4-11] and NO synthase[12-15]) and other tyrosinate-ligated hemes (e.g., HTHP, mauG, cAOS, IsdB).[16-19]

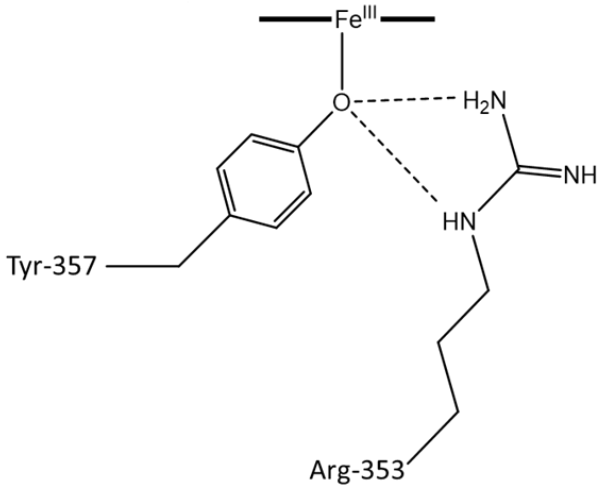

Figure 2.1 Depiction of a heme catalase active site with an arginine residue in the proximal pocket.

Chemical modelling of heme cofactors has frequently employed ruthenium (Ru) as a second-row transition metal to limit available spin states to low spin, enabling the isolation and

^{1}H NMR characterization of the synthetic models. While studies of Ru-porphyrin systems have been reported extensively by us[20-31] and others,[31-39] there are no reports to date describing the effects of such internal H-bonding on the spectral and redox properties in such systems. We and others have reported on the synthesis and redox behavior of (por)Ru(NO)(OR) compounds, but all these compounds lack the desired internal H-bonding feature.

A former lab group member (Adam Warhausen) initiated such a study with the OEP and TPP analogues.[40] In this chapter, I report the preparation, spectral properties, crystal structures, redox behavior and preliminary DFT calculations for a series of (por)Ru(NO)(OAr_{xH}) compounds, where por = OEP (reinvestigated) and T(*p*-OMe)PP. The results delineate the subtle effects of these secondary H-bonding effects on the redox behavior of these compounds.

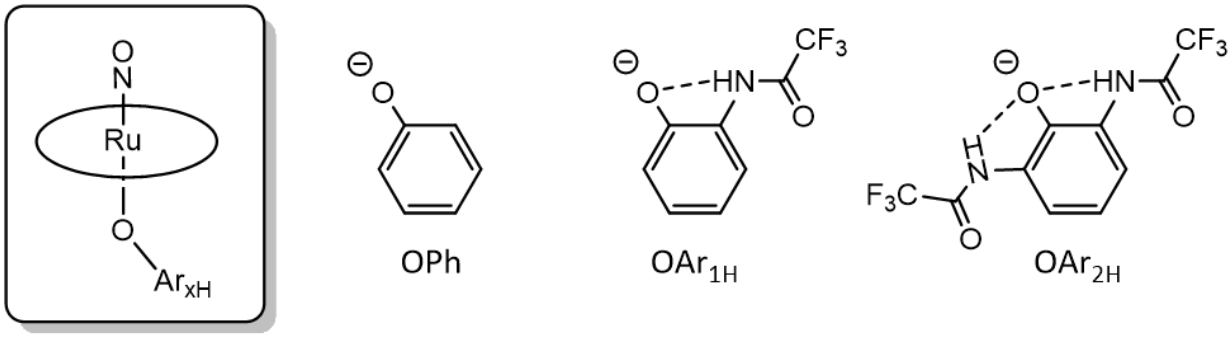

Figure 2.2 Target synthetic ruthenium nitrosyl porphyrin complexes coordinated to aryloxide ligands bearing intramolecular hydrogen bonds.

2.2. Materials and Methods

All reactions were performed under an anaerobic (N_2) atmosphere using standard Schlenk glassware and/or in an Innovative Technology Labmaster 100 Dry Box. Solutions for spectral and electrochemical studies were also prepared under a nitrogen atmosphere. Dichloromethane, benzene and n-hexane were dried using an Innovative Technology Inc. Pure Solv 400-5-MD

Solvent Purification System. 2-Trifluoroacetylaminophenol,[41,42] 2,6-bis(trifluoroacetylamino)phenol,[41,42] and (OEP)Ru(NO)(O-*i*-C_5H_{11})[27] were synthesized as reported previously. The (T(*p*-OMe)PP)Ru(NO)(O-*i*-C_5H_{11}) derivative was prepared using the same procedure as that used for the OEP analogue. Phenol (≥99%) and $AgPF_6$ (98%) were obtained from Aldrich and used as received. The supporting electrolyte NBu_4PF_6 (98%) obtained from Aldrich was recrystallized from hot ethanol and dried in vacuo. Ferrocene (98%) was obtained from Aldrich and sublimed prior to use. Chloroform-*d* ($CDCl_3$, 99.96% atom-D) was purchased from Cambridge Isotope Laboratories, deaerated and dried using activated 4 Å molecular sieves. Infrared spectra were recorded on a Bruker Tensor 27 FTIR spectrometer. ^1H and ^{31}P NMR spectra were obtained on a Varian 400 MHz spectrometer and the ^1H signals were referenced to the residual signal of the solvent employed ($CHCl_3$ at δ = 7.26 ppm), while ^{31}P signals were referenced to H_3PO_4 (85%). X-ray diffraction data was collected using a D8 Quest κ-geometry diffractometer with a Bruker Photon II cpad area detector and Mo-K_α source (λ = 0.71073 Å). The X-ray diffraction data was collected and the structures solved by Dr. Douglas R. Powell.

2.2.1. Preparation of (por)Ru(NO)(OAr_{xH}) complexes

(OEP)Ru(NO)(OPh): To a stirred CH_2Cl_2 (15 mL) solution of (OEP)Ru(NO)(O-*i*-C_5H_{11}) (40 mg, 0.053 mmol) was added phenol (10 mg, 0.11 mmol). The mixture was stirred for 4 h, and the reaction progress was monitored by IR spectroscopy. A new band at 1825 cm^{-1} was formed with concomitant and complete disappearance of the starting ν_{NO} band of (OEP)Ru(NO)(O-*i*-C_5H_{11}) at 1789 cm^{-1}. The solvent was removed in vacuo, and the residue re-dissolved in benzene and passed through an alumina column (Activity Grade III). Benzene was used to elute a dark red band that was collected. The solvent of this collected band was removed in vacuo and the

product obtained in 72% yield (29 mg, 0.038 mmol). IR (KBr, cm^{-1}): ν_{NO} = 1823. ^{1}H NMR (400 MHz; $CDCl_3$): δ 10.28 (s, 4H, *meso*-H of OEP), 5.47 (t, 1H, *p*-H of phenolate moiety, *J* = 8 Hz), 5.32 (t, 2H, *m*-H of phenolate moiety, *J* = 8 Hz), 4.16 (m, 16H, -$\underline{CH_2}CH_3$ of OEP), 1.97 (t, 24H, -$CH_2\underline{CH_3}$ of OEP, *J* = 8 Hz), 1.09 (d, 2H, *o*-H of phenolate moiety, *J* = 8 Hz). X-ray diffraction quality crystals were obtained by liquid/liquid diffusion in a sealed NMR tube using CH_2Cl_2 as the solvent and n-hexane as the antisolvent (1:1).

(OEP)Ru(NO)(O-o-(NHC(=O)CF$_3$)C$_6$H$_4$) ***(OEP)Ru(NO)(OAr$_{1H}$)***: This compound was prepared similarly as above from (OEP)Ru(NO)(O-*i*-C_5H_{11}) (40 mg, 0.053 mmol) using 2-trifluoroacetylamino phenol (16 mg, 0.078 mmol). The chromatographed product was obtained in 76% yield (35 mg, 0.040 mmol). IR (KBr, cm^{-1}): ν_{NH} = 3336, ν_{NO} = 1830, ν_{CO} = 1718. ^{1}H NMR (400 MHz; $CDCl_3$): δ 10.34 (s, 4H, *meso*-H of OEP), 6.46 (d, 1H, *m*-H of phenolate moiety, *J* = 8 Hz), 5.50 (t, 1H, *p*-H of phenolate moiety, *J* = 8 Hz), 5.21 (t, 1H, *m*-H of phenolate moiety, *J* = 8 Hz), 4.15 (app m, 16H, -$\underline{CH_2}CH_3$ of OEP), 2.77 (br s, 1H, NH of axial ligand), 1.97 (t, 24H, -$CH_2\underline{CH_3}$ of OEP, *J* = 8 Hz), 0.44 (d, 1H, *o*-H of phenolate moiety, *J* = 8 Hz).

(OEP)Ru(NO)(O-2,6-(NHC(=O)CF$_3$)$_2$C$_6$H$_3$) ***(OEP)Ru(NO)(OAr$_{2H}$)***: This compound was prepared similarly as above from (OEP)Ru(NO)(O-*i*-C_5H_{11}) (40 mg, 0.053 mmol) using 2,6-bis(trifluoroacetylamino) phenol (25 mg, 0.078 mmol). The chromatographed product was obtained in 61% yield (32 mg, 0.033 mmol). IR (KBr, cm^{-1}): ν_{NH} = 3367 and 3341, ν_{NO} = 1843, ν_{CO} = 1722. ^{1}H NMR (400 MHz; $CDCl_3$): δ 10.32 (s, 4H, *meso*-H of OEP), 6.48 (d, 2H, *m*-H of phenolate moiety, *J* = 8 Hz), 5.73 (t, 1H, *p*-H of phenolate moiety, *J* = 8 Hz), 4.18 (m, 16H, -$\underline{CH_2}CH_3$ of OEP), 2.42 (br s, 2H, NH of axial ligand), 1.97 (t, 24H, -$CH_2\underline{CH_3}$ of OEP, *J* = 8 Hz).

(T(p-OMe)PP)Ru(NO)(OPh): This compound was prepared similarly as above from (T(*p*-OMe)PP)Ru(NO)(O-*i*-C_5H_{11}) (50 mg, 0.053 mmol) using phenol (15 mg, 0.16 mmol). The

chromatographed product was obtained in 69% yield (35 mg, 0.036 mmol). IR (KBr, cm^{-1}): ν_{NO} = 1828. ^{1}H NMR (400 MHz; $CDCl_3$): δ 8.96 (s, 8H, pyrrole-H of T(*p*-OMe)PP), 8.20 (dd, 4H, *o*-H of T(*p*-OMe)PP, *J* = 3 and 8 Hz), 8.05 (dd, 4H, *o'*-H of T(*p*-OMe)PP, *J* = 3 and 8 Hz), 7.31 (app m, 8H, *m*-H of T(*p*-OMe)PP), 5.69 (t, 1H, *p*-H of phenolate moiety, *J* = 8 Hz), 5.55 (t, 2H, *m*-H of phenolate moiety, *J* = 8 Hz), 4.12 (s, 12H, *p*-OMe of T(*p*-OMe)PP), 1.51 (d, 2H, *o*-H of phenolate moiety, *J* = 8 Hz). X-ray diffraction quality crystals were obtained by slow evaporation using CH_2Cl_2 as the solvent and n-hexane as the antisolvent gently layered on top (1:1).

(T(p-OMe)PP)Ru(NO)(O-o-(NHC(=O)CF$_3$)C$_6$H$_4$) ***(T(p-OMe)PP)Ru(NO)(OAr$_{1H}$)***: This compound was prepared similarly as above from (T(*p*-OMe)PP)Ru(NO)(O-*i*-C_5H_{11}) (50 mg, 0.053 mmol) using 2-trifluoroacteylamino phenol (32 mg, 0.16 mmol). The chromatographed product was obtained in 78% yield (44 mg, 0.041 mmol). IR (KBr, cm^{-1}): ν_{NH} = 3349, ν_{NO} = 1833, ν_{CO} = 1720. ^{1}H NMR (400 MHz; $CDCl_3$): δ 9.02 (s, 8H, pyrrole-H of T(*p*-OMe)PP), 8.11 (overlapping dd, 8H, *o*-H of T(*p*-OMe)PP, *J* = 3 and 8 Hz), 7.33 (overlapping dd, 8H, *m*-H of T(*p*-OMe)PP, *J* = 3 and 8 Hz), 6.71 (d, 1H, *p*-H of phenolate moiety, *J* = 8 Hz), 5.67 (t, 1H, *m*-H of phenolate moiety, *J* = 8 Hz), 5.47 (t, 1H, *m*-H of phenolate moiety, *J* = 8 Hz), 4.12 (s, 12H, *p*-OMe of T(*p*-OMe)PP), 3.38 (br s, 1H, NH of axial ligand), 0.86 (d, 1H, *o*-H of phenolate moiety, *J* = 8 Hz). X-ray diffraction quality crystals were obtained by liquid/liquid diffusion in a sealed NMR tube using CH_2Cl_2 as the solvent and n-hexane as the antisolvent (1:1).

(T(p-OMe)PP)Ru(NO)(O-2,6-(NHC(=O)CF$_3$)$_2$C$_6$H$_3$) ***(T(p-OMe)PP)Ru(NO)(OAr$_{2H}$)***: This compound was prepared similarly as above from (T(*p*-OMe)PP)Ru(NO)(O-*i*-C_5H_{11}) (50 mg, 0.053 mmol) using 2,6-bis(trifluoroacteylamino) phenol (50 mg, 0.16 mmol). The chromatographed product was obtained in 56% yield (35 mg, 0.030 mmol). IR (KBr, cm^{-1}): ν_{NH}

= 3339 and 3371, ν_{NO} = 1849, ν_{CO} = 1716. ^{1}H NMR (400 MHz; $CDCl_3$): δ 9.06 (s, 8H, pyrrole-H of T(*p*-OMe)PP), 8.35 (dd, 4H, *o*-H of T(*p*-OMe)PP, *J* = 3 and 8 Hz), 7.93 (dd, 4H, *o*-H of T(*p*-OMe)PP, *J* = 3 and 8 Hz), 7.45 (dd, 4H, *m*-H of T(*p*-OMe)PP, *J* = 3 and 8 Hz) , 6.74 (d, 2H, *m*-H of phenolate moiety, *J* = 8 Hz), 5.79 (t, 1H, *p*-H of phenolate moiety, *J* = 8 Hz), 4.13 (s, 12H, *p*-OMe of T(*p*-OMe)PP), 3.17 (br s, 2H, NH of axial ligand). Partial signal overlap was observed between the $CDCl_3$ solvent peak at 7.26 ppm and the *m*-H's of T(*p*-OMe)PP at 7.28 ppm. X-ray diffraction quality crystals were obtained by slow evaporation using CH_2Cl_2 as the solvent and n-hexane as the antisolvent gently layered on top (1:1).

2.2.2. Electrochemistry and spectroelectrochemistry of (por)Ru(NO)(OAr_{xH})

Cyclic voltammetric measurements were performed using a BAS CV 50W instrument. A three-electrode cell was utilized and consisted of a 3.0 mm diameter Pt disk working electrode, a Pt wire counter electrode and a Ag wire pseudo-reference electrode. Obtained products were dried under high vacuum for a minimum of 24 h prior to experiments. Solutions of the compounds were deaerated prior to use by passing a stream of N_2 gas through the solution for a minimum of 10 min, and a blanket of N_2 was maintained over the solution while performing the experiments. The solutions contained 1.0 mM of the analyte in 0.1 M NBu_4PF_6 as support electrolyte. Ferrocene (Fc, 1.0 mM) was used as an internal standard, and potentials were referenced to the $Fc^{0/+}$ couple set to 0.00 V. An approach for *i*R correction was employed to account for the resistance and capacitance in these solutions by entering these values manually into a Python program written by our collaborator Dr. Michael J. Shaw as described by Saveant.[43] This is similar to the process of *i*R compensation available in some electrochemistry software programs but is performed after data collection. A Bruker Tensor 27 FTIR spectrometer, equipped with a mid-IR fiber-optic dip probe and liquid nitrogen cooled MCT

detector (RemSpec Corporation, Sturbridge, MA, USA), was used for the IR spectroelectrochemistry.

2.2.3. DFT calculations of (porphine)Ru(NO)(OAr_{xH}) complexes and a 5-coordinate [(porphine)Ru(NO)]$^+$

Density functional calculations (functionals: B3LYP, B3P86, BP86; basis set: DGDZVP) were performed using Gaussian-09[44] on the WebMO interface (https://webmo.oscer.ou.edu). Geometric optimizations, vibrational frequency and molecular orbital analyses were performed for the selected complexes: (porphine)Ru(NO)(OPh), (porphine)Ru(NO)(OAr_{1H}), (porphine)Ru(NO)(OAr_{2H}) and [(porphine)Ru(NO)]$^+$. Calculations were performed in the gas phase and in two solvation environments (cyclohexane and *o*-dichlorobenzene).

2.2.4. Chemical oxidation of (OEP)Ru(NO)(OAr_{2H}) with $AgPF_6$

A chemical oxidation was performed by the addition of $AgPF_6$ (2 mg, 0.0079 mmol) to a CH_2Cl_2 (5 mL) solution of (OEP)Ru(NO)(OAr_{2H}) (5 mg, 0.0051 mmol). After 1 hr of stirring in the dark the initial red solution turned to a dark purple color. The reaction mixture was filtered, the solvent removed in vacuo and the product obtained in 31% yield (1 mg, 0.0015 mmol). The residue isolated from the filtrate was crystallized by slow evaporation using CH_2Cl_2 as the solvent and n-hexane as the antisolvent (1:1). IR (KBr, cm^{-1}): ν_{NO} = 1854, ν_{PO} = 1311 and 1125. ^{1}H NMR (400 MHz; $CDCl_3$): δ 10.43 (s, 4H, *meso*-H of OEP), 4.21 (q, 16H, -$\underline{CH_2}CH_3$ of OEP, *J* = 8 Hz), 2.01 (t, 24H, -$CH_2\underline{CH_3}$ of OEP, *J* = 8 Hz).

2.3. Results and Discussion

2.3.1. Preparation, spectroscopy and analysis of trends

The preparation and chemical properties of nitrosyl metalloporphyrin alkoxide complexes, particularly those prepared via alkyl nitrites and subsequent alcohol exchange reactions, have been investigated thoroughly over the years.[26-34,45] However, very little has been reported regarding the aryloxide derivatives[25,30] and there is currently no published information on the effect that internal hydrogen bonding has on these nitrosyl heme model compounds. A series of (por)Ru(NO)(OAr_{xH}) (por = OEP and T(*p*-OMe)PP) compounds bearing an increasing number of intramolecular H-bonds (x = 0, 1 and 2) on the axial phenolate moiety were prepared and isolated in 56-79% yields by an alcohol exchange reaction[46] of the precursor alkoxides (por)Ru(NO)(O-*i*-C_5H_{11})[29] with the corresponding phenol ligands as shown in Figure 2.3. Initial synthesis of the OEP derivatives were performed by a former group member (Adam Warhausen).;[40] however, the compounds were re-synthesized by me for a more complete spectral and structural characterization, along with the additional T(*p*-OMe)PP derivatives. The utilization of this synthetic approach and specific work up routine has yielded tractable amounts of spectroscopically pure samples of (por)Ru(NO)(OAr_{xH}) sufficient for electrochemical studies. The target compounds are air stable as solids at room temperature and show no signs of decomposition over several weeks, as determined by IR and ^{1}H NMR spectroscopy.

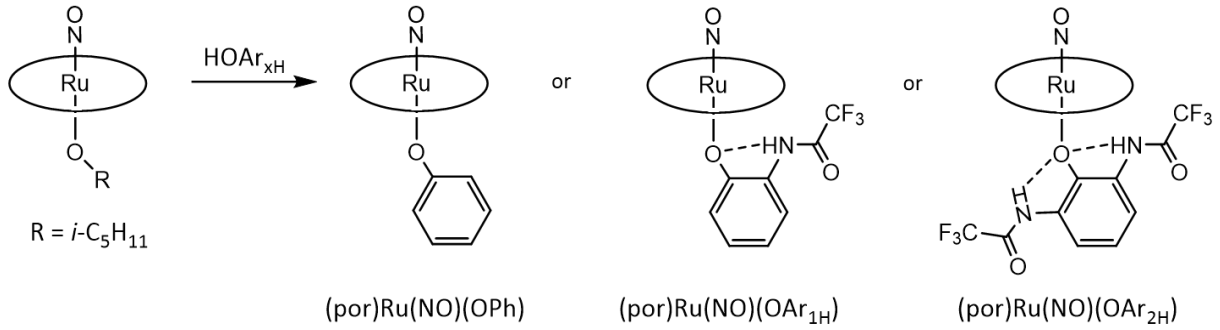

Figure 2.3 General synthesis description for the (por)Ru(NO)(OAr$_{xH}$) complexes.

Progress of the alcohol exchange reaction was monitored by solution IR spectroscopy and considered complete when the ν_{NO}'s of the (por)Ru(NO)(O-*i*-C_5H_{11}) starting materials at 1792 cm^{-1} for OEP and 1807 cm^{-1} for T(*p*-OMe)PP in CH_2Cl_2 were no longer present. The distinctive $\nu_{NO,}$ ν_{CO} and ν_{NH} bands for the isolated aryloxide (OEP)Ru(NO)(OAr$_{xH}$) products are displayed in Figure 2.4. The corresponding ν_{NO} data from related (por)Ru(NO)(*O*-ligand) complexes are listed in Table 2.1. An exchange of the initial axial alkoxide ligands with the aryloxides resulted

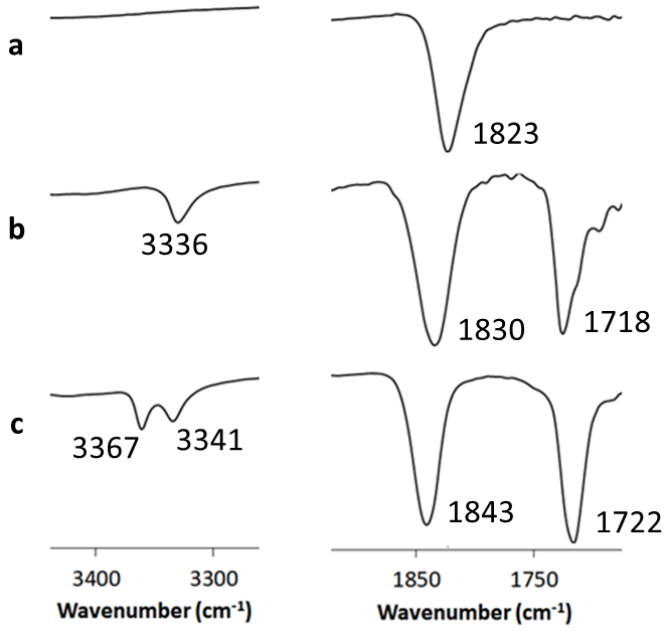

Figure 2.4 Truncated IR spectra of (OEP)Ru(NO)(OAr$_{xH}$) as KBr pellets; (a) 0-H, (b) 1-H, (c) 2-H with ν_{NH} (left) and $\nu_{NO/CO}$ (right) bands labelled.

in a ν_{NO} shift to higher frequencies ($\Delta\nu_{NO}$ ~30 cm^{-1}) due to the slight electron withdrawing nature of the aryl group, coinciding with diminished π-backbonding of electron density to the Ru-NO moiety. This shift is enhanced in systems containing more internal H-bonds (0-1: $\Delta\nu_{NO}$ ~7 cm^{-1}; 1-2: $\Delta\nu_{NO}$ ~13 cm^{-1}) and is a result of the internal hydrogen bond(s) pulling additional electron density away from the coordinated oxygen atom of the Ru-O bond. Removal of electron density from the Ru center is expected to cause a weakening of the Ru-N(O) bond and simultaneous strengthening of the N-O bond, as is observed by the increasing ν_{NO}. The highest observed frequencies for ν_{NO} belong to the OAr_{2H} complexes at ~1845 cm^{-1}, similar in value to those of the related (T(*p*-OMe)PP)Ru(NO)(OC_6HF_4) and (por)Ru(NO)X (por = T(*p*-OMe)PP, T(*p*-Me)PP, T(*p*-CF_3)PP, TPP, TTP, OEP; X = Cl, Br) compounds (ν_{NO} = 1844-1855 cm^{-1}) containing more electron withdrawing ligands.[30,47,48]

Table 2.1 IR ν_{NO}, ν_{CO} and ν_{NH} frequencies of (por)Ru(NO)(OAr_{xH}) and ν_{NO} of related (por)Ru(NO)(*O*-ligand) compounds.

	ν_{NO} (cm^{-1})	ν_{CO} (cm^{-1})	ν_{NH} (cm^{-1})	Ref.
(TPP)Ru(NO)(O-*i*-C_5H_{11})	1800[b]			28
(TTP)Ru(NO)(O-*i*-C_5H_{11})	1809[b]			32
(T(*p*-OMe)PP)Ru(NO)(O-*i*-C_5H_{11})	1807[a], 1801[b]			45
(T(*p*-OMe)PP)Ru(NO)(OC_6HF_4)	1850[a], 1844[b]			30
(T(*p*-OMe)PP)Ru(NO)(OPh)	1831[a], 1828[b]			t.w.
(T(*p*-OMe)PP)Ru(NO)(OAr_{1H})	1837[a], 1833[b]	1721[a], 1720[b]	3339[a], 3349[b]	t.w.
(T(*p*-OMe)PP)Ru(NO)(OAr_{2H})	1852[a], 1849[b]	1725[a], 1716[b]	3378[a]	t.w.
			3339 & 3371[b]	
(OEP)Ru(NO)(O-*i*-C_5H_{11})	1792[a], 1788[b]			28
(OEP)Ru(NO)(OMe)	1780[b]			26
(OEP)Ru(NO)(OEt)	1791[b]			45
(OEP)Ru(NO)(OPh)	1825[a], 1823[b], 1821[c]			t.w.
(OEP)Ru(NO)(OAr_{1H})	1835[a], 1830[b], 1832[c]	1720[a], 1718[b]	3333[a], 3336[b]	t.w.
(OEP)Ru(NO)(OAr_{2H})	1845[a], 1843[b], 1842[c]	1723[a], 1722[b]	3355[a]	t.w.
			3341 & 3367[b]	

[a] CH_2Cl_2
[b] KBr
[c] Toluene

The increase in ν_{NO} in the aryloxide compounds compared to those of the alkoxide compounds (ν_{NO} = 1780-1809 cm^{-1}) is consistent with the removal of additional electron density by these aryloxide ligands. However, alteration to the equatorial porphyrin peripheral substitution does not appear to have a significant effect on the ν_{NO} of the nitrosyl complexes with the same axial *O*-ligand ($\Delta\nu_{NO}$ < 7 cm^{-1}), with the slightly lower frequencies exhibited by the more electron rich OEP derivatives. The frequency shift in ν_{CO} corresponding to the coordination of the axial aryloxide ligands was more apparent in the OAr_{1H} complex (free ligand ν_{CO} = 1692 cm^{-1}; coordinated ligand ν_{CO} = 1718 cm^{-1}) than that observed for the OAr_{2H} (free ligand ν_{CO} = 1715 cm^{-1}; coordinated ligand ν_{CO} = 1722 cm^{-1}), again with minimal differences between the OEP and T(*p*-OMe)PP macrocycles (for T(*p*-OMe)PP: OAr_{1H} ν_{CO} = 1720 cm^{-1}; OAr_{2H} ν_{CO} = 1716 cm^{-1}). An equally compelling feature to the $\Delta\nu_{NO}$ in confirming the coordination of the axial aryloxide ligand by IR is the shift in ν_{NH} observed in both the OAr_{1H} and OAr_{2H} compounds. Comparison of the ν_{NH} values for the free ligands $HOAr_{1H}$ and $HOAr_{2H}$ (ν_{NH} = ~3385 cm^{-1}) to the corresponding coordinated complexes reveals a shift of $\Delta\nu_{NH}$ = ~45 cm^{-1} for (OEP)Ru(NO)(OAr_{1H}) (ν_{NH} = 3336 cm^{-1}), and (OEP)Ru(NO)(OAr_{2H}) (ν_{NH} = 3341 and 3367 cm^{-1}, sym and asym, respectively). The characteristic ν_{CO} and ν_{NH} bands of the coordinated ligands present in 1718-1722 cm^{-1} and 3336-3367 cm^{-1} regions, respectively, are similar to those reported for the five-coordinate (por)Fe(OAr_{xH}) compounds (ν_{CO} = 1722-1728 and ν_{NH} = 3355-3379 cm^{-1}).[41,42] The significant ν_{NH} shift upon coordination is accompanied with an increase for both ν_{CO} and ν_{NH} of the coordinated aryloxide between the OAr_{1H} and OAr_{2H} complexes. Given that the OPh ligand does not possess the additional C=O or N-H functional groups that can be easily monitored by IR spectroscopy, techniques such as ^{1}H NMR spectroscopy and X-ray crystallography were essential for verifying the identity of these derivatives.

The diamagnetism exhibited by low-spin ruthenium(II) porphyrin complexes, as opposed to the commonly observed paramagnetic iron species, is extremely advantageous in the characterization of the target compounds by ^{1}H NMR spectroscopy, in addition to determining purity. While the IR spectra were used initially to verify completion of the alcohol exchange reaction in the presence of excess $HOAr_{xH}$ reagent, ^{1}H NMR spectra were utilized to differentiate between the free and coordinated aryloxide ligand, as well as confirm the successful removal of the unreacted ligand following purification for subsequent electrochemical studies. The resulting spectra from the obtained products confirmed the absence of the signals from the (por)Ru(NO)(O-*i*-C_5H_{11}) precursors between -0.50 and -3.00 ppm.[26,28,45] A description of the ^{1}H NMR spectroscopic data and assignments for the target complexes (OEP)Ru(NO)(OAr_{xH}) are presented in Figures 2.5 and 2.6. Characteristic signals corresponding to the porphyrin macrocycle of the desired products are considerably downfield (i.e., higher ppm values), while the signals belonging to the various bound phenolate moieties are shifted upfield (i.e., lower ppm values) compared to those of the free ligands.

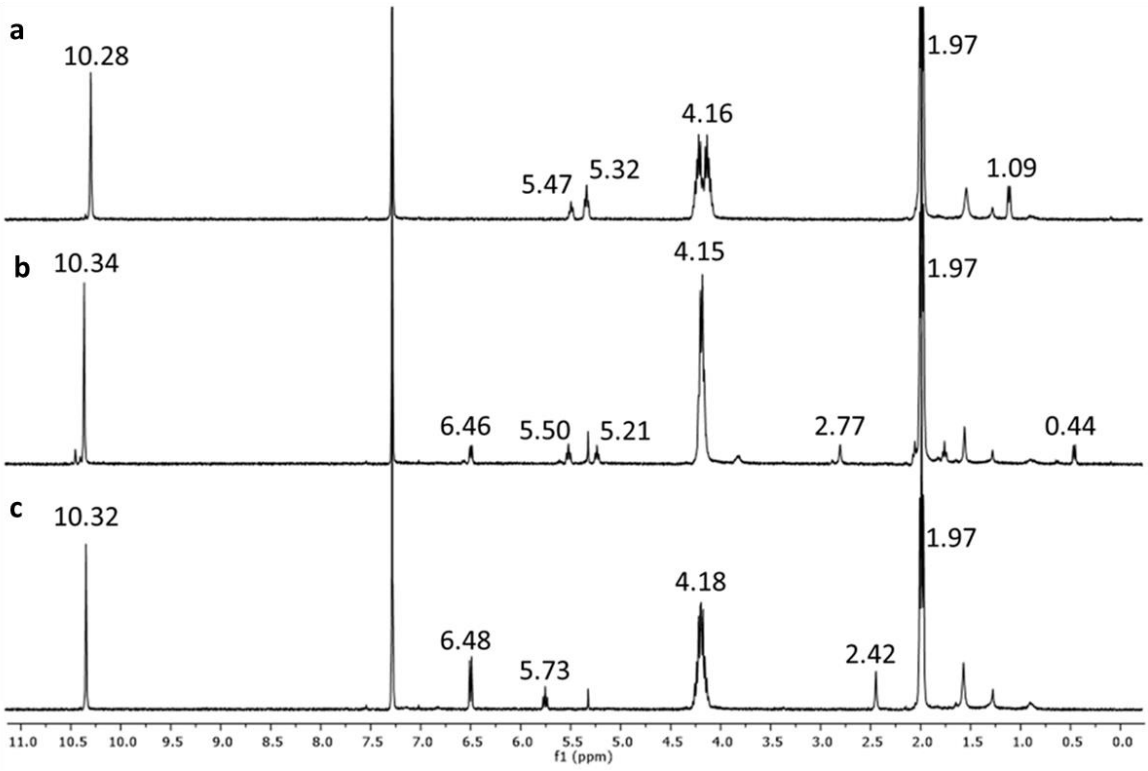

Figure 2.5 Stacked ^{1}H NMR spectra of the (a) 0-H, (b) 1-H and (c) 2-H complexes of (OEP)Ru(NO)(OAr_{xH}) in $CDCl_3$ with characteristic chemical shifts of porphyrin and phenolate proton signals reported. Minor impurity peaks due to CH_2Cl_2 (5.31 ppm), H_2O (1.59 ppm) and n-hexane (0.88 ppm and 1.25 ppm).

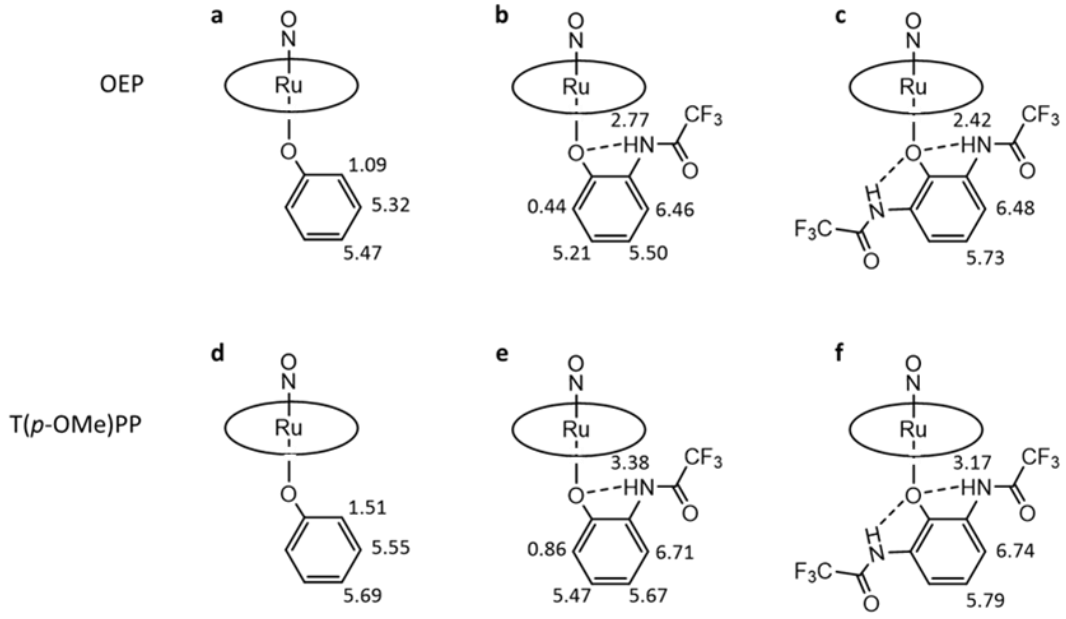

Figure 2.6 ^{1}H NMR chemical shifts (ppm) of the 0-H, 1-H and 2-H axial ligands for (a-c) (OEP)Ru(NO)(OAr_{xH}) and (d-f) (T(p-OMe)PP)Ru(NO)(OAr_{xH}) complexes, respectively.

Table 2.2 lists chemical shift values of previously reported *meso*-H's for various (OEP)Ru(NO)X (X = *O*- and *S*-bound ligands) compared to those of the target compounds. These aryloxide compounds do not exhibit much change in their δ *meso*-H signals upon *O*-ligand exchange and do not display any considerable difference from the related *S*-ligand complexes (< 0.1 ppm). No observable trend was present between the compounds containing varying numbers of intramolecular hydrogen bonds either.

Table 2.2 ^{1}H NMR meso-H signals of (OEP)Ru(NO) complexes with alkoxide and thiolate axial ligands in $CDCl_3$.

	δ *meso*-H (ppm)	**Ref**
(OEP)Ru(NO)Cl	10.39	46
(OEP)Ru(NO)(OEt)	10.29	28
(OEP)Ru(NO)(O-*i*-C_5H_{11})	10.28	26
(OEP)Ru(NO)(SEt)	10.26	28
(OEP)Ru(NO)($SCMe_2CH_2NH(C=O)Me$)	10.30	29
(OEP)Ru(NO)(S-*i*-C_5H_{11})	10.29	26
(OEP)Ru(NO)(SCH_2CF_3)	10.29	45
(OEP)Ru(NO)(SC_6F_4H)	10.25	45
(OEP)Ru(NO)(OPh)	10.28	t.w.
(OEP)Ru(NO)(OAr_{1H})	10.34	t.w.
(OEP)Ru(NO)(OAr_{2H})	10.33	t.w.

The new proton signals of the axial ligand in (OEP)Ru(NO)(OAr_{2H}) can be observed in the range 5.7-6.5 ppm, contrasted to signals of the free $HOAr_{2H}$ between 7.1-7.6 ppm, and most notably a significant shift of the N-H peak from 8.54 ppm to 2.42 ppm upon coordination to form the complex. The signals of the phenolate and N-H protons of the (OEP)Ru(NO)(OAr_{1H}) complex are found in comparable regions (5.2-6.5 ppm and 2.77 ppm, respectively) to the OAr_{2H} derivative, with an additional aromatic proton signal due to the mono-substituted structure shifted significantly upfield at 0.44 ppm. Similarly, the axial ligand proton signals of the (OEP)Ru(NO)(OPh) complex are found between 5.3-5.5 ppm and at 1.09 ppm, due to the lack of

the hydrogen bonding substituent. The upfield protons are believed to belong to the phenolate C-H most near the coordinated metal center. This large shift is the result of an anisotropic shielding effect from the porphyrin macrocycle, which increases with proximity to the macrocycle, hence the greater shift for the N-H's and *o*-H's compared to the *m*- and *p*-H's on the aryloxide ligand. The related (por)Ru(NO)(R) (por = T(*p*-OMe)PP, T(*p*-CF_3)PP; R = Me, Et) compounds demonstrate a similar but more exaggerated effect with the alkyl protons appearing between -4.17 and -6.72 ppm.[49] A likely competing anisotropic deshielding effect from the aromatic fragment of the OAr_{xH} ligands prevents these protons from being shifted further upfield into negative chemical shift values.

The ^{1}H NMR spectra of the (T(*p*-OMe)PP)Ru(NO)(OAr_{xH}) complexes in $CDCl_3$ display signals of the axial ligand protons not unlike those of the OEP derivatives shown in Figure 2.5. With these tetraaryl-substituted porphyrins, however, there appears to be restricted rotation of the porphyrin aryl groups, resulting in an observed AA′BB′ splitting pattern (Figure 2.7), where J_{AB} = 8.8 Hz, $J_{AA'} = J_{BB'}$ = 2.5 Hz and $J_{AB'} = J_{BA'}$ = 0.6 Hz. The signals for the ortho-H's, namely H_A and $H_{A'}$, appear at higher ppm values (in the 7.90-8.40 ppm region) compared to the signals for the *m*-H's (H_B and $H_{B'}$). Overlapping doublet of doublets are observed for the OPh and OAr_{1H} complexes. In addition, the chemical shift differences between H_A and $H_{A'}$ are larger than the differences between H_B and $H_{B'}$, presumably due to the closer proximity of the H_A and $H_{A'}$ protons to the asymmetrical axial Ru-coordinated groups. To confirm this type of spin system, the experimentally obtained chemical shifts and coupling constant values were used to generate the simulated ^{1}H NMR spectra (Figures 2.7 and 2.8), which match for each of the complexes and what was previously observed for other tetraaryl substituted porphyrins.[50,51]

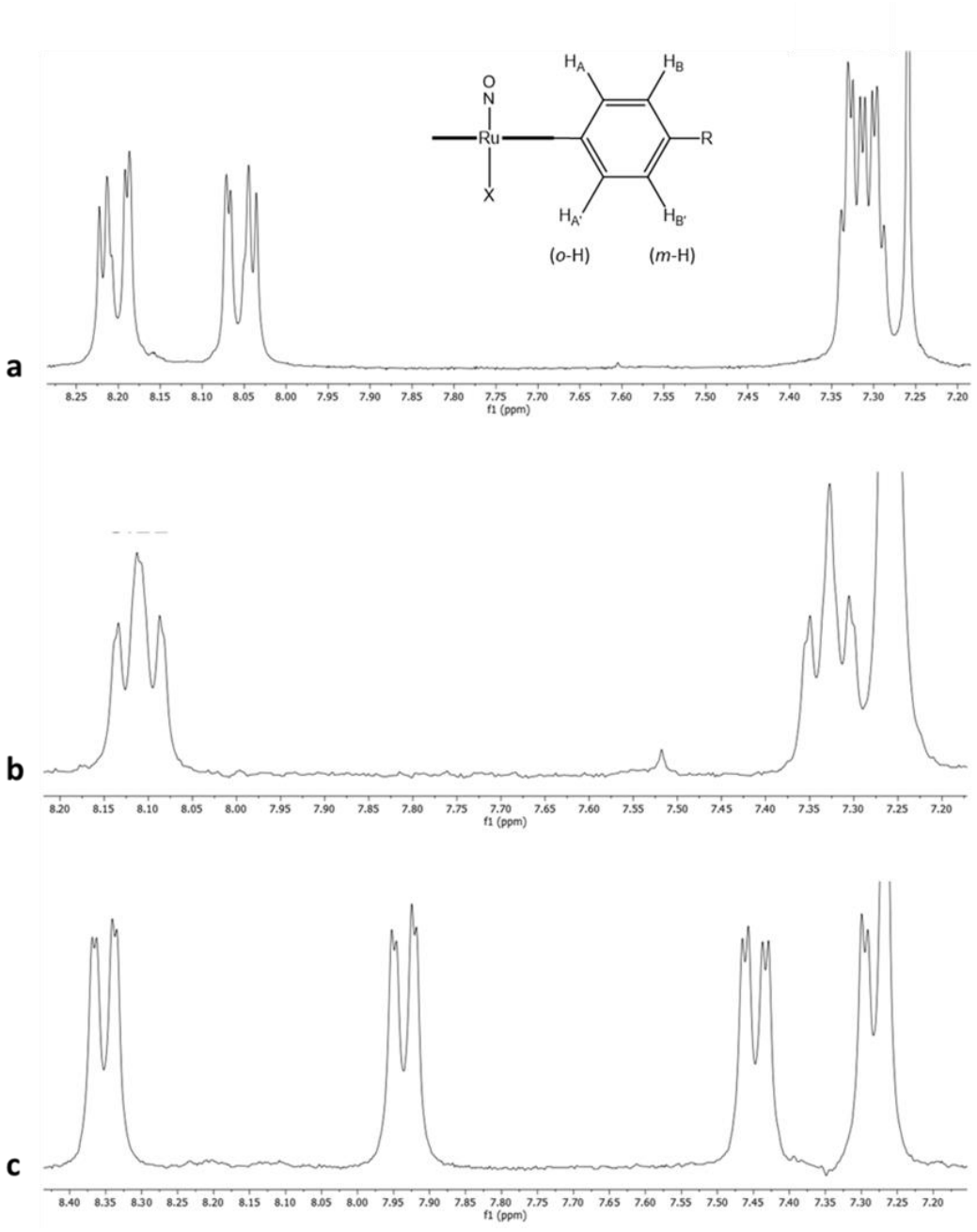

Figure 2.7 Truncated ^{1}H NMR spectra of the (a) 0-H, (b) 1-H and (c) 2-H derivatives of the (T(*p*-OMe)PP)Ru(NO)(OAr_{xH}) complexes in $CDCl_3$, showing the proton signals of the porphyrin aryl groups.

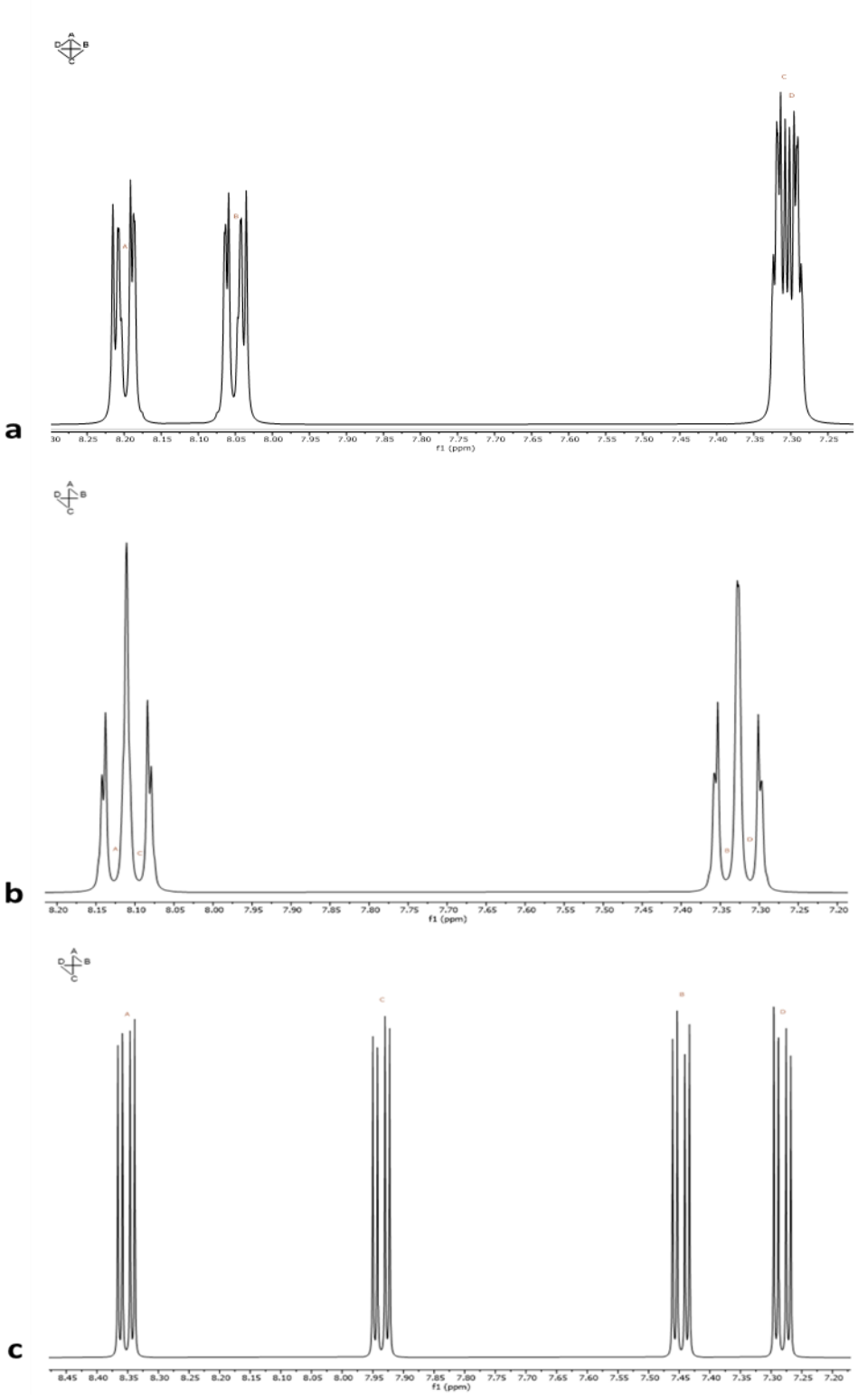

Figure 2.8 Simulated ^{1}H NMR spectra of the (a) 0-H, (b) 1-H and (c) 2-H derivatives of the (T(*p*-OMe)PP)Ru(NO)(OAr$_{xH}$) complexes using chemical shift and coupling constant values for the proton signals of the porphyrin aryl groups obtained experimentally.

2.3.2. Molecular structures

The molecular structures for the target (por)Ru(NO)(OAr_{xH}) complexes are shown in Figures 2.9 and 2.10. Two of the six reported structures exhibited some form of disorder, the ethyl C27-C28 of the (OEP)Ru(NO)(OAr_{2H}) crystal structure was disordered and occupancies for the disordered atoms refined to 0.722(10) and 0.278(10) for the unprimed and primed atoms, respectively. Significant disorder in the crystal structure for the (T(*p*-OMe)PP)Ru(NO)(OAr_{1H}) compound was present. The molecule sits on a crystallographic inversion center, so half of the atoms are unique, and the two axial ligands are disordered 50:50 across the plane of the porphyrin. The aromatic axial ligand was disordered with refined occupancies of 0.3149(14) and 0.1851(14) for the unprimed and primed atoms. The formally $\{RuNO\}^6$ compounds exhibit near linear ∠RuNO bond angles of 172.0(4)-179.3(4)° and Ru-N(O) bond lengths in the range of 1.716(5)-1.810(2) Å, whereas the complexed aryloxide ligands display significant bending at the Ru-O-C linkages with ∠RuOC bond angles around 121.60(10)-131.99(19)° with Ru-O bond lengths between 1.950(2)-2.045(3) Å. Unsurprisingly, these complexes most closely match the reported aryloxide complex (T(*p*-OMe)PP)Ru(NO)(OC_6HF_4) with ∠RuNO and ∠RuOC bond angles of 173.1(3)° and 127.5(2)°, as well as Ru-N(O) and Ru-O bond lengths of 1.739(3) and 2.000(3) Å, respectively.[25,30] Comparison of the structural information of these compounds to the published NO-bound catalase protein structure reveals a moderately bent ∠FeNO of ~160° (heme A) and varying bond angles in other subunits of the tetramer (160-175°).[52]

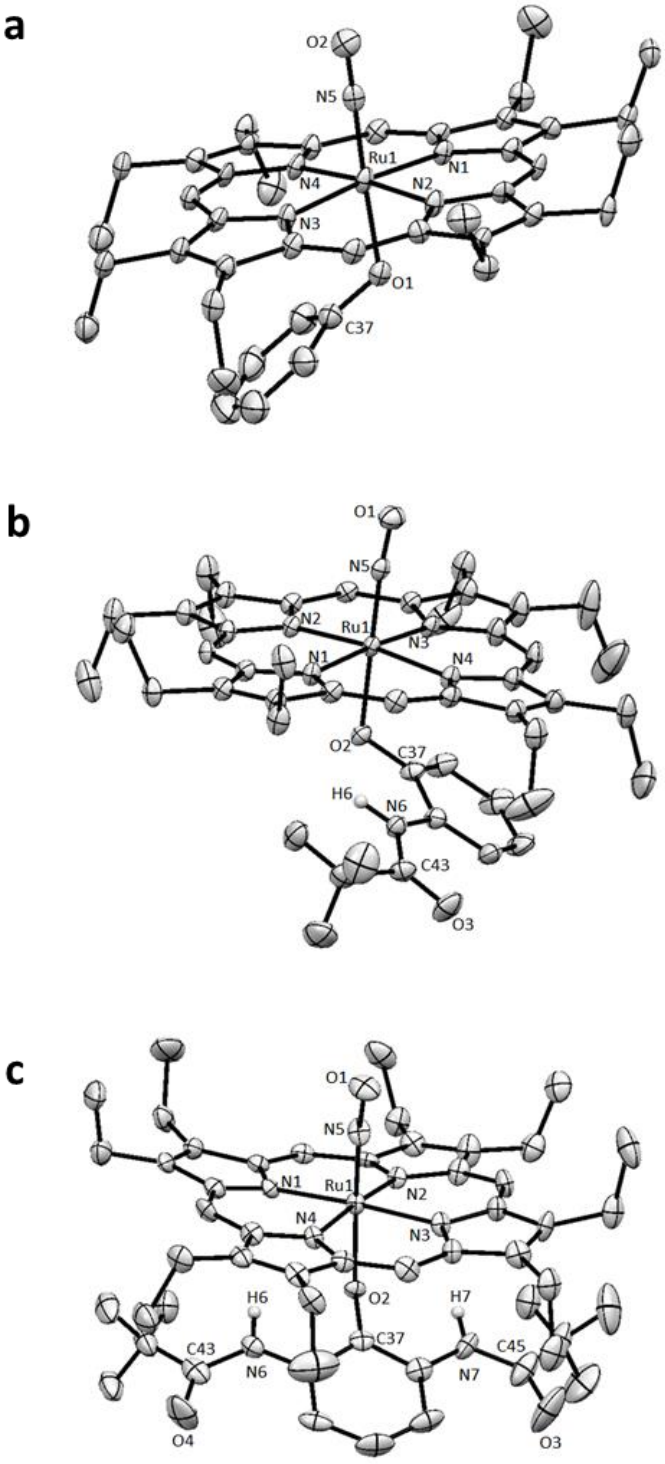

Figure 2.9 Crystal structures of the 0-H (i.d. 19002), 1-H (i.d. 10074a) and 2-H (i.d. 10076) derivatives of (a-c) (OEP)Ru(NO)(OAr_{xH}) complexes, respectively. Hydrogen atoms are omitted for clarity, with the exception of the N6-H6 and N7-H7 hydrogen atoms. Only the major disordered components are shown.

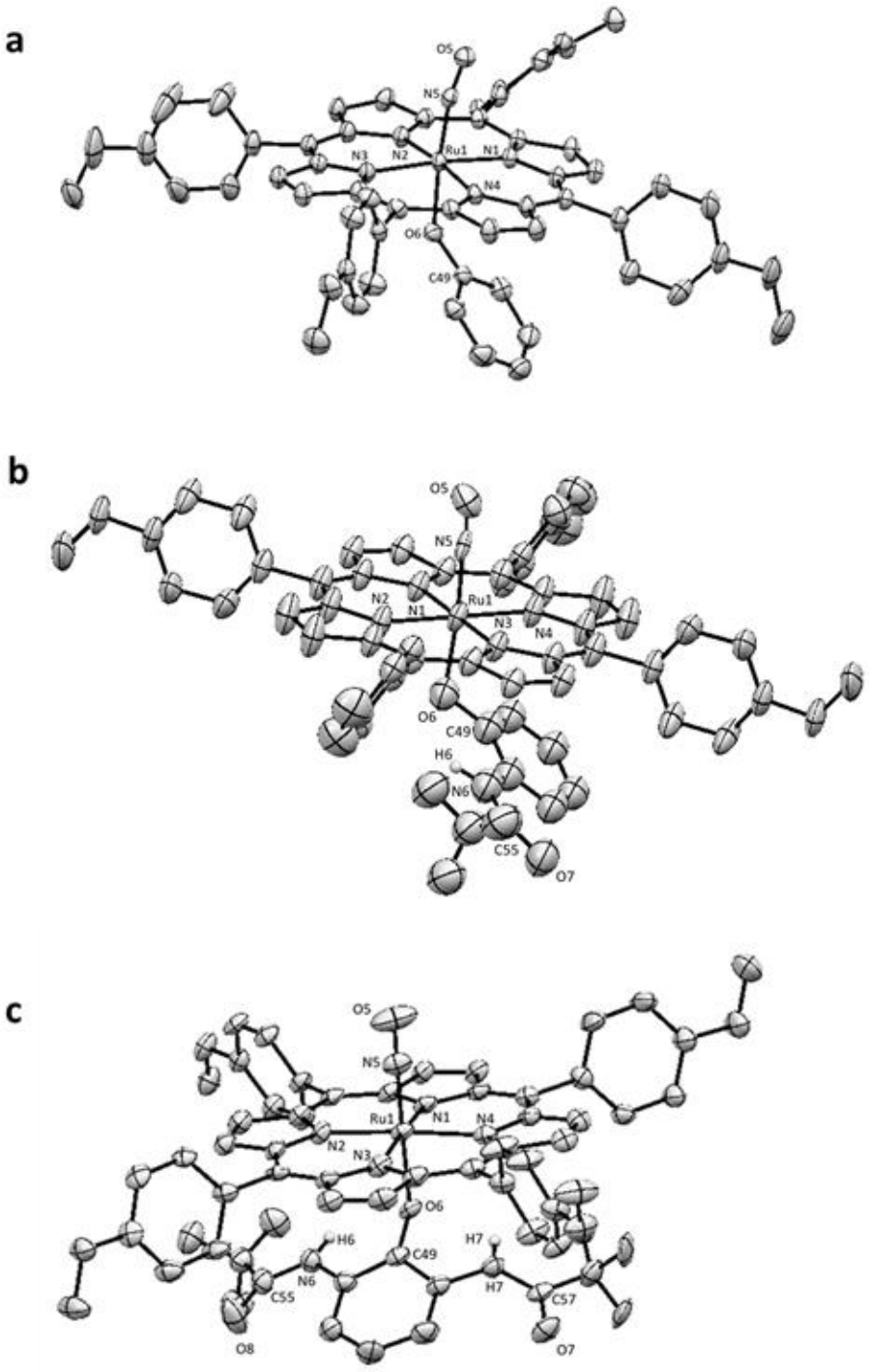

Figure 2.10 Crystal structures of the 0-H (i.d. 18241), 1-H (i.d. 18312) and 2-H derivatives of (a-c) (T(*p*-OMe)PP)Ru(NO)(OAr_{xH}) complexes, respectively. Hydrogen atoms are omitted for clarity, with the exception of the N6-H6 and N7-H7 hydrogen atoms. Only the major disordered components are shown. The X-ray diffraction data for (T(*p*-OMe)PP)Ru(NO)(OAr_{2H}) was collected by Dr. Joseph H. Reibenspies at Texas A&M University and the structure solved by Dr. Douglas R. Powell.

Table 2.3 lists selected lengths and angles for the (por)Ru(NO)(OAr_{xH}) products and other related ruthenium-nitrosyl complexes previously reported. The structural data for the target aryloxide complexes do not differ significantly in either bond lengths or angles to those of the previously reported alkoxide precursor (OEP)Ru(NO)(O-*i*-C_5H_{11}) and similar *O*-ligand derivatives.[27,30,32,45] In the case of the OEP derivatives, a correlation between ∠RuNO angles and Ru-O bond lengths can be observed with increasing number of internal hydrogen bonds. Namely, a decrease in linearity of the ∠RuNO from OPh (179.3(4)°) to OAr_{1H} (174.3(2)°) to OAr_{2H} (172.0(4)°) appears to correlate with a concomitant increase in Ru-O bond length from OPh (1.987(4) Å) to OAr_{1H} (2.0296(18) Å) to OAr_{2H} (2.045(3) Å). Conversely, the OAr_{2H} complex of T(*p*-OMe)PP exhibited the highest degree of ∠RuNO linearity (179.0(6)°). This lengthening of the Ru-O bond length with increasing number of internal hydrogen bonds is also observed for the reported 5-coordinate (OEP)Fe(OAr_{xH}) compounds from OPh (1.848(4) Å) to OAr_{1H} (1.887(2) Å) to OAr_{2H} (1.926(3) Å).[41,42] The cause of this trend arises from the removal of electron density from the coordinated oxygen via intramolecular hydrogen bonding, which results in diminished π-donation from the aryloxide and subsequent lengthening of the Ru-O bond, similar to the apparent change in the IR spectra for ν_{NO}. This trend between ∠RuNO linearity and Ru-O bond length is still present in the T(*p*-OMe)PP complexes but is less apparent. While no correlation between ∠RuOC and Ru-N(O) is evident, the OEP derivatives exhibit much less variation in these structural parameters (< 2.5° and 0.02 Å, respectively) than that of the T(*p*-OMe)PP derivatives (ca. 7.2° and 0.10 Å, respectively). According to a review by Malcolm Chisholm regarding alkoxide and aryloxide metal interactions, these bond lengths are dependent upon the nature of the bonding where purely σ donation demonstrates a M-O bond length of ~2.06 Å while those exhibiting double bond (π) character can be found in a general range of 1.80-1.96

Å.[53] Thus, the OPh compound demonstrates behavior most related to what is expected for the presence of a π donor ligand *trans* to a metal nitrosyl (i.e., shortest Ru-O bond length and highest ∠RuNO bond angle). Consequently, the OAr_{2H} complex displays less π donation with the longest Ru-O bond length and lowest ∠RuNO bond angle. In early transition metal complexes shorter M-O bond lengths are also known to display more linear ∠MOC (160-180°) bond angles and vice versa, with longer M-O bond lengths leading to less linear ∠MOC (120-130°).[52] This is reflected in the much lower ∠RuOC bond angles (121.60(10)-131.99(19)°) observed for these OAr_{xH} complexes, indicative of a more significant σ bond character (i.e., less π character) from the aryloxide ligand, particularly in the compounds containing internal hydrogen bonds, and very minimal π bond character in the OPh derivatives. Aryloxide ligands have been shown to compete for electron density at the oxygen atom between the aryl group and metal (M-O=C ↔ M=O-C), which stabilizes a more linear ∠MOC.[53] The presence of internal hydrogen bonds and a coordinated nitrosyl ligand in the *trans* position, however, appears to have a complex effect on this competition resulting in the decreased linearity of ∠RuOC for these compounds.

Table 2.3 Selected structural data for ruthenium nitrosyl porphyrin complexes containing *O*-ligands.

	Ru-N(O) (Å)	**∠RuNO (º)**	**Ru-O (Å)**	**∠RuOC (º)**	**Ref**
(TPP)Ru(NO)(OMe)	1.840(4)	180.0	1.800(5)	137.70(31)	32
(OEP)Ru(NO)(O-*i*-C_5H_{11})	1.745(4)	176.9(3)	1.932(3)	129.1(9)	27
(T(*p*-OMe)PP)Ru(NO)(OC_6HF_4)	1.739(3)	173.1(3)	2.000(3)	127.5(2)	30
(T(*p*-OMe)PP)Ru(NO)(OC(=O)CF_3)	1.986(11)	178.3(9)	1.773(11)	134.0(9)	30
(T(*p*-OMe)PP)Ru(NO)(OC(=O)Me)	1.856(11)	169.7(14)	1.909(11)	131.40(10)	30
(T(*p*-OMe)PP)Ru(NO)(OC(=O)^{i}-Pr)	1.872(14)	174.0(12)	1.807(11)	127.40(13)	30
(T(*p*-OMe)PP)Ru(NO)(OC(=O)Fc)	1.751(2)	179.6(3)	1.996(2)	131.8(2)	30
(T(*p*-Me)PP)Ru(NO)(OC(=O)Fc)	1.737(6)	169.8(7)	1.968(5)	135.3(5)	30
(OEP)Ru(NO)(OPh)	1.751(5)	179.3(4)	1.987(4)	124.6(4)	t.w.
(OEP)Ru(NO)(OAr_{1H})	1.732(2)	174.3(2)	2.0296(18)	122.28(15)	t.w.
(OEP)Ru(NO)(OAr_{2H})	1.734(5)	172.0(4)	2.045(3)	124.5(3)	t.w.
(T(*p*-OMe)PP)Ru(NO)(OPh)	1.746(3)	173.6(3)	1.968(2)	131.99(19)	t.w.
(T(*p*-OMe)PP)Ru(NO)(OAr_{1H})	1.810(2)	172.50(14)	1.950(2)	121.60(10)	t.w.
(T(*p*-OMe)PP)Ru(NO)(OAr_{2H})	1.716(5)	179.0(6)	2.029(4)	124.7(3)	t.w.

2.3.3. Cyclic voltammetry in CH_2Cl_2

The redox behavior of the (por)Ru(NO)(OAr_{xH}) compounds were investigated via cyclic voltammetry (CV). Table 2.4 lists the formal potentials ($E^{\circ\prime}$), peak anodic potentials (E_{pa}), peak potential separation (ΔE_p) and peak current ratios (i_{pc}/i_{pa}) of the first oxidations for the various (por)Ru(NO)(OAr_{xH}) compounds. In general, the porphyrin identity and number of intramolecular hydrogen bonds present in the complex play a significant role in the electrochemical/chemical processes. As observed in the voltammograms below, the first oxidations take place at less positive potentials in OEP than in the T(*p*-OMe)PP derivatives, and an increase in the number of internal hydrogen bonds shifts these E_{pa} even further positive, i.e., (OEP)Ru(NO)(OPh) has the least positive E_{pa} while (T(*p*-OMe)PP)Ru(NO)(OAr_{2H}) has the most positive E_{pa}. To determine whether the first oxidations were fully chemically reversible, i_{pc}/i_{pa} values were calculated,[54] which confirmed that none of the compounds had a completely chemically reversible first oxidation. The compound closest to full reversibility (i_{pc}/i_{pa} of 1.0) at

400 mV/s was (OEP)Ru(NO)(OPh) at 0.88 and the lowest ratio was (T(*p*-OMe)PP)Ru(NO)(OAr_{1H}) at 0.70. Since the OAr_{2H} compounds have irreversible first oxidations at all scan rates employed, values for $E^{\circ\prime}$, ΔE_p and i_{pc}/i_{pa} could not be determined.

Table 2.4 Redox potentials and peak current ratios for the first oxidations of (por)Ru(NO)(OAr_{xH}) (por = OEP and T(*p*-OMe)PP)[a].

	$E^{\circ\prime}$ (V)	E_{pa} (V)	ΔE_p (mV)	i_{pc}/i_{pa}
(OEP)Ru(NO)(OPh)	+0.430	+0.460	70 (60)	0.88
(OEP)Ru(NO)(OAr_{1H})	+0.525	+0.550	78 (58)	0.81
(OEP)Ru(NO)(OAr_{2H})	-	+0.580	-	-
(T(*p*-OMe)PP)Ru(NO)(OPh)	+0.550	+0.580	67 (62)	0.79
(T(*p*-OMe)PP)Ru(NO)(OAr_{1H})	+0.620	+0.660	78 (61)	0.70
(T(*p*-OMe)PP)Ru(NO)(OAr_{2H})	-	+0.690	-	-

[a] Experimental conditions: 1.0 mM analyte in CH_2Cl_2 containing 0.1 M NBu_4PF_6. Formal ($E^{\circ\prime}$) and peak anodic (E_{pa}) potentials were measured with a Pt working electrode and referenced to $Fc^{0/+}$ and set to 0.00 V. ΔE_p values in parentheses refer to peak potential separation of $Fc^{0/+}$. Determined from voltammograms recorded at 400 mV/s.

Phenoxide complexes:

Figure 2.11 depicts the voltammograms of the OPh complexes for both porphyrin derivatives (OEP in Figures 2.11a-c; T(*p*-OMe)PP in Figures 2.11d-f) in CH_2Cl_2 with 0.1M NBu_4PF_6 as the supporting electrolyte. The full voltammograms (Figures 2.11c,f) within the solvent system limits were recorded at 200 mV/s with potentials referenced against the internal standard ferrocene ($Fc^{0/+}$) set to 0 V. No redox events were observed when scanning the reduction (-) potentials up to -1.60 V vs Fc. Consequently, all electrochemical and spectroelectrochemical studies will focus on the anodic processes. The 1-electron first oxidation of (OEP)Ru(NO)(OPh) at 100 mV/s was observed at a peak anodic potential (E_{pa}) of +0.46 V, which becomes increasingly chemically reversible when the switching potential (E_{sw}) is altered to isolate this initial feature (Figure 2.11a; i_{pc}/i_{pa} = 0.88) and upon increasing the scan rate (e.g., dashed line at 400 mV/s). This behavior is characteristic of an electrochemical transfer step

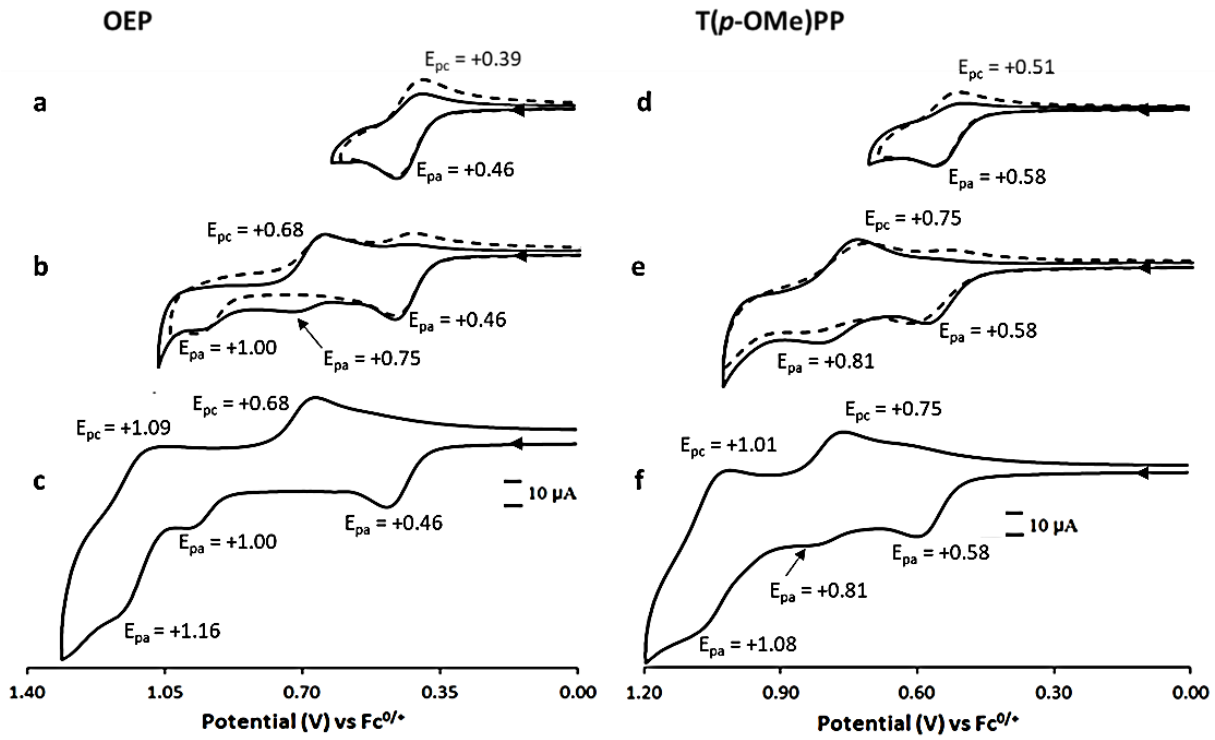

Figure 2.11 Cyclic voltammograms of 1.0 mM (a-c) (OEP)Ru(NO)(OPh) and (d-f) (T(p-OMe)PP)Ru(NO)(OPh) containing 0.1 M NBu_4PF_6 showing (a,d) first oxidation and (b,e) second oxidation features at scan rates of 100 mV/s (solid line) and 400 mV/s (dashed line), and (c,f) third oxidation feature at a scan rate of 200 mV/s, respectively.

involving a subsequent chemical change, or EC mechanism, which is likely a result of the aryloxide dissociation (Eq. 2.1a,b) to generate a $[(por)Ru(NO)]^+$ product. In cyclic voltammetry experiments, an EC mechanism is known to demonstrate increased reversibility with increased scan rate (i.e., rate of electron transfer outpaces ligand dissociation) in the absence of an additional source of the species being lost.[55] However, without any structural/spectroscopic information there is not enough evidence to conclusively designate the site of oxidation. The first oxidation of the T(*p*-OMe)PP derivative displayed similar features, such as the effect of E_{sw} and scan rate on the reversibility of the first oxidation (Figure 2.11d) but at a slightly more positive E_{pa} = +0.58 V.

$$(por)Ru(NO)(OAr_{xH}) \rightleftharpoons [(por)Ru(NO)(OAr_{xH})]^{+} + e^{-} \quad \textbf{(2.1a)}$$

$$[(por)Ru(NO)(OAr_{xH})]^{+} \longrightarrow [(por)Ru(NO)]^{+} + {}^{\bullet}OAr_{xH} \quad \textbf{(2.1b)}$$

The second oxidation is slightly more complex given that two distinct features appear in the OEP derivatives while only one feature is clearly observed for T(*p*-OMe)PP. In the case of OEP, the second oxidation occurs at +1.00 V with a 200 mV/s scan rate but as seen in Figure 2.11b, a lower scan rate (100 mV/s; solid line) yields an additional feature at +0.75 V. This feature disappears after increasing the scan rate (400 mV/s; dashed line) and results in an improved degree of reversibility in the cathodic wave of the first oxidation (E_{pc} = +0.39 V), which aligns with the formation of a scan rate-dependent species and its ensuing oxidation. With the proposed aryloxide dissociation at slower scan rates and overlap with the return cathodic wave at +0.68 V, the most likely scenario would be the oxidation of the previously mentioned $[(OEP)Ru(NO)]^{+}$ complex to $[(OEP^{\bullet})Ru(NO)]^{2+}$ species (Eq. 2.2a). This value is in close proximity to the previously reported E_{pa} of $[(OEP^{\bullet})Ru(NO)(H_2O)]^{2+}$ ($E_{1/2}$ = +0.71 V).[56,57] When the scan rate is increased (400 mV/s) this feature is no longer present but the redox event at +1.00 V remains and is most likely the generation of a short-lived $[(OEP)Ru(NO)(OAr_{xH})]^{2+}$ complex (Eq. 2.2b) that leads to dissociation of any remaining coordinated aryloxide. In the case of the T(*p*-OMe)PP derivative in Figure 2.11e, only the feature at +0.81 V with a return cathodic wave at +0.75 V was observed and the proposed product (Eq. 2.2b) is comparable to the published value for $[(TPP^{\bullet})Ru(NO)(H_2O)]^{2+}$ ($E_{1/2}$ = +0.78 V).[56,57] It is likely that the second oxidation feature for the unstable $[(T(p\text{-}OMe)PP)Ru(NO)(OPh)]^{2+}$ intermediate is not observed due to an overlap with the third oxidation feature, given the ΔE_{pa} of ~270 mV between the second and third oxidation features (Figure 2.11f).

$$[(por)Ru(NO)]^{+} \rightleftharpoons [(por^{\bullet})Ru(NO)]^{2+} + e^{-} \quad \textbf{(2.2a)}$$

$$[(por)Ru(NO)(OAr_{xH})]^{+} \longrightarrow [(por)Ru(NO)(OAr_{xH})]^{2+} + e^{-} \quad \textbf{(2.2b)}$$

A third oxidation feature (Figures 2.11c,f) occurs at a E_{pa} = +1.16 V (T(*p*-OMe)PP: E_{pa} = +1.08 V) with a corresponding E_{pc} = +1.09 V (T(*p*-OMe)PP: E_{pa} = +1.01 V), which also falls in the range of the reported oxidation product $(por^{\bullet})Ru(NO)(H_2O)]^{3+}$ ($E_{1/2}$ = +1.13 V), as described in Eq. 2.3.[56,57] It is difficult to assign what degree of reversibility this feature exhibits given its proximity to the solvent limit. Extending out to these potentials leads to the first oxidation becoming completely irreversible.

$$[(por^{\bullet})Ru(NO)]^{2+} \rightleftharpoons [(por^{\bullet})Ru(NO)]^{3+} + e^{-} \quad \textbf{(2.3)}$$

<u>OAr_{1H} complexes:</u>

The OAr_{1H} complexes exhibit generally similar redox behaviors to the OPh derivatives as seen in Figure 2.12. An initially irreversible first oxidation, at a more positive E_{pa} (OEP = +0.55 V; T(*p*-OMe)PP = +0.66 V) than the OPh analogues, becomes more reversible upon altering the E_{sw} to isolate the first oxidation at 200 mV/s and when increasing the scan rate from 100 to 400 mV/s (Figure 2.10a; i_{pc}/i_{pa} = 0.80) as observed previously in Figure 2.11. The slight decrease in reversibility in the OAr_{1H} complexes suggests the aryloxide dissociation is more prevalent compared to that of OPh when producing the $[(por)Ru(NO)]^{+}$ species. A scan rate-dependent second oxidation feature is observed that results in a returning cathodic wave at the same E_{pc} as the OPh complexes (OEP = +0.68 V; T(*p*-OMe)PP = +0.75 V). Figure 2.12b illustrates two additional redox events (for OEP) when the voltammogram is recorded at 100 mV/s. A subtle faradaic response (Figure 2.12b) at +0.75 V (same as in the OPh case) is present, which again

likely yields $[(por^{\bullet})Ru(NO)]^{2+}$, followed by a more distinct wave at +1.02 V. The E_{pa} of this second feature in the second oxidation for (OEP)Ru(NO)(OAr_{1H}) occurs at a slightly more positive value than the OPh derivative (+1.00V) by ca. 20 mV. This increase in redox potential suggests the species being oxidized is minimally more electron deficient than the OPh complex and is in agreement with the formation of the $[(OEP)Ru(NO)(OAr_{1H})]^{2+}$ product. The small feature at +0.75 V disappears once the scan rate is increased to 400 mV/s, leaving the latter wave unchanged. An even more subtle singular faradaic response (Figure 2.12e) appears at ca. +0.81 V for the T(*p*-OMe)PP derivative (i.e., similar to OPh). Lastly, a third oxidation is observed near the edge of the solvent window at the same potential as those of the OPh compounds (OEP = +1.16 V; T(*p*-OMe)PP = +1.08 V) shown in Figures 2.12c,f, and similarly results in the formation of the $[(por^{\bullet})Ru(NO)]^{3+}$ complex.

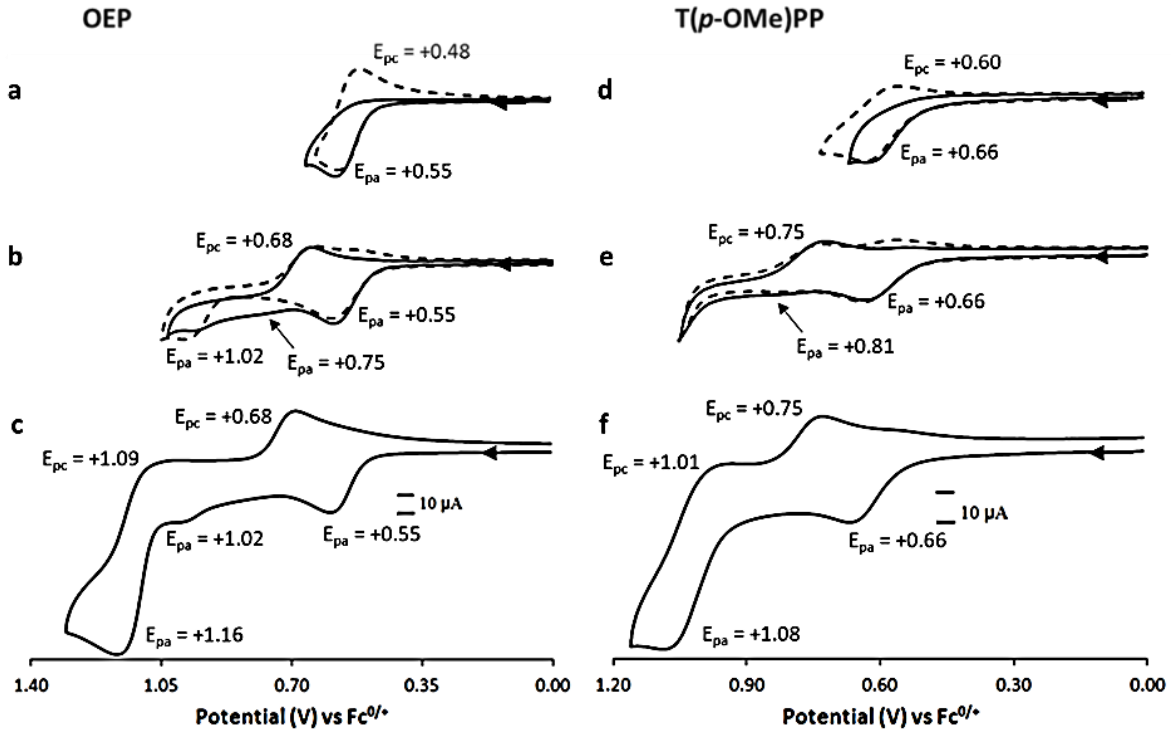

Figure 2.12 Cyclic voltammograms of 1.0 mM (a-c) (OEP)Ru(NO)(OAr_{1H}) and (d-f) (T(*p*-OMe)PP)Ru(NO)(OAr_{1H}) containing 0.1 M NBu_4PF_6 showing (a,d) first oxidation and (b,e) second oxidation features at scan rates of 100 mV/s (solid line) and 400 mV/s (dashed line), and (c,f) third oxidation feature at a scan rate of 200 mV/s, respectively.

OAr_{2H} complexes:

The most notable differences observed between the voltammogram of the OAr_{2H} compound (Figure 2.13) from those of the OPh and OAr_{1H} derivatives pertain to the first oxidations. Specifically, the complete irreversibility at all scan rates employed for both porphyrin derivatives and occurs at more positive E_{pa}'s (OEP = +0.58 V; T(*p*-OMe)PP = +0.69 V), indicating the aryloxide is readily dissociated. The first oxidation features occur at more positive E_{pa}'s than the OPh and OAr_{1H} species (OEP = +0.58 V; T(*p*-OMe)PP = +0.69 V) and supports the proposed trend of the electron deficient OAr_{2H} compound being more difficult to oxidize. The second oxidation features (Figure 2.13b) appear to be well-behaved reversible single electron oxidations for both compounds ($E^{\circ\prime}$: OEP = +0.71 V; T(*p*-OMe)PP = +0.78 V), unlike the scan rate-dependent features observed previously in Figures 2.11 and 2.12. I conclude that complete dissociation of the aryloxide ligand following the first oxidation allows increased formation of $[(por)Ru(NO)]^{+}$ and subsequent oxidation to $[(por^{\bullet})Ru(NO)]^{2+}$. As was seen in the OPh and OAr_{1H} complexes, an apparent reversible third oxidation (Figures 2.13c,f) takes place near the edge of the solvent window (OEP = +1.16 V; T(*p*-OMe)PP = +1.08 V) and corresponds to the production of $[(por^{\bullet})Ru(NO)]^{3+}$. Given that there was no detectable difference in any of the redox features within the chosen range of scan rates (50-1600 mV/s), only the data from the 200 mV/s scan rate is shown for the OAr_{2H} complexes in Figure 2.13.

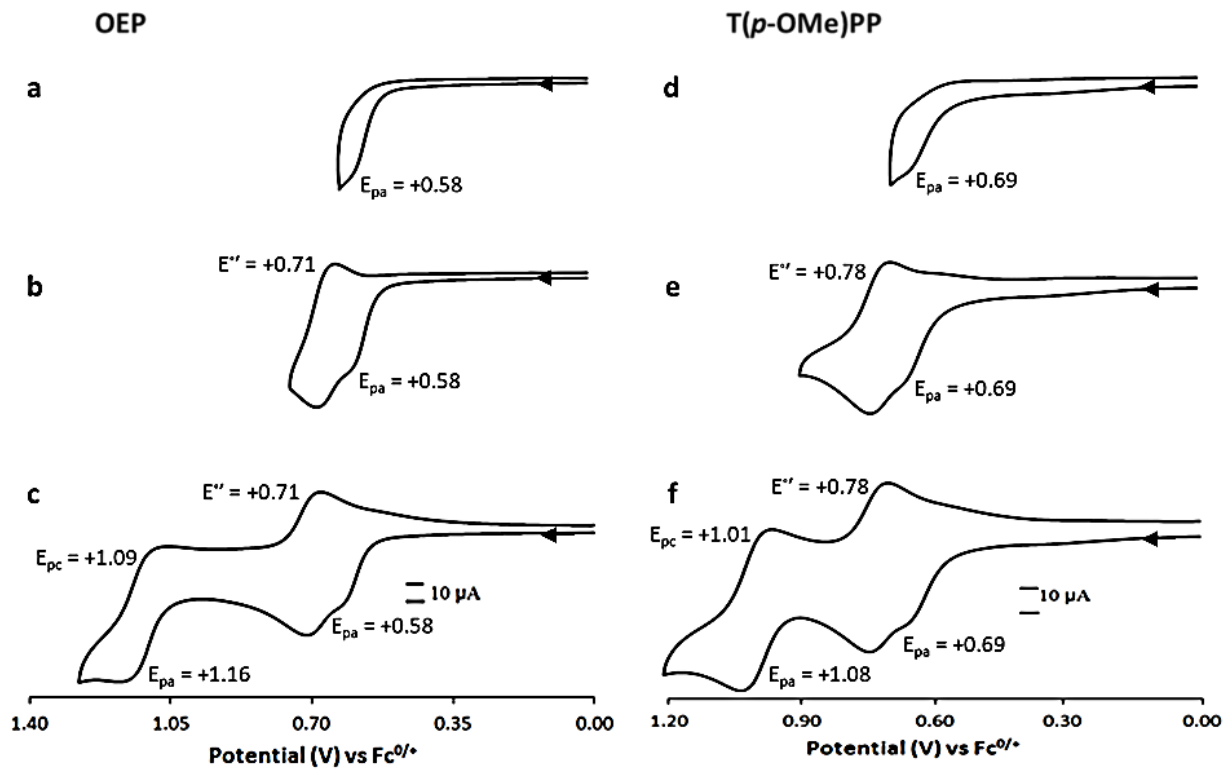

Figure 2.13 Cyclic voltammograms of 1.0 mM (a-c) (OEP)Ru(NO)(OAr_{2H}) and (d-f) (T(*p*-OMe)PP)Ru(NO)(OAr_{2H}) containing 0.1 M NBu_4PF_6 showing (a,d) first oxidation and (b,e) second oxidation features, and (c,f) third oxidation feature at a scan rate of 200 mV/s, respectively.

2.3.4. IR spectroelectrochemistry in CH_2Cl_2

IR spectroelectrochemistry was employed in order to extract structural information and probe the site(s) of oxidation for the electrochemical/chemical processes observed in the cyclic voltammograms in Figures 2.11-2.13. To obtain this information a series of difference IR spectra are recorded prior to and during the application of a predetermined potential, which was chosen to be sufficiently passed the E_{pa} (~50 mV) for each redox event in the voltammogram. I reinvestigated the OEP derivative and begin with its discussion. The IR-SEC results for (OEP)Ru(NO)(OPh) in CH_2Cl_2 containing 0.1 M NBu_4PF_6, illustrating the anodic products generated at the first, second and third oxidations events, are displayed in Figures 2.14a-c. The

difference IR spectrum of (OEP)Ru(NO)(OPh) resulting from the first oxidation (Figure 2.14a) reveals the consumption of the initial ν_{NO} at 1820 cm^{-1} and appearance of a new ν_{NO} at 1876 cm^{-1} ($\Delta\nu_{NO}$ = +56 cm^{-1}) after the analyte was held at a potential of +0.50 V. Appearance of this band on the timescale of the spectroelectrochemical experiment and magnitude of the shift suggests formation of the likely solvated $[(OEP)Ru(NO)]^{+}$ complex following the 1-electron oxidation that results in dissociation of the aryloxide ligand (Eq. 2.1 and 2.2a). An additional low intensity band at 1581 cm^{-1} shifts to 1595 cm^{-1} during the first oxidation as well, which match published values for the $\nu_{C=C}$ of a phenoxide radical and supports the notion of an initial ligand-centered oxidation.[58,59] The electrochemically generated products from holding the potential at +1.00 V (i.e., capturing the second oxidation features) displayed a new ν_{NO} at 1897 cm^{-1} with a shoulder at 1912 cm^{-1}. This $\Delta\nu_{NO}$ of ~20 cm^{-1} (from the first oxidation product) and appearance of the new band at 1529 cm^{-1} are characteristic of a porphyrin-centered oxidation to form the π-radical $[(OEP^{\bullet})Ru(NO)]^{2+}$ complex (Eq. 2.2b).[56,57] The shoulder present during the second oxidation is likely the short-lived $[(OEP)Ru(NO)(OAr_{xH})]^{2+}$ species (Eq. 2.3). However, it is difficult to definitively identify the site of electron removal leading to the dicationic complex, but with a moderate $\Delta\nu_{NO}$ of ~40 cm^{-1} it is likely either a porphyrin- or aryloxide ligand-centered oxidation. When probing the third oxidation (applied potential of +1.30 V) a low intensity band at 1949 cm^{-1} appears, as well as the ν_{NO} bands between 1876-1912 cm^{-1} discussed previously in the first and second oxidations. This new band with a $\Delta\nu_{NO}$ of ~50 cm^{-1} (from the second oxidation product) to higher frequencies has been assigned as a metal-centered oxidation to the newly formed $[(por^{\bullet})Ru(NO)]^{3+}$ complex, which is lower than what is generally expected of a metal-center oxidation in a nitrosyl complex ($\Delta\nu_{NO}$ = ~80 cm^{-1}).[60] Previous reports on the IR spectroelectrochemistry of the related $[(por)Ru(NO)(L)]^{+}$ (por = OEP and TPP; L = H_2O and py)

compounds list the ν_{NO} bands of $[(OEP)Ru(NO)(H_2O)]^+$ at 1877 cm^{-1}, $[(OEP^{\bullet})Ru(NO)(H_2O)]^{2+}$ at 1895 cm^{-1} and $[(OEP^{\bullet})Ru(NO)(H_2O)]^{3+}$ at 1950 cm^{-1} that match the products observed in the oxidations described above (following dissociation of the aryloxide ligand).[56,57]

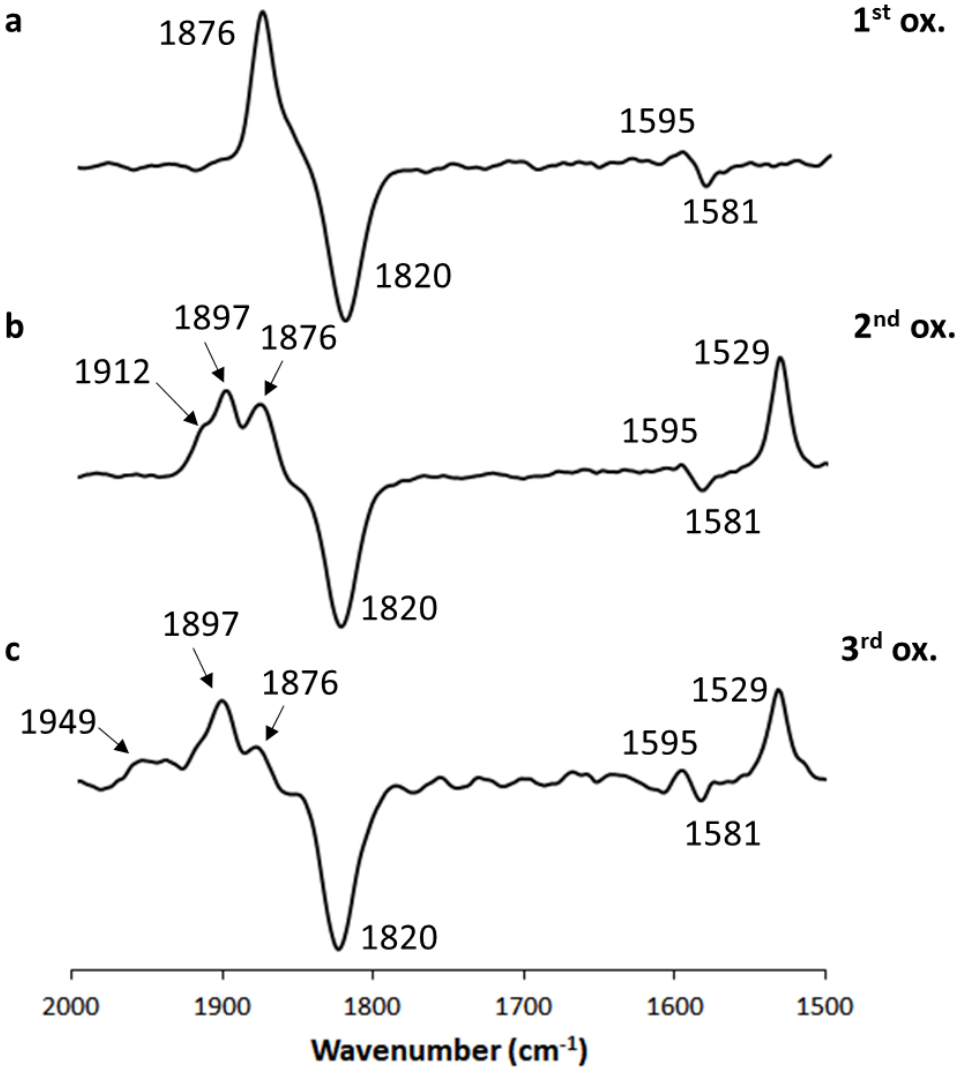

Figure 2.14 Difference IR spectra showing the products from the (a) first, (b) second and (c) third oxidation features of (OEP)Ru(NO)(OPh) in CH_2Cl_2 containing 0.1 M NBu_4PF_6, with the potential held at +0.50, +1.00 and +1.30 V vs $Fc^{0/+}$ couple, respectively.

Analysis of the spectroelectrochemical data for the (OEP)Ru(NO)(OAr_{1H}) compound reveals qualitatively similar results to what was observed for the OPh derivative. Following an applied potential of +0.60 V, the first oxidation reveals the consumption of the initial ν_{NO} at 1836 cm^{-1} and the appearance of the ν_{NO} band at 1876 cm^{-1} ($\Delta\nu_{NO}$ = +40 cm^{-1}). Medium to high intensity bands corresponding to the ν_{CO} of OAr_{1H} also shift to higher frequencies during the first oxidation from 1708 cm^{-1} to 1732 cm^{-1} ($\Delta\nu_{CO}$ = +24 cm^{-1}), in agreement with the proposed site of oxidation . An additional low intensity band at 1589 cm^{-1} shifts to 1612 cm^{-1}, along with an enhancement of the 1541 cm^{-1} band (Figure 2.15a), are associated with changes in the phenolate absorbances. The electrochemically generated products when the applied potential is held at +1.02 V (i.e., after the second oxidation feature) displayed a new ν_{NO} at 1897 cm^{-1} and a shoulder at 1914 cm^{-1} (shoulder observed at 1912 cm^{-1} in OPh complex) with a similar peak enhancement at 1529 cm^{-1}. This product is believed to be the unstable $[(OEP)Ru(NO)(OAr_{1H})]^{2+}$ species. The 1897 cm^{-1} and 1529 cm^{-1} bands in Figure 2.15b were also detected for the OPh derivative (Figure 2.12b). As with the OPh case, the IR bands detected after the first oxidation were present during the second oxidation process. A similar ν_{NO} band to that seen in the OPh at 1949 cm^{-1} appeared when the potential was held at +1.30 V (i.e., encompassing the third oxidation), along with products of the first and second oxidations. With the exception of the proposed $[(OEP)Ru(NO)(OAr_{1H})]^{2+}$ intermediate during the second oxidation, products formed under the described anodic conditions match those of the OPh complex.

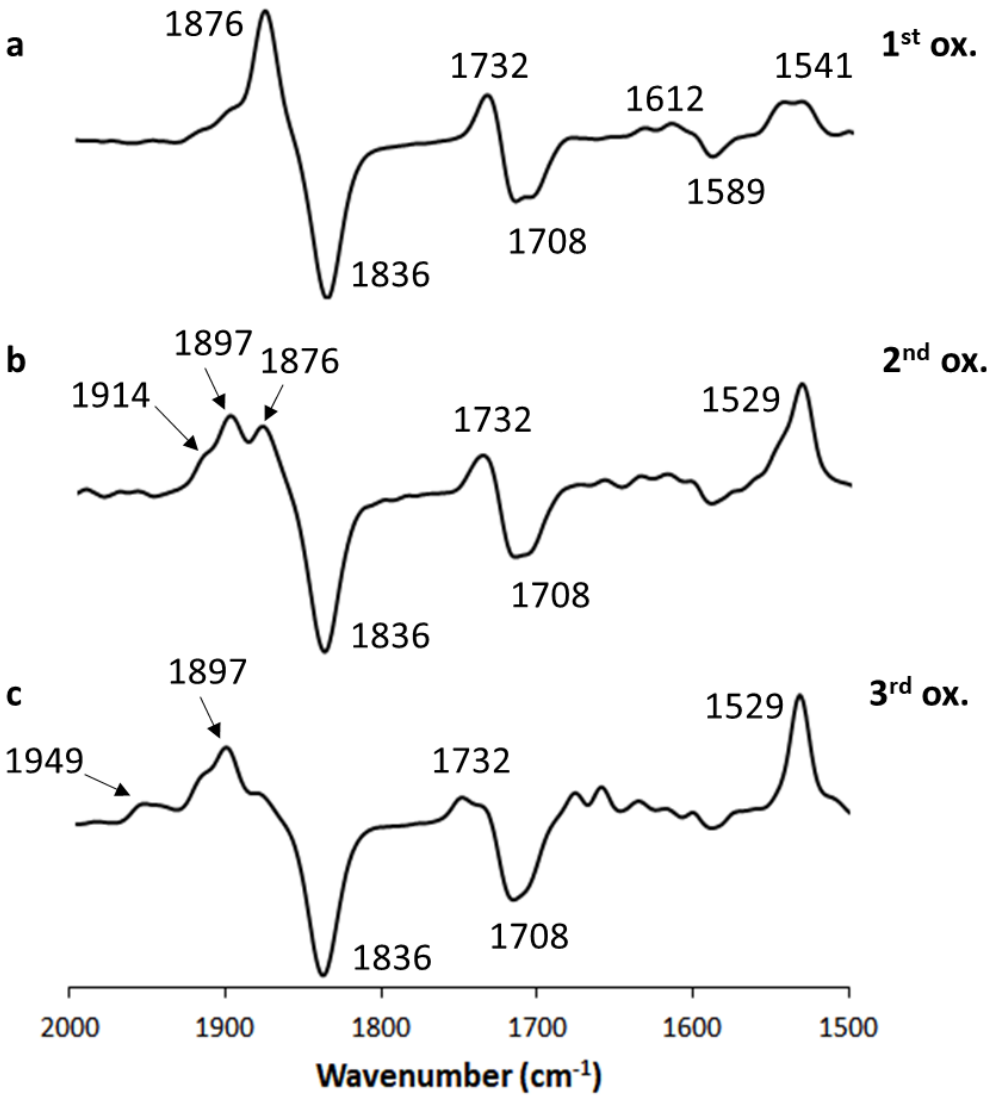

Figure 2.15 Difference IR spectra showing the products from the (a) first, (b) second and (c) third oxidation features of (OEP)Ru(NO)(OAr_{1H}) in CH_2Cl_2 containing 0.1 M NBu_4PF_6, with the potential held at +0.60, +1.02 and +1.30 V vs $Fc^{0/+}$ couple, respectively.

The spectroelectrochemical results for the OAr_{2H} complexes were not unlike those of the OPh and OAr_{1H} analogues (Figure 2.16). The product generated at the first oxidation of the OAr_{2H} compound with an applied potential of +0.62 V results in the appearance of the ν_{NO} band at 1876 cm^{-1} with concomitant consumption of the starting ν_{NO} at 1849 cm^{-1}. Several medium to high intensity bands corresponding to the ν_{CO} of OAr_{2H} underwent changes during the first

oxidation, similar to those seen for the OAr_{1H} case. The ν_{CO} signal shifted from 1714 cm^{-1} to 1735 cm^{-1}, along with a shift of the band at 1591 cm^{-1} to 1616 cm^{-1} and what appear to be enhancements of the 1541 cm^{-1} and 1649 cm^{-1} bands. These are associated with changes in absorbances of the phenolate moiety. Increasing the potential to +1.02 V (i.e., capturing the second oxidation) leads to a new ν_{NO} at 1897 cm^{-1} and an enhancement of the 1529 cm^{-1} band (these were also observed for the OPh and OAr_{1H} complexes). A shoulder at 1918 cm^{-1} was detected with appearance of the ν_{NO} at 1897 cm^{-1}, this band is at a slightly higher frequency that what was seen for the OPh (1912 cm^{-1}) and OAr_{1H} (1914 cm^{-1}) complexes but is believed to reflect formation of the intermediate $[(OEP)Ru(NO)(OAr_{2H})]^{2+}$ complex. Applying a potential of +1.30 V to capture the third oxidation feature yields similar results to the previous compounds with the formation of a new ν_{NO} band at 1949 cm^{-1}. The electrochemically generated oxidation products of OAr_{2H} match those observed in the OPh and OAr_{1H} compounds following dissociation of their respective aryloxide ligands. Specifically, formation of $[(OEP)Ru(NO)]^{+}$ at the first oxidation, $[(OEP^{\bullet})Ru(NO)]^{2+}$ during the second oxidation, and $[(OEP^{\bullet})Ru(NO)]^{3+}$ for the third oxidation. The only significant difference between the compounds were in the proposed intermediate $[(OEP)Ru(NO)(OAr_{xH})]^{2+}$ complexes.

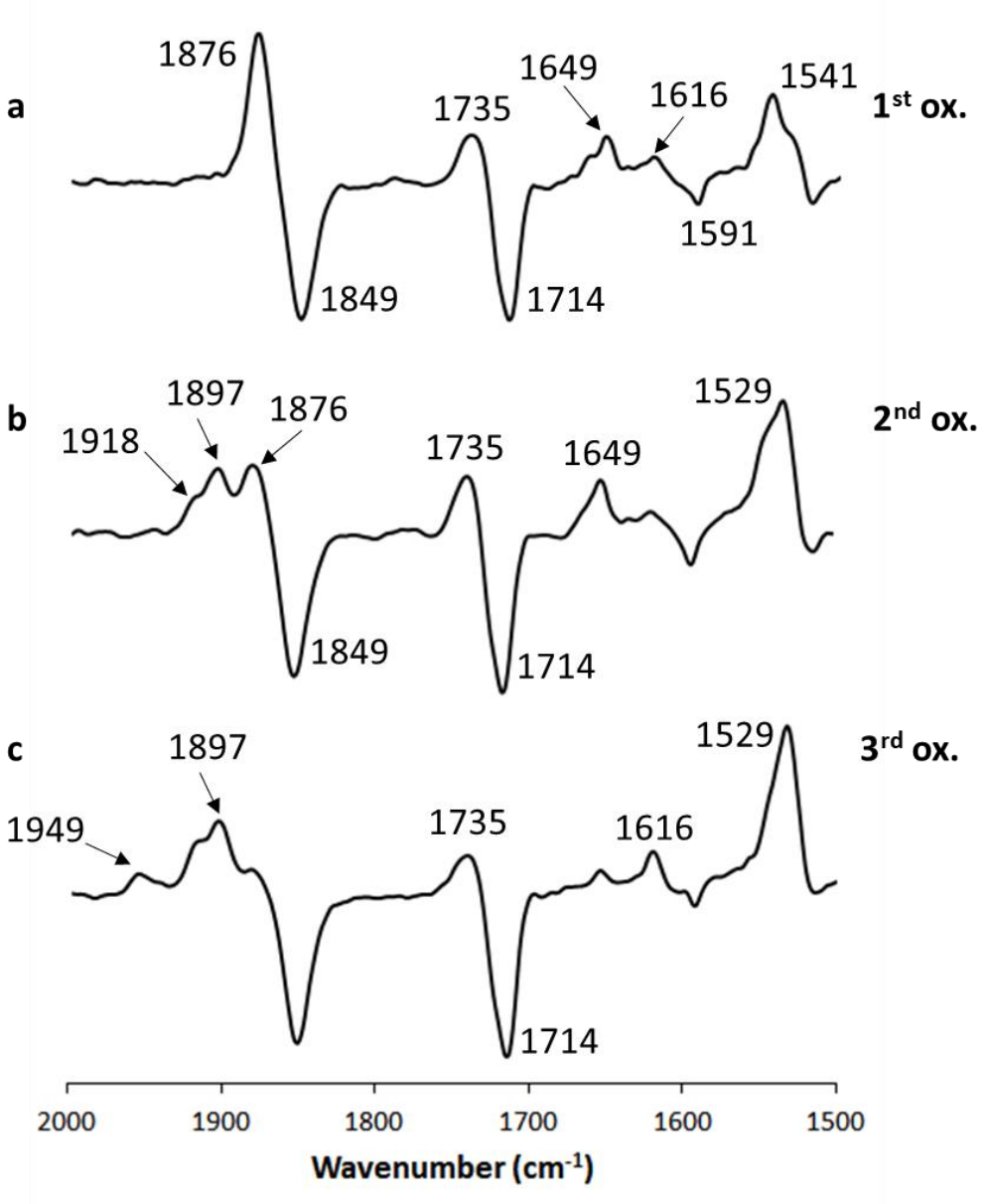

Figure 2.16 Difference IR spectrum showing the products from the (a) first, (b) second and (c) third oxidation features of (OEP)Ru(NO)(OAr_{2H}) in CH_2Cl_2 containing 0.1 M NBu_4PF_6, with the potential held at +0.62, +1.02 and +1.30 V vs $Fc^{0/+}$ couple, respectively.

Table 2.5 lists the ν_{NO} values obtained from the IR-SEC results for the anodic processes. As noted earlier, the IR ν_{NO} bands corresponding to the neutral (por)Ru(NO)(OAr_{xH}) form of the complexes being studied in the supporting electrolyte solution, exhibit a similar trend of increasing ν_{NO} value with increasing number of internal hydrogen bonds, as well as higher ν_{NO}

values in the *meso*-substituted porphyrin compounds (OEP is more electron rich than T(*p*-OMe)PP). The products generated during the first oxidations of all the OEP/OAr_{xH} complexes display new ν_{NO} bands at 1876 cm^{-1} (T(*p*-OMe)PP = 1884 cm^{-1}) with subtle shifts in the 1540-1650 cm^{-1} region corresponding to the various phenolate moieties. Similarly, one of the two ν_{NO} bands observed during the second oxidation (OEP = 1897 cm^{-1}; T(*p*-OMe)PP = 1901 cm^{-1}), as well as the ν_{NO} band in the third oxidation (OEP = 1949 cm^{-1}; T(*p*-OMe)PP = 1956 cm^{-1}), are shared between all the OAr_{xH} complexes. One slight change is observed between these compounds, namely the position of the shoulder at higher wavenumbers associated with the ν_{NO} bands 1876 cm^{-1} (OEP) and 1884 cm^{-1} (T(*p*-OMe)PP) during the second oxidation (OEP = 1912-1918 cm^{-1}; T(*p*-OMe)PP = 1919-1922 cm^{-1}), assigned as the intermediate $[(por)Ru(NO)(OAr_{xH})]^{2+}$ species. Consequently, with the exception of the enhancements corresponding to changes occurring at the porphyrin macrocycle (OEP = 1529 cm^{-1}; T(*p*-OMe)PP = 1600 cm^{-1}), no significant differences were observed between the porphyrin derivatives.

Table 2.5 IR nitrosyl stretching frequencies for the neutral precursors and the electrochemically generated oxidation products of $(por)Ru(NO)(OAr_{xH})$[a].

	Neutral (cm^{-1})	**1st ox (cm^{-1})**	**2nd ox (cm^{-1})**	**3rd ox (cm^{-1})**
OEP				
OPh	1820	1876	1897, 1912	1949
OAr_{1H}	1836	1876	1897, 1914	1949
OAr_{2H}	1849	1876	1897, 1918	1949
T(*p*-OMe)PP				
OPh	1831	1884	1901, 1919	1956
OAr_{1H}	1845	1884	1901, 1921	1956
OAr_{2H}	1856	1884	1901, 1922	1956

[a] Experimental conditions: 1.0 mM analyte in CH_2Cl_2 containing 0.1 M NBu_4PF_6 with a Pt working electrode.

2.3.5. Computational consideration

In an effort to further probe the electronic and redox behavior (e.g., site of oxidation) proposed from the electrochemical and spectroelectrochemical results, I performed DFT calculations of the 6-coordinate (porphine)Ru(NO)(OAr_{xH}) species in the ground state, where "porphine" is the unsubstituted porphyrin macrocycle. Data for the optimized geometries of the various (porphine)Ru(NO)(OAr_{xH}) complexes are listed in Table 2.6 with direct comparisons to the obtained experimental values for both OEP and T(*p*-OMe)PP derivatives. The calculations performed utilized the DGDZVP basis set with a series of functionals (BP86, B3LYP and B3P86) with and without dispersion correction, while also varying the solvent models (gas phase, cyclohexane, *o*-dichlorobenzene) to determine which parameters provide the best match with experimental. It appears that for geometry optimizations, the B3P86 method in conjunction with DGDZVP yields the closest values to those obtained from the (por)Ru(NO)(OAr_{xH}) (por = OEP and T(*p*-OMe)PP) crystal structures. In most instances, slightly improved results were obtained when the *o*-dichlorobenzene solvent model was included. For this work the BP86 and B3LYP functionals appear to overestimate Ru-N(O), Ru-O and ∠RuOC values, while underestimating ∠RuNO. A few of the bonding parameters were significantly different from the experimental values regardless of the functional or solvent model used (e.g., ∠RuNO for OPh and ∠RuOC for OPh and OAr_{1H}).

The extent to which this computational work was conducted reflects more on becoming more adept with DFT, specifically the Gaussian software, than a basis of the intrinsic chemical properties of the complexes being investigated. Particularly during a time when the COVID-19 pandemic led to restrictive access to research labs.

Table 2.6 Calculated bonding parameters of the (porphine)Ru(NO)(OAr_{xH}) optimized geometries.

0-H			**Ru-N(O) (Å)**	**∠RuNO (°)**	**Ru-O (Å)**	**∠RuOC (°)**
Experimental	OEP		1.751(5)	179.3(4)	1.987(4)	124.6(4)
	T(*p*-OMe)PP		1.746(3)	173.6(3)	1.968(2)	131.99(19)
Calculated[a]	BP86	Gas	1.798	163.418	2.011	131.645
		Cy	1.795	164.364	2.016	131.396
		o-DCB	1.791	165.394	2.026	130.901
	B3LYP	Gas	1.785	165.537	2.009	132.334
		Cy	1.781	166.972	2.016	132.018
		o-DCB	1.777	169.634	2.033	130.969
	B3P86	Gas	1.77	166.432	1.991	130.286
		Cy	1.767	167.903	1.998	130.017
		o-DCB	1.763	170.402	2.015	129.085
1-H			**Ru-N(O) (Å)**	**∠RuNO (°)**	**Ru-O (Å)**	**∠RuOC (°)**
Experimental	OEP		1.732(2)	174.3(2)	2.0296(18)	122.28(15)
	T(*p*-OMe)PP		1.810(2)	172.50(14)	1.950(2)	121.60(10)
Calculated[a]	BP86	Gas	1.791	166.024	2.044	133.273
		Cy	1.787	167.646	2.05	133.353
		o-DCB	1.782	170.329	2.06	133.617
	B3LYP	Gas	1.777	168.732	2.04	133.986
		Cy	1.774	170.608	2.049	133.941
		o-DCB	1.77	173.093	2.063	134.386
	B3P86	Gas	1.764	169.16	2.022	131.314
		Cy	1.76	170.915	2.03	131.427
		o-DCB	1.757	173.124	2.043	131.68
2-H			**Ru-N(O) (Å)**	**∠RuNO (°)**	**Ru-O (Å)**	**∠RuOC (°)**
Experimental	OEP		1.734(5)	172.0(4)	2.045(3)	124.5(3)
	T(*p*-OMe)PP		1.716 (5)	179.0(6)	2.029(4)	124.7(3)
Calculated[a]	BP86	Gas	1.785	165.813	2.1	126.513
		Cy	1.782	167.442	2.106	126.463
		o-DCB	1.777	170.789	2.119	125.682
	B3LYP	Gas	1.77	169.828	2.097	127.632
		Cy	1.768	172.044	2.107	127.198
		o-DCB	1.765	174.529	2.124	126.663
	B3P86	Gas	1.757	170.839	2.073	125.286
		Cy	1.755	172.875	2.082	124.995
		o-DCB	1.752	175.167	2.097	124.527

Cy = cyclohexane, *o*-DCB = *o*-dichlorobenzene;
[a] DGDZVP basis set

The same approach of utilizing various functionals and solvent models was applied in the vibrational frequency analysis of the (porphine)Ru(NO)(OAr_{xH}) complexes as well. The values

in Table 2.7 were obtained from the optimized geometries in Table 2.6, and that the experimental ν_{NO} values were recorded for the complexes as KBr pellets. No imaginary frequencies were observed in the vibrational frequency analyses. While the B3P86 functional appears to yield results closest to the experimentally obtained ν_{NO} values, a scaling factor of 0.93 was required. Using the BP86 functional provided results that were not significantly far off from the ν_{NO} results in B3P86, although utilizing BP86 resulted in ν_{CO} frequencies much closer to the experimental values while significantly overestimating the ν_{NH} frequencies (B3P86 considerably underestimated both ν_{CO} and ν_{NH} values). However, using B3LYP on the B3P86 optimized structure was the most accurate in determining the ν_{NH} frequencies, although a scaling factor 0.95 was applied with this functional.

Table 2.7 Calculated vibrational frequency analyses of the (porphine)Ru(NO)(OAr_{xH}) optimized geometries employing the B3P86 functional and DGDZVP basis set.

0-H			**ν_{NO} (cm^{-1})**	**ν_{CO} (cm^{-1})**	**ν_{NH} (cm^{-1})**
Experimental	OEP		1823	-	-
	T(*p*-OMe)PP		1828	-	-
Calculated[a]	BP86	Gas	1807.1	-	-
		Cy	1798.7	-	-
		o-DCB	1791.3	-	-
	B3LYP[b]	Gas	1803.2	-	-
		Cy	1796.5	-	-
		o-DCB	1792.7	-	-
	B3P86[c]	Gas	1807.5	-	-
		Cy	1800.8	-	-
		o-DCB	1796.8	-	-
1-H			**ν_{NO} (cm^{-1})**	**ν_{CO} (cm^{-1})**	**ν_{NH} (cm^{-1})**
Experimental	OEP		1830	1718	3336
	T(*p*-OMe)PP		1833	1720	3349
Calculated[a]	BP86	Gas	1823	1710	3404.5
		Cy	1818.9	1696.8	3396.9
		o-DCB	1815.9	1678	3389.8
	B3LYP[b]	Gas	1821.1	1684.2	3360.8
		Cy	1816.6	1669.4	3350.7
		o-DCB	1813.4	1648.7	3342.5
	B3P86[c]	Gas	1824.1	1673.3	3288.2
		Cy	1819.6	1659.3	3276.9

		o-DCB	1815.7	1639.4	3268.5
2-H			**ν_{NO} (cm^{-1})**	**ν_{CO} (cm^{-1})**	**ν_{NH} (cm^{-1})**
Experimental	OEP		1843	1722	3341, 3367
	T(*p*-OMe)PP		1849	1716	3339, 3371
Calculated[a]	BP86	Gas	1834.1	1713.6, 1708.8 (2:1)	3424.1, 3425.8 (2:7)
		Cy	1830.1	1702.7, 1696.1 (9:4)	3411.1, 3420.1 (6:7)
		o-DCB	1830.5	1687.5, 1677.8 (3:1)	3403.0, 3412.2 (7:8)
	B3LYP[b]	Gas	1834.3	1687.6, 1683 (2:1)	3370.7, 3374.9 (3:4)
		Cy	1831.4	1675.4, 1668.9 (5:2)	3363.2, 3368.8 (4:5)
		o-DCB	1828.8	1658.8, 1649.5 (7:2)	3357.6, 3358.7 (3:10)
	B3P86[c]	Gas	1837.9	1677.1, 1672.1 (7:3)	3297.4, 3304.0 (4:5)
		Cy	1834.7	1665.6, 1658.8 (8:3)	3289.7, 3296.5 (5:6)
		o-DCB	1831.7	1649.3, 1639.6 (7:2)	3278.9, 3287.1 (7:8)

[a] DGDZVP basis set
[b] Scaling Factor: 0.95
[c] Scaling Factor: 0.93
Cy = cyclohexane, *o*-DCB = *o*-dichlorobenzene
Values in parentheses below calculated frequencies are the corresponding relative intensities

To reconcile results obtained from cyclic voltammetry and IR spectroelectrochemistry data, electron density maps of the frontier molecular orbitals were calculated in the gas phase of the 6-coordinate (porphine)Ru(NO)(OAr_{xH}) species from the previously optimized geometries using the DGDZVP basis set and B3P86 functional that yielded the closest results to those obtained experimentally for the OEP derivatives. As seen in Figures 2.17a-c, the primary contribution of electron density in the HOMO is attributed to the axial aryloxide ligand in all three 6-coordinate complexes (OPh, OAr_{1H} and OAr_{2H}), with a minor contribution from the bound Ru-NO fragment. Extending these calculations to a 5-coordinate $[(porphine)Ru(NO)]^+$ (Figure 2.17d) complex reveals the majority of the electron density in the HOMO is located on

the porphine macrocycle, specifically, the α- and β-carbons. These results are consistent with the notion that the first oxidation (electron removal) of the (por)Ru(NO)(OAr_{xH}) compounds occur along the axial ON-Ru-OC moiety with a large contribution from the phenoxide ligands, a process that will likely result in dissociation of the aryloxide moiety. Such an electrochemical step (Eq. 2.1a) followed by a chemical step (Eq. 2.1b) will be consistent with the apparent low chemical reversibility features seen in the cyclic voltammograms in Figures 2.11a, 2.12a and 2.13a at slow scan rates (100 mV/s). Faster scan rates (400 mV/s) would thus increase reversibility by minimizing the probability of the dissociation step in Eq. 2.1b. As mentioned earlier, the HOMO electron density map for the $[(porphine)Ru(NO)]^+$ (Figure 2.17d) is consistent with a porphyrin-centered oxidation to form the π-radical cation observed in the spectroelectrochemical experiments.

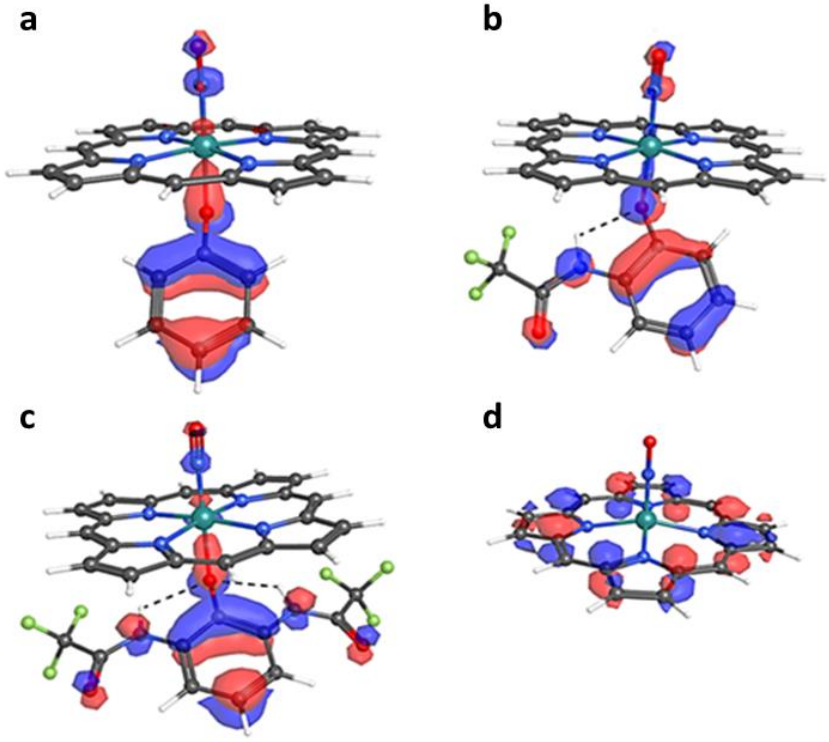

Figure 2.17 Calculated frontier molecular orbitals (HOMO) from the optimized geometries of the 6-coordinate (porphine)Ru(NO)(OAr_{xH}); x = (a) 0, (b) 1, (c) 2, and (d) a 5-coordinate $[(porphine)Ru(NO)]^+$ complex.

2.3.6. Chemical oxidation: spectroscopy and molecular structure of (OEP)Ru(NO)($OPOF_2$)

To supplement the cyclic voltammetry, IR spectroelectrochemistry and DFT results, and in an attempt to confirm the proposed mechanism of the first oxidation process, a chemical oxidation of (OEP)Ru(NO)(OAr_{2H}) was performed using $AgPF_6$ as the oxidant. A comparison of the IR spectra prior to and following the chemical oxidation of (OEP)Ru(NO)(OAr_{2H}) with $AgPF_6$ is shown in Figure 2.18. The disappearance of the ν_{CO} at 1722 cm^{-1} associated with the aryloxide ligand is observed in the spectrum of the crystallized oxidation product, obtained in 31% yield, along with a slight shift of the ν_{NO} band to a higher frequency at 1855 cm^{-1} ($\Delta\nu_{NO}$ = +12 cm^{-1}). Additionally, new peaks at 1124 cm^{-1} and 1312 cm^{-1} were detected and match previously reported values for the ν_{PO} bands corresponding to a coordinated $OPOF_2^-$ ligand.[61] Formation of $OPOF_2^-$ from PF_6^- is the result of hydrolysis, likely during the crystallization process due to adventitious air. Shifting of the ν_{NO} to slightly higher frequencies and simultaneous disappearance of the ν_{CO} band implies dissociation and subsequent substitution of the OAr_{2H} ligand (Figure 2.18b).

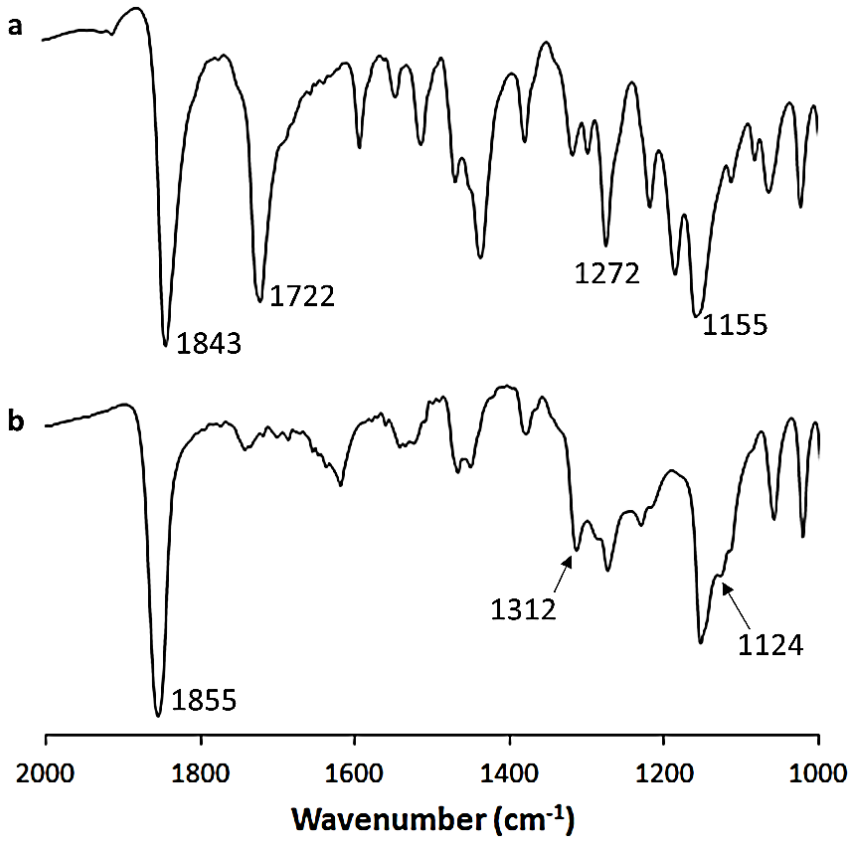

Figure 2.18 IR spectra of (OEP)Ru(NO)(OAr_{2H}) (a) before and (b) after chemical oxidation with $AgPF_6$, highlighting the ν_{PO} signals at 1124 cm^{-1} and 1312 cm^{-1}.

The ^{1}H NMR spectrum of the crystallized oxidation product (Figure 2.19) displays the absence of all the phenolate protons previously observed in the aryloxide complex, supporting the proposed dissociation of the aryloxide ligand. Peaks associated with the *meso*- and ethyl-H's of the OEP macrocycle are retained with a minimal chemical shift of the *meso*-H's to 10.44 ppm ($\Delta\delta$ = 0.1 ppm). Although the only proton signals detected correspond to the porphyrin macrocycle, a triplet in the ^{31}P NMR spectrum (Figure 2.19 inset) is observed at -25.97 ppm (referenced to H_3PO_4) matching published values for a coordinated $OPOF_2^-$.[62]

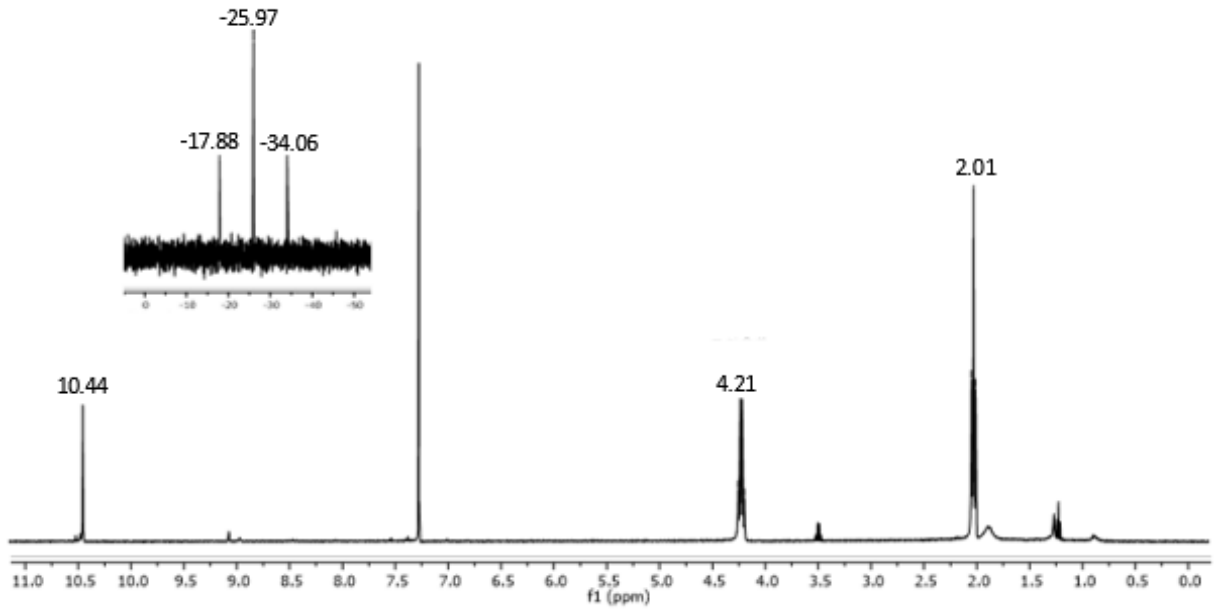

Figure 2.19 ^{1}H and ^{31}P NMR (inset) spectra of the crystallized product from the chemical oxidation of (OEP)Ru(NO)(OAr_{2H}) with $AgPF_6$ in $CDCl_3$.

A preliminary molecular structure was obtained for the crystallized oxidation product of (OEP)Ru(NO)(OAr_{2H}) with $AgPF_6$. However, the intensity data collected was not sufficient to obtain a publishable finalized structure. This approximate model in Figure 2.20 displays Ru-N(O) (Ru1-N5(O1)) and Ru-O(POF_2) (Ru1-O3) components in the *trans* position. It is likely the [(OEP)Ru(NO)]PF_6 is generated followed by anion reactivity with trace air to give the coordinated $OPOF_2^-$ ligand. Coordination of the $OPOF_2^-$ to the cation $[(OEP)Ru(NO)]^+$ results in a (OEP)Ru(NO)(*O*-ligand) product, and accounts for the minimal observed $\Delta\nu_{NO}$ of only 12 cm^{-1}. These results are consistent with the proposed EC mechanism for the first oxidation, which follows a single electron transfer resulting in dissociation of the aryloxide ligand.

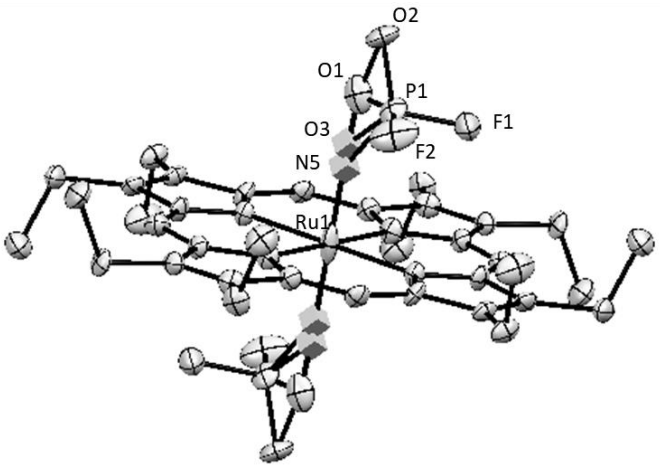

Figure 2.20 Preliminary molecular structure for the crystallized chemical oxidation product of (OEP)Ru(NO)(OAr_{2H}) with $AgPF_6$.

2.4. Summary and Conclusions

This study demonstrates the spectroscopic and structural properties of NO-bound Ru porphyrins and investigates the effect of the internal hydrogen bonding network present in these compounds through the preparation and electrochemical investigation of the model compounds (por)Ru(NO)(OAr_{xH}) (por = OEP and T(*p*-OMe)PP; x = 0, 1 and 2). The IR data reveals higher ν_{NO} frequencies in complexes with an increasing number of internal hydrogen bonds. This shift is the result of a decrease in electron density at the oxygen atom through these internal hydrogen bonds leading to diminished π-backdonation to the Ru-NO fragment. The structural information of the OEP complexes exhibited slightly less linear ∠RuNO bond angles and longer Ru-O bond lengths with increasing intramolecular hydrogen bonds, which may be competing with the Ru center for non-bonding lone pair electrons on the oxygen. ^{1}H NMR spectra of the T(*p*-OMe)PP derivatives display unique splitting patterns for the tetraaryl substituents on the porphyrin macrocycle, due to the axially unsymmetric environments around the porphyrin macrocycle.

The anodic behavior of these complexes has shown that the redox potential for the first oxidation is increasingly positive with more intramolecular hydrogen bonds present (i.e., requiring a higher potential to oxidize). A 1-electron first oxidation and subsequent chemical process was observed that becomes more reversible at faster scan rates (> 200 mV/s) for the OPh and OAr_{1H} compounds, while the oxidations of the OAr_{2H} derivatives were chemically irreversible at all scan rates employed. The proposed successive chemical step was probed by IR spectroelectrochemistry which suggested an aryloxide ligand-centered oxidation and dissociation to generate what is likely a solvated $[(por)Ru(NO)]^{+}$ complex. This was confirmed via chemical oxidation of $(OEP)Ru(NO)(OAr_{2H})$ with $AgPF_6$, yielding the loss of the OAr_{2H} ligand and coordination of a $OPOF_2^{-}$ (following PF_6^{-} hydrolysis) ligand. A proposed short-lived $[(por)Ru(NO)(OAr_{xH})]^{2+}$ intermediate appears to form during the second oxidation at more positive potentials than the scan rate-dependent generation of the porphyrin π-radical $[(por^{\bullet})Ru(NO)]^{2+}$ species. It is difficult to definitively assign the identity of the intermediate since immediate irreversible dissociation of the aryloxide takes place to produce more of the dicationic radical complex. DFT calculations show that for the frontier molecular orbitals of these $(porphine)Ru(NO)(OAr_{xH})$ complexes are in support of the proposed EC mechanism for the first oxidation and a porphyrin-centered second oxidation to generate the π-radical cation as the primary product. The third oxidations for these complexes occur near the solvent limit and display low intensity bands matching those of a $[(por^{\bullet})Ru(NO)]^{3+}$ product. These Ru-NO complexes offer an advantage over the unstable iron analogues of biologically relevant protein model complexes with metal bound tyrosinate.

2.5 References

1. Reid, T. J.; Murthy, M. R. N.; Sicignano, A.; Tanaka, N.; Musick, W. D. L.; Rossmann, M. G. *Proc. Natl. Acad. Sci*. **1981**, *78*, 4767–4771.

2. Ko, T. P.; Day, J.; Malkin, A. J.; McPherson, A. *Acta Cryst*. **1999**, *D55*, 1383–1394.

3. Murshudov, G. N.; Grebenko, A. I.; Brannigan, J. A.; Antson, A. A.; Barynin, V.; Dodson, G. G.; Dauter, Z.; Wilson, K. S.; Melik-Adamyan, W. R. *Acta Cryst*. **2002**, *D58*, 1972–1982.

4. Schoch, G. A.; Yano, J. K.; Wester, M. R.; Griffin, K. J.; Stout, C. D.; Johnson, E. F. *J. Biol. Chem.* **2004**, *279*, 9497-9503.

5. Scott, E. E.; He, Y. A.; Wester, M. R.; White, M. A.; Chin, C. C.; Halpert, J. R.; Johnson, E. F.; Stout, C. D. *Proc. Natl. Acad. Sci.* **2003**, *100*, 13196-13201.

6. Wester, M. R.; Johnson, E. F.; Marques-Soares, C.; Dijols, S.; Dansette, P. M.; Mansuy, D.; Stout, C. D. *Biochem.* **2003**, *42*, 9335-9345.

7. Yano, J. K.; Wester, M. R.; Schoch, G. A.; Griffin, K. J.; Stout, C. D.; Johnson, E. F. *J. Biol. Chem.* **2004**, *279*, 38091-38094.

8. Williams, P. A.; Cosme, J.; Sridhar, V.; Johnson, E. F.; McRee, D. E. *Mol. Cells*. **2000**, *5*, 121-131.

9. Williams, P. A.; Cosme, J.; Ward, A.; Angove, H. C.; Matak Vinkovic, D.; Jhoti, H. *Nature*. **2003**, *424*, 464-468.

10. Williams, P. A.; Cosme, J.; Vinkovic, D. M.; Ward, A.; Angove, H. C.; Day, P. J.; Vonrhein, C.; Tickle, I. J.; Jhoti, H. *Science.* **2004**, *305*, 683-686.

11. Wester, M. R.; Yano, J. K.; Schoch, G. A.; Yang, C.; Griffin, K. J.; Stout, C. D.; Johnson, E. F. *J. Biol. Chem.* **2004**, *279*, 35630-35637.

12. Voegtle, H. L.; Sono, M.; Adak, S.; Pond, A. E.; Tomita, T.; Perera, R.; Goodin, D. B.; Ikeda-Saito, M.; Stuehr, D. J.; Dawson, J. H. *Biochemistry*. **2003**, *42*, 2475-2484.

13. Wilson, D. J.; Rafferty, S. P. *Biochem. Biophys. Res. Comm*. **2001**, *287*, 126-129.

14. Couture, M.; Adak, S.; Stuehr, D. J.; Rousseau, D. L. *J. Biol. Chem*. **2001**, *276*, 38280-38288.

15. Adak, S.; Crooks, C.; Wang, Q.; Crane, B. R.; Tainer, J. A.; Getzoff, E. D.; Stuehr, D. J. J. *Biol. Chem*. **1999**, *274*, 26907-26911.

16. Jeoung, J.-H.; Pippig, D. A.; Martins, B. M.; Wagener, N.; Dobbek, J. *J. Mol. Biol*. **2007**, *368*, 1122–1131.

17. Oldham, M. L.; Brash, A. R.; Newcomer, M. E. *Proc. Natl. Acad. Soc.* **2005**, *102*, 297-302.

18. Genga, J.; Dornevil, K.; Davidson, V. L.; Liu, A. *Proc. Natl. Acad. Soc.* **2013**, *110*, 9639-9644.

19. Gaudin, C. F. M.; Grigg, J. C.; Arrieta, A. L.; Murphy, M. E. P. *Biochem.* **2011**, *50*, 5443-5452.

20. Zink, J. R.; Abucayon, E. G.; Ramuglia, A. R.; Fadamin, A.; Eilers, J. E.; Richter-Addo, G. B.; Shaw, M. J. *ChemElectroChem*. **2018**, *5*, 861-871.

21. Abucayon, E. G.; Powell, D. R.; Richter-Addo, G. B. *J. Am. Chem. Soc*. **2017**, *139*, 9495-9498.

22. Yi, B.-B.; Khan, M. A.; Powell, D. R.; Richter-Addo, G. B. *Inorg. Chem*. **1998**, *37*, 208-214.

23. Lee, J.; Twamley, B.; Richter-Addo, G. B. *Dalton Trans*. **2004**, *2*, 189-196.

24. Yi, G.-B.; Khan, M. A.; Richter-Addo, G. B. *Inorg. Chem*. **1996**, *35*, 3453-3454.

25. Awasabisah, D.; Xu, N.; Sharmah Gautam, K. P.; Powell, D. R.; Shaw, M. J.; Richter-Addo, G. B. *Dalton Trans*. **2013**, *42*, 8537-8540.

26. Carter, S. M.; Lee, J.; Hixson, C. A.; Powell, D. R.; Wheeler, R. A.; Shaw, M. J.; Richter-Addo, G. B. *Dalton Trans*. **2006**, *10*, 1338-1346.

27. Fomitchev, D. V.; Coppens, P.; Li, T.; Bagley, K. A.; Chen, L.; Richter-Addo, G. B. *Chem. Comm*. **1999**, *19*, 2013-2014.

28. Lee, J.; Yi, G.-B.; Khan, M. A.; Richter-Addo, G. B. *Inorg. Chem*. **1999**, *38*, 4578-4584.

29. Yi, G.-B.; Chen, L.; Khan, M. A.; Richter-Addo, G. B. *Inorg. Chem*. **1997**, *36*, 3876-3885.

30. Awasabisah, D.; Xu, N.; Sharmah Gutman, K. P.; Powell, D. R.; Shaw, M. J.; Richter-Addo, G. B. *Eur. J. Inorg.* **2016**, *19*, 509-518.

31. Cheng, L.; Powell, D. R.; Khan, M. A.; Richter-Addo, G. B. *Inorg. Chem.* **2001**, *40*, 125-133.

32. Bohle, D. S.; Goodson, P. A.; Smith, B. D. *Polyhedron*. **1996**, *15*, 3147-3150.

33. Antipas, A.; Buchler, J. W.; Gouterman, M.; Smith, P. D. *J. Am. Chem. Soc.* **1978**, *100*, 3015-3024.

34. Bohle, D. S.; Hung, C.-H.; Smith, B. D. *Inorg. Chem.* **1998**, *37*, 5798-5806.

35. Paulson, D. R.; Addison, A. W.; Dolphin, D.; James, B. R. *J. Biol. Chem*. **1979**, *254*, 7002-7006.

36. Groves, John. T.; Quinn, R. *Inorg. Chem*. **1984**, *23*, 3844-3846.

37. Higuchi, T.; Hirobe, M. *J. Mol. Cat.* **1996**, *113*, 403-422.

38. Reboucas, J. S.; Patrick, B. O.; James, B. R. *J. Am. Chem. Soc*. **2012**, *134*, 3555-3570.

39. Gonzalez, E.; Brothers, P. J.; Ghosh, A. *J. Phys. Chem*. **2010**, *114*, 15380-15388.

40. Warhausen, A. J. Ph.D. Dissertation, University of Oklahoma, 2011.

41. Kanamori, D.; Yamada, Y.; Onoda, A.; Okamura, T.; Adachi, S.; Yamamoto, H.; Ueyama,N. *Inorganica Chimica Acta.* **2005**, *358*, 331-338.

42. Ueyama, N.; Nishikawa, N.; Yamada, Y.; Okamura, T.; Nakamura, A. *Inorg. Chim. Acta*. **1998**, *283*, 91-97.

43. Imbeaux, J. C.; Saveant, J. M. *J. Electroanal. Chem. Interf. Electrochem.* **1973**, *44*, 169-187.

44. Frisch, M. J.; Trucks, G. W.; Schlegel, H. B.; Scuseria, G. E.; Robb, M. A.; Cheeseman, J. R.; Scalmani, G.; Barone, V.; Mennucci, B.; Petersson, G. A.; Nakatsuji, H.; Caricato, M.; Li, X.; Hratchian, H. P.; Izmaylov, A. F.; Bloino, J.; Zheng, G.; Sonnenberg, J. L.; Hada, M.; Ehara, M.; Toyota, K.; Fukuda, R.; Hasegawa, J.; Ishida, M.; Nakajima, T.; Honda, Y.; Kitao, O.; Nakai, H.; Vreven, T.; Montgomery Jr., J. A.; Peralta, J. E.; Ogliaro, F.; Bearpark, M. J.; Heyd, J.; Brothers, E. N.; Kudin, K. N.; Staroverov, V. N.; Kobayashi, R.; Normand, J.; Raghavachari, K.; Rendell, A. P.; Burant, J. C.; Iyengar, S. S.; Tomasi, J.; Cossi, M.; Rega, N.; Millam, N. J.; Klene, M.; Knox, J. E.; Cross, J. B.; Bakken, V.; Adamo, C.; Jaramillo, J.; Gomperts, R.; Stratmann, R. E.; Yazyev, O.; Austin, A. J.; Cammi, R.; Pomelli, C.; Ochterski, J. W.; Martin, R. L.; Morokuma, K.; Zakrzewski, V. G.; Voth, G. A.; Salvador, P.; Dannenberg, J. J.; Dapprich, S.; Daniels, A. D.; Farkas, Ö.; Foresman, J. B.; Ortiz, J. V.; Cioslowski, J.; Fox, D. J.; Gaussian, Inc.: Wallingford, CT, USA, 2009.

45. Carter, S. M. Ph.D. Dissertation, University of Oklahoma, 2006.

46. Shaffer, C. D. and Straub, D. K. *Inorg. Chim. Acta*. **1989**, *158*, 167-180.

47. Xu, N.; Powell, D. R.; Cheng, L.; Richter-Addo, G. B. *Chem. Comm.* **2006**, 2030–2032.

48. Xu, N.; Lee, J.; Powell, D. R.; Richter-Addo, G. B. *Inorg. Chim. Acta*. **2005**, *358*, 2855–2860.

49. Xu, N.; Lilly, J.; Powell, D. R.; Richter-Addo, G. B. *Organometallics*. **2012**, *31*, 827-834.

50. Eaton, S. S. and Eaton, G. R. *J. Am. Chem. Soc.* **1977**, *99*, 6594-6599.

51. Eaton, S. S. and Eaton, G. R. *J. Am. Chem. Soc.* **1974**, *97*, 3660-3666.

52. Purwar, N.; McGarry, J. M.; Kostera, J.; Pacheco, A. A.; Schmidt, M. *Biochemistry*. **2011**, *50*, 4491-4503.

53. Chisholm, M. H. *Chemtracts: Inorg. Chem.* **1992**, *4*, 273-301.

54. Mabbott, G. A. *J. Chem. Ed.* **1983**, *60*, 697-702.

55. Saveant, J. M.; Editor, *Elements of Molecular and Biomolecular Electrochemistry: An Electrochemical Approach to Electron Transfer Chemistry*. John Wiley & Sons, Inc.: 2006; 7-22.

56. Singh, P.; Kumar Das, A.; Sarkar, B.; Niemeyer, M.; Roncaroli, F.; Olabe, J. A.; Fiedler, J.; Zalis, S.; Kaim, W. *Inorg. Chem.* **2008**, *47*, 7106-7113.

57. Kadish, K. M.; Adamian, V. A.; Van Caemelbecke, E.; Tan, Z.; Tagliatesta, P.; Bianco, P.; Boschi, T.; Yi, G.-B.; Khan, M. A.; Richter-Addo, G. B. *Inorg. Chem.* **1996,** *35*, 1343-1348.

58. Schnepf, R.; Sokolowski, A.; Muller, J.; Bachler, V.; Wieghardt, K.; Hildebrandt, P. *J. Am. Chem. Soc.* **1998**, *120*, 2352-2364.

59. Spanget-Larsen, J.; Gil, M.; Gorski, A.; Blake, D. M.; Waluk, J.; Radziszewski, J. G. *J. Am. Chem. Soc.* **2001**, *123*, 11253-11261.

60. Sieger, M.; Sarkar, B.; Zailas, S.; Fiedler, J.; Escola, N.; Doctorovich, F.; Olabe, J. A.; Kaim, W. *Dalton Trans*. **2004**, *12*, 1797-1800.

61. Bruno, G.; Schiavo, S. L.; Piraino, P.; Faraone, F. *Organometallics*. **1985**, *4*, 1098-1100.

62. Bauer, H.; Nagel, U.; Beck, W. *J. Organomet. Chem*. **1985**, *290*, 219-229.

Chapter 3: Nitroxyl (HNO) complexes of Ruthenium porphyrins

3.1. Introduction

Nitroxyl (HNO) is the conjugate acid of the 1-electron redox partner of nitric oxide (NO). HNO is believed to be capable of both muscle relaxation and contraction, making it an attractive treatment for heart failure.[1] In addition to the potential role of free HNO in mammalian physiology, heme-HNO species have been considered active intermediates in several vital biological processes involving cytochrome P450 NO reductase (P450nor), cytochrome cd_1 and hydroxylamine oxidoreductase (HAO). Heme-HNO intermediates in biology may be generated either from proton attack at a reduced NO moiety, such as proposed in ccNiR,[2,3] or from hydride attack by NADH at the ferric-NO center in P450nor (Figure 3.1) during NO detoxification by fungi.[4,5] Elegant work by the Farmer group resulted in detailed spectroscopic characterization of a Mb-HNO adduct via the HNO donor compounds Angeli's salt and MHSA.[6] Several reviews have detailed many other commonly used HNO donor compounds, their pharmacological potential and interaction with metalloporphyrins.[7-11]

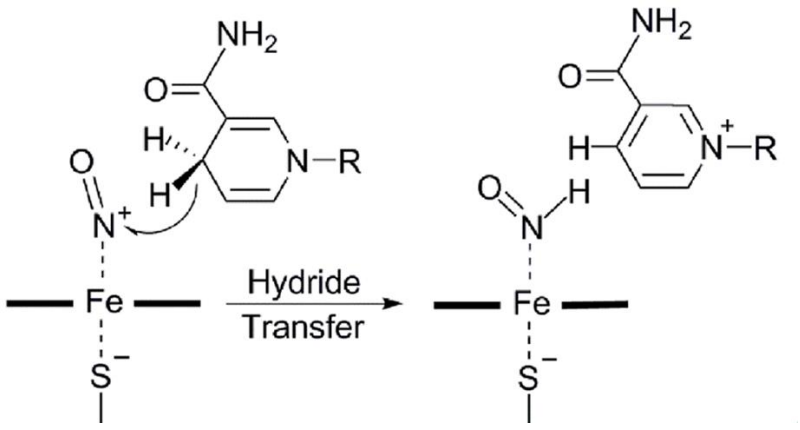

Fig. 3.1 Hydride attack at the ferric-NO moiety in P450nor by NADH.

Synthetic routes most commonly employed in the generation of heme model and non-heme metal HNO complexes appear to mimic those observed in nature mentioned previously, including nucleophilic attack (H^- at M-NO^+),[12-16] protonation (H^+ at M-NO^-)[17-22] and use of known HNO donors.[6,23,24] Our group has shown previous success in preparing heme model compounds with both Fe-HNO[12,13] and Ru-HNO[14] by hydride attack of the M-NO^+ precursor complexes. The biologically relevant iron analogues proved to be extremely unstable, decomposing almost immediately upon formation, as shown spectroscopically.[12,13] Although the published (TTP)Ru(HNO)(1-MeIm) compound was notably more stable, no significant efforts were made into studying its reactivity. There have been reports investigating the reactivity of freshly generated free HNO with thiols,[25] dienes[26-28] and nitrosobenzene[29] as well as complexed Fe-HNO with triphenylphosphine[12,13,30] and nitric oxide[13]. In this chapter, several derivatives of (por)Ru(HNO)(L_{Im}) (por = TPP, T(*p*-OMe)PP, T(*p*-Cl)PP; L_{Im} = 1-methylimidazole, 1-ethylimidazole, 1-phenylimidazole) have been prepared and characterized, along with a series of reactivity studies using the representative sample (TPP)Ru(HNO)(1-MeIm).

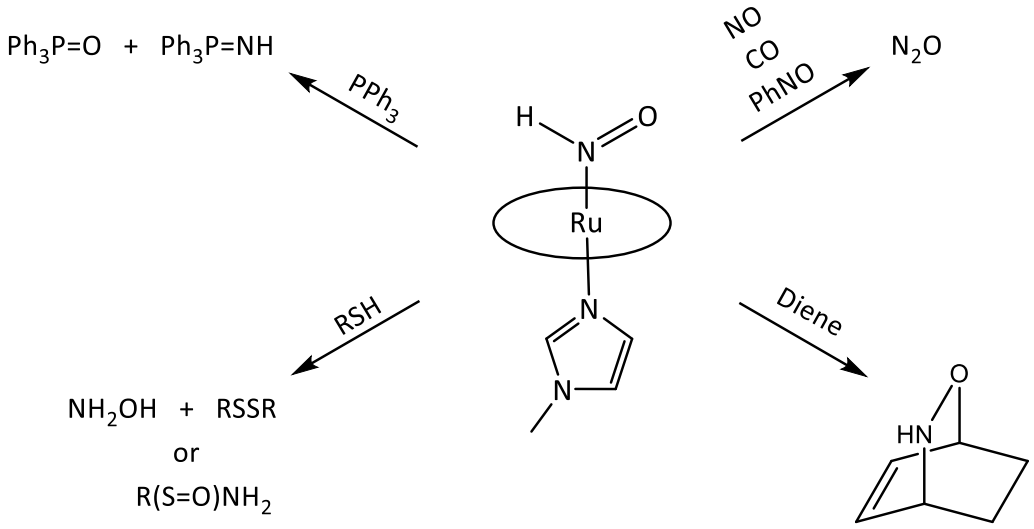

Figure 3.2 Depiction of the reactivity studies of (TPP)Ru(HNO)(1-MeIm) with various reagents and their expected products.

3.2. Materials and Methods

All reactions were performed under an anaerobic (N_2) atmosphere using standard Schlenk glassware and/or in an Innovative Technology Labmaster 100 Dry Box. Solutions for spectral studies were also prepared under a nitrogen atmosphere. Dichloromethane and n-hexane used in the experiments were dried using an Innovative Technology Inc. Pure Solv 400-5-MD Solvent Purification System. Compounds (por)Ru(CO) (por = T(*p*-OMe)PP, TPP, T(*p*-Cl)PP),[31] $^{15}NOBF_4$,[32] [(TPP)Ru(NO)(1-MeIm)]BF_4[14] and (TPP)Ru(NO)(ONO)[33] were synthesized following procedures reported previously. Anhydrous ethanol (99.5%), $NOBF_4$ (≥99%), 1-methylimidazole (≥99%), 1-phenylimidazole (97%), $NaBH_4$ (99%), NBu_4BH_4 (98%), triphenylphosphine (99%), nitrosobenzene (97%), 2-methyl-2-propanethiol (99%) and 1,3-cyclohexadiene (97%) were obtained from Aldrich and used as received. 1-ethylimidazole (98%) was obtained from TCI and used as received. The supporting electrolyte NBu_4PF_6 (98%) obtained from Aldrich was recrystallized from hot ethanol and dried in vacuo. Ferrocene (98%) was obtained from Aldrich and sublimed prior to use. Chloroform-*d* ($CDCl_3$, 99.96% atom-D) was purchased from Cambridge Isotope Laboratories, deaerated and dried using activated 4 Å molecular sieves. Natural abundance carbon monoxide (CO) and nitric oxide (NO) gas were obtained from AirGas. NO gas was passed through a KOH column and cold trap (-78°C) prior to its contact with the precursor solution to avoid the introduction of NO_x impurities. Infrared spectra were recorded on a Bruker Tensor 27 FTIR spectrometer. ^1H and ^{31}P NMR spectra were obtained on a Varian 400 MHz spectrometer and the ^1H signals were referenced to the residual signal of the solvent employed ($CHCl_3$ at δ = 7.26 ppm), while ^{31}P signals were referenced to H_3PO_4 (85%). X-ray diffraction data was collected using a D8 Quest κ-geometry diffractometer with a Bruker Photon II cpad area detector and Mo-K_α source (λ = 0.71073 Å). EI mass spectra

were recorded on an Agilent 6890N gas chromatograph with an Agilent 5973 Mass Selective Detector and electron impact ion source operated by Dr. Steve Foster. The X-ray diffraction data was collected and the structures solved by Dr. Douglas R. Powell.

3.2.1. Electrochemistry and spectroelectrochemistry of the [(TPP)Ru(NO)(1-MeIm)]BF_4 precursor

Cyclic voltammetric measurements were performed using a BAS CV 50W instrument. A three-electrode cell was utilized and consisted of a 3.0 mm diameter Pt disk working electrode, a Pt wire counter electrode and a Ag wire pseudo-reference electrode. Obtained products were dried under high vacuum for a minimum of 24 hours prior to experiments. Solutions of the compounds were deaerated prior to use by passing a stream of N_2 gas through the solution for a minimum of 10 min, and a blanket of N_2 was maintained over the solution while performing the experiments. The solutions contained 1.0 mM of the analyte in 0.1 M NBu_4PF_6 as support electrolyte. Ferrocene (Fc, 1.0 mM) was used as an internal standard, and potentials were referenced to the $Fc^{0/+}$ couple set to 0.00 V. An approach for *i*R correction was employed to account for the resistance and capacitance in these solutions by entering these values manually into LabVIEW software written by our collaborator Dr. Michael J. Shaw as described by Saveant.[34] This is similar to the process of *i*R compensation available in some electrochemistry software programs but is performed after data collection. A Bruker Tensor 27 FTIR spectrometer, equipped with a mid-IR fiber-optic dip probe and liquid nitrogen cooled MCT detector (RemSpec Corporation, Sturbridge, MA, USA), was used for the IR spectroelectrochemistry.

3.2.2. DFT calculations of [(porphine)Ru(NO)(1-MeIm)]$^+$ and (porphine)Ru(NO)(1-MeIm)

Density functional calculations (functional: BP86; basis set: DGDZVP) were performed using Gaussian-09[35] on the WebMO interface (https://webmo.oscer.ou.edu). Geometric optimizations, vibrational frequency and molecular orbital analyses were performed for the selected complexes: [(porphine)Ru(NO)(1-MeIm)]$^+$ and (porphine)Ru(NO)(1-MeIm) . Calculations were performed in the gas phase.

3.2.3. Hydride attack on the 6-coordinate [(por)Ru(NO)(L_{Im})]$^+$ precursors to generate (por)Ru(HNO)(L_{Im})

(TPP)Ru(HNO)(1-MeIm): To a Schlenk tube containing (TPP)Ru(CO) (30 mg, 0.040 mmol) was added $NOBF_4$ (6 mg, 0.051 mmol) and CH_2Cl_2 (15 mL). This mixture was stirred for 2 h while applying a slight vacuum for a few seconds every 30 min, and the reaction progress was monitored by IR spectroscopy. A new band at 1881 cm^{-1} (ν_{NO}) formed with concomitant and complete disappearance of the starting ν_{CO} band of (TPP)Ru(CO) at 1944 cm^{-1}. This solution containing [(TPP)Ru(NO)]BF_4 was filter-cannulated in its entirety to a new Schlenk tube and concentrated down to ~10 mL. 1-methylimidazole (4 μL, 0.051 mmol) was added to the solution and the mixture stirred for 30 min, where a shift in the ν_{NO} band to 1869 cm^{-1} was observed. N-Hexane (5 mL) was added to the reaction mixture and the solvent removed in vacuo, the resulting powder was washed 3 times with n-hexane (10 mL ea.) to yield the crude [(TPP)Ru(NO)(1-MeIm)]BF_4 product. To this reaction vessel containing the solid [(TPP)Ru(NO)(1-MeIm)]BF_4 sample was added $NaBH_4$ (3 mg, 0.060 mmol) and the vessel placed in a chlorobenzene/dry ice bath (ca. -45 °C). Subsequently, CH_2Cl_2 (3 mL, ca. -45 °C) was added to the mixture (to dissolve the cationic precursor) followed by cold anhydrous ethanol (15 mL, ca. -45 °C). This reaction mixture was stirred for 30 min at this temperature, wherein the

dark red/orange solution turned to a cloudy, bright red/brown color. The vessel was sealed and stored in a -28 °C freezer for 4 h. A red/purple precipitate formed and was isolated via filter cannulation, washed twice with n-hexane (15 mL) and the isolated product obtained in 72% yield (24 mg, 0.032 mmol). IR (KBr, cm^{-1}): ν_{NO} = 1372; ν_{15NO} = 1341. ^{1}H NMR (400 MHz; $CDCl_3$, -30 °C): δ 13.62 (s, 1H, HNO), 8.48 (s, 8H, pyrrole-H of TPP), 8.16 (app d, 4H, *o*-H of TPP, *J* = 8 Hz), 8.03 (app d, 4H, *o′*-H of TPP, *J* = 8 Hz), 7.68 (app m, 12H, *m*- and *p*-H of TPP), 4.81 (s, 1H, =CH of imidazole moiety), 2.23 (s, 3H, -CH_3 of imidazole moiety), 1.61 (s, 1H, =CH of imidazole moiety), 1.20 (s, 1H, =CH of imidazole moiety); δ 13.61 (d, 1H, ^{15}N-H of H^{15}NO, *J* = 72 Hz).

The synthesis of (TPP)Ru(HNO)(1-MeIm) was attempted in a similar manner as above using NBu_4BH_4 (11 mg, 0.043 mmol) as the hydride source and the spectral signals of the isolated product match those from the $NaBH_4$ reaction, but with a diminished yield of 24% (8 mg, 0.010 mmol).

(TPP)Ru(HNO)(1-EtIm): This compound was prepared similarly as above using 1-ethylimidazole (5 μL, 0.052 mmol) and the isolated product was obtained in 64% yield (20 mg, 0.024 mmol). IR (KBr, cm^{-1}): ν_{NO} = 1374. ^{1}H NMR (400 MHz; $CDCl_3$, -30 °C): δ 13.62 (s, 1H, HNO), 8.47 (s, 8H, pyrrole-H of TPP), 8.16 (br m, 4H, *o*-H of TPP) 8.01 (app d, 4H, *o′*-H of TPP, *J* = 8 Hz), 7.71 (app m, 12H, *m*- and *p*-H of TPP), 4.86 (s, 1H, =CH of imidazole moiety), 2.49 (q, 2H, -$\underline{CH_2}$-CH_3 of imidazole moiety, *J* = 8 Hz), 1.67 (s, 1H, =CH of imidazole moiety), 1.20 (s, 1H, =CH of imidazole moiety), 0.35 (t, 3H, CH_2-$\underline{CH_3}$ of imidazole moiety, *J* = 8 Hz).

(TPP)Ru(HNO)(1-PhIm): This compound was prepared similarly as above using 1-phenylimidazole (9 μL, 0.054 mmol) and the isolated product was obtained in 49% yield (18 mg,

0.020 mmol). IR (KBr, cm^{-1}): ν_{NO} = 1378. ^{1}H NMR (400 MHz; $CDCl_3$, -30 °C): δ 13.65 (s, 1H, HNO), 8.50 (s, 8H, pyrrole-H of TPP), 8.18 (app d, 4H, *o*-H of TPP, *J* = 8Hz) 8.04 (app d, 4H, *o′*-H of TPP, *J* = 8 Hz), 7.71 (app m, 12H, *m*- and *p*-H of TPP), 7.00 (br m, 3H, *m*- and *p*-H of imidazole moiety), 5.92 (d, 2H, *o*-H of imidazole moiety, *J* = 8 Hz), 5.20 (s, 1H, =CH of imidazole moiety), 1.88 (s, 1H, =CH of imidazole moiety), 1.36 (s, 1H, =CH of imidazole moiety).

(T(p-Cl)PP)Ru(HNO)(1-MeIm): This compound was prepared similarly as above from (T(*p*-Cl)PP)Ru(CO) (35 mg, 0.040 mmol) and 1-methylimidazole (4 μL, 0.051 mmol) and the isolated product was obtained in 57% yield (22 mg, 0.023 mmol). IR (KBr, cm^{-1}): ν_{NO} = 1375. ^{1}H NMR (400 MHz; $CDCl_3$, -30 °C): δ 13.51 (s, 1H, HNO), 8.48 (s, 8H, pyrrole-H of T(*p*-Cl)PP), 8.07 (app d, 4H, *o*-H of T(*p*-Cl)PP, *J* = 8 Hz), 7.98 (app d, 4H, *o′*-H of T(*p*-Cl)PP, *J* = 8 Hz), 7.69 (br m, 8H, *m*-H of T(*p*-Cl)PP), 4.83 (s, 1H, =CH of imidazole moiety), 2.25 (s, 3H, -CH_3 of imidazole moiety), 1.58 (s, 1H, =CH of imidazole moiety), 1.16 (s, 1H, =CH of imidazole moiety).

(T(p-Cl)PP)Ru(HNO)(1-EtIm): This compound was prepared similarly as above from (T(*p*-Cl)PP)Ru(CO) (35 mg, 0.040 mmol) and 1-ethylimidazole (5 μL, 0.052 mmol) and the isolated product obtained in 41% yield (16 mg, 0.016 mmol). IR (KBr, cm^{-1}): ν_{NO} = 1376. ^{1}H NMR (400 MHz; $CDCl_3$, -30 °C): δ 13.51 (s, 1H, HNO), 8.46 (s, 8H, pyrrole-H of T(*p*-Cl)PP), 8.07 (app d, 4H, *o*-H of T(*p*-Cl)PP, *J* = 8 Hz), 7.94 (app d, 4H, *o′*-H of T(*p*-Cl)PP, *J* = 8 Hz), 7.67 (br m, 8H, *m*-H of T(*p*-Cl)PP), 4.87 (s, 1H, =CH of imidazole moiety), 2.49 (q, 2H, -$\underline{CH_2}$-CH_3 of imidazole moiety, *J* = 8 Hz), 1.55 (s, 1H, =CH of imidazole moiety), 1.13 (s, 1H, =CH of imidazole moiety), 0.35 (t, 3H, CH_2-$\underline{CH_3}$ of imidazole moiety, *J* = 8 Hz).

(T(p-Cl)PP)Ru(HNO)(1-PhIm): This compound was prepared similarly as above from (T(*p*-Cl)PP)Ru(CO) (35 mg, 0.040 mmol) and 1-phenylimidazole (9 μL, 0.054 mmol) and the isolated product obtained in 32% yield (13 mg, 0.013 mmol). IR (KBr, cm^{-1}): ν_{NO} = 1382. ^{1}H NMR (400 MHz; $CDCl_3$, -30 °C): δ 13.54 (s, 1H, HNO), 8.48 (s, 8H, pyrrole-H of T(*p*-Cl)PP), 8.08 (app d, 4H, *o*-H of T(*p*-Cl)PP, *J* = 8Hz) 7.95 (app d, 4H, *o′*-H of T(*p*-Cl)PP, *J* = 8 Hz), 7.65 (br m, 8H, *m*-H of T(*p*-Cl)PP), 6.99 (br m, 3H, *m*- and *p*-H of imidazole moiety), 5.90 (d, 2H, *o*-H of imidazole moiety, *J* = 8 Hz), 5.18 (s, 1H, =CH of imidazole moiety), 1.87 (s, 1H, =CH of imidazole moiety), 1.36 (s, 1H, =CH of imidazole moiety).

(T(p-OMe)PP)Ru(HNO)(1-MeIm): This compound was prepared similarly as above from (T(*p*-OMe)PP)Ru(CO) (34 mg, 0.040 mmol) and 1-methylimidazole (4 μL, 0.051 mmol) and the isolated product obtained in 44% yield (16 mg, 0.017 mmol). IR (KBr, cm^{-1}): ν_{NO} = 1374. ^{1}H NMR (400 MHz; $CDCl_3$, -30 °C): δ 13.60 (s, 1H, HNO), 8.50 (s, 8H, pyrrole-H of T(*p*-OMe)PP), 8.07 (app d, 4H, *o*-H of T(*p*-OMe)PP, *J* = 8 Hz), 7.94 (app d, 4H, *o′*-H of T(*p*-OMe)PP, *J* = 8 Hz), 4.78 (s, 1H, =CH of imidazole moiety), 4.07 (s, 12H, *p*-OMe of T(*p*-OMe)PP), 2.21 (s, 3H, -CH_3 of imidazole moiety), 1.58 (s, 1H, =CH of imidazole moiety), 1.17 (s, 1H, =CH of imidazole moiety). Partial signal overlap was observed between the $CDCl_3$ solvent peak at 7.26 ppm and the *m*-H's of T(*p*-OMe)PP.

(T(p-OMe)PP)Ru(HNO)(1-EtIm): This compound was prepared similarly as above from (T(*p*-OMe)PP)Ru(CO) (34 mg, 0.040 mmol) and 1-ethylimidazole (5 μL, 0.052 mmol) and the isolated product obtained in 32% yield (12 mg, 0.013 mmol). IR (KBr, cm^{-1}): ν_{NO} = 1373. ^{1}H NMR (400 MHz; $CDCl_3$, -30 °C): δ 13.61 (s, 1H, HNO), 8.50 (s, 8H, pyrrole-H of T(*p*-OMe)PP), 8.07 (app d, 4H, *o*-H of T(*p*-OMe)PP, *J* = 8 Hz), 7.93 (app d, 4H, *o′*-H of T(*p*-OMe)PP, *J* = 8 Hz), 4.83 (s, 1H, =CH of imidazole moiety), 4.07 (s, 12H, *p*-OMe of T(*p*-

OMe)PP), 2.46 (q, 2H, -$\underline{CH_2}$-CH_3 of imidazole moiety, *J* = 8 Hz), 1.56 (s, 1H, =CH of imidazole moiety), 1.16 (s, 1H, =CH of imidazole moiety), 0.33 (t, 3H, CH_2-$\underline{CH_3}$ of imidazole moiety, *J* = 8 Hz). Partial signal overlap was observed between the $CDCl_3$ solvent peak at 7.26 ppm and the *m*-H's of T(*p*-OMe)PP.

(T(p-OMe)PP)Ru(HNO)(1-PhIm): This compound was prepared similarly as above from (T(*p*-OMe)PP)Ru(CO) (34 mg, 0.040 mmol) and 1-phenylimidazole (9 μL, 0.054 mmol) and the isolated product obtained in 21% yield (9 mg, 0.010 mmol). IR (KBr, cm^{-1}): ν_{NO} = 1377. ^1H NMR (400 MHz; $CDCl_3$, -30 °C): δ 13.64 (s, 1H, HNO), 8.49 (s, 8H, pyrrole-H of T(*p*-OMe)PP), 8.08 (app d, 4H, *o*-H of T(*p*-OMe)PP, *J* = 8Hz) 7.94 (app d, 4H, *o′*-H of T(*p*-OMe)PP, *J* = 8 Hz), 7.93 (app d, 8H, *m*-H of T(*p*-OMe)PP, *J* = 8 Hz), 7.00 (br m, 3H, *m*- and *p*-H of imidazole moiety), 5.91 (d, 2H, *o*-H of imidazole moiety, *J* = 8 Hz), 5.21 (s, 1H, =CH of imidazole moiety), 4.07 (s, 12H, *p*-OMe of T(*p*-OMe)PP), 1.87 (s, 1H, =CH of imidazole moiety), 1.35 (s, 1H, =CH of imidazole moiety). Partial signal overlap was observed between the $CDCl_3$ solvent peak at 7.26 ppm and the *m*-H's of T(*p*-OMe)PP.

3.2.4. Decomposition products of (TPP)Ru(HNO)(1-MeIm)

A sealed J. Young NMR tube containing (TPP)Ru(HNO)(1-MeIm) (3 mg, 0.0036 mmol) was dissolved in $CDCl_3$ (ca. -45 °C) under N_2 and then transferred to a -28 °C freezer for a 24 h period. The IR spectrum of the resulting mixture after this period displayed new ν_{NO} bands at 1813 cm^{-1} and 1864 cm^{-1} (KBr), with the latter displaying a significantly greater relative intensity. ^1H NMR (400 MHz; $CDCl_3$): δ 8.97 (s, 8H, pyrrole-H of TPP), 8.31 (d, 4H, *o*-H of TPP, *J* = 8 Hz), 8.25 (d, 4H, *o′*-H of TPP, *J* = 8 Hz), 7.79 (app m, 12H, *m*- and *p*-H of TPP). This species accounted for 72% of the sample determined by ^1H NMR with a minor product detected at 9.14 ppm, corresponding to the pyrrole-H of a $[(TPP)Ru(NO)(1\text{-}MeIm)]^+$ complex.

3.2.5. HNO abstraction from (TPP)Ru(HNO)(1-MeIm) with PPh_3

To a stirred solution of (TPP)Ru(HNO)(1-MeIm) (5 mg, 0.0060 mmol) in $CHCl_3$ (3 mL, ca. -45 °C) in a cold bath at ca. -45 °C was added PPh_3 (3 mg, 0.012 mmol) and the mixture stirred for 30 min at this temperature before being allowed to slowly warm to room temperature. The solvent of the reaction mixture was removed in vacuo and the solid product isolated. ^{31}P NMR (400 MHz; $CDCl_3$): δ 30.9 (s, 1P) and 29.1 (s, 1P). High resolution EI mass spectrum of the product mixture: *m/z* of $[O=PPh_3]^+$ = 278, *m/z* of $[HN=PPh_3]^+$ = 277.

3.2.6. Coupling reaction of (TPP)Ru(HNO)(1-MeIm) and (TPP)Ru(H^{15}NO)(1-MeIm) with NO gas

A solution of (TPP)Ru(HNO)(1-MeIm) (5 mg, 0.0060 mmol) in CH_2Cl_2 (3 mL, ca. -45 °C) in a cold bath at ca. -45 °C was exposed to NO gas (250 μL, 0.010 mmol) and the mixture stirred for 30 min at this temperature before being allowed to slowly warm to room temperature. The headspace of the reaction vessel was analyzed by IR spectroscopy which displayed the characteristic N_2O stretching frequencies at 2212 cm^{-1} and 2237 cm^{-1} in 12% yield. The solvent of the reaction mixture was removed in vacuo and the solid product [(TPP)Ru(NO)(1-MeIm)]ONO was isolated in 98% yield (5 mg, 0.0060 mmol). X-ray diffraction quality crystals were obtained by slow evaporation using CH_2Cl_2 as the solvent with n-hexane as the antisolvent gently layered on top (1:1). IR (KBr, cm^{-1}): ν_{NO} = 1871; ν_{ONO} = 1326. ^1H NMR (400 MHz; $CDCl_3$): δ 9.16 (s, 8H, pyrrole-H of TPP), 8.25 (d, 8H, *o*-H of TPP, *J* = 8 Hz), 7.85 (m, 12H, *m*- and *p*-H of TPP), 4.96 (s, 1H, =CH of imidazole moiety), 2.11 (s, 3H, $-CH_3$ of imidazole moiety), 0.71 (s, 1H, =CH of imidazole moiety), -0.10 (s, 1H, =CH of imidazole moiety).

The above procedure was repeated with the (TPP)Ru($H^{15}NO$)(1-MeIm) compound and the mixed isotopic $^{14}N^{15}NO$ gas product was observed in the gas IR spectrum at 2169 cm^{-1} and 2191 cm^{-1}, as well as unlabeled N_2O at 2212 cm^{-1} and 2237 cm^{-1}.

Several attempts were made to react separately prepared (TPP)Ru(NO)(ONO)[33] with 1-methylimidazole in an effort to generate [(TPP)Ru(NO)(1-MeIm)]ONO with no change to the IR or ^1H NMR spectra observed.

3.2.7. Displacement of HNO from (TPP)Ru(HNO)(1-MeIm) with CO gas

A solution of (TPP)Ru(HNO)(1-MeIm) (5 mg, 0.0060 mmol) in CH_2Cl_2 (3 mL, ca. -45 °C) in a cold bath at ca. -45 °C was exposed to CO gas (250 μL, 0.010 mmol) and the mixture stirred for 30 min at this temperature before being allowed to slowly warm to room temperature. The headspace of the reaction vessel was analyzed by IR spectroscopy which displayed the characteristic N_2O stretching frequency at 2237 cm^{-1} in 4% yield. The band at 2212 cm^{-1} for N_2O was not distinctive due to the overlapping free CO gas stretching frequencies at 2117 cm^{-1} and 2171 cm^{-1}. The solvent of the reaction mixture was removed in vacuo and the known solid product (TPP)Ru(CO)(1-MeIm)[31] isolated in 85% yield (4 mg, 0.48 mmol). IR (KBr, cm^{-1}): ν_{CO} = 1938. ^1H NMR (400 MHz; $CDCl_3$): δ 8.58 (s, 8H, pyrrole-H of TPP), 8.24 (br m, 4H, *o*-H of TPP), 8.04 (d, 4H, *o′*-H, *J* = 8 Hz) 7.71 (app m, 12H, *m*- and *p*-H of TPP), 4.62 (s, 1H, =CH of imidazole moiety), 2.11 (s, 3H, -CH_3 of imidazole moiety), 1.32 (s, 1H, =CH of imidazole moiety), 0.94 (s, 1H, =CH of imidazole moiety). The remainder of the sample corresponds to the products observed in the decomposition study.

3.2.8. Attempted nitroso Diels-Alder reaction of (TPP)Ru(HNO)(1-MeIm) with 1,3-cyclohexadiene in the absence and presence of CO gas

To a stirred solution of (TPP)Ru(HNO)(1-MeIm) (5 mg, 0.0060 mmol) in CH_2Cl_2 (3 mL, ca. -45 °C) in a cold bath at ca. -45 °C was added 1,3-cyclohexadiene (6 μL, 0.060 mmol) and the mixture stirred for 30 min at this temperature before being allowed to slowly warm to room temperature. The solvent of the reaction mixture was removed in vacuo and the solid product isolated. IR and ^{1}H NMR spectra showed similar results to that of the anaerobic decomposition but no presence of the expected soluble Diels-Alder product.[26]

To a stirred solution of (TPP)Ru(HNO)(1-MeIm) (5 mg, 0.0060 mmol) in CH_2Cl_2 (3 mL, ca. -45 °C) in a cold bath at ca. -45 °C was added 1,3-cyclohexadiene (6 μL, 0.063 mmol). An excess of CO gas was bubbled through the solution, the reaction vessel sealed, and the mixture stirred for 30 min at this temperature before being allowed to slowly warm to room temperature. The solvent of the reaction mixture was removed in vacuo and the solid product isolated. IR and ^{1}H NMR spectra matched that of previously reported (TPP)Ru(CO)(1-MeIm)[31] but no formation of the expected soluble Diels-Alder product was present.[26]

3.2.9. Attempted HNO displacement from (TPP)Ru(HNO)(1-MeIm) with PhNO

To a stirred solution of (TPP)Ru(HNO)(1-MeIm) (5 mg, 0.0060 mmol) in CH_2Cl_2 (3 mL, ca. -45 °C) in a cold bath at ca. -45 °C was added nitrosobenzene (2 mg, 0.018 mmol) and the mixture stirred for 30 min at this temperature before being allowed to slowly warm to room temperature. Headspace IR gas analysis did not display the characteristic N_2O bands. The solvent of the reaction mixture was removed in vacuo and the known solid product (TPP)Ru(PhNO)(1-MeIm)[36] isolated in 67% yield (3 mg, 0.0040 mmol). IR (KBr, cm^{-1}): ν_{NO} = 1309. ^{1}H NMR (400

MHz; $CDCl_3$): δ 8.39 (s, 8H, pyrrole-H of TPP), 8.03 (d, 4H, *o′*-H of TPP, *J* = 8 Hz), 6.40 (app t, 1H, *p*-H of PhNO moiety, *J* = 7 Hz), 5.97 (t, 2H, *m*-H of PhNO moiety, *J* = 8 Hz), 4.75 (s, 1H, =CH of imidazole moiety), 2.64 (d, 2H, *o*-H of PhNO moiety, *J* = 8 Hz) 2.19 (s, 3H, -CH_3 of imidazole moiety), 1.60 (s, 1H, =CH of imidazole moiety), 1.24 (s, 1H, =CH of imidazole moiety). The remainder of the sample corresponds to the products observed in the decomposition study.

This reaction was repeated in a sealed J. Young NMR tube using $CDCl_3$ at -30 °C to monitor reaction progress. A metastable product is formed, prior to the generation of (TPP)Ru(PhNO)(1-MeIm), with a pyrrole-H chemical shift of 8.93 ppm and the appearance of signals corresponding to free 1-methylimidazole.

3.2.10. Attempted coupling reaction of 2-methyl-2-propanethiol and (TPP)Ru(HNO)(1-MeIm)

To a stirred solution of (TPP)Ru(HNO)(1-MeIm) (5 mg, 0.0060 mmol) in CH_2Cl_2 (3 mL, ca. -45 °C) in a cold bath at ca. -45 °C was added 2-methyl-2-propanethiol (7 μL, 0.060 mmol) and the mixture stirred for 30 min at this temperature before being allowed to slowly warm to room temperature. The solvent of the reaction mixture was removed in vacuo and the solid product, tentatively formulated as (TPP)Ru(NO)(S-C(CH_3)$_3$), was isolated in 59% yield (3 mg, 0.0036 mmol). IR (KBr, cm^{-1}): ν_{NO} = 1784. ^{1}H NMR (400 MHz; $CDCl_3$): δ 8.91 (s, 8H, pyrrole-H of TPP), 8.24 (br m, 8H, *o*-H of TPP), 7.76 (br m, 12H, *m*- and *p*-H of TPP), -1.85 (s, 9H, -CH_3 of SC(CH_3)$_3$). The remainder of this initial sample corresponds to the product observed in the decomposition study at 8.96 ppm, as well as free 1-methylimidazole and unreacted 2-methyl-2-propanethiol. This reaction was left to stir at room temperature for an additional 24 h, upon which a new pyrrole-H signal was observed at 9.15 ppm with significant increase in the signal at

1.30 ppm. The (TPP)Ru(NO)(S-C(CH_3)$_3$) compound was prepared separately by fellow group member Tsitsi Kapfunde from the alcohol exchange reaction of (TPP)Ru(NO)(OH) (5 mg, 0.006 mmol) with HS-C(CH_3)$_3$ (10 μL, 0.088 mmol) in CH_2Cl_2 after 1 h of stirring at room temperature. The ^{1}H NMR and IR spectral signals of this isolated product match those listed above. Synthesis of the hydroxo compound is detailed in chapter 4 (see section 4.2.1).

3.3. Results and Discussion

3.3.1. Redox behavior of the NO^+ precursor

The redox behavior of a representative cationic nitrosyl precursor was determined in an effort to understand the $2e^-/H^+$ transfer necessary to form HNO from bound NO^+. The precursor [(TPP)Ru(NO)(1-MeIm)]BF_4 was prepared as previously reported,[14] with the crystal structure depicted in Figure 3.3a, where the BF_4^- counterion was disordered. As is commonly observed in {RuNO}^{6} porphyrin complexes, a near linear ∠RuNO bond angle of 175.36(14)° and Ru-N(O) bond length of 1.7619(19) Å can be seen, whereas the coordinated imidazole ligand was found to have a Ru-N_{Im} (Ru-N6) bond length of 2.0949(11) Å. I prepared and crystallized several other [(por)Ru(NO)(1-MeIm)]BF_4 (por = TPP, TTP, T(*p*-OMe)PP, OEP) and [(por)Ru(NO)(5-MeHIm)]BF_4 (por = TPP, TTP) complexes which are included in Figure 3.3 with bond lengths and angles, which yielded similar geometrical information as other ruthenium nitrosonium porphyrin complexes, particularly in regard to the ∠RuNO bond angles (171.0(7)-178.1(3)°) and short Ru-N(O) bond lengths (1.695(9)-1.7305(17) Å) in these complexes.[37-40]

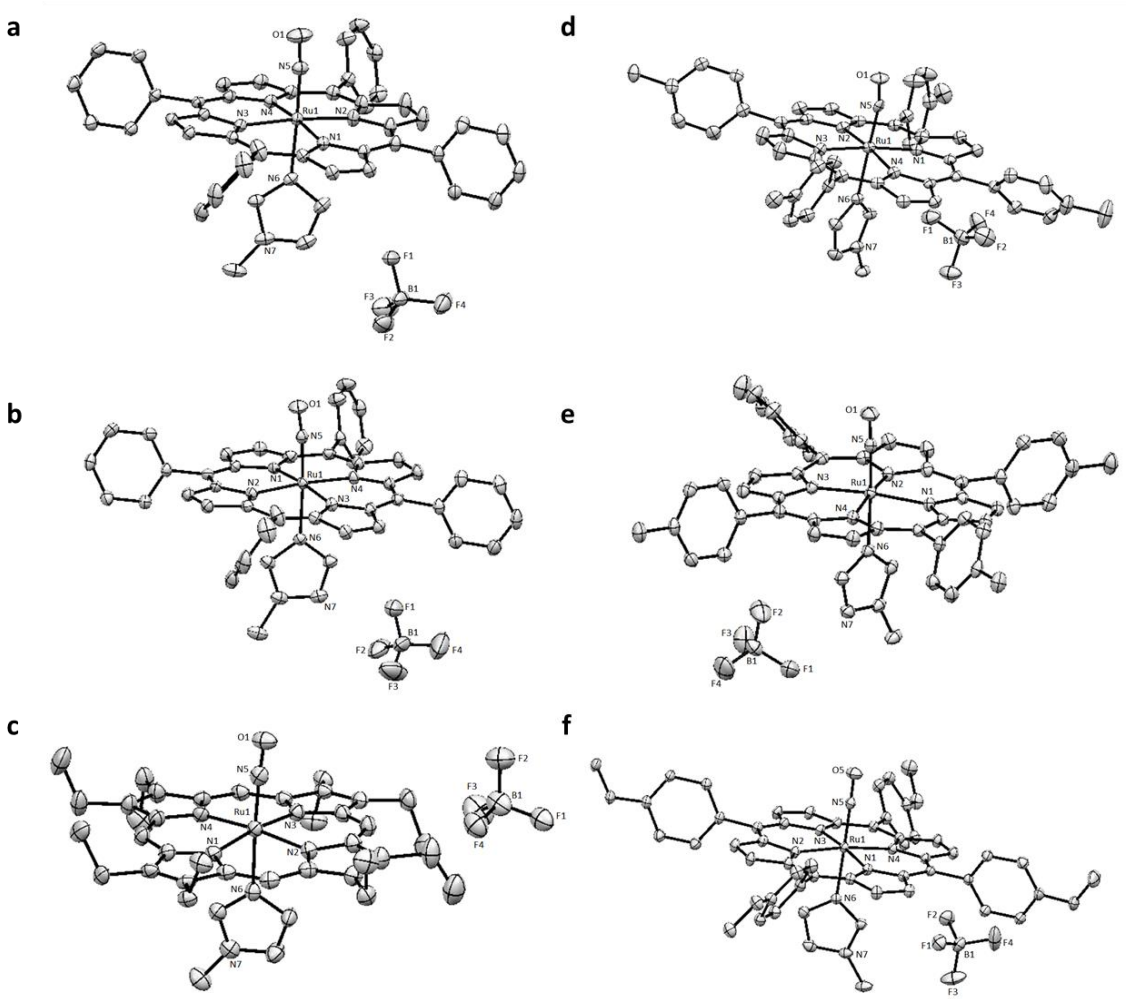

Figure 3.3 Crystal structures of (a) [(TPP)Ru(NO)(1-MeIm)]BF_4 (i.d. 19137), (b) [(TPP)Ru(NO)(5-MeHIm)]BF_4 (i.d. 19220), (c) [(OEP)Ru(NO)(1-MeIm)]BF_4 (i.d. 20022), (d) [(TTP)Ru(NO)(1-MeIm)]BF_4 (i.d. 19162), (e) [(TTP)Ru(NO)(5-MeHIm)]BF_4 (i.d. 20026) and (f) (T(*p*-OMe)PP)Ru(NO)(1-MeIm)]BF_4 (i.d. 19164). Hydrogen atoms have been omitted for clarity. Thermal ellipsoids are drawn at 50%.

Table 3.1 Selected structural data and IR nitrosyl stretching frequencies for several [(por)Ru(NO)(L_{Im})]BF_4 compounds.

	Ru-N(O) (Å)	**∠RuNO (°)**	**Ru-N_{Im} (Å)**	**ν_{NO} (cm^{-1})**
[(TPP)Ru(NO)(1-MeIm)]BF_4	1.7619(19)	175.36(14)	2.0949(11)	1864
[(TPP)Ru(NO)(5-MeHIm)]BF_4	1.752(3)	173.5(3)	2.089(3)	1863
[(OEP)Ru(NO)(1-MeIm)]BF_4	1.741(4)	176.3(3)	2.099(3)	1852
[(TTP)Ru(NO)(1-MeIm)]BF_4	1.747(3)	169.0(3)	2.0875(19)	1859
[(TTP)Ru(NO)(5-MeHIm)]BF_4	1.7420(18)	177.67(17)	2.0843(17)	1861
[(T(*p*-OMe)PP)Ru(NO)(1-MeIm)]BF_4	1.7508(18)	175.25(18)	2.0900(17)	1865

The cathodic behavior of the [(TPP)Ru(NO)(1-MeIm)]BF_4 precursor in CH_2Cl_2 containing 0.1 M NBu_4PF_6 as the supporting electrolyte was investigated via cyclic voltammetry (CV). Figure 3.4 depicts the voltammogram recorded at 200 mV/s with all potentials measured against an internal standard, ferrocene ($Fc^{0/+}$), set to 0 V. A relatively well-behaved 1-electron reduction can be observed at $E^{\circ\prime}$ = -0.90 V, followed by a second quasi-reversible reduction at E_{pc} = -1.65 V. On the return wave of the second reduction two subtle anodic features are present at E_{pa} = -1.25 and -1.50 V. No significant changes were observed for either redox feature upon changing scan rate in the chosen range (50-1600 mV/s). These general features are very similar to those observed in the related [(por)Ru(NO)(L_{py})]$^+$ (por = OEP and TPP; L_{py} = pyridine, 4-cyanopyridine and 4-N,N-dimethylaminopyridine) compounds.[37,41]

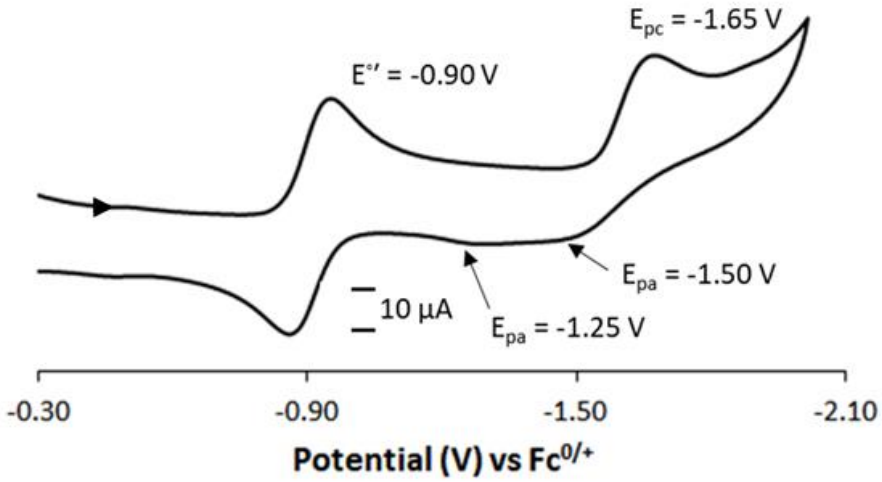

Figure 3.4 Cyclic voltammogram of 1.0 mM [(TPP)Ru(NO)(1-MeIm)]BF_4 in CH_2Cl_2 containing 0.1 M NBu_4PF_6 showing the reductions at a scan rate of 200 mV/s.

IR-spectroelectrochemistry (IR-SEC) was employed to ascertain structural information relating to the cathodic processes observed in the cyclic voltammogram. The IR-SEC results for [(TPP)Ru(NO)(1-MeIm)]BF_4 in CH_2Cl_2 containing 0.1 M NBu_4PF_6, illustrating the cathodic products generated at the first and second reductions, are displayed in Figure 3.5. An IR

difference spectrum of the first reduction after the potential was held at -1.00 V (vs $Fc^{0/+}$) (Figure 3.5a) reveals the disappearance of the initial ν_{NO} at 1881 cm^{-1} and appearance of a new ν_{NO} at a significantly lower frequency to 1575 cm^{-1} ($\Delta\nu_{NO}$ = 306 cm^{-1}). This large shift is characteristic of an electron transfer to π^* orbitals associated with the nitrosyl ligand (i.e., $\{RuNO\}^6 \rightarrow \{RuNO\}^7$).[42-46] For the second reduction a potential of -1.70 V (vs $Fc^{0/+}$) was applied, again, resulting in a loss of the initial ν_{NO} at 1881 cm^{-1} but a new ν_{NO} was not detected within the observable range (Figure 3.5b); no indication of product formation from the first reduction (ν_{NO} = 1575 cm^{-1}) was observed during the second reduction. It is unclear if any dissociation of the nitrosyl ligand takes place but is unlikely due to the reversible first reduction feature in the voltammogram. The shift of ν_{NO} outside of the observable range in the IR difference spectrum at the second reduction supports another NO-centered reduction.

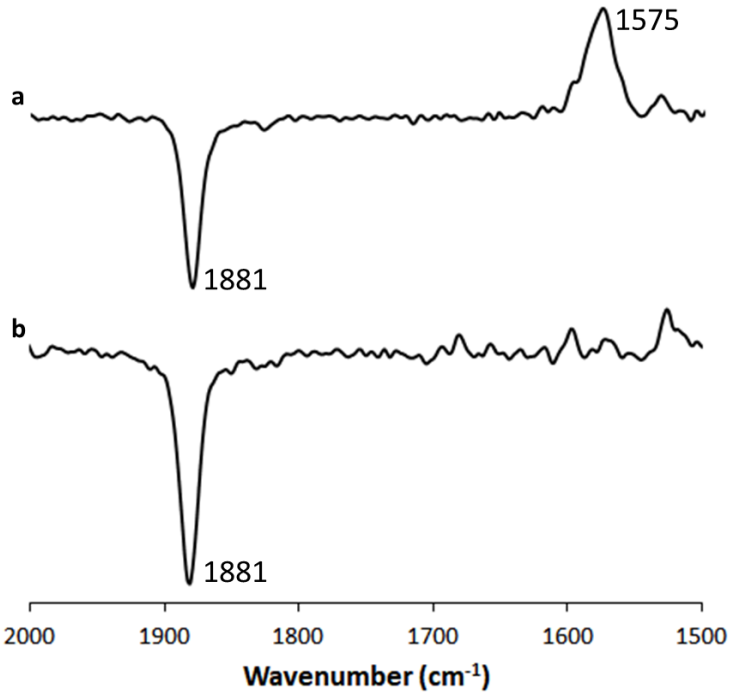

Figure 3.5 Difference IR spectra showing the products from the (a) first and (b) second reduction of $[(TPP)Ru(NO)(1\text{-}MeIm)]BF_4$ in CH_2Cl_2 containing 0.1 M NBu_4PF_6, with the potential held at -1.00 and -1.70 V vs the $Fc^{0/+}$ couple, respectively. Band intensities below the baseline reflect depleted bands, and those above the baseline reflect new bands.

DFT calculations of $\{RuNO\}^6$ [(porphine)Ru(NO)(1-MeIm)]$^+$ and $\{RuNO\}^7$ (porphine)Ru(NO)(1-MeIm) (porphine = unsubstituted porphyrin) complexes were utilized to probe the likely redox active sites involved in the reductions. To accomplish this, electron density maps of the frontier molecular orbitals were calculated from optimized geometries using the BP86 functional and DGDZVP basis set. Table 3.2 shows the calculated bond lengths and angles for the $\{RuNO\}^6$ and $\{RuNO\}^7$ species in comparison to the experimentally obtained values for [(TPP)Ru(NO)(1-MeIm)]BF_4. In general, the calculated bond lengths and angles for the cationic precursor agree very well (< 3% error) with the experimental values, including the ν_{NO} of 1862.77 cm^{-1} obtained from a vibrational frequency analysis. A slight lengthening of the Ru-N(O) bond from 1.782 Å to 1.890 Å and Ru-N_{Im} from 2.155 Å to 2.227 Å is observed in moving from the calculated cationic $\{RuNO\}^6$ to neutral $\{RuNO\}^7$ geometries, along with a significant bending in ∠RuNO from 179.989° to 138.585°. A vibrational frequency analysis of the $\{RuNO\}^7$ complex resulted in the calculated ν_{NO} of 1625.83 cm^{-1} ($\Delta\nu_{NO}$ = ~237 cm^{-1}), indicative of a significant bend at the nitrosyl ligand and consistent with what was observed during the first reduction from Figure 3.5 (ν_{NO} = 1575 cm^{-1}). This is in close proximity to the reported calculated values of 140° (Ru-N-O) and a $\Delta\nu_{NO}$ of 240 cm^{-1} for related $\{RuNO\}^7$ (por)Ru(NO)(py) (por = TPP and OMP) complexes.[47]

Table 3.2 Calculated parameters of the $\{RuNO\}^6$ [(porphine)Ru(NO)(1-MeIm)]$^+$ and $\{RuNO\}^7$ (porphine)Ru(NO)(1-MeIm) optimized geometries using the BP86 functional and DGDZVP basis set.

		Ru-N(O) (Å)	**∠RuNO (°)**	**Ru-N_{Im} (Å)**	**ν_{NO} (cm^{-1})**
Experimental	$\{RuNO\}^6$	1.7619(19)	175.36(14)	2.0949(11)	1864
Calculated	$\{RuNO\}^6$	1.782	179.989	2.155	1862.77
	$\{RuNO\}^7$	1.890	138.585	2.227	1625.83

The LUMO of the cationic $\{RuNO\}^6$ complex (Figure 3.6a) is centered on the RuNO fragment (d_π-p_{π^*} orbital), consistent with the view that nucleophilic attack of the hydride (from BH_4^-) could occur directly at this fragment. The antibonding nature of the Ru-NO interaction depicted in the LUMO is also consistent with the calculated Ru-N(O) bond lengthening upon 1-electron reduction. Extending these calculations to the $\{RuNO\}^7$ (porphine)Ru(NO)(1-MeIm) reduction product (Figure 3.6b) reveals the second reduction site is isolated on the NO ligand and porphyrin macrocycle. These results support the proposed multielectron reduction occurring primarily at the nitrosyl ligand, although the observed quasi-reversible second reduction with two anodic return features could be the result of electron density being delocalized across the NO and porphyrin moieties.

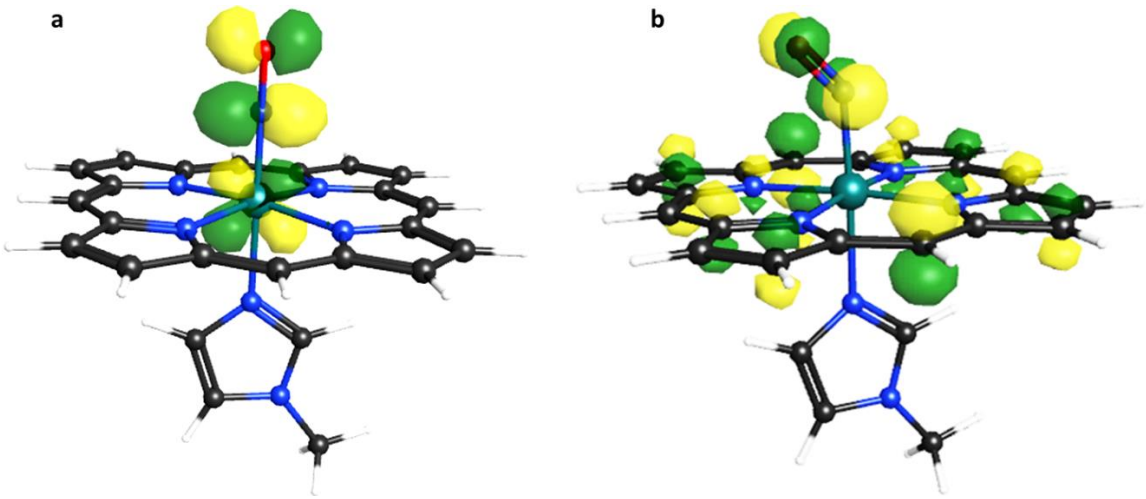

Figure 3.6 Calculated LUMO's from the optimized geometries of the (a) $\{RuNO\}^6$ $[(porphine)Ru(NO)(1\text{-}MeIm)]^+$ and (b) $\{RuNO\}^7$ (porphine)Ru(NO)(1-MeIm) complexes.

3.3.2. Preparation, spectroscopy and analysis of trends

The development of M-HNO systems has become a field of considerable interest over the last several years given the biological and environmental impact as a vital intermediate species observed in nature.[1-5] With the known instability of HNO complexes, a primary focus has been placed on characterization of heme models and obtaining structural information of non-heme coordination compounds. However, very few examples have been published regarding the reactivity of bound HNO in hemes and heme models. The first (por)Ru(HNO)(L_{Im}) complex was reported by our group in 2005, namely the (TTP)Ru(HNO)(1-MeIm) compound. At the time, and since then no other analogue was able to be prepared and characterized. A series of (por)Ru(HNO)(L_{Im}) (por = T(*p*-OMe)PP, TPP, T(*p*-Cl)PP; L_{Im} = 1-methylimidazole, 1-ethylimidazole, 1-phenylimidazole) compounds, where the imidazole ligand is in the axial position *trans* to HNO, have been prepared and isolated in yields ranging 21-72%, from hydride attack at the cationic [(por)Ru(NO)(L_{Im})]BF_4 precursor (Figure 3.7). The desired compounds are air sensitive and thermally unstable in solution. As solids, these compounds are moderately stable in a glovebox for a few days at room temperature before signs of decomposition are apparent, as determined by IR and ^{1}H NMR spectroscopy.

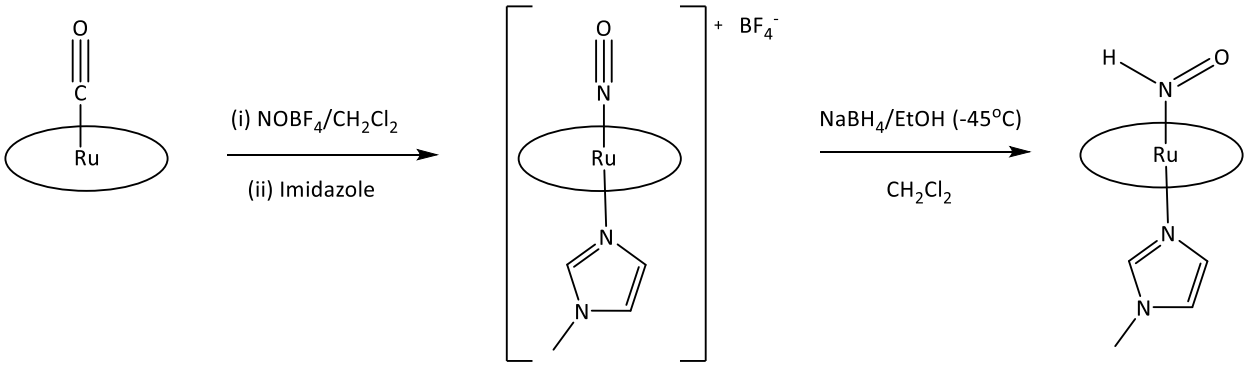

Figure 3.7 General synthesis description for the (por)Ru(HNO)(L_{Im}) complexes.

The reactants and products can be differentiated by IR spectroscopy. For example, that for the hydride attack of the six-coordinate cationic precursor [(TPP)Ru(NO)(1-MeIm)]BF_4 to form the target neutral (TPP)Ru(HNO)(1-MeIm) compound is illustrated in Figure 3.8. Reaction progress from the carbonyl starting material to generate the cationic nitrosyl precursor was monitored by solution IR spectroscopy (CH_2Cl_2), and the final product characterized by solid IR and low temperature ^{1}H NMR spectroscopy ($CDCl_3$; -30 °C). A significant shift to the ν_{NO} can be observed upon reaction with $NaBH_4$ from 1864 cm^{-1} to 1372 cm^{-1} ($\Delta\nu_{NO}$ = 492 cm^{-1}), along with a concomitant disappearance of the anion ν_{BF} band at 1054 cm^{-1}. This large shift is in good agreement with what has been reported for many heme and non-heme complexes bearing an HNO moiety and supports the expected substantial bending of the RuNO fragment discussed previously. Specifically, non-heme compounds (comprised of group 7-9 metals) tend to exhibit ν_{NO} range of 1335-1493 cm^{-1},[15-19,47-49] while group 8 heme model compounds lie between 1371-1389 cm^{-1}.[6,13,14] There was minimal difference between the various porphyrin and imidazole derivatives ($\Delta\nu_{NO}$ < 10 cm^{-1}) for both the NO^+ (1862-1869 cm^{-1}; [(TPP)Ru(^{15}NO)(1-MeIm)]BF_4 ν_{15NO} = 1834 cm^{-1}) and HNO (1372-1381 cm^{-1}; (TPP)Ru(H^{15}NO)(1-MeIm) ν_{15NO} = 1341 cm^{-1}) complexes.

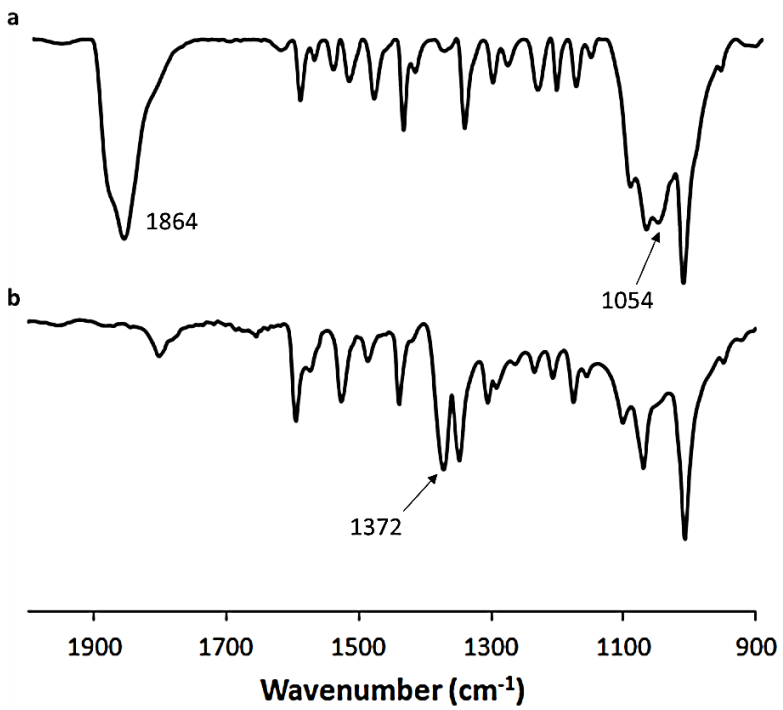

Figure 3.8 Truncated IR spectra of the (a) [(TPP)Ru(NO)(1-MeIm)]BF_4 precursor and the isolated (b) (TPP)Ru(HNO)(1-MeIm) as KBr pellets.

While IR spectroscopy is very effective in identifying changes to the bound NO fragment, ^{1}H NMR spectroscopy is critical in confirming the identity of the HNO ligand. The ^{1}H NMR spectrum of the representative (TPP)Ru(HNO)(1-MeIm) compound (Figure 3.9) exhibits a chemical shift at a significantly higher value (downfield) at δ 13.62 ppm than the other proton peaks corresponding to the complex, which matches closely with the previously reported (TTP)Ru(HNO)(1-MeIm)[14] and other heme-HNO model compounds (δ_{HNO} = 13.64-14.26 ppm).[6,13] An advantage to these HNO systems is that an isotopically labelled ^{15}N analogue can be easily prepared and used to confirm the previously observed singlet for H-^{14}N(O) split into a doublet (J = 72 Hz) with H-^{15}N(O) (Figure 3.9 inset), which was observed for (TPP)Ru(H^{15}NO)(1-MeIm). A moderately large chemical shift of the pyrrole-H from δ 9.16 ppm to a lower value (upfield) at δ 8.48 ppm (Δδ = ~0.70 ppm) was observed upon conversion of the

NO^+ precursor to the HNO complex. The pyrrole-H chemical shifts from the obtained products did not differ significantly between the various derivatives (δ 8.46-8.50 ppm). Peaks assigned to the imidazole ligand are located between δ 1.20 ppm and 4.80 ppm with the -CH_3 group of the methylimidazole at δ 2.23 ppm. Similar to what was detected previously in the IR spectra, the porphyrin and imidazole identities have a minimal effect on the δ_{HNO} values with a noted range of δ 13.51-13.65 ppm. The isolated samples displaying the highest purity were the 1-MeIm derivatives, on average 98% pure by the pyrrole-H integration values in the ^{1}H NMR spectra, followed by the 1-EtIm (88%) complexes, then 1-PhIm (61%). I attribute these differences to slight changes in solubility between the target HNO compound and the corresponding decomposition products with the mixed solvent systems used during isolation. However, the porphyrin identity did not appear, by itself, to have much effect on the final purity of the (por)Ru(HNO)(L_{Im}) complexes.

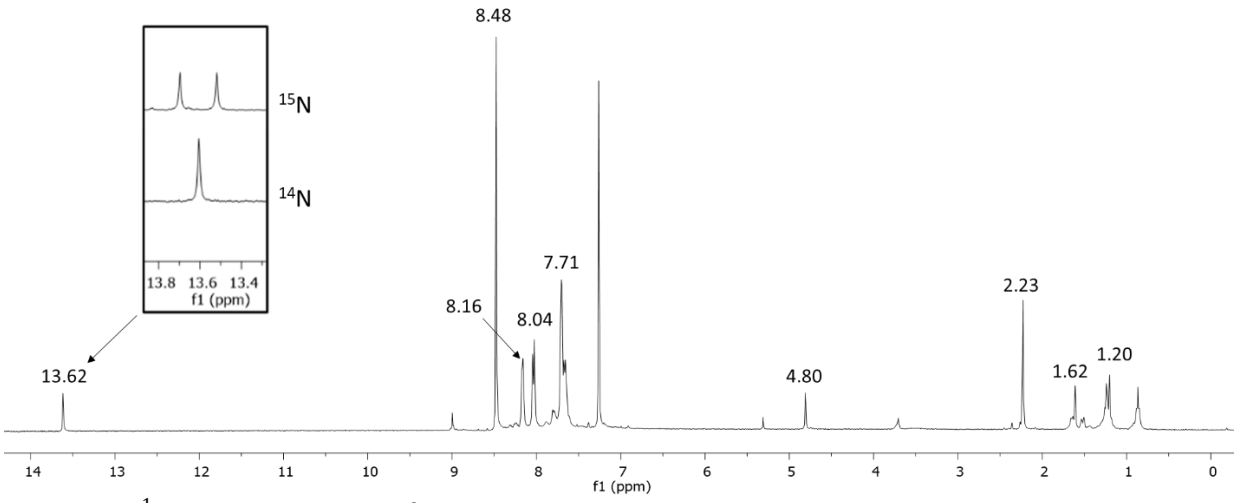

Figure 3.9 ^{1}H NMR spectrum of (TPP)Ru(HNO)(1-MeIm) in $CDCl_3$ at -30 °C; the inset compares the $H^{15}NO$ vs $H^{14}NO$ peaks.

Table 3.3 compares previously reported ν_{NO} and δ_{HNO} values of metal-HNO complexes to those prepared in this work. The non-heme compounds consisting of group 7-9 metals (e.g., Re,

Ru, Os and Ir) tend to exhibit a larger ν_{NO} range from 1335-1493 cm^{-1} and significantly higher δ_{HNO} values, between 19.56-22.75 ppm, than those of the group 8 (Fe and Ru) heme model compounds, although the published J_{N-H} coupling constant values are all comparable for the ^{15}N-derivatives of non-heme and heme model complexes (J = 66-78 Hz).[6,13,14,16-19,23,48] Conversely, the heme model compounds have a much narrower ν_{NO} range of 1371-1389 cm^{-1} and relatively lower δ_{HNO} values between 13.51-14.26 ppm, while the δ_{HNO} of the more biologically relevant nitroxyl complexed myoglobin, Mb(HNO), is reported to be δ 14.80 ppm (D_2O). The large difference in δ_{HNO} between the heme model and non-heme compounds are attributed to the lack of the porphyrin macrocycle (i.e., loss of anisotropic shielding) placing the HNO chemical shifts of these reported non-heme complexes further downfield.[15,16-19,47-49]

Table 3.3 IR nitrosyl stretching frequencies and ^{1}H NMR chemical shifts of metal-HNO complexes.

	ν_{NO} (cm^{-1})	δ_{HNO} (ppm)[a]	Ref.
Non-heme model complexes			
$Os(HNO)Cl_2(CO)(PPh_3)_2$	1393[a,b], 1410[b]	21.20 (75)[c]	17,18
$Os(HNO)HCl(CO)(P^iPr_3)_2$	1388[c]	20.90[c]	47
$[Os(HNO)Br(CO)_2(PPh_3)_2]OTf$	1365[d]	20.70[g]	16
$[Re(HNO)(CO)_3(PPh_3)_2]OTf$	1391[d]	21.66 (72)[g]	16,23
$Re(HNO)Cl(CO)_2(PPh_3)_2$	1376[d]	20.66 (66)[g]	19
$Re(HNO)Cl(CO)_2(PCy_3)_2$	1335[d]	21.35[g]	19
$Ir(HNO)H(Cl)_2(PPh_3)_2$	1493[d]	22.75 (77)[g]	37
Ru(HNO)('$py^{bu}S_4$')	1358[a,d], 1378[d]	19.56[h]	47,49
$Ru(HNO)HCl(CO)(P^iPr_3)_2$	1392[e]	20.95[i]	15
Heme and heme models			
Mb(HNO)		14.80 (72)[j]	6
(OEP)Fe(HNO)(ImH)	1381[f]	13.93 (78)[k]	12
(OEP)Fe(HNO)(5-MeIm)	1383[f]	13.99 (76)[k]	12
(OEP)Fe(HNO)(1-MeIm)	1388[f]	13.72 (77)[k]	12
(PPDME)Fe(HNO)(ImH)	1382[f]	13.90 (76)[k]	12
(PPDME)Fe(HNO)(5-MeIm)	1382[f]	13.93 (77)[k]	12
(PPDME)Fe(HNO)(1-MeIm)	1384[f]	13.64 (77)[k]	12
(TTP)Fe(HNO)(ImH)	1385[f]	14.20 (76)[k]	12
(TTP)Fe(HNO)(5-MeIm)	1381[f]	14.26 (76)[k]	12
(TTP)Fe(HNO)(1-MeIm)	1389[f]	14.02 (76)[k]	12
(TTP)Ru(HNO)(1-MeIm)	1348[a,e], 1380[e]	13.64 (72)[k]	14
(T(*p*-OMe)PP)Ru(HNO)(1-MeIm)	1374[e]	13.60[k]	t.w.
(T(*p*-OMe)PP)Ru(HNO)(1-EtIm)	1373[e]	13.61[k]	t.w.
(T(*p*-OMe)PP)Ru(HNO)(1-PhIm)	1371[e]	13.64[k]	t.w.
(TPP)Ru(HNO)(1-MeIm)	1341[a,e], 1372[e]	13.62 (72)[k]	t.w.
(TPP)Ru(HNO)(1-EtIm)	1374[e]	13.62[k]	t.w.
(TPP)Ru(HNO)(1-PhIm)	1378[e]	13.65[k]	t.w.
(T(*p*-Cl)PP)Ru(HNO)(1-MeIm)	1375[e]	13.51[k]	t.w.
(T(*p*-Cl)PP)Ru(HNO)(1-EtIm)	1376[e]	13.51[k]	t.w.
(T(*p*-Cl)PP)Ru(HNO)(1-PhIm)	1381[e]	13.54[k]	t.w.

[a] $H^{15}NO$; J_{N-H} coupling constants (Hz) for $H^{15}NO$ derivatives are in parentheses
[b] Nujol
[c] Benzene-d_6
[d] Fluorolube/CaF_2
[e] KBr
[f] $CHCl_3$
[g] CD_2Cl_2
[h] THF-d_8
[i] Toluene-d_8
[j] D_2O
[k] $CDCl_3$

Due to the instability of the (por)Ru(HNO)(L_{Im}) compounds in solution, I proceeded to identify the decomposition products, as some of them might be present (or form) during subsequent reactivity studies. The products formed from the decomposition of the HNO complexes, with (TPP)Ru(HNO)(1-MeIm) chosen as a representative sample, at low temperatures (-28 °C) under an anaerobic environment were investigated. Figure 3.10 depicts the IR spectrum of the solid product isolated under these conditions. The absence of the initial ν_{NO} band observed previously at 1372 cm^{-1} and appearance of two new bands at 1813 cm^{-1} and 1864 cm^{-1} attributed to ν_{NO}, signifies complete conversion to these new species with the majority of the sample consisting of the band at the lower frequency. The ν_{NO} band at 1813 cm^{-1} is in the range typically seen for neutral (por)Ru(NO)(OR) (R = H or alkyl) compounds,[40,50,51] while the band at 1864 cm^{-1} matches that of the $[(TPP)Ru(NO)(1\text{-}MeIm)]^+$ precursor.

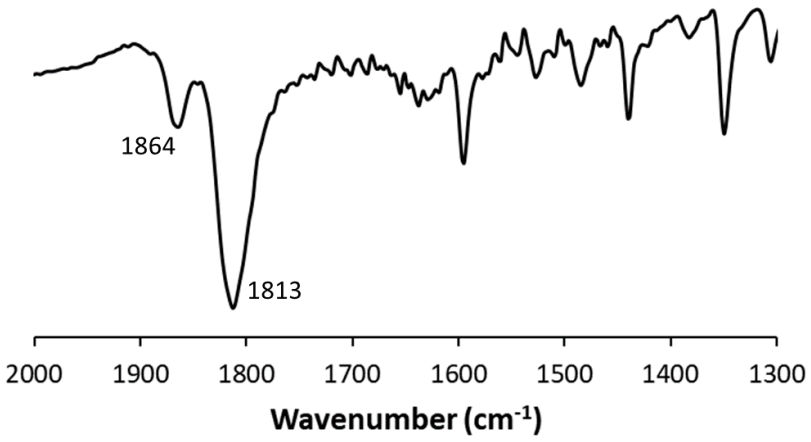

Figure 3.10 Truncated IR spectrum of the decomposition products (as a KBr pellet) formed from the (TPP)Ru(HNO)(1-MeIm) compound after 24 h in solution at -28 °C.

The ^1H NMR spectrum from the products formed under anaerobic conditions in solution at -28 °C after 24 h (Figure 3.11) display chemical shifts at δ 8.97 and 9.14 ppm corresponding to the pyrrole-H signals of two distinct Ru-porphyrin species in a ca. 3:1 ratio. These values are

consistent with the generation of a neutral complex at δ 8.97 ppm and reformation of a cationic complex at δ 9.14 ppm. The neutral complex matches spectroscopic data to that of the previously reported (por)Ru(NO)(OH) (por = TPP, TTP, OEP, TmTP).[33,52,53] An additional signal appears at a significantly lower value (upfield) of -6.39 ppm, which is in line with hydridic chemical shifts reported for other transition metal complexes[13,54,55] and has been tentatively assigned as the (TPP)Ru(NO)(H) compound. It is likely that this complex is converted into the hydroxide derivative in the presence of adventitious water through an unknown mechanism. A lack of detectable H_2 gas (δ = 4.62 ppm) is due to the instability of the $\{RuNO\}^7$ species that would form as a byproduct enroute to coupling of hydrogen radicals (i.e., like that observed for the Fe analogues),[13] and is supported by published DFT studies investigating the relativistic effects in $\{MNO\}^7$ porphyrin complexes (M = Ru and Os).[56]

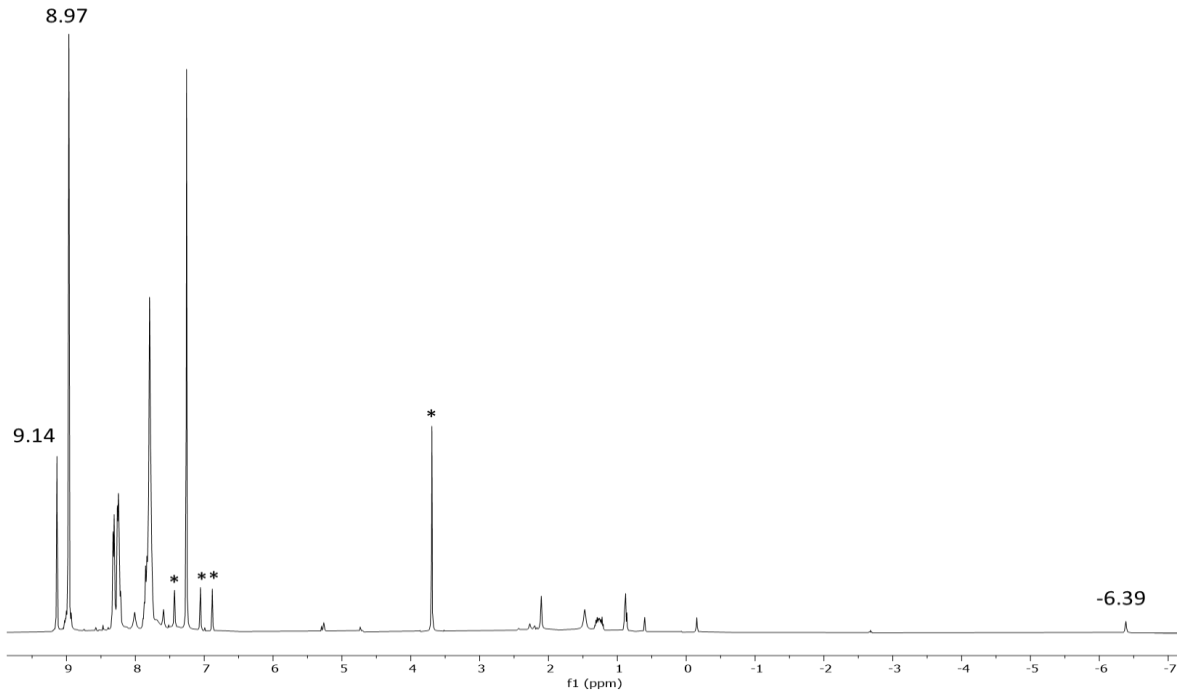

Figure 3.11 ^{1}H NMR spectrum of the decomposition products from the (TPP)Ru(HNO)(1-MeIm) compound dissolved with $CDCl_3$ in a sealed J. Young NMR tube at -28 °C for 24 h. Free 1-methylimidazole peaks highlighted by *.

3.3.3. Reactivity studies of Ru-HNO

3.3.3.1. Reaction of (TPP)Ru(HNO)(1-MeIm) with PPh_3

To supplement the spectroscopic data for the formation of the Ru-HNO derivatives by hydride attack described in the synthetic methodology, attempts were made to abstract the HNO ligand from the resulting (TPP)Ru(HNO)(1-MeIm) complex. A well-established reaction between HNO and an excess of PPh_3 was utilized that results in the splitting of the HNO moiety to form $O=PPh_3$ and $HN=PPh_3$ (eq. 3.1).[12] Figure 3.12 illustrates the results from the reaction of (TPP)Ru(HNO)(1-MeIm) with PPh_3, in which the ^{31}P NMR spectrum ($CDCl_3$) displays two distinct peaks at δ 29.1 ppm and 30.9 ppm corresponding to the imine and oxide forms of triphenylphospine, respectively, as well as the unreacted excess phosphine reagent at δ -5.5 ppm.[57] An aliquot of the reaction mixture (without any separation performed) was used to obtain an EI mass spectrum in $CHCl_3$ (Figure 3.12 inset), which yielded the expected *m/z* signals at 277 and 278 with a relative intensity of 3:1. Triphenylphosphine oxide has a known mass spectrum with signals at 277 and 278 with a relative intensity of 5:3, while the triphenylphosphine imine overlaps with the triphenylphosphine oxide at 277.

$$HNO + 2\ PPh_3 \longrightarrow Ph_3P{=}O + Ph_3P{=}NH \qquad \textbf{(3.1)}$$

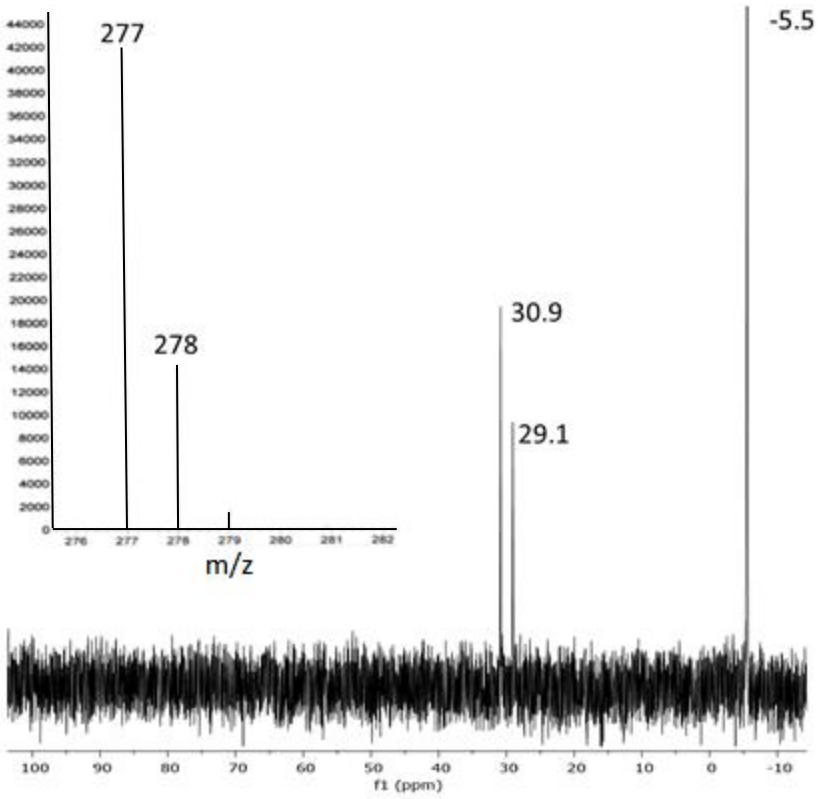

Figure 3.12 ^{31}P NMR and EI mass (inset) spectra of the products formed from the reaction of (TPP)Ru(HNO)(1-MeIm) with excess PPh_3.

3.3.3.2. Reaction of (TPP)Ru(HNO)(1-MeIm) and (TPP)Ru(H^{15}NO)(1-MeIm) with NO gas

The coupling of nitric oxide with complexed Fe-HNO has been reported by us[13] and is known to result in the production of N_2O. Employing ^{15}N- and ^{18}O-labelled experiments, it was determined that the internal nitrogen in NNO originates from external NO gas while the HNO ligand contributes the terminal nitrogen during N-N bond formation.[13] Repeating this reaction for the new (TPP)Ru(HNO)(1-MeIm) compound (eq. 3.2), N_2O was detected (12% yield) by gas phase IR spectroscopy following headspace analysis of the reaction vessel, which displayed the characteristic bands at 2212 cm^{-1} and 2237 cm^{-1} (Figure 3.13). The yield of N_2O was determined by the calibration curve (Figure 3.14) generated from known volumes of analytically pure N_2O

in a 10 mL IR gas cell (consisting of N_2 as the remainder) with absorbance values of the major 2237 cm^{-1} band.

$$(TPP)Ru(HNO)(1\text{-}MeIm) \xrightarrow{NO\ (g)} [(TPP)Ru(NO)(1\text{-}MeIm)]^{+} + N_2O \qquad \textbf{(3.2)}$$

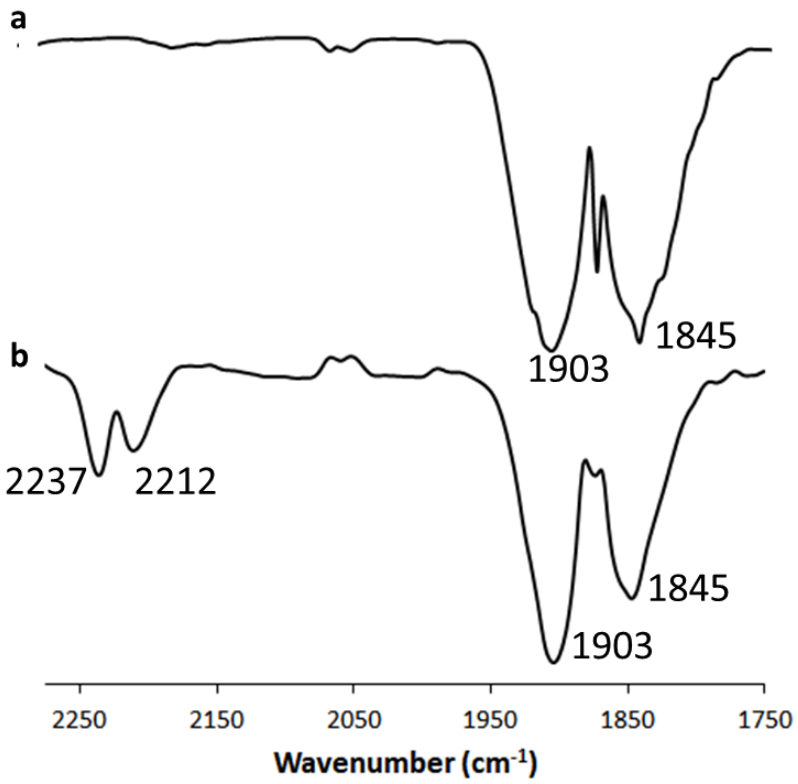

Figure 3.13 Truncated gas phase IR spectra of (a) purified NO gas line and (b) headspace from the reaction of (TPP)Ru(HNO)(1-MeIm) with NO gas.

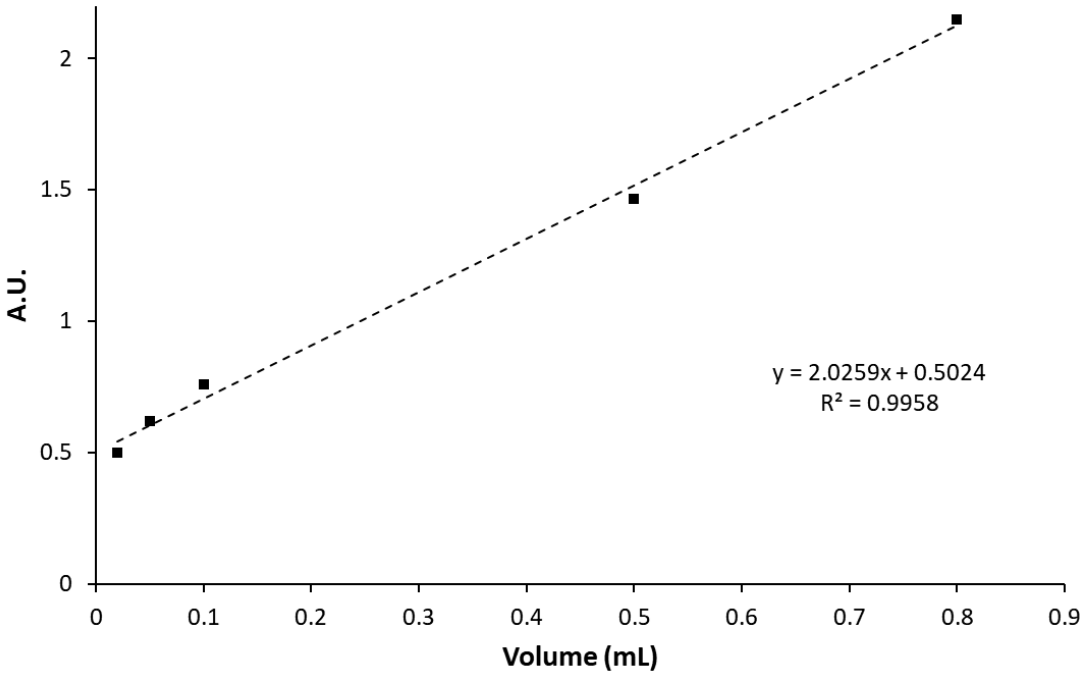

Figure 3.14 N_2O calibration curve determined from gas phase IR spectra from known syringed volumes of analytically pure N_2O.

The solid product obtained from the reaction of (TPP)Ru(HNO)(1-MeIm) with NO gas was crystallized and the molecular structure shown in Figure 3.15. The identity of the product was determined to be [(TPP)Ru(NO)(1-MeIm)]ONO (98% yield), where the oxygens of the NO_2^- counterion were disordered over three sites with occupancies of O2 = 0.678(5), O3 = 0.661(5) and O4 = 0.661(5). As seen for the cationic precursor, a near linear ∠RuNO bond angle of 177.3(3)° was observed with a Ru-N(O) bond length of 1.747(3)Å, while the Ru-N_{Im} (Ru-N6) bond length was found to be 2.091(2)Å. Surprisingly the imidazole moiety *trans* to NO remains intact in the final product, even though the mechanism for (por)Ru(CO) complexes converting excess NO to N_2O is believed to require both axial sites,[33,58-61] it is unclear whether that is the case throughout this reaction. Separate control experiments failed in attempts to substitute the *O*-bound nitrite of independently generated (TPP)Ru(NO)(ONO)[33] with 1-methylimidazole.

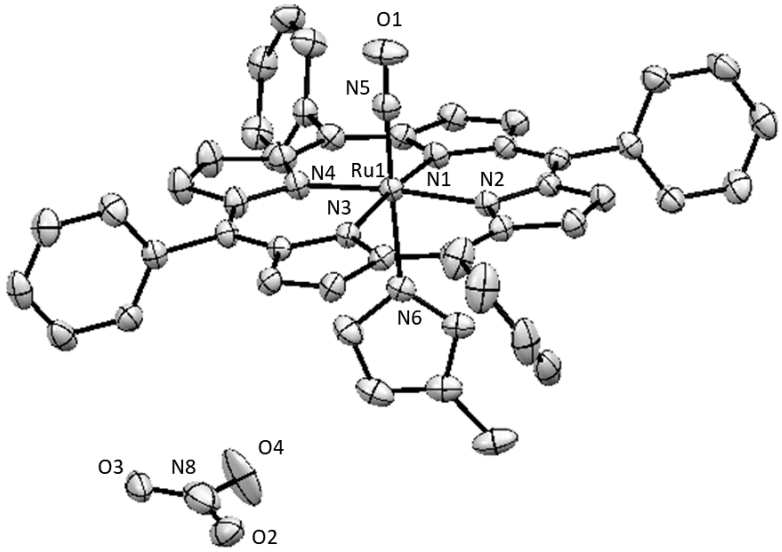

Figure 3.15 Molecular structure of the [(TPP)Ru(NO)(1-MeIm)]ONO (i.d. 20081) product from the reaction of (TPP)Ru(HNO)(1-MeIm) with NO gas. Hydrogen atoms have been omitted for clarity.

The IR spectrum of the crystallized [(TPP)Ru(NO)(1-MeIm)]ONO (Figure 3.16) product yielded a ν_{NO} band at 1871 cm^{-1}, consistent with the generation of a positively charged nitrosonium product. A new band was also detected at 1326 cm^{-1} and has been assigned to the ν_{ONO} of the NO_2^- counterion.[62,63] Further confirmation of the product formed following the reaction of (TPP)Ru(HNO)(1-MeIm) with NO gas (Figure 3.17) via ^1H NMR spectroscopy displays a pyrrole-H peak at δ 9.16 ppm and imidazole peaks between δ -0.11 ppm and 4.75 ppm, similar to that exhibited by the cationic precursor complex.

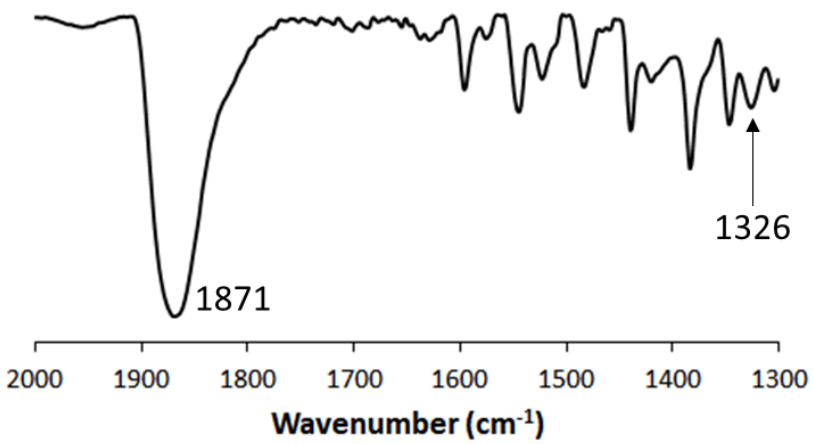

Figure 3.16 Truncated IR spectrum of the crystallized product as a KBr pellet from the reaction of (TPP)Ru(HNO)(1-MeIm) with NO gas.

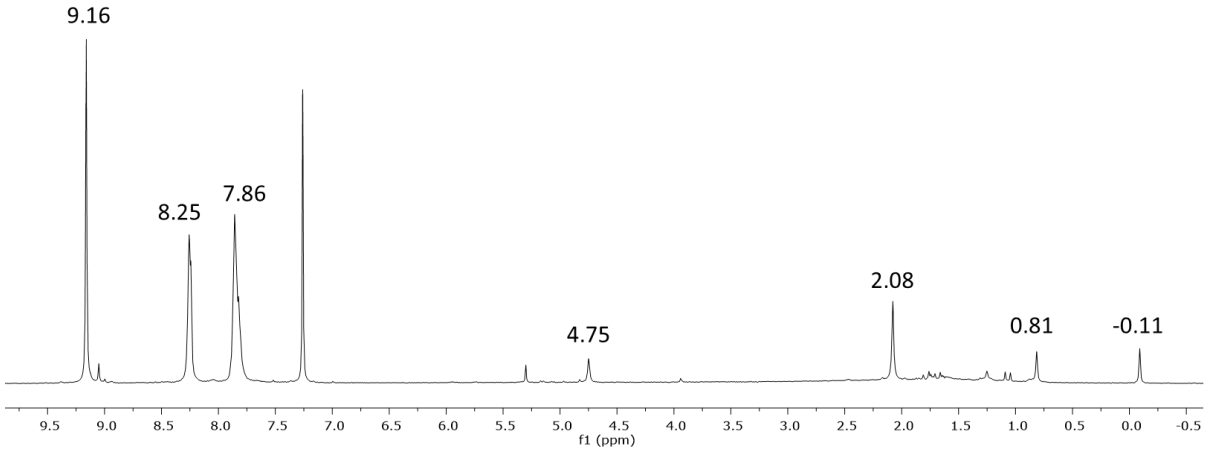

Figure 3.17 ^{1}H NMR spectrum of the crystallized product in $CDCl_3$ from the reaction of (TPP)Ru(HNO)(1-MeIm) with NO gas.

As mentioned previously, Ru-heme model compounds are known to disproportionate nitric oxide into N_2O; however, to confirm the contribution of HNO to the N_2O formation, rather than the Ru-porphyrin complex itself, ^{15}N-labelled experiments were employed. Figure 3.18 illustrates the gas phase IR spectrum obtained from the headspace of the reaction of (TPP)Ru(H^{15}NO)(1-MeIm) with NO. Two new bands were observed at 2169 cm^{-1} and 2191 cm^{-1}

for the mixed isotope $^{14}N^{15}NO$ overlapping with the unlabeled N_2O, consistent with the internal ^{15}NO fragment of NNO being derived from the labeled $H^{15}NO$ and the terminal ^{14}N from the unlabeled NO gas.[13,64] The percent yield for the labeled product could not be determined from the calibration curve used previously.

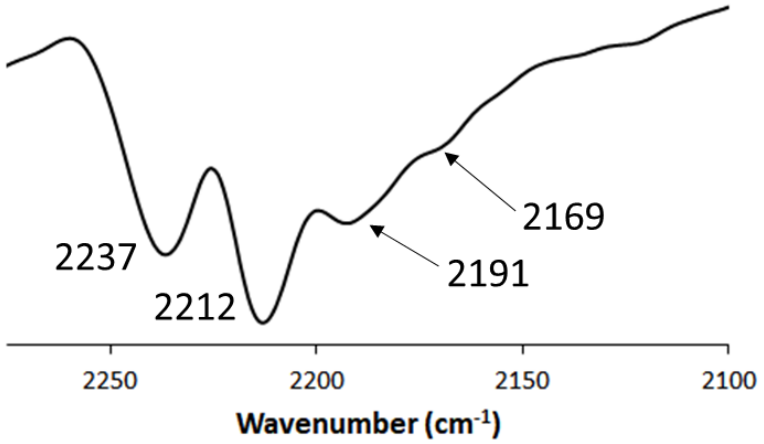

Figure 3.18 Truncated gas phase IR spectrum of the headspace from the reaction of (TPP)Ru($H^{15}NO$)(1-MeIm) with NO gas. The unlabeled N_2O bands are at 2212 cm^{-1} and 2237 cm^{-1} and the labeled bands are at 2169 cm^{-1} and 2191 cm^{-1}.

3.3.3.3. Reaction of (TPP)Ru(HNO)(1-MeIm) with CO gas

The rapid dimerization of two HNO molecules (k = 8.0 x 10^6 M^{-1} s^{-1}) in the absence of other active species to yield N_2O and H_2O is well-established.[65] Efforts have been made to investigate potential reagents capable of initiating displacement of the HNO ligand to allow this dimerization (Eq. 3.3). Initial attempts utilizing CO gas were successful in substituting the HNO ligand leading to the generation of N_2O gas (4% yield), as indicated by the 2212 cm^{-1} and 2237 cm^{-1} bands in the gas phase IR spectrum (Figure 3.17), and the (TPP)Ru(CO)(1-MeIm) byproduct (85% yield). The identity of this byproduct was confirmed by ^1H NMR and IR spectroscopy with comparison to reported values of this known compound.[31] Again, this yield of

N_2O was determined from the calibration curve discussed earlier. This is the first example of CO initiating HNO dissociation to form N_2O in heme model complexes. The signals corresponding to free CO gas at 2117 cm^{-1} and 2171 cm^{-1} overlap slightly with the other expected band of N_2O at 2212 cm^{-1}.

$$(TPP)Ru(HNO)(1\text{-}MeIm) + CO\ (g) \longrightarrow (TPP)Ru(CO)(1\text{-}MeIm) + N_2O \qquad \textbf{(3.3)}$$

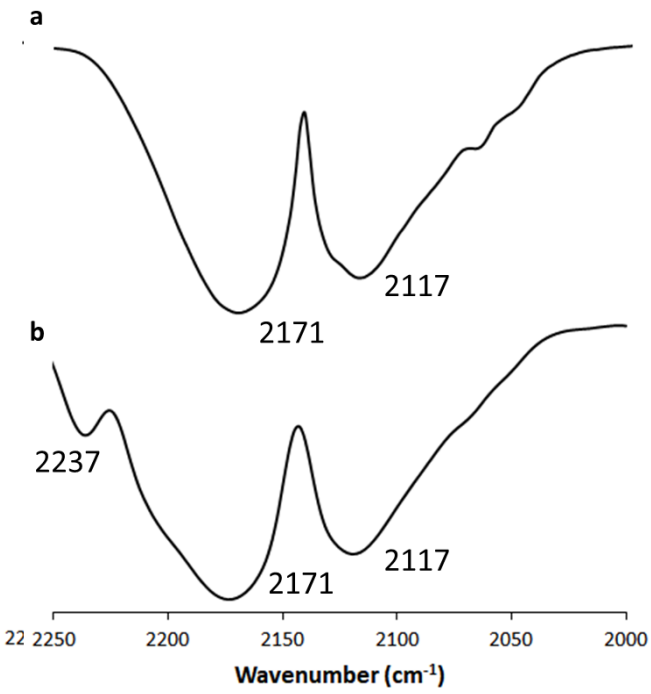

Figure 3.19 Gas phase IR spectra of the (a) CO gas line and (b) headspace from the reaction of CO gas with (TPP)Ru(HNO)(1-MeIm).

Following the headspace analysis, the reaction products remaining in the solution were characterized to determine their identities and in what yields the products were formed. The IR spectrum of the solid product obtained from the reaction of (TPP)Ru(HNO)(1-MeIm) with CO gas (Figure 3.20) displays two new bands at 1868 cm^{-1} and 1938 cm^{-1}, with the latter being the most prominent. These frequencies are consistent with the ν_{NO} of a $[(TPP)Ru(NO)(1\text{-}MeIm)]^+$ complex and the ν_{CO} of previously reported (TPP)Ru(CO)(1-MeIm), respectively.[31]

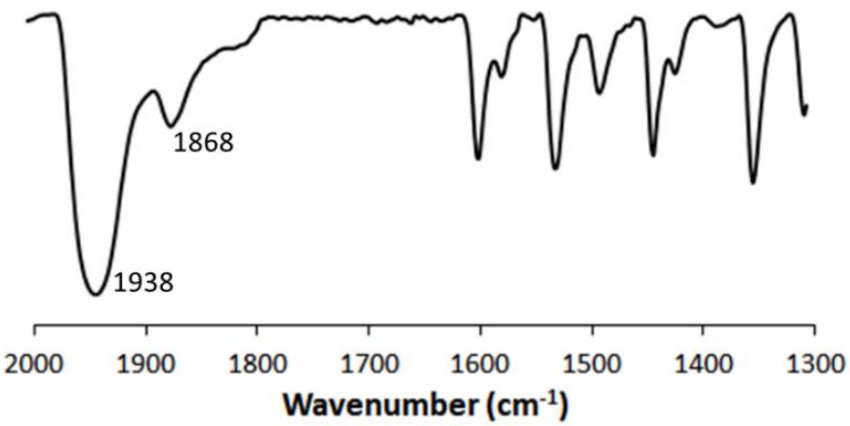

Figure 3.20 Truncated IR spectrum of the solid product as a KBr pellet isolated from the reaction of (TPP)Ru(HNO)(1-MeIm) with CO gas.

The ^{1}H NMR spectrum of this product (Figure 3.19) reveals two primary species with pyrrole-H peaks at δ 8.58 ppm and 9.16 ppm, with coordinated imidazole found to be shifted slightly from the (TPP)Ru(HNO)(1-MeIm) compound from δ 1.20-4.80 ppm to δ 0.94-4.62 ppm. These pyrrole-H signals correspond to the reported values of (TPP)Ru(CO)(1-MeIm),[31] obtained in 85% yield, and match a previously observed nitrosonium product, respectively.

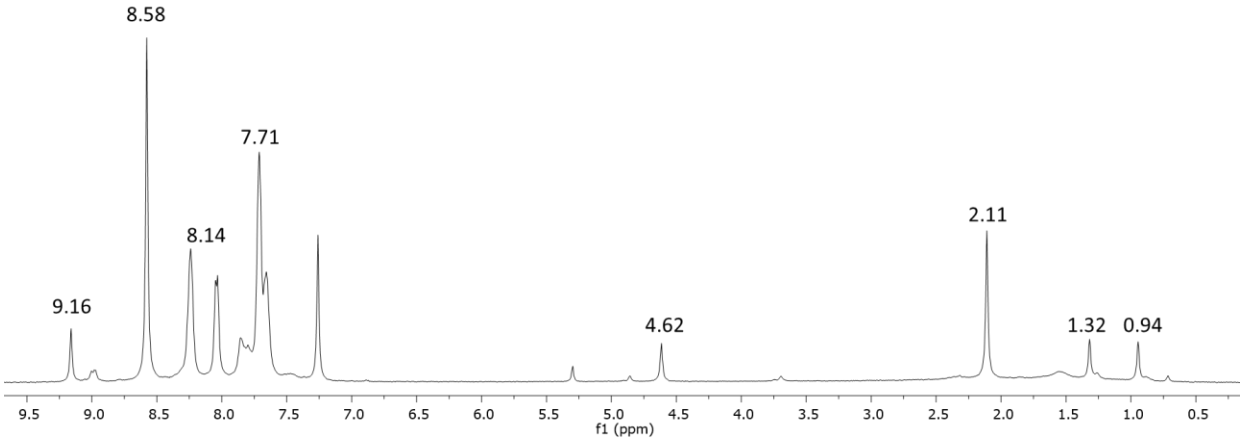

Figure 3.21 ^{1}H NMR spectrum of the solid products in $CDCl_3$ formed from the reaction of (TPP)Ru(HNO)(1-MeIm) with CO gas.

3.3.3.4. Reaction of (TPP)Ru(HNO)(1-MeIm) with 1,3-cyclohexadiene in the absence and presence of CO gas

Another known approach to trapping HNO is a nitroso Diels-Alder type reaction, in which HNO and a diene undergo coupling (eq. 3.4).[28] The diene chosen for this reactivity study was 1,3-cyclohexadiene, given that the expected reaction product has been reported previously,[26] and was performed in the absence and presence of CO gas, in an effort to encourage liberation of the HNO ligand from the (TPP)Ru(HNO)(1-MeIm) complex. No reaction was observed between excess diene and the HNO in the presence of CO gas, even though the ^{1}H NMR spectrum of the product from this reaction (Figure 3.22) is consistent with the formation of the previously reported (TPP)Ru(CO)(1-MeIm), following displacement of HNO. Peaks associated with unreacted 1,3-cyclohexadiene are highlighted by * in Figure 3.22. Attempts to react the diene directly with the Ru-HNO compound only resulted in generation of the previously observed anaerobic decomposition products and unreacted 1,3-cyclohexadiene. It is not surprising that this particular HNO trap failed given the reported conditions necessary for the nitroso adduct to form from the diene. For example, a potent HNO donor (e.g., Angeli's salt) in the presence of the diene reagent required high temperatures (refluxing THF or benzene) to proceed.[26] As discussed earlier, these Ru-HNO compounds are thermally unstable, decomposing into other stable six-coordinate ruthenium nitrosyl porphyrin complexes even at temperatures as low as -28 °C.

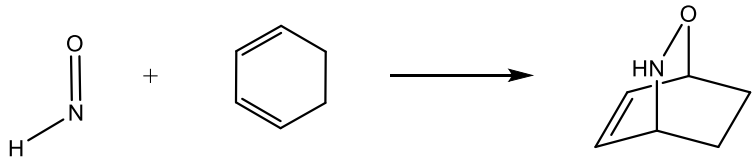

(3.4)

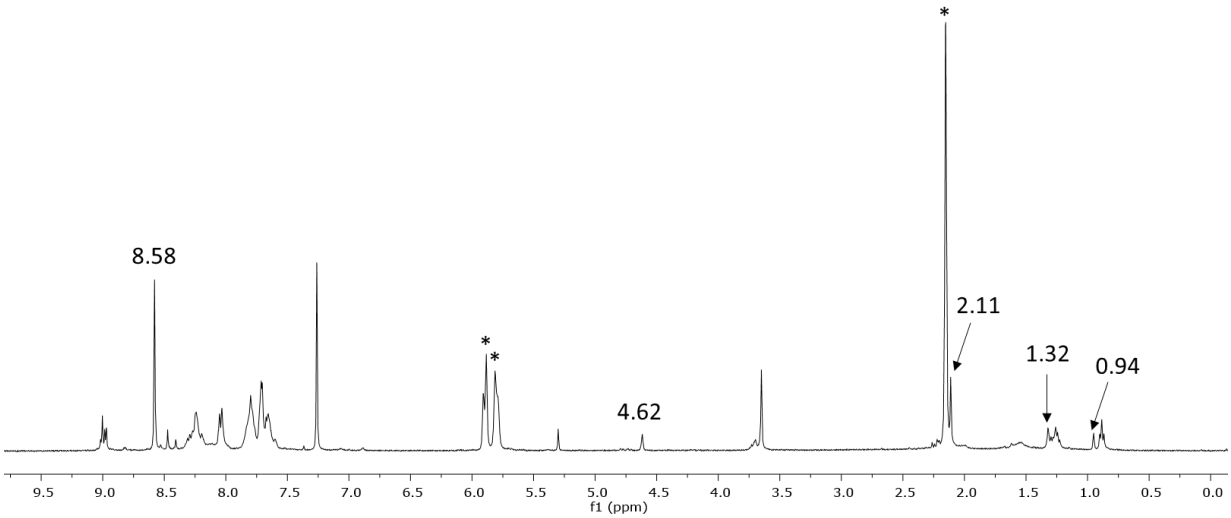

Figure 3.22 ^{1}H NMR spectrum of the products formed from the reaction of (TPP)Ru(HNO)(1-MeIm) with 1,3-cyclohexadiene (*) in the presence of CO gas.

3.3.3.5. Reaction of (TPP)Ru(HNO)(1-MeIm) with PhNO

Initial efforts to displace HNO using PhNO to generate N_2O (Eq. 3.5) were unsuccessful; such reactions have been mentioned briefly in literature.[14] The IR spectrum from the solid product obtained from the reaction of (TPP)Ru(HNO)(1-MeIm) with ~2 equiv. of PhNO reveals a band at 1309 cm^{-1} (Figure 3.23), consistent with the ν_{NO} of the previously reported (TPP)Ru(PhNO)(1-MeIm) expected product as well as unreacted PhNO at 1481 cm^{-1}. A ^{1}H NMR spectrum of the same reaction mixture (Figure 3.24) reveals peaks corresponding to the known (TPP)Ru(PhNO)(1-MeIm) complex (67% yield).[36] Some minor species are detected with assorted peaks between δ 8.96 ppm and 9.16 ppm, assigned primarily to the decomposition products characterized previously. Absence of N_2O in the headspace with confirmed presence of the expected (TPP)Ru(PhNO)(1-MeIm) complex implies an alternative mechanism to HNO displacement.

$$\text{(TPP)Ru(HNO)(1-MeIm)} + \text{PhNO} \longrightarrow \text{(TPP)Ru(PhNO)(1-MeIm)} + N_2O \qquad \textbf{(3.5)}$$

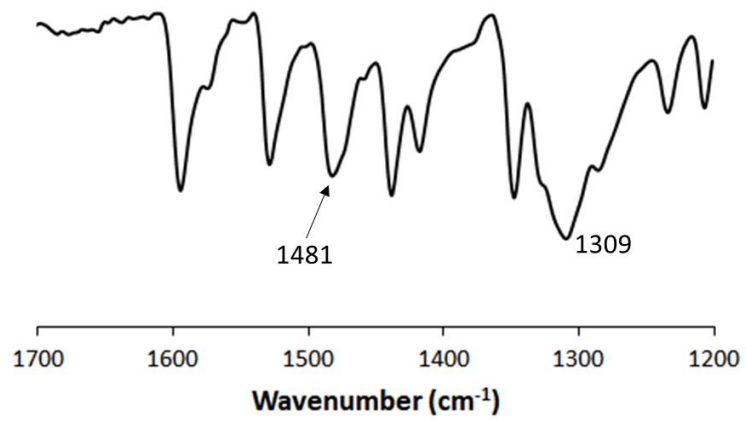

Figure 3.23 Truncated IR spectrum of the product formed from the reaction of (TPP)Ru(HNO)(1-MeIm) with PhNO in KBr pellet.

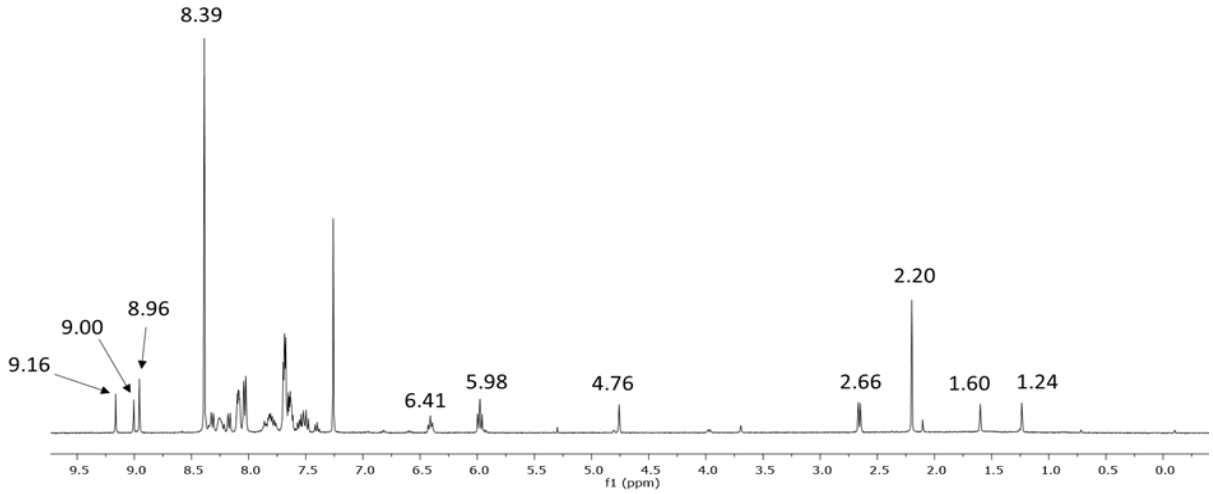

Figure 3.24 ^{1}H NMR spectrum of the products formed from the reaction of (TPP)Ru(HNO)(1-MeIm) with PhNO in $CDCl_3$.

The lack of N_2O production, despite the expected (TPP)Ru(PhNO)(1-MeIm) complex being present as the major product, suggests a potential alternative mechanism to HNO displacement. Repeating this reaction in a sealed J. Young NMR tube at low temperatures (-30 °C) revealed the formation of a metastable species with a pyrrole-H signal at δ 8.93 ppm with peaks in the region commonly associated with coordinated aromatic protons at δ 6.07 and 6.18

ppm, along with a new singlet at δ -0.45 ppm (Figure 3.25). Allowing this mixture to reach room temperature leads to the appearance of peaks matching those of (TPP)Ru(PhNO)(1-MeIm), as described in Figures 3.23 and 3.24. While it is difficult to definitively identify this intermediate species it is possible that an unstable *N*-nitroso-*N*-phenylhydroxylamine ruthenium porphyrin complex forms prior to the various products mentioned earlier, given the known reaction of HNO donors in the presence of PhNO to generate cupferron.[29]

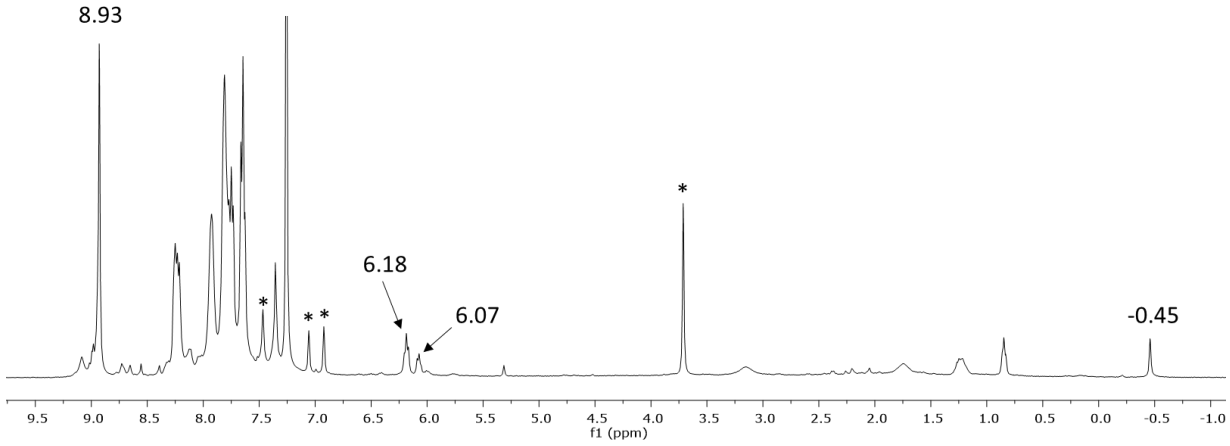

Figure 3.25 ^{1}H NMR spectrum of the J. Young tube reaction of (TPP)Ru(HNO)(1-MeIm) with PhNO at -30 °C in $CDCl_3$.

3.3.3.6. Reaction of (TPP)Ru(HNO)(1-MeIm) with 2-methyl-2-propanethiol

Attempts at employing a thiol (HS-C$(CH_3)_3$) at various concentrations to couple with the Ru-HNO (Eq. 3.6a,b) to produce the expected free hydroxylamine or the corresponding sulfinamide (R(S=O)NH_2)[25] were unsuccessful, although the known organic disulfide compound was detected by ^{1}H NMR spectroscopy.[66] The IR spectrum of the product isolated from the reaction of (TPP)Ru(HNO)(1-MeIm) with a 10-fold equiv. of the thiol resulted in new ν_{NO} band at 1784 cm^{-1} (Figure 3.26), which matches the separately prepared (TPP)Ru(NO)(S-C$(CH_3)_3$)

compound and falls in the range of previously reported (por)Ru(NO)(*S*-ligand) complexes (ν_{NO} = 1770-1798 cm^{-1}).[38-40,50] Two other ν_{NO} bands associated with the decomposition products at 1813 cm^{-1} and 1868 cm^{-1} are present as well.

$$HNO + RSH \longrightarrow R(S{=}O)NH_2 \qquad \textbf{(3.6a)}$$

$$HNO + \text{xs } RSH \longrightarrow NH_2OH + RSSR \qquad \textbf{(3.6b)}$$

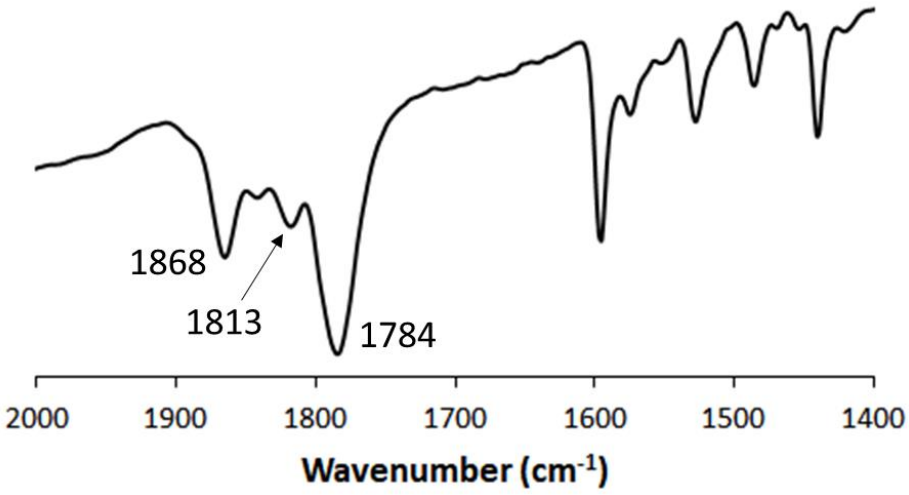

Figure 3.26 Truncated IR spectrum of the solid product (as a KBr pellet) obtained from the reaction of (TPP)Ru(HNO)(1-MeIm) with HS-C$(CH_3)_3$ after 24 h at room temperature.

This reaction was repeated in a J. Young tube (-30 °C), in order to monitor the progress by ^{1}H NMR spectroscopy, with the spectra recorded at the 1 h mark at -30°C (Figure 3.27a), then was allowed to slowly reach room temperature and the ^{1}H NMR spectrum recorded again 24 h later. Attempts were unsuccessful in detecting the formation of free hydroxylamine or the sulfinamide compound in either ^{1}H NMR or IR spectroscopy from reacting (TPP)Ru(HNO)(1-MeIm) with various concentrations of HS-C$(CH_3)_3$ (at room temperature and as low as -45 °C). However, di-*tert*-butyl disulfide was detected during the reaction within a J. Young tube in the presence of a large excess of HS-C$(CH_3)_3$ at room temperature. Formation of the thiolate

compound is expected to be due to decomposition of the HNO compound to the hydroxide complex that subsequently undergoes an exchange with the thiol that is in excess and matches signals associated with the separately prepared (TPP)Ru(NO)(S-C(CH_3)$_3$. After 24 h the new pyrrole-H signal at δ 9.15 ppm (Figure 3.27b) appears and is assigned to the [(TPP)Ru(NO)(1-MeIm)]$^+$ decomposition product. A noticeable increase in the signal at δ 1.30 ppm is detected, which matches the known chemical shift value for di-*tert*-butyl disulfide.[66] This generation of the [(TPP)Ru(NO)(1-MeIm)]$^+$ complex and simultaneous increase in the disulfide signal suggests dissociation of the coordinated thiolate ligand contributes to the formation of the organic disulfide product. Similar to what was observed in the diene experiments, the change in reactivity between coordinated (Ru-HNO) and free HNO results in products being formed outside of those reported. The initial spectrum (blue trace) was recorded 1 h after the sample had thawed at -30 °C in a sealed J. Young tube and again 24 h later at room temperature (black trace).

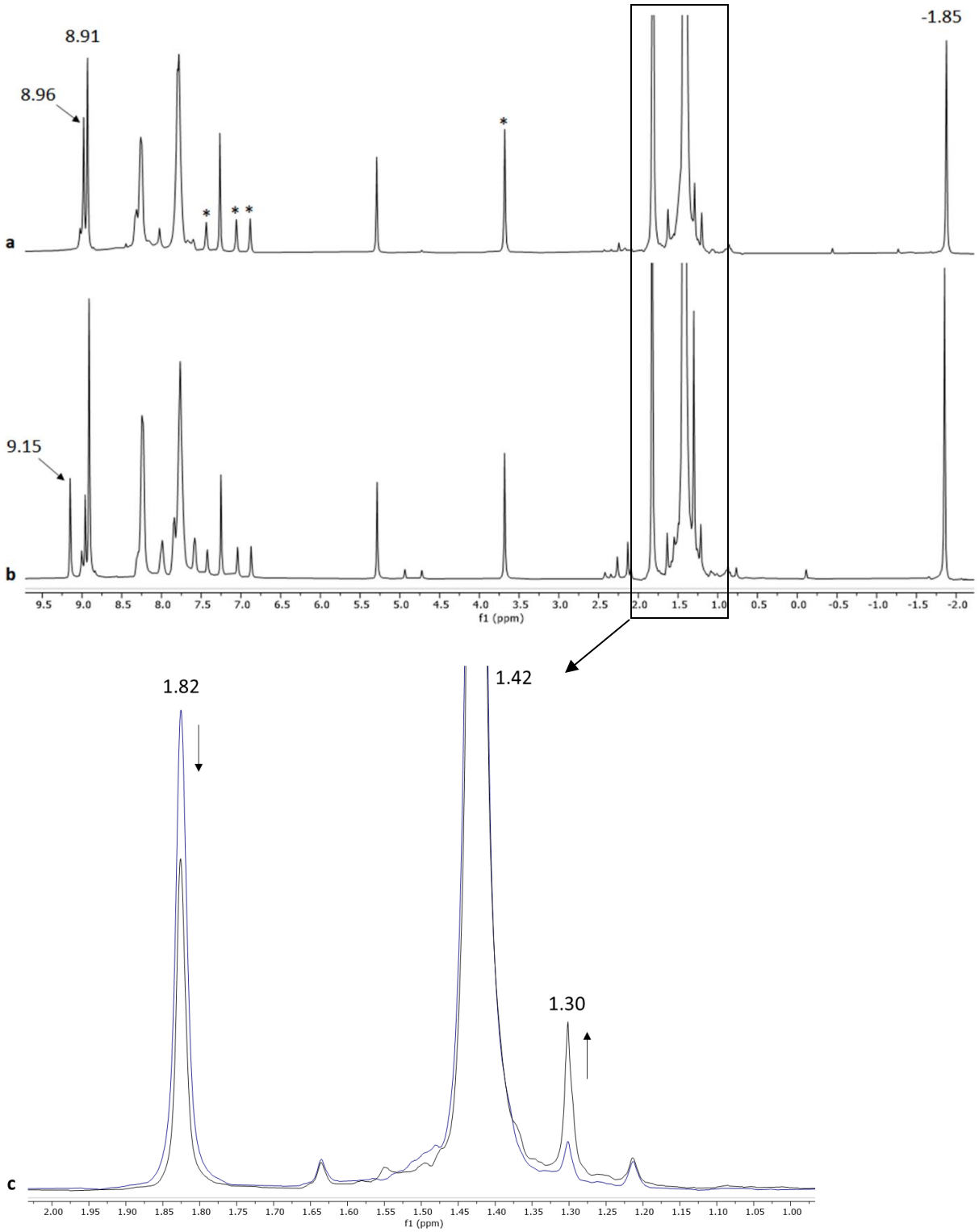

Figure 3.27 ^{1}H NMR spectra of the J. Young tube reaction of (TPP)Ru(HNO)(1-MeIm) with HS-C(CH_3)$_3$ after (a) 1 h at -30 °C, (b) 24 h at room temperature and (c) a stacked and zoomed-in view of these spectra. Free 1-metyhlimidazole highlighted by *.

3.5. Summary and Conclusions

A preliminary investigation into the properties and cathodic behavior of the $[(TPP)Ru(NO)(1\text{-}MeIm)]^+$ precursor yielded results similar to the previous in-depth study of the biologically relevant iron analogues,[13] in particular site of the multielectron reduction (i.e., N-pathway hydride attack). Successful synthesis of significantly more stable and purer (por)Ru(HNO)(L_{Im}) (por = TPP, T(*p*-OMe)PP, T(*p*-Cl)PP; L_{Im} = 1-MeIm, -EtIm, -PhIm) compounds, from an adapted procedure of former group member Jonghyuk Lee, have allowed for greater insight into the reactivity of Ru-HNO heme models. IR data for the isolated solid samples display ν_{NO} bands at lower frequencies (1372-1381 cm^{-1}) than reported values for free HNO (1500 cm^{-1}) and significantly lower from the experimentally obtained [(por)Ru(NO)(L_{Im})]BF_4 precursors (1862-1869 cm^{-1}), as has been shown with previous heme model compounds and non-heme coordination complexes. The exceptionally large shifts observed upon conversion of [(por)Ru(NO)(L_{Im})]BF_4 to (por)Ru(HNO)(L_{Im}) are indicative of significant bending of the NO^+ moiety following reduction (occupying π^* orbitals), while the minimal shifts between the porphyrin and imidazole derivatives suggests a relatively insignificant impact these ligands exhibit on the Ru-HNO fragment. ^{1}H NMR spectra revealed δ_{HNO} signals similar to other heme-HNO model compounds but differ significantly from the group 7-9 transition metal non-heme coordination complexes, likely due to the absence of the porphyrin macrocycle that causes an anisotropic deshielding effect.

The decomposition products of (TPP)Ru(HNO)(1-MeIm), as the representative sample, differed considerably from what was reported for the iron species. Neither N_2O (by headspace IR gas analysis) or H_2 (by ^{1}H NMR spectroscopy) gas were detected following decomposition in sealed reaction vessels at low temperature. However, formation of the (TPP)Ru(NO)(H) and

$[(TPP)Ru(NO)(1\text{-}MeIm)]^+$ complexes were present under anaerobic conditions and implies that the loss of hydride from the Ru-HNO moiety is the most probable pathway. This is supported by the lack of detectable H_2 gas, as seen in the Fe analogues, as well as the favored 6-coordinate geometry and low spin nature of ruthenium(II), which is unlikely to result in rapid dissociation and dimerization of HNO forming N_2O (without ligand substitution).

Attempts at probing the reactivity of complexed Ru-HNO revealed that strong field ligands like PPh_3, CO and NO interacted at the Ru-HNO site to generate the expected products. For example, the commonly employed HNO trap PPh_3 yielded the corresponding oxide and imine derivatives of triphenylphosphine, confirming the presence of coordinated HNO. The reactions using carbon monoxide and nitric oxide with (TPP)Ru(HNO)(1-MeIm) resulted in the formation of N_2O, although the mechanisms by which it is generated differ. A simple ligand substitution takes place when CO is utilized that leads to dissociation and subsequent dimerization of HNO. This is the first reported instance of carbon monoxide displacing HNO as a ligand and may behave like a competitive inhibitor in biological systems at physiological conditions. However, external NO couples with bound HNO, as confirmed by N_2O mixed isotope from ^{15}N-labelled experiments. Reactivity with PhNO did not yield N_2O, despite formation of the proposed byproduct, and is believed to be the result of an alternative mechanism involving an as yet unidentified intermediate (possibly a coordinated nitroso phenylhydroxylamine complex). The diene and thiol reagents, namely 1,3-cyclohexadiene and $HS\text{-}C(CH_3)_3$, did not directly interact with the coordinated HNO ligand due to the increased stability of these complexes and reaction conditions being too mild (i.e., (TPP)Ru(HNO)(1-MeIm) is not potent enough of an HNO donor and temperatures being too low to elicit such reactions). Through the synthetic route described in this chapter, a larger variety of isolable Ru-

HNO complexes are achievable, including different porphyrin and imidazole derivatives. This work offers insight into the difference in reactivity of coordinated HNO complexes and free HNO. Namely, the increased stability of (por)Ru(HNO)(L_{Im}) complexes, and the corresponding decomposition products, come with a trade-off that the reactivity is limited by comparison to the more unstable and difficult to characterize iron systems.

3.5 References

1. Miranda, K. M.; Ridnour, L.; Esprey, M.; Citrin, D.; Thomas, D.; Mancardi, D.; Donzelli, S.; Wink, D. A.; Katori, T.; Tocchetti, C. G.; Ferlito, M.; Paolocci, N.; Fukuto, J. M. *Prog. Inorg. Chem*. **2005**, *54*, 349-384.

2. Einsle, O.; Messerschmidt, A.; Huber, R.; Kroneck, P. M. H.; Neese, F. *J. Am. Chem. Soc*. **2002**, *124*, 11737-11745.

3. Bykov, D.; Neese, F. *Inorg. Chem*. **2015**, *54*, 9303-9316.

4. Daiber, A.; Shoun, H.; Ullrich, V. *J. Inorg. Biochem*. **2005**, *99*, 185-193.

5. Nomura, T.; Kimura, T.; Kanematsu, T.; Yamada, D.; Yamashita, K.; Hirata, K.; Ueno, G.; Murakami, H.; Hisano, T.; Yamagiwa, R.; Takeda, H.; Gopalasingam, C.; Kousaka, R.; Yanagisawa, S.; Shoji, O.; Kumasaka, T.; Yamamoto, M.; Takano, Y.; Sugimoto, H.; Tosha, T.; Kubo, M.; Shiro, Y. *Proc. Natl. Acad. Soc.* **2021**, *118*, 1-5.

6. Sulc, F.; Fleischer, E.; Farmer, P .J.; Ma, D.; La Mar, G. N. *J. Bio. Inorg. Chem*. **2003**, *8*, 348–352.

7. Doctorovich, F.; Bikiel, D.; Pelligrino, J.; Suarez, S. A.; Larsen, A.; Marti, M. A. *Coord. Chem. Rev.* **2011**, *255*, 2764-2784.

8. Miranda, K. M. *Coord. Chem. Rev.* **2005**, *249*, 433-455.

9. Morales Vasquez, M. A.; Pellegrino, J.; Alvarez, L.; Neuman, N. I.; Doctorovich, F.; Marti, M. A. *The Chemistry and Biology of Nitroxyl (HNO)*.Elsevier Inc.: **2017**; 193-205.

10. Fukuto, J. M. *Brit. J. Pharm.* **2019**, *176*, 135-146.

11. Carvalho, E. M.; Sousa, E. H. S.; Bernardes-Génisson, V.; de França Lopes, L. G. *Eur. J. Inorg. Chem.* **2021**, 1-34.

12. Abucayon, E. G.; Khade, R. L.; Zhang, Y.; Richter-Addo, G. B. *J. Am. Chem. Soc*. **2016**, *38*, 104-107.

13. Abucayon, E. G.; Khade, R. L.; Powell, D. R.; Shaw, M. J.; Zhang, Y.; Richter-Addo, G. B. *Dalton Trans.* **2016**, *45*, 18259-18266

14. Lee, J.; Richter-Addo, G. B. *J. Inorg. Biochem.* **2004**, *98*, 1247-1250.

15. Sellmann, D.; Gottschalk-Gaudig, T.; Haussinger, D; Heinemann, F. W.; Hess, B. A. *Chem. Eur. J.* **2001**, *7*, 2099–2103.

16. Melenkivitz, R.; Southern, J. S.; Hillhouse, G. L.; Concolino, T. E.; Liable-Sands, L. M.; Rheingold, A. L. *J. Am. Chem. Soc.* **2002**, *124*, 12068–12069.

17. Grundy, K. R.; Reed, C. A.; Roper, W. R. *J. Chem. Soc., Chem. Commun.* **1970**, 1501–1502.

18. Wilson, R. D.; Ibers, J. A. *Inorg. Chem.* **1979**, *18*, 336–343.

19. Southern, J. S.; Green, M. T.; Hillhouse, G. L.; Guzei, I. A.; Rheingold, A. L. *Inorg. Chem.* **2001**, *40*, 6039–6046.

20. Melenkivitz, R.; Hillhouse, G. L. *Chem. Comm*. **2002**, *6*, 660–661.

21. Codesido, N. O.; Weyhurmuller, T.; Olabe, J. A.; Slep, L. D. *Inorg. Chem*. **2014**, *53*, 981-997.

22. Rahman, M. H.; Ryan, M. D. *Inorg. Chem*. **2017**, *56*, 3302-3309.

23. Southern, J. S.; Hillhouse, G. L.; Rheingold, A. L. *J. Am. Chem. Soc.* **1997**, *119*, 12406–12407.

24. Polaczek, J.; Subedi, H.; Orzel, L.; Lisboa, L. S.; Cink, R. B.; Stochel, G.; Brasch, N. E.; van Eldik, R. *Inorg. Chem*. **2021**, *60*, 2964-2975.

25. Zarenkiewicz, J.; Khodade, V. S.; Toscano, J. P. *J. Org. Chem.* **2021**, *86*, 868-877.

26. Ensley, H. E.; Mahadevan, S. *Tetrahedron Lett.* **1989**, *30*, 3255-3258.

27. Kesler, E. *J. Heterocyclic Chem.* **1980**, *17*, 1113.

28. Leach, A. G.; Houk, K. N. *J. Am. Chem. Soc.* **2002**, *124*, 14820-14821.

29. Shoeman, D. W.; Nagasawa, H. T. *Nitric Oxide: Biol. Chem*. **1998**, *2*, 66-72.

30. Reisz, J. A.; Zink, C. N.; King, S. B.; *J. Am. Chem. Soc.* **2011**, *133*, 11675-11685.

31. Slebodnick, C.; Seok, W. K.; Kim, K. M.; Ibers, J. A. *Inorg. Chim. Acta.* **1996**, *243*, 57-65.

32. Connelly, N. G.; Draggett, P. T.; Green, M.; Kuc, T. A. *J.C.S. Dalton Trans.* **1977**, *1*, 70-73.

33. Miranda, K. M.; Bu, X.; Lorkovic´, I.; Ford, P .C. *Inorg. Chem.* **1997,** *36*, 4838-4848.

34. Imbeaux, J. C.; Saveant, J. M. *J. Electroanal. Chem. Interf. Electrochem.* **1973**, *44*, 169-187.

35. Frisch, M. J.; Trucks, G. W.; Schlegel, H. B.; Scuseria, G. E.; Robb, M. A.; Cheeseman, J. R.; Scalmani, G.; Barone, V.; Mennucci, B.; Petersson, G. A.; Nakatsuji, H.; Caricato, M.; Li, X.; Hratchian, H. P.; Izmaylov, A. F.; Bloino, J.; Zheng, G.; Sonnenberg, J. L.; Hada, M.; Ehara, M.; Toyota, K.; Fukuda, R.; Hasegawa, J.; Ishida, M.; Nakajima, T.; Honda, Y.; Kitao, O.; Nakai, H.; Vreven, T.; Montgomery Jr., J. A.; Peralta, J. E.; Ogliaro, F.; Bearpark, M. J.; Heyd, J.; Brothers, E. N.; Kudin, K. N.; Staroverov, V. N.; Kobayashi, R.; Normand, J.; Raghavachari, K.; Rendell, A. P.; Burant, J. C.; Iyengar, S. S.; Tomasi, J.; Cossi, M.; Rega, N.; Millam, N. J.; Klene, M.; Knox, J. E.; Cross, J. B.; Bakken, V.; Adamo, C.; Jaramillo, J.; Gomperts, R.; Stratmann, R. E.; Yazyev, O.; Austin, A. J.; Cammi, R.; Pomelli, C.; Ochterski, J. W.; Martin, R. L.; Morokuma, K.; Zakrzewski, V. G.; Voth, G. A.; Salvador, P.; Dannenberg, J. J.; Dapprich, S.; Daniels, A. D.; Farkas, Ö.; Foresman, J. B.; Ortiz, J. V.; Cioslowski, J.; Fox, D. J.; Gaussian, Inc.: Wallingford, CT, USA, 2009.

36. Lee, J.; Twamley, B.; Richter-Addo, G. B. *Dalton Trans*. **2004**, 189-196.

37. Singh, P.; Kumar Das, A.; Sarkar, B.; Niemeyer, M.; Roncaroli, F.; Olabe, J. A.; Fiedler, J.; Zalis, S.; Kaim, W. *Inorg. Chem.* **2008**, *47*, 7106-7113.

38. Yi, G.-B.; Khan, M. A.; Richter-Addo, G. B. *Inorg. Chem.* **1996**, *35*, 3453-3454.

39. Yi, G.-B.; Khan, M. A.; Powell, D. R.; Richter-Addo, G. B. *Inorg. Chem.* **1998**, *37*, 208-214.

40. Carter, S. M. Ph.D. Dissertation, University of Oklahoma, 2006.

41. Kadish, K. M.; Adamian, V. A.; Van Caemelbecke, E.; Tan, Z.; Tagliatesta, P.; Bianco, P.; Boschi, T.; Yi, G.-B.; Khan, M. A.; Richter-Addo, G. B. *Inorg. Chem.* **1996,** *35*, 1343-1348.

42. Wanner, M.; Scheiring, T.; Kaim, W.; Slep, L. D.; Baraldo, L. M.; Olabe, J. A.; Za´lisˇ, S.; Baerends, E. J. *Inorg. Chem.* **2001**, *40*, 5704-5707.

43. Sieger, M.; Sarkar, B.; Zalis, S.; Fiedler, J.; Escola, N.; Doctorovich, F.; Olabe, J. A.; Kaim, W. *Dalton Trans.* **2004**, 1797-1800.

44. Sarkar, S.; Sarkar, B.; Chanda, N.; Kar, S.; Mobin, S. M.; Fiedler, J.; Kaim, W.; Lahiri, G. K. *Inorg. Chem.* **2005**, *44*, 6092-6099.

45. Singh, P.; Sarkar, B.; Sieger, M.; Niemeyer, M.; Fiedler, J.; Zalis, S.; Kaim, W. *Inorg. Chem.* **2006**, *45*, 4602-4609.

46. Videla, M.; Jacinto, J. S.; Baggio, R.; Garland, M. T.; Singh, P.; Kaim, W.; Slep, L. D.; Olabe, J. A. *Inorg. Chem.* **2006**, *45*, 8608-8617.

47. Marchenko, A. V.; Vedernikov, A. N.; Dye, D. F.; Pink, M.; Zaleski, J. M.; Caulton, K. G. *Inorg. Chem.* **2004**, *43*, 351–360.

48. Melenkivitz, R.; Hillhouse, G. L. *Chem. Comm*. **2002**, 660–661.

49. Marchenko, A. V.; Vedernikov, A. N.; Dye, D. F.; Pink, M.; Zaleski, J. M.; Caulton, K. G. *Inorg. Chem.* **2002**, *41*, 4087–4089.

50. Lee, J.; Yi, G.; Masood, K. A.; Richter-Addo, G. B. *Inorg. Chem.*, **1999**, *38*, 4578-4584.

51. Carter, S. M.; Lee, J.; Hixson, C. A.; Powell, D. R.; Wheeler, R. A.; Shaw, M. J.; Richter-Addo, G. B. *Dalton Trans*. **2006**, 1338-1347.

52. Bohle, D. S.; Goodson, P. A.; Smith, B. D. *Polyhedron*. **1996**, *15*, 3147-3150.

53. Bohle, D. S.; Hung, C.-H.; Smith, B. D. *Inorg. Chem.* **1998**, *37*, 5798-5806.

54. Ruiz-Morales, Y.; Schreckenbach, G.; Ziegler, T. *Organometallics.* **1996**, *15*, 3920-3923.

55. Bullock, R. M.; Song, J.-S.; Szalda, D. J. *Organometallics* **1996**, *15*, 2504-2516.

56. Demissie, T. B.; Conradie, J.; Vazquez-Lima, H.; Ruud, K.; Ghosh, A. *ACS Omega*. **2013**, *3*, 10513-10516.

57. Berthon, C.; Boubals, N.; Charushnikova, I. A.; Collison, D.; Cornet, S. M.; Den Auwer, C.; Gaunt, A. J.; Kaltsoyannis, N.; May, I.; Petit, S.; Redmond, M. P.; Reilly, S. D.; Scott, B. L. *Inorg. Chem*. **2010**, *49*, 9554–9562

58. Lorkovic, I. M.; Miranda, K. M.; Lee, B.; Bernhard, S.; Schoonover, J. R.; Ford, P. C. *J. Am. Chem. Soc.* **1998**, *120*, 11674-11683.

59. Kang, Y.; Zyryanov, G. V.; Rudkevich, D. M. *Chem. Comm*. **2003**, *19*, 2470-2471.

60. Azizyan, A. S.; Kurtikyan, T. S.; Martirosyan, G. G.; Ford, P. C. *Inorg. Chem.* **2013**, *52*, 5201-5205.

61. Kurtikyan, T. S.; Martirosyan, G. G.; Lorkovic, I. M.; Ford, P. C. *J. Am. Chem. Soc.* **2002**, *124*, 10124-10129.

62. Weston Jr., R. E.; Brodasky, T. F. *J. Chem. Phys.* **1957**, *27*, 683-689.

63. Lymar, S. V.; Shafirovich, V.; Poskrebyshev, G. A. *Inorg Chem.* **2005**, *44*, 5212-5221.

64. Esler, M. B.; Griffith, D. W. T.; Turatti, F.; Wilson, S. R.; Rahn, T.; Zhang, H. *Chemosphere: Global Change Sci.* **2000**, *2*, 445-454.

65. Shafirovich, V.; Lymar, S. V. *Proc. Natl. Acad. Sci*. **2002**, *99*, 7340–7345.

66. Oba, M.; Tanaka, K.; Nishiyama, K.; Ando, W. *J. Org. Chem*. **2011**, *76*, 4173–4177.

Chapter 4: Synthesis, characterization and electrochemical investigation of symmetrical and unsymmetrical dicarboxylate bridged dimetallic complexes of nitrosyl metalloporphyrins and their monometallic ester derivatives

4.1. Introduction

The preparation and redox behavior of ruthenium nitrosyl porphyrins containing coordinated carboxylate ligands have been reported from our group previously.[1,2] These complexes look to shed light on the interaction of nitric oxide with ferric heme *O*-ligand active sites such as catalase and Hb M Milwaukee [β67(E11)Val→Glu].[3-5] The work of former group members (Lee and Cheng) with dithiolate bridging ruthenium nitrosyl heme models[6,7] detailed the spectral properties of these compounds. However, there is currently no literature precedent for probing the unique redox behavior of dimetallic μ-dicarboxylate porphyrins. Other dimetallic species, such as biferrocene, have a considerable number of studies dedicated to investigating their redox behaviors, specifically the effect of linkage (e.g., aromatic vs alkyl and chain length) on electron transfer mechanisms (i.e., concerted vs sequential).[8-13] Additionally, several reports describing bridged species of group 8 metals (Fe, Ru, Os) have been published over the years for non-heme coordination complexes.[14-23]

In this chapter, the synthesis, spectral characterization and redox behavior for several new (por)M(NO)(OC(=O)$(CH_2)_n$C(=O)OR) and (por)M(NO)(OC(=O)$(CH_2)_n$C(=O)O)M′(NO)(por) (por = TPP, T(*p*-OMe)PP, OEP; M, M′ = Ru, Os; n = 2, 4, 6; R = H, Me) compounds are reported. The goal of this work was to probe the effect that altering the *C*-length (i.e., -CH_2-) of the alkyl/bridging-alkyl chains has on the redox properties of the target compounds in Figure 4.1, and to probe the nature of electronic communication (if any) between the metals in the dimetallic species. The presence of several redox active sites and the ability to tune certain aspects in these

complexes including alkyl chain length, porphyrin and metal identity may shed light on the impact each has on the redox behavior of these complexes.

por = TPP, T(*p*-OMe)PP, OEP
M, M' = Ru, Os
n = 2, 4, 6

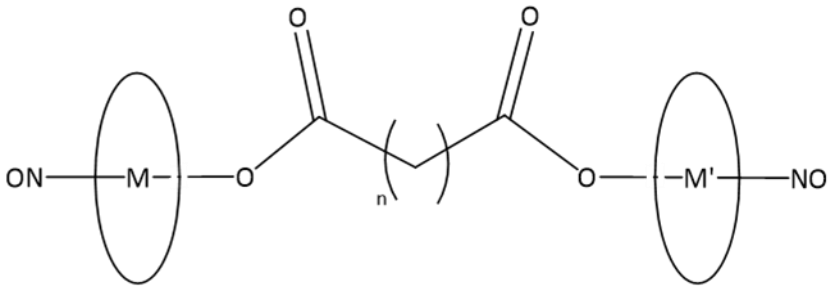

Figure 4.1 Target synthetic bridged dicarboxylate ruthenium nitrosyl porphyrin complexes.

4.2. Materials and Methods

All reactions were performed under an anaerobic (N_2) atmosphere using standard Schlenk glassware and/or in an Innovative Technology Labmaster 100 Dry Box. Solutions for spectral studies were also prepared under a nitrogen atmosphere. Chlorobenzene, toluene, chloroform, dichloromethane and *n*-hexane used in the experiments were dried using an Innovative Technology Inc. Pure Solv 400-5-MD Solvent Purification System. The (por)Ru(NO)(OH) and (OEP)Os(NO)(O-*i*-C_5H_{11}) precursors were synthesized from an adapted literature preparation for (por)Ru(NO)(O-*i*-C_5H_{11}),[6] described below. $O^{15}NO$-C_5H_{11} was prepared as previously reported.[24] Oxalic acid (98%), succinic acid (99%), adipic acid (99%), suberic acid (98%), monomethyl succinate (95%), monomethyl adipate (99%), monomethyl suberate (97%), decahydronapthalene ($\geq$ 99%), $AgPF_6$ (98%) and bis(pentamethylcyclopentadienyl)cobalt(II), (Cp^*_2Co, 97%) were purchased from Aldrich and used as received. The supporting electrolyte NBu_4PF_6 (98%) obtained from Aldrich was recrystallized from hot ethanol and dried in vacuo. Ferrocene (98%) was obtained from Aldrich and sublimed prior to use. Chloroform-*d* ($CDCl_3$,

99.96% atom-%D) was purchased from Cambridge Isotope Laboratories, deaerated and dried using activated 4 Å molecular sieves. Infrared spectra were recorded on a Bruker Tensor 27 FTIR spectrometer. Proton NMR spectra were obtained on a Varian 400 MHz spectrometer and the signals referenced to the residual signal of the solvent employed ($CHCl_3$ at δ = 7.26 ppm). X-ray diffraction data was collected using a D8 Quest κ-geometry diffractometer with a Bruker Photon II cpad area detector and Mo-K_α source (λ = 0.71073 Å). The X-ray diffraction data was collected and the structures solved by Dr. Douglas R. Powell.

4.2.1. Preparation of (por)M(NO)(OC(=O)$(CH_2)_n$C(=O)OR) and (por)M(NO)(OC(=O)$(CH_2)_n$C(=O)O)M′(NO)(por) (por = TPP, T(*p*-OMe)PP, OEP; M, M′ = Ru, Os; n = 2, 4, 6; R = H, Me) complexes

(T(p-OMe)PP)Ru(NO)(OH): To a stirred CH_2Cl_2 (20 mL) solution of (T(*p*-OMe)PP)Ru(CO) (233 mg, 0.27 mmol) was added isoamyl nitrite (72 μL, 0.54 mmol). The mixture was refluxed for 2 h and the reaction progress was monitored by IR spectroscopy; a new band at 1815 cm^{-1} grew with concomitant and complete disappearance of the starting ν_{CO} at 1938 cm^{-1}. The reaction mixture was concentrated to ca. 2-3 mL and *n*-hexane (20 mL) was added to the solution while stirring. A red precipitate formed and was isolated via vacuum filtration, then washed twice with *n*-hexane (10 mL). This powder was dissolved in CH_2Cl_2 and loaded on a Florisil (60-100 mesh) column developed in *n*-hexane. A red-brown band was eluted with CH_2Cl_2 and discarded, followed by a dark red band eluted with 10% acetone/CH_2Cl_2. This band was collected, the solvent removed in vacuo and the product obtain in 82% yield (168 mg, 0.22 mmol). IR (KBr, cm^{-1}): ν_{OH} = 3592, ν_{NO} = 1815. ^{1}H NMR (400 MHz; $CDCl_3$): δ 8.99 (s, 8H, pyrrole-H of TPP), 8.28 (d, 4H, *o*-H of TPP, *J* = 8 Hz), 8.20 (d, 4H, *o′*-H of TPP, *J* = 8 Hz), 7.79 (m, 12H, *m*- and *p*-H of TPP).

(OEP)Ru(NO)(OH): This compound was prepared similarly as above from (OEP)Ru(CO) (100 mg, 0.15 mmol). The isolated product was obtained in 68% yield (68 mg, 0.10 mmol) with IR and ^{1}H NMR spectral signals matching previously reported values.[25]

(TPP)Ru(NO)(OH): This compound was prepared similarly as above from (TPP)Ru(CO) (200 mg, 0.27 mmol). The isolated product was obtained in 72% yield (147 mg, 0.19 mmol) with IR and ^{1}H NMR spectral signals matching previously reported values.[26]

(T(p-OMe)PP)Os(NO)(O-i-C_5H_{11}): This compound was prepared similarly as above (following the nitrosyl hydroxo procedure) from (T(*p*-OMe)PP)Os(CO) (100 mg, 0.11 mmol). The isolated product was obtained in 63% yield (68 mg, 0.066 mmol). IR (KBr, cm^{-1}): ν_{NO} = 1769. ^{1}H NMR (400 MHz; $CDCl_3$): δ 8.96 (s, 8H, pyrrole-H of T(*p*-OMe)PP), 8.18 (d, 4H, *o*-H of T(*p*-OMe)PP, *J* = 8 Hz), 8.14 (d, 4H, *o′*-H of T(*p*-OMe)PP, *J* = 8 Hz), 7.31 (app m, 8H, *m*-H of T(*p*-OMe)PP), 4.10 (s, 12H, -OMe of T(*p*-OMe)PP), -0.60 (d, 6H, -$OCH_2CH_2CH(\underline{CH_3})_2$ of alkoxide, *J* = 7 Hz), -1.08 (m, 1H, -$OCH_2CH_2\underline{CH}(CH_3)_2$ of alkoxide), -2.29 (app t, 2H, -$O\underline{CH_2}CH_2CH(CH_3)_2$ of alkoxide, *J* = 7 Hz), -2.75 (app q, 2H, -$OCH_2\underline{CH_2}CH(CH_3)_2$ of alkoxide, *J* = 7 Hz).

(TPP)Ru(NO)(OC(=O)(CH_2)$_2$C(=O)OH) ***(PRuC$_2$OH)***: To a stirred toluene (5 mL) solution of (TPP)Ru(NO)(OH) (25 mg, 0.033 mmol) was added succinic acid (5 mg, 0.042 mmol) and refluxed overnight. The reaction mixture was allowed to cool to room temperature before being stored in a -28°C freezer for 4 h. A red-brown precipitate formed and was isolated via vacuum filtration and was subsequently washed with toluene (10 mL) followed by *n*-hexane (20 mL). This crude powder was dissolved in $CHCl_3$ and filtered (in part to remove unreacted succinic acid). The collected filtrate was taken to dryness in vacuo and the product obtained in 82% yield (21 mg, 0.024 mmol). IR (KBr, cm^{-1}): ν_{NO} = 1850, $\nu_{C=O}$ = 1712 and 1640. ^{1}H NMR (400 MHz; $CDCl_3$): δ 9.04 (s, 8H, pyrrole-H of TPP), 8.29 (d, 4H, *o*-H of TPP, *J* = 8 Hz), 8.22 (d, 4H, *o′*-H

of TPP, J = 8 Hz), 7.80 (m, 12H, *p*- and *m*-H of TPP), 0.21 (app t, 2H, see text), -0.82 (app t, 2H, see text). X-ray diffraction quality crystals were obtained by slow evaporation of a $CHCl_3$ solution of the product.

(TPP)Ru(NO)(OC(=O)(CH₂)₄C(=O)OH) ***(PRuC₄OH)***: This compound was prepared similarly as above from the reaction of (TPP)Ru(NO)(OH) (25 mg, 0.033 mmol) with adipic acid (6 mg, 0.041 mmol). The isolated product was obtained in 92% yield (27 mg, 0.030 mmol). IR (KBr, cm^{-1}): ν_{NO} = 1845, $\nu_{C=O}$ = 1721 and 1657. ^{1}H NMR (400 MHz; $CDCl_3$): δ 9.00 (s, 8H, pyrrole-H of TPP), 8.27 (d, 4H, *o*-H of TPP, J = 8 Hz), 8.23 (d, 4H, *o′*-H of TPP, J = 8 Hz), 7.79 (m, 12H, *p*- and *m*-H of TPP), 0.69 (t, 2H, -OC(=O)$CH_2CH_2CH_2\underline{CH_2}$ of carboxylate, J = 7 Hz), -0.20 (quin, 2H, -OC(=O)$CH_2\underline{CH_2}CH_2CH_2$ of carboxylate, J = 7 Hz), -0.78 (quin, 2H, -OC(=O)$CH_2CH_2\underline{CH_2}CH_2$ of carboxylate, J = 7 Hz), -1.08 (t, 2H, -OC(=O)$\underline{CH_2}CH_2CH_2CH_2$ of carboxylate, J = 7 Hz).

(TPP)Ru(NO)(OC(=O)(CH₂)₆C(=O)OH) ***(PRuC₆OH)***: This compound was prepared similarly as above from the reaction of (TPP)Ru(NO)(OH) (25 mg, 0.033 mmol) with suberic acid (7 mg, 0.040 mmol). The isolated product was obtained in 91% yield (27 mg, 0.029 mmol). IR (KBr, cm^{-1}): ν_{NO} = 1844, $\nu_{C=O}$ = 1717 and 1653. ^{1}H NMR (400 MHz; $CDCl_3$): δ 8.98 (s, 8H, pyrrole-H of TPP), 8.29 (d, 4H, *o*-H of TPP, J = 8 Hz), 8.21 (d, 4H, *o′*-H of TPP, J = 8 Hz), 7.79 (m, 12H, *p*- and *m*-H of TPP), 2.31 (t, 2H, -OC(=O)$\underline{CH_2}CH_2CH_2CH_2CH_2CH_2$ of carboxylate, J = 7 Hz), 1.74 (t, 2H, -OC(=O)$CH_2CH_2CH_2CH_2CH_2\underline{CH_2}$ of carboxylate, J = 7 Hz), 0.95 (quin, 2H, -OC(=O)$CH_2CH_2CH_2CH_2\underline{CH_2}CH_2$ of carboxylate, J = 7 Hz), 0.18 (quin, 2H, -OC(=O)$CH_2\underline{CH_2}CH_2CH_2CH_2CH_2$ of carboxylate, J = 7 Hz), -0.96 (m, 2H, -OC(=O)$CH_2CH_2CH_2\underline{CH_2}CH_2CH_2$ of carboxylate, J = 7 Hz), -1.46 (quin, 2H, -OC(=O)$CH_2CH_2\underline{CH_2}CH_2CH_2CH_2$ of carboxylate, J = 7 Hz).

(TPP)Ru(NO)(OC(=O)(CH$_2$)$_2$C(=O)OMe) ***(PRuC$_2$OMe)***: To a stirred toluene (5 mL) solution of (TPP)Ru(NO)(OH) (25 mg, 0.033 mmol) was added monomethyl succinate (5 mg, 0.038 mmol) and refluxed overnight. The reaction mixture was allowed to cool to room temperature and the entirety of the mixture was loaded onto a silica gel column (60 Å, 230-400 mesh) developed in *n*-hexane. A light brown band was eluted first with 5% Et_2O/CH_2Cl_2 and discarded, followed by a dark red-brown band with 25% Et_2O/CH_2Cl_2 as the eluent. This band was collected and the solvent removed in vacuo. The chromatographed product was obtained in 67% yield (19 mg, 0.022 mmol). IR (KBr, cm^{-1}): ν_{NO} = 1843, $\nu_{C=O}$ = 1740 and 1662. ^{1}H NMR (400 MHz; $CDCl_3$): δ 8.99 (s, 8H, pyrrole-H of TPP), 8.30 (d, 4H, *o*-H of TPP, *J* = 8 Hz), 8.26 (d, 4H, *o′*-H of TPP, *J* = 8 Hz), 7.80 (m, 12H, *p*- and *m*-H of TPP), 2.92 (s, 3H, -OC(=O)Me of carboxylate), -0.55 (t, 2H, -OC(=O)CH$_2$<u>CH$_2$</u> of carboxylate, *J* = 7 Hz), -0.72 (t, 2H, -OC(=O)<u>CH$_2$</u>CH$_2$ of carboxylate , *J* =7 Hz).

(TPP)Ru(NO)(OC(=O)(CH$_2$)$_4$C(=O)OMe) ***(PRuC$_4$OMe)***: This compound was prepared similarly as above from the reaction of (TPP)Ru(NO)(OH) (25 mg, 0.033 mmol) with monomethyl adipate (6 μL, 0.040 mmol). The chromatographed product was obtained in 65% yield (19 mg, 0.021 mmol). IR (KBr, cm^{-1}): ν_{NO} = 1840, $\nu_{C=O}$ = 1737 and 1653. ^{1}H NMR (400 MHz; $CDCl_3$): δ 8.98 (s, 8H, pyrrole-H of TPP), 8.30 (d, 4H, *o*-H of TPP, *J* = 8 Hz), 8.21 (d, 4H, *o′*-H of TPP, *J* = 8 Hz), 7.80 (m, 12H, *p*- and *m*-H of TPP), 3.40 (s, 3H, -C(=O)OMe of carboxylate ester), 1.05 (t, 2H, -OC(=O)CH$_2$CH$_2$CH$_2$<u>CH$_2$</u> of carboxylate, *J* = 7 Hz), -0.64 (quin, 2H, -OC(=O)CH$_2$CH$_2$<u>CH$_2$</u>CH$_2$ of carboxylate, *J* = 7 Hz), -0.97 (t, 2H, -OC(=O)<u>CH$_2$</u>CH$_2$CH$_2$CH$_2$ of carboxylate , *J* = 7 Hz), -1.43 (q, 2H, - OC(=O)CH$_2$<u>CH$_2$</u>CH$_2$CH$_2$ of carboxylate , *J* = 7 Hz).

(TPP)Ru(NO)(OC(=O)(CH$_2$)$_6$C(=O)OMe) ***(PRuC$_6$OMe)***: This compound was prepared similarly as above from the reaction of (TPP)Ru(NO)(OH) (25 mg, 0.033 mmol) with

monomethyl suberate (8 μL, 0.044 mmol). The chromatographed product was obtained in 52% yield (16 mg, 0.017 mmol). IR (KBr, cm^{-1}): ν_{NO} = 1840, $\nu_{C=O}$ = 1736 and 1660. ^1H NMR (400 MHz; $CDCl_3$): δ 8.97 (s, 8H, pyrrole-H of TPP), 8.30 (d, 4H, *o*-H of TPP, *J* = 8 Hz), 8.20 (d, 4H, *o'*-H of TPP, *J* = 8 Hz), 7.79 (m, 12H, *p*- and *m*-H of TPP), 3.57 (s, 3H, -C(=O)OMe of carboxylate), 1.89 (t, 2H, -OC(=O)$CH_2CH_2CH_2CH_2CH_2\underline{CH_2}$ of carboxylate, *J* = 7 Hz), 0.95 (quin, 2H, -OC(=O)$CH_2CH_2CH_2CH_2\underline{CH_2}CH_2$ of carboxylate, *J* = 7 Hz), 0.16 (quin, 2H, -OC(=O)$CH_2\underline{CH_2}CH_2CH_2CH_2CH_2$ of carboxylate, *J* = 7 Hz), -0.90 (quin, 2H, -OC(=O)$CH_2CH_2CH_2\underline{CH_2}CH_2CH_2$ of carboxylate, *J* = 7 Hz), -1.01 (t, 2H, -OC(=O)$\underline{CH_2}CH_2CH_2CH_2CH_2CH_2$ of carboxylate, *J* = 7 Hz) -1.50 (quin, 2H, -OC(=O)$CH_2CH_2\underline{CH_2}CH_2CH_2CH_2$, of carboxylate, *J* = 7 Hz).

[(TPP)Ru(NO)]$_2$-μ-OC(=O)$(CH_2)_2$C(=O)O' ***(PRuC$_2$RuP)***: To a stirred chlorobenzene (5 mL) solution of $PRuC_2OH$ (25 mg, 0.030 mmol) was added (TPP)Ru(NO)(OH) (25 mg, 0.033 mmol) and refluxed for 24 h. The reaction mixture was allowed to cool to room temperature before being stored in a -28°C freezer for 4 h to decrease solubility of the product. A red-brown precipitate formed and was isolated via vacuum filtration and was subsequently washed with CH_2Cl_2 (10 mL). The isolated product was obtained in 61% yield (29 mg, 0.018 mmol). IR (KBr, cm^{-1}): ν_{NO} = 1836, $\nu_{C=O}$ = 1656. Anal. Calc. for $C_{92}H_{60}N_{10}O_6Ru_2$: C, 68.90; N, 8.73; H, 3.77%. Found: C, 68.53; N, 8.67; H, 3.80%.

[(TPP)Ru(NO)]$_2$-μ-OC(=O)$(CH_2)_4$C(=O)O' ***(PRuC$_4$RuP)***: This compound was prepared similarly as above from the reaction of $PRuC_4OH$ (26 mg, 0.030 mmol) with (TPP)Ru(NO)(OH) (25 mg, 0.033 mmol). The isolated product was obtained in 56% yield (27 mg, 0.017 mmol). IR (KBr, cm^{-1}): ν_{NO} = 1838, $\nu_{C=O}$ = 1656. Anal. Calc. for $C_{94}H_{64}N_{10}O_6Ru_2 \bullet CH_2Cl_2$: C, 66.70; N, 8.10; H, 3.84%. Found: C, 66.79; N, 8.07; H, 3.98%.

[(TPP)Ru(NO)]$_2$-μ-OC(=O)(CH$_2$)$_6$C(=O)O′ ***(PRuC$_6$RuP)***:This compound was prepared similarly as above from the reaction of PRuC$_6$OH (27 mg, 0.030 mmol) with (TPP)Ru(NO)(OH) (25 mg, 0.033 mmol). The isolated product was obtained in 48% yield (24 mg, 0.014 mmol). IR (KBr, cm^{-1}): ν_{NO} = 1838, $\nu_{C=O}$ = 1653. Anal. Calc. for $C_{96}H_{68}N_{10}O_6Ru_2$•0.5$CH_2Cl_2$: C, 68.20; N, 8.20; H, 4.07%. Found: C, 68.02; N, 8.02; H, 4.24%.

(T(p-OMe)PP)Ru(NO)(OC(=O)(CH$_2$)$_2$C(=O)OH) ***(TRuC$_2$OH)***: To a stirred toluene (5 mL) solution of (T(*p*-OMe)PP)Ru(NO)(OH) (28 mg, 0.031 mmol) was added succinic acid (5 mg, 0.042 mmol) and refluxed overnight. The reaction mixture was allowed to cool to room temperature and *n*-hexane (10 mL) was added to this mixture while stirring. A dark purple precipitate formed that was isolated via vacuum filtration and was subsequently washed with *n*-hexane (10 mL). This crude powder was dissolved in CH_2Cl_2 and filtered to remove solids including unreacted succinic acid. The collected filtrate was dried in vacuo and the product obtained in 92% yield (28 mg, 0.028 mmol). IR (KBr, cm^{-1}): ν_{NO} = 1845, $\nu_{C=O}$ = 1719 and 1647. ^{1}H NMR (400 MHz; $CDCl_3$): δ 9.06 (s, 8H, pyrrole-H of T(*p*-OMe)PP), 8.19 (dd, 4H, *o*-H of T(*p*-OMe)PP, *J* = 2 and 9 Hz), 8.12 (dd, 4H, *o′*-H of T(*p*-OMe)PP, *J* = 2 and 9 Hz), 7.32 (overlapping dd, 8H, *m,m′*-H of T(*p*-OMe)PP, *J* = 2 and 9 Hz), 4.12 (s, 12H, -OMe of T(*p*-OMe)PP), 0.18 (app t, 2H, see text), -0.85 (app t, 2H, see text).

(T(p-OMe)PP)Ru(NO)(OC(=O)(CH$_2$)$_4$C(=O)OH) ***(TRuC$_4$OH)***: This compound was prepared similarly as above from the reaction of (T(*p*-OMe)PP)Ru(NO)(OH) (28 mg, 0.031 mmol) with adipic acid (6 mg, 0.041 mmol). The isolated product was obtained in 85% yield (26 mg, 0.026 mmol). IR (KBr, cm^{-1}): ν_{NO} = 1845, $\nu_{C=O}$ = 1718 and 1650. ^{1}H NMR (400 MHz; $CDCl_3$): δ 9.02 (s, 8H, pyrrole-H of T(*p*-OMe)PP), 8.15 (overlapping dd, 8H, *o,o′*-H of T(*p*-OMe)PP, *J* = 2 and 9 Hz), 7.30 (overlapping dd, 8H, *m,m′*-H of T(*p*-OMe)PP, *J* = 2 and 9 Hz), 4.09 (s, 12H, -OMe of

T(*p*-OMe)PP), 0.70 (t, 2H, -OC(=O)$CH_2CH_2CH_2\underline{CH_2}$ of carboxylate, *J* = 7 Hz), -0.27 (quin, 2H, -OC(=O)$CH_2CH_2\underline{CH_2}CH_2$ of carboxylate, *J* = 7 Hz), -0.86 (quin, 2H, -OC(=O)$CH_2\underline{CH_2}CH_2CH_2$ of carboxylate, *J* = 7 Hz), -1.08 (t, 2H, -OC(=O)$\underline{CH_2}CH_2CH_2CH_2$ of carboxylate, *J* = 7 Hz).

(T(p-OMe)PP)Ru(NO)(OC(=O)$(CH_2)_6$C(=O)OH) ***(TRuC$_6$OH)***: This compound was prepared similarly as above from the reaction of (T(*p*-OMe)PP)Ru(NO)(OH) (28 mg, 0.031 mmol) with suberic acid (7 mg, 0.040 mmol). The isolated product was obtained in 73% yield (23 mg, 0.022 mmol). IR (KBr, cm^{-1}): ν_{NO} = 1843, $\nu_{C=O}$ = 1721 and 1652. ^{1}H NMR (400 MHz; $CDCl_3$): δ 9.01 (s, 8H, pyrrole-H of T(*p*-OMe)PP), 8.18 (dd, 4H, *o*-H of T(*p*-OMe)PP, *J* = 2 and 9 Hz), 8.12 (dd, 4H, *o′*-H of T(*p*-OMe)PP, *J* = 2 and 9 Hz), 7.30 (overlapping dd, 8H, *m,m′*-H of T(*p*-OMe)PP, *J* = 2 and 9 Hz), 4.10 (s, 12H, -OMe of T(*p*-OMe)PP), 2.28 (t, 2H, -OC(=O)$\underline{CH_2}CH_2CH_2CH_2CH_2CH_2$ of carboxylate, *J* = 7 Hz), 1.72 (t, 2H, -OC(=O)$CH_2CH_2CH_2CH_2CH_2\underline{CH_2}$ of carboxylate, *J* = 7 Hz), 0.95 (quin, 2H, -OC(=O)$CH_2CH_2CH_2CH_2\underline{CH_2}CH_2$ of carboxylate, *J* = 7 Hz), 0.15 (quin, 2H, -OC(=O)$CH_2\underline{CH_2}CH_2CH_2CH_2CH_2$ of carboxylate, *J* = 7 Hz), -0.98 (m, 2H, -OC(=O)$CH_2CH_2CH_2\underline{CH_2}CH_2CH_2$ of carboxylate), -1.48 (quin, 2H, -OC(=O)$CH_2CH_2\underline{CH_2}CH_2CH_2CH_2$ of carboxylate, *J* = 7 Hz).

(T(p-OMe)PP)Ru(NO)(OC(=O)$(CH_2)_2$C(=O)OMe) ***(TRuC$_2$OMe)***: To a stirred toluene (5 mL) solution of (T(*p*-OMe)PP)Ru(NO)(OH) (28 mg, 0.031 mmol) was added monomethyl succinate (5 mg, 0.038 mmol) and refluxed overnight. The reaction mixture was allowed to cool to room temperature and the mixture in its entirety loaded onto a silica gel column (60 Å, 230-400 mesh) developed in *n*-hexane. A light green band was eluted first with 5% Et_2O/CH_2Cl_2 and discarded, followed by a dark green-brown band with 25% Et_2O/CH_2Cl_2 as the eluent. This second band was collected and the solvent removed in vacuo. The chromatographed product was obtained in

71% yield (22 mg, 0.022 mmol). IR (KBr, cm^{-1}): ν_{NO} = 1840, ν_{15NO} = 1816, $\nu_{C=O}$ = 1735 and 1657 (^{15}N = 1734 and 1649). ^1H NMR (400 MHz; $CDCl_3$): δ 9.02 (s, 8H, pyrrole-H of T(*p*-OMe)PP), 8.18 (overlapping dd, 8H, *o,o′*-H of T(*p*-OMe)PP, *J* = 2 and 9 Hz), 7.31 (overlapping dd, 8H, *m,m′*-H of T(*p*-OMe)PP), 4.12 (s, 12H, -OMe of T(*p*-OMe)PP), 2.92 (s, 3H, -C(=O)OMe of carboxylate), -0.56 (t, 2H, -OC(=O)$CH_2\underline{CH_2}$ of carboxylate, *J* = 7 Hz), -0.74 (t, 2H, -OC(=O)CH_2CH_2 of carboxylate, *J* = 7 Hz). X-ray diffraction quality crystals were obtained by liquid/liquid diffusion using CH_2Cl_2 as the solvent and *n*-hexane as the antisolvent (2:1).

(T(p-OMe)PP)Ru(NO)(OC(=O)(CH₂)₄C(=O)OMe) ***(TRuC₄OMe)***: This compound was prepared similarly as above from the reaction of (T(*p*-OMe)PP)Ru(NO)(OH) (28 mg, 0.031 mmol) with monomethyl adipate (6 μL, 0.040 mmol). The chromatographed product was obtained in 76% yield (23 mg, 0.023 mmol). IR (KBr, cm^{-1}): ν_{NO} = 1840, $\nu_{C=O}$ = 1732 and 1652. ^1H NMR (400 MHz; $CDCl_3$): δ 9.01 (s, 8H, pyrrole-H of T(*p*-OMe)PP), 8.20 (dd, 4H, *o*-H of T(*p*-OMe)PP, *J* = 2 and 9 Hz), 8.12 (dd, 4H, *o′*-H of T(*p*-OMe)PP, *J* = 2 and 9 Hz), 7.31 (overlapping dd, 8H, *m,m′*-H of T(*p*-OMe)PP, *J* = 2 and 9 Hz), 4.11 (s, 12H, -OMe of T(*p*-OMe)PP), 3.41 (s, 3H, -C(=O)OMe of carboxylate), 1.05 (t, 2H, -OC(=O)$CH_2CH_2CH_2\underline{CH_2}$ of carboxylate, *J* = 7 Hz), -0.65 (quin, 2H, -OC(=O)$CH_2CH_2\underline{CH_2}CH_2$ of carboxylate, *J* = 7 Hz), -1.00 (t, 2H, -OC(=O)$\underline{CH_2}CH_2CH_2CH_2$ of carboxylate, *J* = 7 Hz), -1.45 (quin, 2H, -OC(=O)$CH_2\underline{CH_2}CH_2CH_2$ of carboxylate, *J* = 7 Hz).

(T(p-OMe)PP)Ru(NO)(OC(=O)(CH₂)₆C(=O)OMe) ***(TRuC₆OMe)***: This compound was prepared similarly as above from the reaction of (T(*p*-OMe)PP)Ru(NO)(OH) (28 mg, 0.031 mmol) with monomethyl suberate (8 μL, 0.044 mmol). The chromatographed product was obtained in 42% yield (13 mg, 0.013 mmol). IR (KBr, cm^{-1}): ν_{NO} = 1838, $\nu_{C=O}$ = 1734 and 1651. ^1H NMR (400 MHz; $CDCl_3$): δ 9.00 (s, 8H, pyrrole-H of T(*p*-OMe)PP), 8.20 (dd, 4H, *o*-H of T(*p*-OMe)PP, *J* =

2 and 9 Hz), 8.11 (dd, 4H, *o′*-H of T(*p*-OMe)PP, *J* = 2 and 9 Hz), 7.30 (m, 8H, *m*-H of T(*p*-OMe)PP), 4.11 (s, 12H, -OMe of T(*p*-OMe)PP), 3.57 (s, 3H, -C(=O)OMe of carboxylate), 1.90 (t, 2H, -OC(=O)$CH_2CH_2CH_2CH_2CH_2\underline{CH_2}$ of carboxylate, *J* = 7 Hz), 0.94 (quin, 2H, -OC(=O)$CH_2CH_2CH_2CH_2\underline{CH_2}CH_2$ of carboxylate, *J* = 7 Hz), 0.16 (quin, 2H, -OC(=O)$CH_2CH_2CH_2\underline{CH_2}CH_2CH_2$ of carboxylate, *J* = 7 Hz), -0.91 (quin, 2H, -OC(=O)$CH_2CH_2\underline{CH_2}CH_2CH_2CH_2$ of carboxylate, *J* = 7 Hz), -1.04 (t, 2H, -OC(=O)$\underline{CH_2}CH_2CH_2CH_2CH_2CH_2$ of carboxylate, *J* = 7 Hz), -1.45 (quin, 2H, -OC(=O)$CH_2\underline{CH_2}CH_2CH_2CH_2CH_2$ of carboxylate, *J* = 7 Hz).

[(T(p-OMe)PP)Ru(NO)]₂-μ-OC(=O)(CH₂)₂C(=O)O′ ***(TRuC₂RuT)***: To a stirred chlorobenzene (5 mL) solution of $TRuC_2OH$ (30 mg, 0.030 mmol) was added (T(*p*-OMe)PP)Ru(NO)(OH) (31 mg, 0.035 mmol) and refluxed for 24 h. The reaction mixture was allowed to cool to room temperature and loaded onto a silica gel column (60 Å, 230-400 mesh) developed in *n*-hexane. A green band was eluted first with 5% Et_2O/CH_2Cl_2 and discarded, followed by a dark green-brown band with 15% Et_2O/CH_2Cl_2 as the eluent. This second band was collected and the solvent removed in vacuo. The chromatographed product was obtained in 40% yield (22 mg, 0.012 mmol). IR (KBr, cm^{-1}): ν_{NO} = 1831, $\nu_{C=O}$ = 1661. ^{1}H NMR (400 MHz; $CDCl_3$): δ 8.69 (s, 16H, pyrrole-H of T(*p*-OMe)PP), 7.97 (dd, 8H, *o*-H of T(*p*-OMe)PP, *J* = 2 and 9 Hz), 7.65 (dd, 8H, *o′*-H of T(*p*-OMe)PP, *J* = 2 and 9 Hz), 7.20 (dd, 8H, *m*-H of T(*p*-OMe)PP, *J* = 2 and 9 Hz), 7.12 (dd, 8H, *m′*-H of T(*p*-OMe)PP, *J* = 2 and 9 Hz), 4.11 (s, 24H, -OMe of T(*p*-OMe)PP), -3.86 (app s, 4H, $-CH_2CH_2-$ of carboxylate).

[(T(p-OMe)PP)Ru(NO)]₂-μ-OC(=O)(CH₂)₄C(=O)O′ ***(TRuC₄RuT)***: This compound was prepared similarly as above from the reaction of $TRuC_4OH$ (30 mg, 0.030 mmol) with (T(*p*-OMe)PP)Ru(NO)(OH) (31 mg, 0.035 mmol). The chromatographed product was obtained in

36% yield (20 mg, 0.010 mmol). IR (KBr, cm^{-1}): ν_{NO} = 1844, $\nu_{C=O}$ = 1651. ^{1}H NMR (400 MHz; $CDCl_3$): δ 8.74 (s, 16H, pyrrole-H of T(*p*-OMe)PP), 8.00 (dd, 8H, *o*-H of T(*p*-OMe)PP, *J* = 2 and 9 Hz), 7.67 (dd, 8H, *o′*-H of T(*p*-OMe)PP, *J* = 2 and 9 Hz), 7.21 (dd, 8H, *m*-H of T(*p*-OMe)PP, *J* = 2 and 9 Hz), 7.09 (dd, 8H, *m′*-H of T(*p*-OMe)PP, *J* = 2 and 9 Hz), 4.07 (s, 24H, -OMe of T(*p*-OMe)PP), -2.04 (app s, 4H, -$CH_2\underline{CH_2CH_2}CH_2$- of carboxylate), -3.86 (app s, 4H, -$\underline{CH_2}CH_2CH_2\underline{CH_2}$- of carboxylate).

[(T(p-OMe)PP)Ru(NO)]$_2$-μ-OC(=O)(CH$_2$)$_6$C(=O)O′ ***(TRuC$_6$RuT)***:This compound was prepared similarly as above from the reaction of $TRuC_6OH$ (31 mg, 0.030 mmol) with (T(*p*-OMe)PP)Ru(NO)(OH) (31 mg, 0.035 mmol). The chromatographed product was obtained in 45% yield (26 mg, 0.013 mmol). IR (KBr, cm^{-1}): ν_{NO} = 1849, $\nu_{C=O}$ = 1651. ^{1}H NMR (400 MHz; $CDCl_3$): δ 8.84 (s, 16H, pyrrole-H of T(*p*-OMe)PP), 8.08 (dd, 8H, *o*-H of T(*p*-OMe)PP, *J* = 2 and 9 Hz), 7.82 (dd, 8H, *o′*-H of T(*p*-OMe)PP, *J* = 2 and 9 Hz), 7.23 (dd, 8H, *m*-H of T(*p*-OMe)PP, *J* = 2 and 9 Hz), 7.00 (dd, 8H, *m′*-H of T(*p*-OMe)PP, *J* = 2 and 9 Hz), 4.00 (s, 24H, -OMe of T(*p*-OMe)PP), -1.35 (t, 4H, -$CH_2CH_2\underline{CH_2CH_2}CH_2CH_2$- of carboxylate, *J* = 7 Hz), -1.86 (app t, 4H, -$\underline{CH_2}CH_2CH_2CH_2CH_2\underline{CH_2}$- of carboxylate, *J* = 7 Hz), -2.30 (quin, 4H, -$CH_2\underline{CH_2}CH_2CH_2\underline{CH_2}CH_2$- of carboxylate, *J* = 7 Hz).

Attempted synthesis of [(T(p-OMe)PP)Ru(NO)]$_2$-μ-OC(=O)C(=O)O′ ***(TRuC$_0$RuT)***: To a stirred toluene (5 mL) solution of (T(*p*-OMe)PP)Ru(NO)(OH) (28 mg, 0.031 mmol) was added oxalic acid (5 mg, 0.042 mmol) and refluxed for 24 h. The reaction mixture was allowed to cool to room temperature and *n*-hexane (10 mL) was added to this mixture. A dark purple precipitate formed that was isolated via vacuum filtration, which was subsequently washed with *n*-hexane (10 mL). The crude powder was dissolved in CH_2Cl_2 and filtered to remove solids including unreacted oxalic acid. The collected filtrate was taken to dryness in vacuo. This synthesis

procedure was repeated with solvents of increasing boiling points such as chlorobenzene (132°C) and decahydronapthalene (190°C), to compensate for the increased melting point of oxalic acid (189°C); these conditions displayed formation of the known compound (T(*p*-OMe)PP)Ru(CO)[27] at 22% yield in chlorobenzene and 54% yield in decahydronapthalene. The isolated mixture was subjected to IR and ^{1}H NMR spectral analysis, but it was evident that several products were likely present in the sample and the following signals are tentatively assigned to the dimetallic species. IR (KBr, cm^{-1}): ν_{NO} = 1835, $\nu_{C=O}$ = 1662. ^{1}H NMR (400 MHz; $CDCl_3$): δ 8.61 (s, 16H, pyrrole-H of T(*p*-OMe)PP), 7.87 (d, 8H, *o*-H of T(*p*-OMe)PP, *J* = 8 Hz), 7.62 (d, 8H, *o′*-H of T(*p*-OMe)PP, *J* = 8 Hz) 4.12 (br s, -OMe of T(*p*-OMe)PP). Overlap of the -OMe proton signals of the various products formed complicates the integration value. The *m*-H signals of T(*p*-OMe)PP for the tentative dimer complex were also obscured by the *meso*-substituted aryl groups of the porphyrin from the multiple species present.

(T(p-OMe)PP)Os(NO)(OC(=O)(CH$_2$)$_2$C(=O)OH) ***(TOsC$_2$OH)***: This compound was prepared similarly as above from the reaction of (T(*p*-OMe)PP)Os(NO)(O-*i*-C_5H_{11}) (31 mg, 0.030 mmol) with succinic acid (5 mg, 0.042 mmol). The isolated product was obtained in 67% yield (22 mg, 0.020 mmol). IR (KBr, cm^{-1}): ν_{NO} = 1804, $\nu_{C=O}$ = 1727 and 1709. ^{1}H NMR (400 MHz; $CDCl_3$): δ 9.07 (s, 8H, pyrrole-H of T(*p*-OMe)PP), 8.20 (dd, 4H, *o*-H of T(*p*-OMe)PP, *J* = 2 and 9 Hz), 8.11 (dd, 4H, *o′*-H of T(*p*-OMe)PP, *J* = 2 and 9 Hz), 7.11 (dd, 4H, *m*-H of T(*p*-OMe)PP, *J* = 2 and 9 Hz), 6.79 (dd, 4H, *m′*-H of T(*p*-OMe)PP, *J* = 2 and 9 Hz), 4.12 (s, 12H, -OMe of T(*p*-OMe)PP), 0.15 (app t, 2H, -OC(=O)$CH_2\underline{CH_2}$ of carboxylate, *J* = 7 Hz), -0.94 (app t, 2H, -OC(=O)$\underline{CH_2}CH_2$ of carboxylate, *J* = 7 Hz).

Attempted synthesis of [(T(p-OMe)PP)Ru(NO)](μ-OC(=O)(CH$_2$)$_2$C(=O)O')[(OEP)Ru(NO)] ***(TRuC$_2$RuE)***: To a stirred $CHCl_3$ (5 mL) solution of $TRuC_2OH$ (20 mg, 0.023 mmol) was added

(OEP)Ru(NO)(OH) (30 mg, 0.044 mmol) and refluxed for one week. The reaction mixture was allowed to cool to room temperature and the solvent removed in vacuo. The desired dimetallic $TRuC_2RuE$ was present in 37%, as determined by ^1H NMR, along with the symmetric $TRuC_2RuT$ complex, and unreacted $TRuC_2OH$ and (OEP)Ru(NO)(OH). Several attempts were made to purify this reaction mixture, but a spectroscopically pure sample of the desired product could not be obtained. The following ^1H NMR data has been tentatively assigned to the dimetallic $TRuC_2RuE$ complex. ^1H NMR (400 MHz; $CDCl_3$): δ 9.93 (s, 4H, *meso*-H of OEP), 8.67 (s, 8H, pyrrole-H of T(*p*-OMe)PP), 7.94 (dd, 4H, *o*-H of T(*p*-OMe)PP, *J* = 2 and 9 Hz), 7.75 (dd, 4H, *o′*-H of T(*p*-OMe)PP, *J* = 2 and 9 Hz), 7.18 (overlapping dd, 8H, *m,m′*-H of T(*p*-OMe)PP, *J* = 2 and 9 Hz), 4.09 (s, -OMe of T(*p*-OMe)PP), 3.96, (m, 16H, -$\underline{CH_2}CH_3$ of OEP), 1.77 (t, 24H, -$CH_2\underline{CH_3}$ of OEP, *J* = 8 Hz), - 3.87 (app m, 4H, -CH_2CH_2- of carboxylate).

Attempted synthesis of [(T(p-OMe)PP)Ru(NO)](μ-OC(=O)(CH₂)₂C(=O)O')[(T(p-OMe)PP)Os(NO)] ***(TRuC₂OsT)***: To a stirred CH_2Cl_2 (5 mL) solution of $TOsC_2OH$ (20 mg, 0.020 mmol) was added (T(*p*-OMe)PP)Ru(NO)(OH) (41 mg, 0.040 mmol) and refluxed for one week. The reaction mixture was allowed to cool to room temperature and the solvent removed in vacuo. The target putative compound $TRuC_2OsT$ was formed in 11% yield (as judged by ^1H NMR spectroscopy), along with several impurities including the various derivatives of nitrosyl hydroxo and succinate monomer. Several attempts were made to purify this reaction mixture, but a spectroscopically pure sample could not be obtained. The following ^1H NMR data has been tentatively assigned to the heterodimetallic $TRuC_2OsT$ complex. ^1H NMR (400 MHz; $CDCl_3$): δ 8.71 (s, 8H, pyrrole-H of (T(*p*-OMe)PP)Os), 8.69 (s, 8H, pyrrole-H of (T(*p*-OMe)PP)Ru), 4.05 (s, 12H, -OMe of (T(*p*-OMe)PP)Os), 4.03 (s, 12H, -OMe of (T(*p*-OMe)PP)Ru), -3.89 (br s, 4H, -CH_2CH_2- of carboxylate).

4.2.2. Electrochemistry and spectroelectrochemistry of PRuC$_n$OMe, TRuC$_n$OMe and TRuC$_n$RuT (n = 2, 4, 6)

Cyclic voltammetric measurements were performed using a BAS CV 50W instrument. A three-electrode cell was utilized and consisted of a 3.0 mm diameter Pt disk working electrode, a Pt wire counter electrode and a Ag wire pseudo-reference electrode. Obtained products were dried under high vacuum for a minimum of 24 h prior to experiments. Solutions of the compounds were deaerated before use by passing a stream of N_2 gas through the solution for a minimum of 10 min, and a blanket of N_2 was maintained over the solution while performing the experiments. The solutions contained ~1.0 mM of the analyte in 0.1 M NBu_4PF_6 as support electrolyte. Ferrocene (Fc, 1.0 mM) was used as an internal standard, and potentials were referenced to the $Fc^{0/+}$ couple set to 0.00 V. An approach for *i*R correction was employed to account for the resistance and capacitance in these solutions by entering these values manually for the voltammograms that plot potential vs dimensionless current into a Python program written by our collaborator Dr. Michael J. Shaw as described by Saveant.[28] This is similar to the process of *i*R compensation available in some electrochemistry software programs but is performed after data collection. Semi-integral and semi-derivative plots from the resulting voltammograms were generated using the same Python program based on the work of Oldham.[29,30] A Bruker Tensor 27 FTIR spectrometer, equipped with a mid-IR fiber-optic dip probe and liquid nitrogen cooled MCT detector (RemSpec Corporation, Sturbridge, MA, USA), was used for the IR spectroelectrochemistry.

4.2.3. DFT calculations of (porphine)Ru(NO)(OC(=O)(CH$_2$)$_2$C(=O)OMe)

Density functional calculations (functional: ωB97XD; basis set: DGDZVP) were performed using Gaussian-09[31] via the WebMO interface (https://webmo.oscer.ou.edu).

Geometric optimizations, vibrational frequency and molecular orbital analyses were performed for the selected complex: (porphine)Ru(NO)(OC(=O)$(CH_2)_2$C(=O)OMe). Calculations were performed in the gas phase.

4.2.4. Chemical oxidation of $TRuC_2RuT$ with $AgPF_6$

A chemical oxidation was performed by the addition of $AgPF_6$ (2 mg, 0.0080 mmol) to a CH_2Cl_2 (5 mL) solution of $TRuC_2RuT$ (5 mg, 0.0027 mmol). After 1 h of stirring in the dark the initial green-brown solution turned to dark red. The reaction mixture was filtered, the solvent removed in vacuo and the isolated (T(*p*-OMe)PP)Ru(NO)(FPF_5) product obtained in 78% yield based on Ru (4 mg, 0.0042 mmol). IR (KBr, cm^{-1}): ν_{NO} = 1870, ν_{PF} = 730 and 849.[32,33]

4.2.5. Chemical reduction of $TRuC_2RuT$ with Cp^*_2Co

A chemical reduction was performed by the addition of Cp^*_2Co (2 mg, 0.0061 mmol) to a CH_2Cl_2 (5 mL) solution of $TRuC_2RuT$ (5 mg, 0.0027 mmol). After 1 h of stirring, the initial brown-green solution turned to a red-orange color. The reaction mixture was filtered, the solvent from the collected filtrate removed in vacuo and the isolated (T(*p*-OMe)PP)Ru(NO)(OH) product obtained in ~50% yield based on Ru (3 mg, 0.0027 mmol). IR (KBr, cm^{-1}): ν_{NO} = 1815. ^{1}H NMR (400 MHz; $CDCl_3$): δ 8.98 (s, 8H, pyrrole-H of T(*p*-OMe)PP), 8.21 (dd, 4H, *o*-H of T(*p*-OMe)PP, *J* = 2 and 8 Hz), 8.15 (dd, 4H, *o′*-H of T(*p*-OMe)PP, *J* = 2 and 8 Hz), 7.31 (d, 8H, *m*-H of T(*p*-OMe)PP, *J* = 8 Hz), 4.11 (s, 12H, -OMe of T(*p*-OMe)PP). Additional signals at δ 1.79 ppm and 2.54 ppm were detected, with integration values of 5:1 and 1:6 vs the -OMe of the porphyrin, respectively. These have been tentatively assigned to the carboxylate salt of $[Cp^*_2Co]^+$.[34]

4.3. Results and Discussion

4.3.1. Preparation, spectroscopy and analysis of trends

Studies investigating monometallic carboxylate (por)Ru(NO)(OC(=O)R)[1,2] and dimetallic thiolate-bridged [(por)Ru(NO)]$_2$-μ-S(CH$_2$)$_n$S′[6] complexes have been reported previously. These compounds were synthesized by our group employing a similar exchange reaction as that presented in chapter 2. Structural and spectroscopic information for both species are known, as well as the redox behavior for the carboxylate compounds. Although various group 8 transition metal (Fe, Ru and Os) coordination complexes containing dicarboxylate bridges have been reported,[14-23] there is no published information to date for the metalloporphyrin analogues. A series of (por)M(NO)(OC(=O)(CH$_2$)$_n$C(=O)O)M′(NO)(por) (por = TPP, T(*p*-OMe)PP, OEP; M, M′ = Ru, Os; n = 2, 4, 6) complexes were prepared and characterized by IR and ^{1}H NMR spectroscopy (Figure 4.2). Additional characterization by X-ray crystallography and elemental analysis for selected compounds were obtained. The monometallic and dimetallic complexes were synthesized via condensation reactions (Figure 4.3) from the hydroxide precursors with various dicarboxylic acids and the products obtained in yields of 36-61%. The monomethyl ester analogues were also prepared in 42-76% yield for comparison with their monometallic acid and dimetallic analogues. The target compounds are moderately air stable in solution and can be stored in air as solids at room temperature for several weeks with no signs of decomposition as judged by IR and ^{1}H NMR spectroscopy.

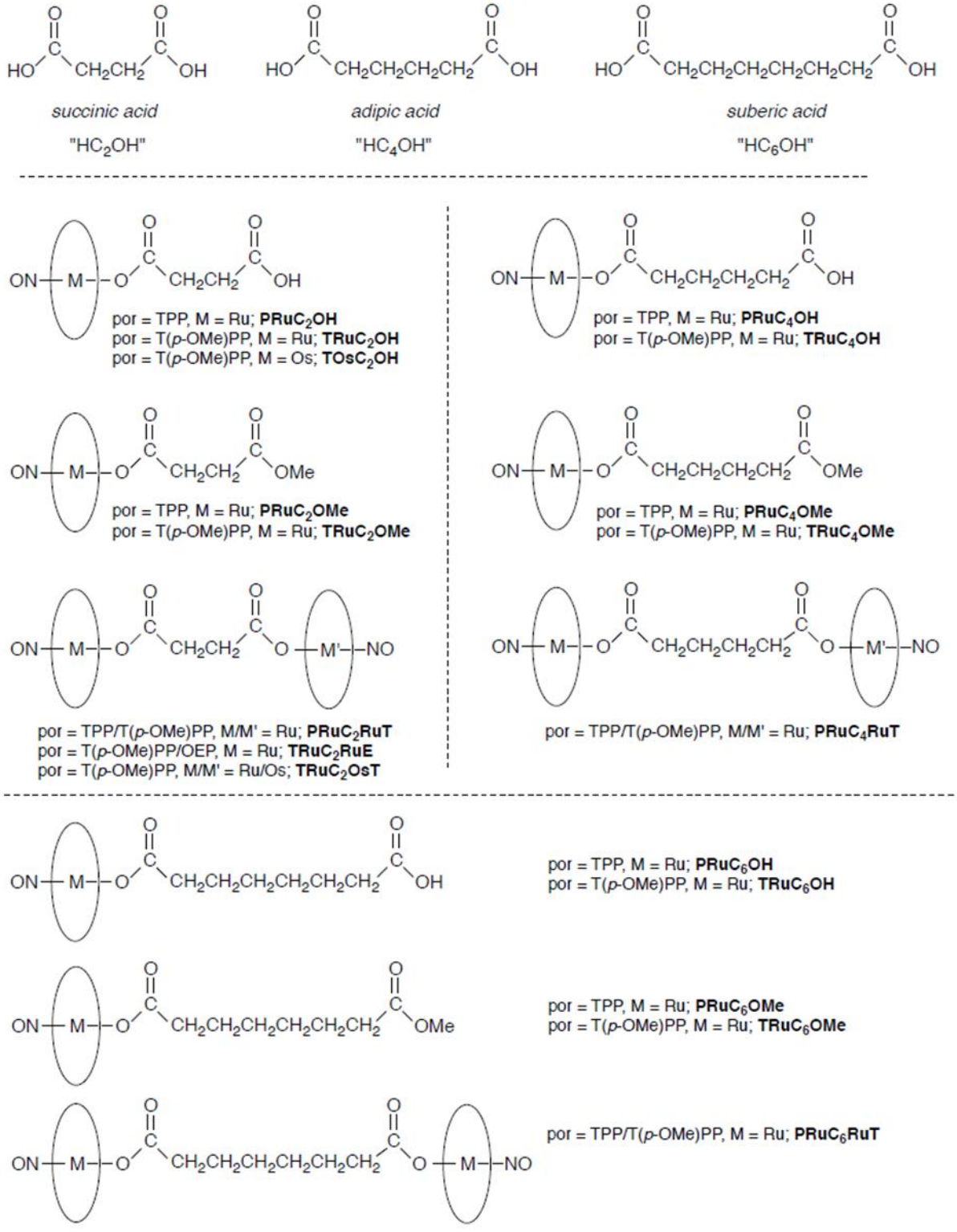

Figure 4.2 Depiction of target monometallic acid/ester and dimetallic compounds and their corresponding abbreviations.

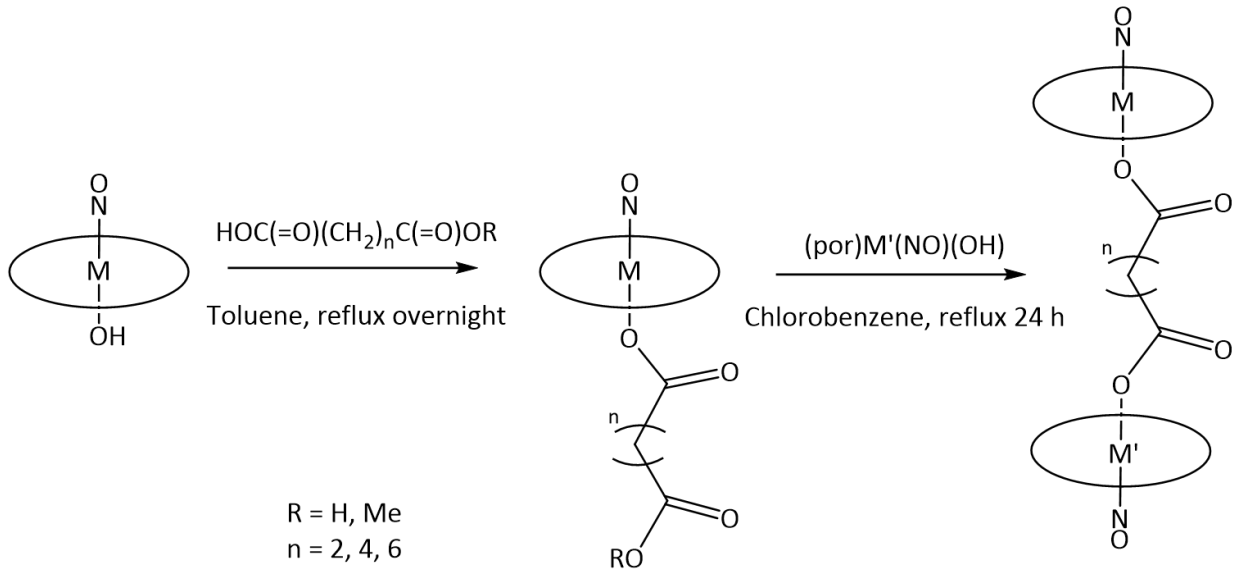

Figure 4.3 General synthesis description for the (por)M(NO)(OC(=O)$(CH_2)_n$C(=O)OR) and (por)M(NO)(OC(=O)$(CH_2)_n$C(=O)O)M′(NO)(por) complexes.

The IR spectra of the target monometallic and dimetallic carboxylate complexes of the ruthenium nitrosyl porphyrin products displayed bands attributed to ν_{NO} and $\nu_{C=O}$ (e.g., Figure 4.4). The exchange reaction of the initial hydroxide complexes with the corresponding carboxylic acid reagent generated the monometallic (por)M(NO)(OC(=O)$(CH_2)_n$C(=O)OR) (por = TPP, T(*p*-OMe)PP, OEP; M = Ru, Os; n = 2, 4, 6; R = H, Me) products, resulting in ν_{NO} shifts to higher frequencies with ($\Delta\nu_{NO}$ = ca. +30 cm^{-1}). This is a result of the electron withdrawing nature of the carboxylate functional group that leads to diminished π-backbonding to the NO ligand and matches published values of related (T(*p*-OMe)PP)Ru(NO)(OC(=O)R) (R = Me, ^{i}Pr, ^{t}Bu, CF_3, C_6H_4-*p*-NO_2, Fc) compounds.[1,2] Although the difference between ν_{NO} of the carboxylate complexes is minimal with increasing alkyl chain length it is reflective of the very slight change in pK_a values of these components (e.g., pK_{a1} and pK_{a2} of succinic acid = 4.21 and 5.41, adipic acid = 4.41 and 5.41, suberic acid 4.53 and 5.49).[35] In the monometallic complexes, the highest ν_{NO} obtained was for the compound $PRuC_2OH$ at 1850 cm^{-1} and the lowest (for Ru)

at 1838 cm^{-1} for the compound $TRuC_6OMe$ (Table 4.1), which is in good agreement with the increasing donor ability of the more electron rich porphyrin and carboxylate components (e.g., T(*p*-OMe)PP > TPP, $C_6 > C_2$, Me > H). A slight decrease in ν_{NO} for the dimetallic compounds was observed with a deacrease in the bridging alkyl chain length, as seen in the comparison between the $TRuC_2RuT$ (ν_{NO} = 1831 cm^{-1}) and $TRuC_6RuT$ (ν_{NO} = 1849 cm^{-1}) compounds, likely the result of weak electronic communication between the porphyrin macrocycles in close proximity. The frequency shift of the single observed $\nu_{C=O}$ band to two detectable bands upon coordination of the carboxylate ligand (e.g., free succinic acid $\nu_{C=O}$ = 1697 cm^{-1}; coordinated ligand $\nu_{C=O}$ = 1647 cm^{-1} and 1719 cm^{-1}) is characteristic of the (por)Ru(NO)(OC(=O)R) compounds reported previously ($\nu_{C=O}$ = 1646-1665 cm^{-1}),[1,2] where the second band at higher frequencies ($\nu_{C=O}$ = 1719-1735 cm^{-1}) corresponds to the uncoordinated -C(=O)OR (R = H, Me) fragment. This band disappears again upon formation of the symmetric dimetallic compound with the presence of similar $\nu_{C=O}$ values ($\nu_{C=O}$ = 1651-1661 cm^{-1}) to that of the coordinated carboxylate frequency.

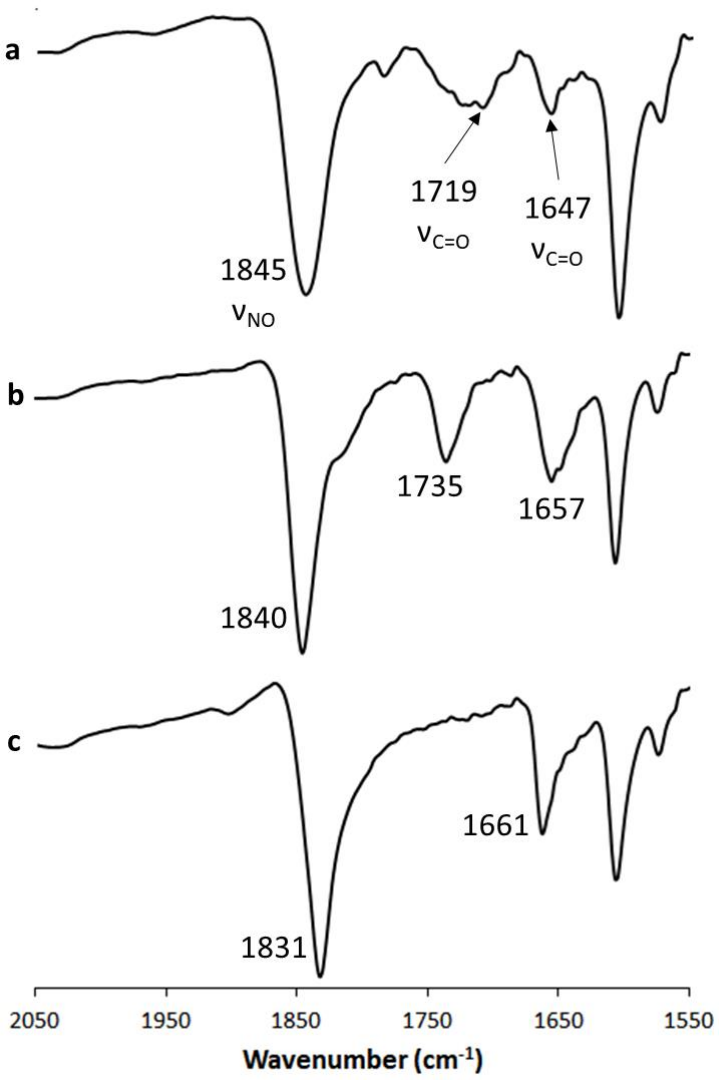

Figure 4.4 Truncated IR spectra of compounds (a) $TRuC_2OH$, (b) $TRuC_2OMe$ and (c) $TRuC_2RuT$ as KBr pellets. See Figure 4.2 for compound identification.

Table 4.1 IR ν_{NO} and $\nu_{C=O}$ frequencies of (por)M(NO)(OC(=O)$(CH_2)_n$C(=O)OR) and (por)M(NO)(OC(=O)$(CH_2)_n$C(=O)O)M′(NO)(por) complexes, and of related (por)Ru(NO)(OC(=O)R) compounds.

	ν_{NO} (cm^{-1})	$\nu_{C=O}$ (cm^{-1})	Ref.
(T(*p*-OMe)PP)Ru(NO)(OC(=O)Me)	1843[a]	1665[a]	1
(T(*p*-OMe)PP)Ru(NO)(OC(=O)^{i}Pr)	1842[a]	1663[a]	1
(T(*p*-OMe)PP)Ru(NO)(OC(=O)^{t}Bu)	1839[a]	1659[a]	1
(T(*p*-OMe)PP)Ru(NO)(OC(=O)C_6H_4-*p*-NO_2)	1849[a]	1656[a]	1
(T(*p*-OMe)PP)Ru(NO)(OC(=O)Fc)	1840[a]	1647[a]	1
(T(*p*-Me)PP)Ru(NO)(OC(=O)Fc)	1839[a]	1646[a]	1
(T(*p*-OMe)PP)Ru(NO)(OC(=O)CF_3)	1861[a]	1719[a]	2
P$Ru C_2$OH	1850[a]	1712, 1640[a]	t.w.
P$Ru C_4$OH	1845[a]	1721, 1657[a]	t.w.
P$Ru C_6$OH	1844[a]	1717, 1653[a]	t.w.
P$Ru C_2$OMe	1843[a]	1740, 1662[a]	t.w.
P$Ru C_4$OMe	1840[a]	1737, 1653[a]	t.w.
P$Ru C_6$OMe	1840[a]	1736, 1660[a]	t.w.
P$Ru C_2$RuP	1836[a]	1656[a]	t.w.
P$Ru C_4$RuP	1838[a]	1656[a]	t.w.
P$Ru C_6$RuP	1838[a]	1653[a]	t.w.
T$Ru C_2$OH	1845[a]	1719, 1647[a]	t.w.
T$Ru C_4$OH	1845[a]	1718, 1650[a]	t.w.
T$Ru C_6$OH	1843[a]	1721, 1652[a]	t.w.
T$Ru C_2$OMe	1840[a]	1735, 1657[a]	t.w.
	(1816)[b]	(1734, 1649)[b]	
T$Ru C_4$OMe	1840[a]	1732, 1652[a]	t.w.
T$Ru C_6$OMe	1838[a]	1734, 1651[a]	t.w.
T$Ru C_2$RuT	1831[a]	1661[a]	t.w.
T$Ru C_4$RuT	1844[a]	1651[a]	t.w.
T$Ru C_6$RuT	1849[a]	1651[a]	t.w.
T$Ru C_0$RuT	1835[a]	1662[a]	t.w.
T$Os C_2$OH	1804[b]	1727, 1709[b]	t.w.

[a] KBr

[b] CH_2Cl_2; values in parentheses are ^{15}N-labelled nitrosyl complex.

See Figure 4.2 for compound identification.

Utilizing IR spectroscopy to track the changes in characteristic ν_{NO} and $\nu_{C=O}$ bands aided in monitoring the conversion of the nitrosyl hydroxo precursor complex to the target monometallic and dimetallic carboxylate compounds. However, ^{1}H NMR spectroscopy is especially useful in distinguishing between the symmetric and unsymmetric species, as well as

verifying purity of the compounds for subsequent electrochemical studies. A depiction of the ^{1}H NMR spectra for the isolated $TRuC_2OH$, $TRuC_2OMe$ and $TRuC_2RuT$ products in $CDCl_3$ is shown in Figures 4.5a-c, which display peaks corresponding to the axial -CH_2- signals of the monometallic (δ -0.85-0.18 ppm) and dimetallic (δ -3.86 ppm) carboxylate compounds. Additionally, between complexes $TRuC_2RuT$, $TRuC_4RuT$ and $TRuC_6RuT$ the innermost methylenes single peak shifts from a more negative value (δ -3.86 ppm) in $TRuC_2RuT$ to multiple signals at noticeably less negative values ($TRuC_4RuT$: δ -2.04 ppm and -3.86 ppm; $TRuC_6RuT$: δ -1.35 ppm, -1.86 ppm and -2.30 ppm). This shift of the bridging alkyl peaks is indicative of a deshielding ring current effect (i.e., shifting downfield) that becomes lessened as the protons move further away from the porphyrin macrocycles. Conversely, an enhanced ring current effect leading to anisotropic shielding (i.e., shifting upfield) is observed for the pyrrole-H signals of the dimetallic species in comparison to the monometallic complexes, which is demonstrated by the signal shift for the $TRuC_2OH$ compound at δ 9.06 ppm upon formation of $TRuC_2RuT$ at δ 8.69 ppm (Δδ = -0.37 ppm). A progressive decrease in this enhancement is apparent as the alkyl chain length increases in $TRuC_4RuT$ (δ 8.74 ppm; Δδ = -0.32 ppm) and $TRuC_6RuT$ (δ 8.84 ppm; Δδ = -0.22 ppm). The singly coordinate compounds fall in the range of the previously reported nitrosyl carboxylates,[1,2] while the dimetallic compounds are in good agreement with published nitrosyl dithiolate complexes from our group.[3] In addition to the distinct splitting patterns of the methylene protons on the axial carboxylate ligands, unique patterns are also observed for the tetraaryl proton signals of the T(*p*-OMe)PP macrocycle from the restricted rotation of these aryl groups, similar to those discussed in chapter 2. Due to the insolubility of the TPP dimetallic derivatives, ^{1}H NMR spectra could not be recorded for the $PRuC_2RuP$, $PRuC_4RuP$ and $PRuC_6RuP$ complexes; however, elemental analyses were obtained

for these compounds, and the results are presented in Table 4.2. The pyrrole-H signals from the ^{1}H NMR spectra of the compounds prepared in this work and other related complexes are listed in Table 4.3.

Table 4.2 Chemical composition of $PRuC_nRuP$ (n = 2, 4, 6).

	Found (Calc.) (%)		
	C	**H**	**N**
$PRuC_2RuP$	68.53 (68.90)	3.80 (3.77)	8.67 (8.73)
$PRuC_4RuP•CH_2Cl_2$	66.79 (66.70)	3.98 (3.84)	8.07 (8.10)
$PRuC_6RuP•0.5CH_2Cl_2$	68.02 (68.20)	4.24 (4.07)	8.02 (8.20)

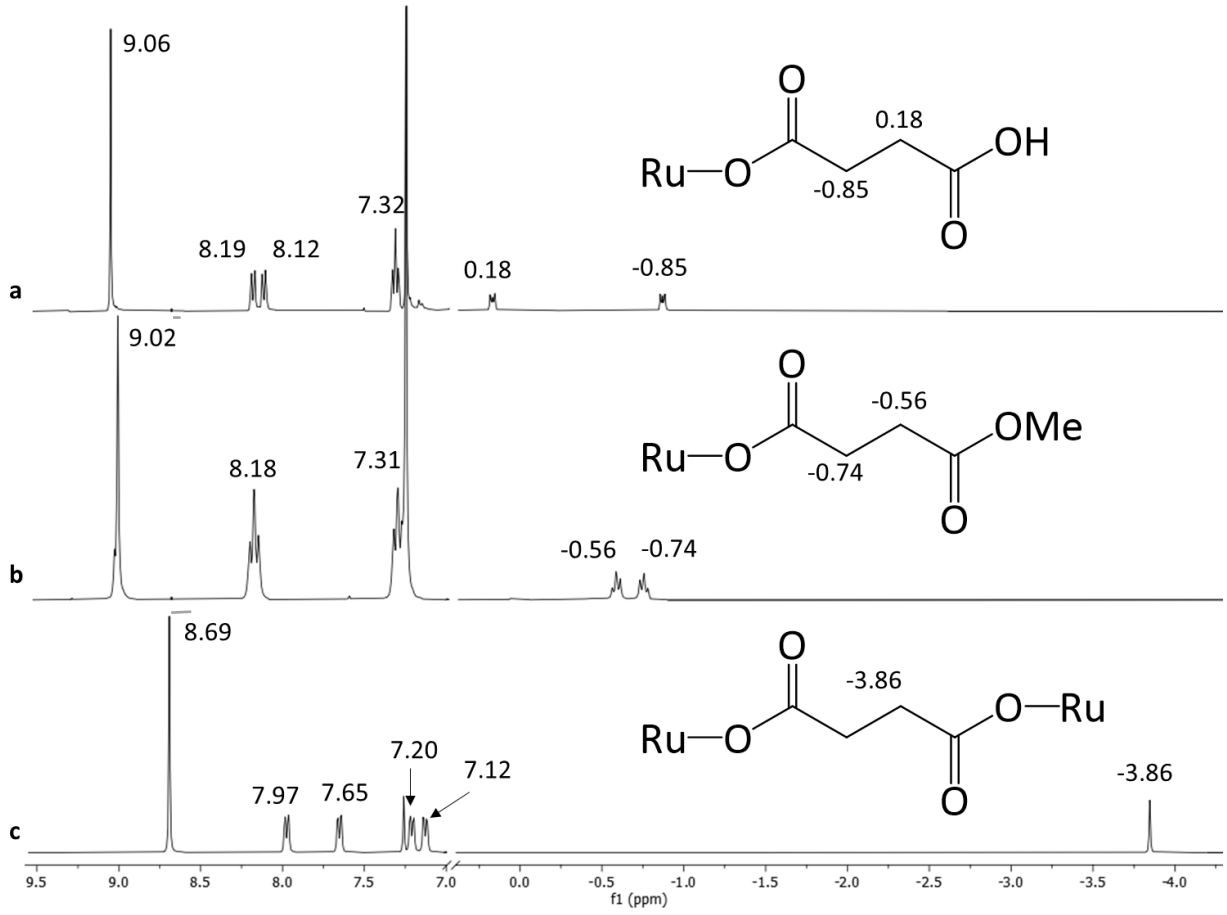

Figure 4.5 ^{1}H NMR spectra of compounds (a) $TRuC_2OH$, (b) $TRuC_2OMe$ and (c) $TRuC_2RuT$ in $CDCl_3$ with the corresponding tetraaryl and carboxylate regions labelled.

Table 4.3 ^{1}H NMR pyrrole-H signals of (por)M(NO)(OC(=O)$(CH_2)_n$C(=O)OR) (por)M(NO)(OC(=O)$(CH_2)_n$C(=O)O)M′(NO)(por) complexes, and related (por)Ru(NO)(OC(=O)R) compounds in $CDCl_3$.

	δ pyrrole-H (ppm)	Ref.
(T(*p*-OMe)PP)Ru(NO)(OC(=O)Me)	9.00	1
(T(*p*-OMe)PP)Ru(NO)(OC(=O)^{i}-Pr)	8.99	1
(T(*p*-OMe)PP)Ru(NO)(OC(=O)^{t}-Bu)	8.98	1
(T(*p*-OMe)PP)Ru(NO)(OC(=O)C_6H_4-*p*-NO_2)	9.04	1
(T(*p*-OMe)PP)Ru(NO)(OC(=O)Fc)	9.02	1
(T(*p*-Me)PP)Ru(NO)(OC(=O)Fc)	9.02	1
(T(*p*-OMe)PP)Ru(NO)(OC(=O)CF_3)	9.04	2
PRuC_2OH	9.04	t.w.
PRuC_4OH	9.00	t.w.
PRuC_6OH	8.98	t.w.
PRuC_2OMe	8.99	t.w.
PRuC_4OMe	8.98	t.w.
PRuC_6OMe	8.97	t.w.
TRuC_2OH	9.06	t.w.
TRuC_4OH	9.02	t.w.
TRuC_6OH	9.01	t.w.
TRuC_2OMe	9.02	t.w.
TRuC_4OMe	9.01	t.w.
TRuC_6OMe	9.00	t.w.
TRuC_2RuT	8.69	t.w.
TRuC_4ORuT	8.74	t.w.
TRuC_6ORuT	8.84	t.w.
TOsC_2OH	9.07	t.w.

Upon further investigation of the methylene proton peaks associated with the carboxylate ligands for TRuC_2OH and TRuC_2OMe it was revealed that “apparent” triplets were present for the carboxylic acid and monomethyl ester derivatives. From the simulated spectra, the monometallic acid complex exhibits an AA′BB′ splitting pattern centered at δ -0.85 ppm and 0.18 ppm (Figure 4.6a) with measured coupling constants of $J_{AA'} = J_{BB'} = 8.11$ Hz, $J_{AB} = J_{A'B'} = 6.05$ Hz and $J_{AB'} = J_{A'B} = 2.11$ Hz,[36,37] while the ester derivative demonstrated a simple AB splitting pattern at δ -0.74 ppm and -0.56 ppm (Figure 4.6b) with a $J = 7.0$ Hz. This AA′BB′ splitting pattern is unique to the PRuC_2OH and TRuC_2OH analogues. All spectra recorded for

the monometallic and symmetric dimetallic compounds with varied alkyl chain length, excluding $PRuC_2OH$ and $TRuC_2OH$, all displayed the AB splitting patterns for the coordinated carboxylate ligands.

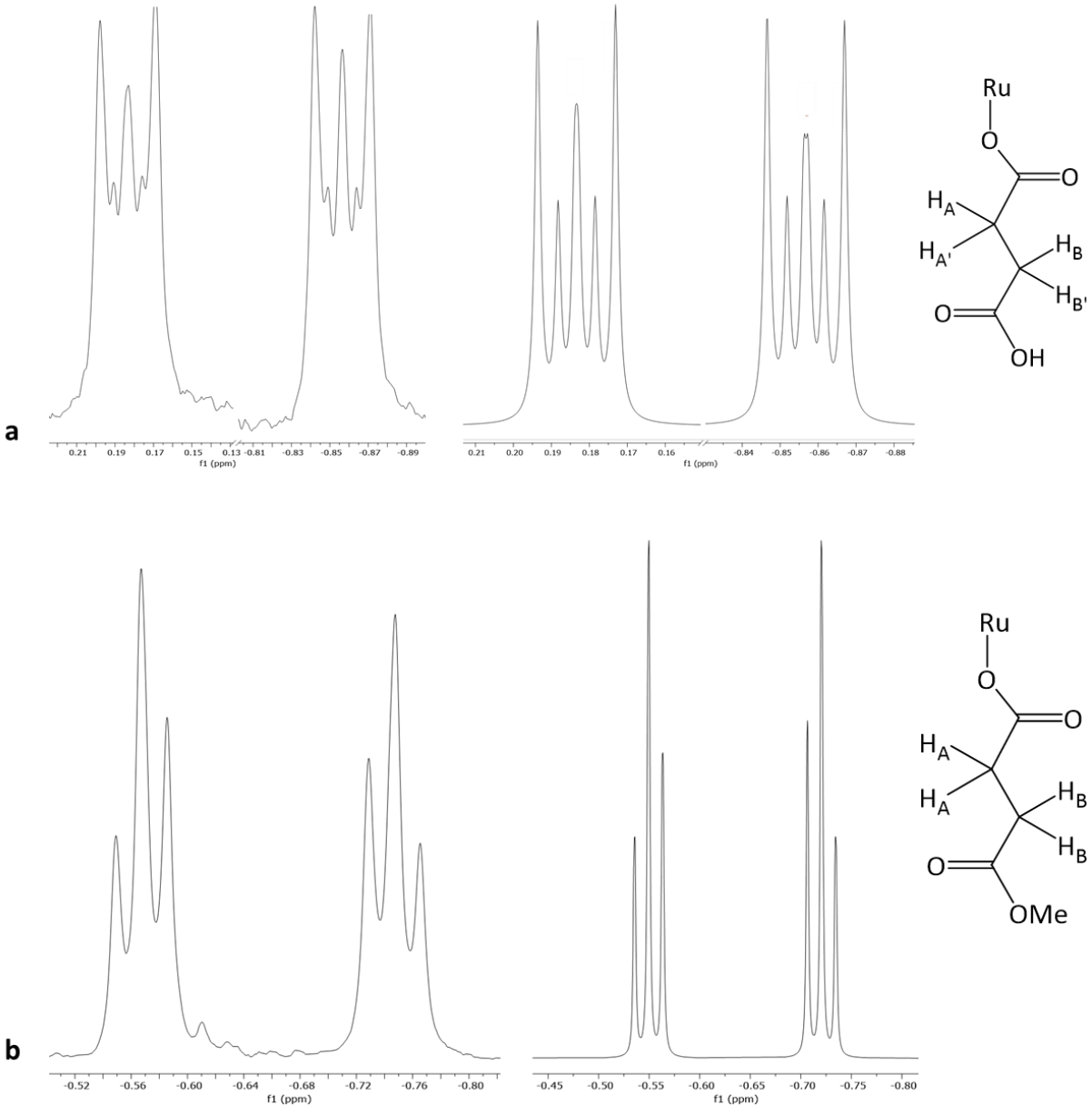

Figure 4.6 Truncated ^1H NMR spectra of compounds (a) $TRuC_2OH$ and (b) $TRuC_2OMe$ in $CDCl_3$ (left), and simulated spectra (right) using chemical shift and coupling constant values for the proton signals of the carboxylate ligand obtained experimentally.

Attempts to prepare and isolate a spectroscopically pure oxalic, -OC(=O)C(=O)O-, derivative of the dimetallic ruthenium nitrosyl porphyrin complex were unsuccessful. In an effort to compensate for the insolubility of oxalic acid in organic solvents at room temperature and its high melting point (189 °C), high boiling point solvents were employed, such as chlorobenzene (132 °C) and decahydronapthalene (190 °C). The IR spectra of the products display bands at 1662 cm^{-1} and 1835 cm^{-1} in Figure 4.7a and are in good agreement with other symmetric dimetallic complexes described in this work. Consequently, I tentatively assign these bands to the $\nu_{C=O}$ and ν_{NO}, respectively, of $TRuC_0RuT$. An additional band at 1936 cm^{-1} was detected as a minor product (13%) that matches the reported ν_{CO} of (T(*p*-OMe)PP)Ru(CO),[27] which shows significant increase in intensity as the solvent system is changed based on increasing boiling point. The yield of this byproduct present in the reaction mixture increases to 22% in chlorobenzene (Figure 4.7b) and 58% in decahydronapthalene (Figure 4.7c), suggesting a split of the dicarboxylic acid to generate the ruthenium carbonyl porphyrin complex. This is the first instance for the cleavage of a dicarboxylic acid leading to the formation of a transition metal carbonyl complex to my knowledge. Two new bands at 1840 cm^{-1} and 1848 cm^{-1} are also present in Figures 4.7b and 4.7c, respectively, that are tentatively assigned to the ν_{NO} of an as-yet unidentified byproduct of these reactions.

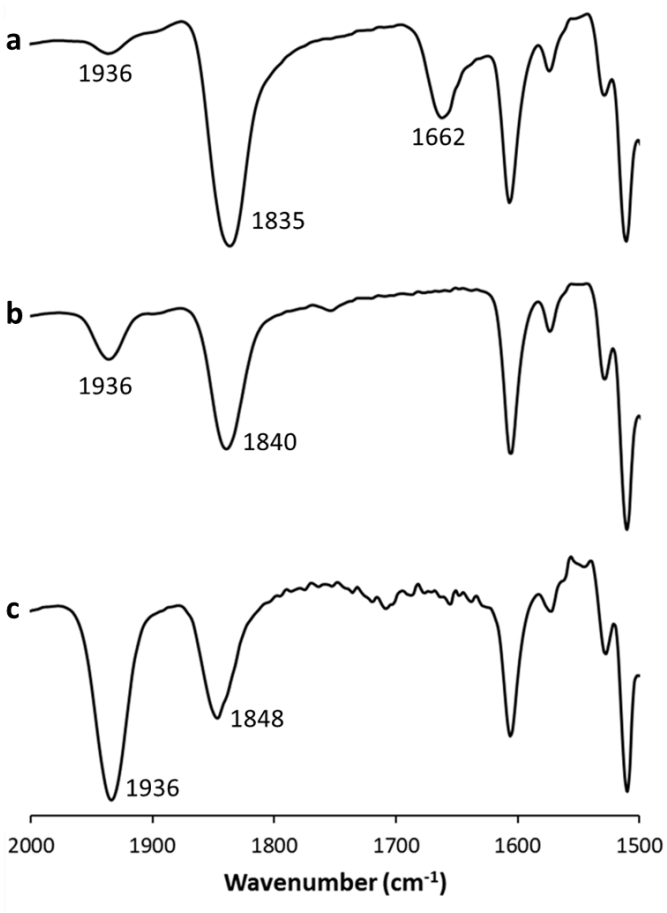

Figure 4.7 IR spectra of the isolated products (as KBr pellets) from the reactions of (T(*p*-OMe)PP)Ru(NO)(OH) with oxalic acid using (a) toluene (110 °C), (b) chlorobenzene (132 °C) and (c) decahydronapthalene (190 °C).

A similar synthetic approach used for the symmetric dimetallic complex was employed to generate the unsymmetric mixed porphyrin TRuC$_2$RuE (i.e., T(*p*-OMe)PP and OEP) complex. Although a purified product could not be obtained, the ^{1}H NMR spectra of the reaction progress (Figure 4.8) displays a complex multiplet centered at δ -3.87 ppm, assigned to the bridging -CH$_2$- signals. These protons exhibit an AA′BB′ splitting pattern with measured coupling constants of $J_{AA'} = J_{BB'} = -13.2$ Hz, $J_{AB'} = J_{A'B} = 11.4$ Hz, $J_{AB} = 5.3$ Hz, and $J_{A'B'} = 2.3$ Hz with a $\Delta\nu_{AB} = 52$ Hz, as demonstrated by the simulated spectrum. The presence of two distinctive porphyrin species leading to such a splitting pattern has been observed previously for the bridged dithiolate

complexes, including similar measured coupling constant values.[6] Efforts to purify the mixture and isolate the target compound resulted in decomposition.

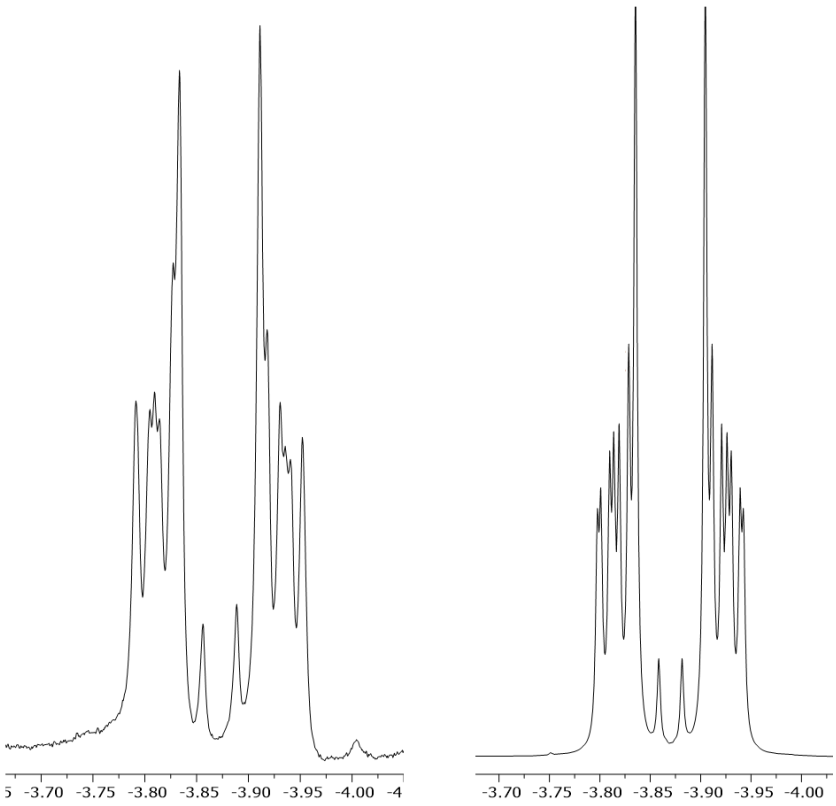

Figure 4.8 Truncated ^{1}H NMR spectrum of the mixture containing the (left) compound $TRuC_2RuE$ in $CDCl_3$ and (right) simulated spectrum using chemical shift and coupling constant values for the proton signals of the carboxylate ligand obtained experimentally.

The synthesis of a different type of unsymmetric metalloporphyrin complex was attempted involving a heterobimetallic system. Specifically, the target $TRuC_2OsT$ compound that contains a ruthenium nitrosyl bridged by a succinate linker to an osmium nitrosyl possessing the same T(*p*-OMe)PP macrocycle. This reaction was monitored by ^{1}H NMR spectroscopy and the results, illustrated in Figure 4.9, display two signals at δ 8.69 ppm and 8.71 ppm, in the pyrrole-H region of the other dimetallic compounds discussed in this work, with identical integration values and have corresponding -OMe (from T(*p*-OMe)PP macrocycle) peaks at δ 4.03 ppm and

4.05 ppm. A broad singlet is observed at δ -3.89 ppm with an integration value matching the expected bridging dicarboxylate ligand. Similar to the mixed porphyrin species, initial attempts at purification of the reaction mixture led to the decomposition of the desired heterobimetallic complex.

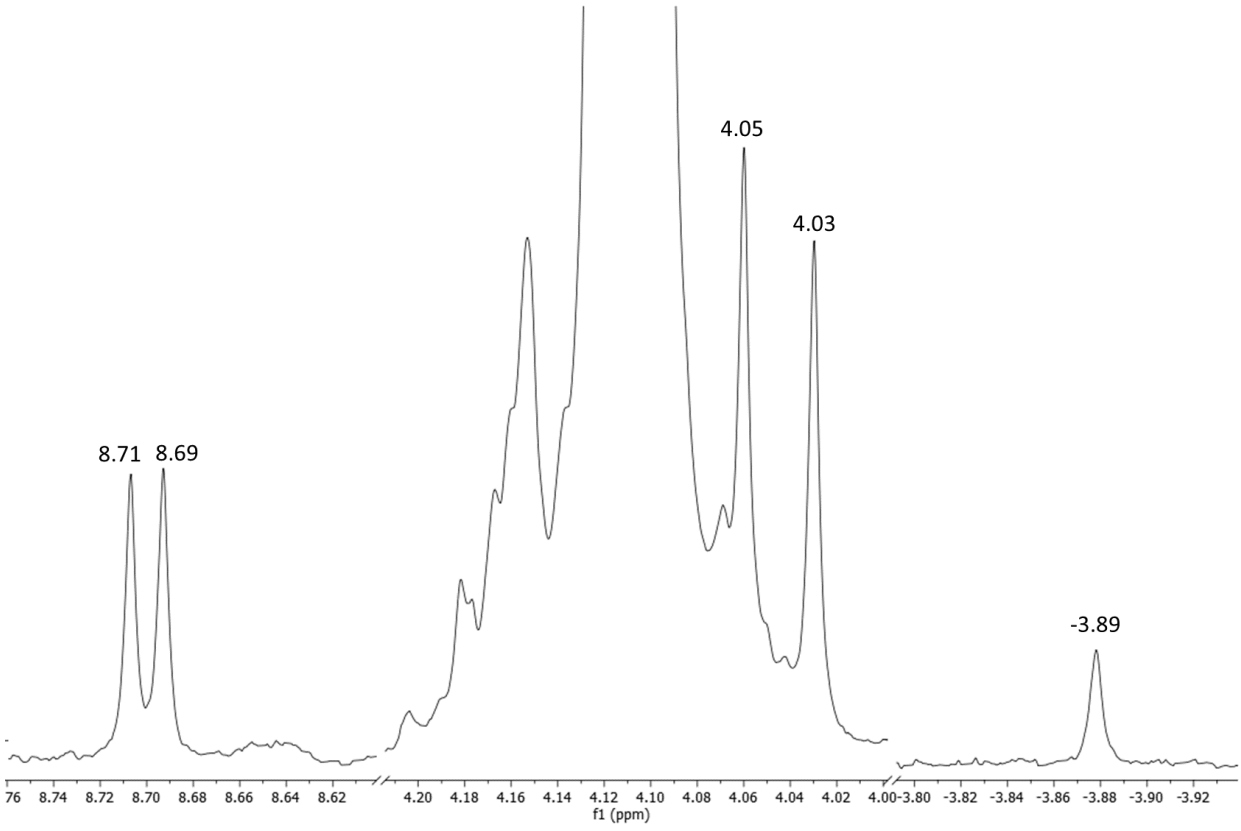

Figure 4.9 Truncated ^{1}H NMR spectra for the reaction of TOsC_2OH with (T(*p*-OMe)PP)Ru(NO)(OH) in $CDCl_3$.

The molecular structures of compounds PRuC_2OH and TRuC_2OMe are shown in Figure 4.10, which display conventional {RuNO}^{6} geometries. Specifically, near linear ∠RuNO bond angles of 173.89(10)° and 179.2(5)°, and Ru-N(O) bond lengths of 1.7401(19) and 1.716(5) Å, respectively, were obtained. These complexes also exhibit axial Ru-O bond lengths of 2.0131(15) Å for the acid derivative and 2.002(4) Å for the ester, matching closely with

previously reported carboxylate crystal structures.[1,2] The Ru-O bond lengths of these complexes are in good agreement with other non-heme group 8 metal bridged dicarboxylates as well.[14,18,22]

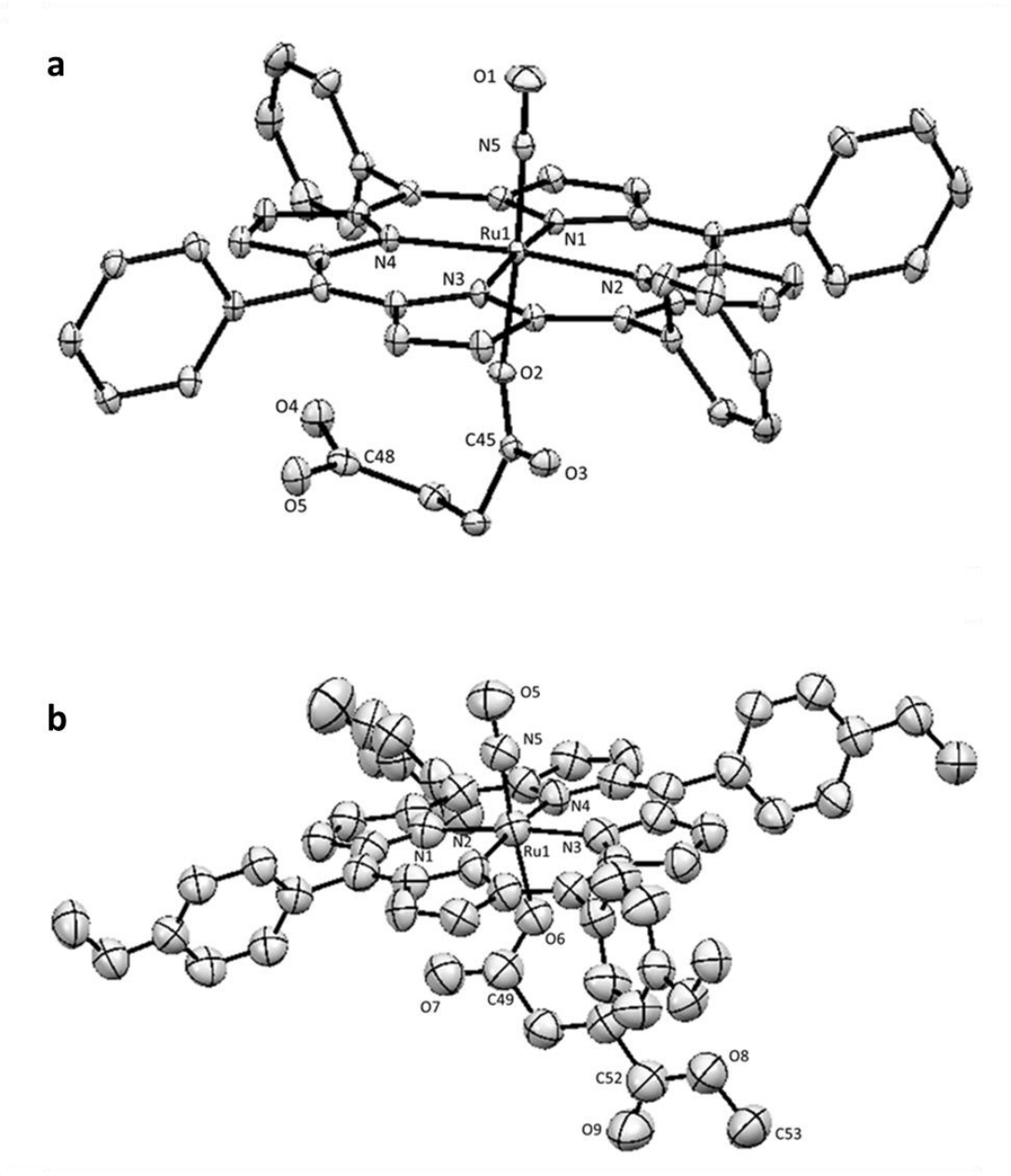

Figure 4.10 Molrcular structures of (a) PRuC$_2$OH (i.d. 21031) and (b) TRuC$_2$OMe. Hydrogen atoms are omitted for clarity and only the major disordered components are shown. The X-ray diffraction data for TRuC$_2$OMe was collected and the structure solved by Dr. Joseph H. Reibenspies at Texas A&M University.

4.3.2. Cyclic voltammetry in CH_2Cl_2

Cyclic voltammetry (CV) was employed to probe the redox behavior of the various symmetric dicarboxylate bridged complexes of ruthenium nitrosyl porphyrins and their corresponding monometallic carboxylate ester derivatives. Table 4.4 displays the measured peak anodic (E_{pa}) and cathodic (E_{pc}) potentials of the redox features observed for these compounds at 200 mV/s. From the electrochemical data collected, porphyrin identity and carboxylate chain length appear to have a clear influence on the redox behavior of the systems studied. For example, the first and second oxidations in the monometallic species take place at more positive potentials (i.e., more difficult to oxidize) in the TPP derivatives than those of the more electron donating T(*p*-OMe)PP derivatives. As seen in the voltammograms of the monometallic ester and dimetallic T(*p*-OMe)PP complexes below in Figures 4.11-4.13 and Table 4.4, a slight shift in the E_{pa} for the first oxidations to more positive values is observed with a decrease in alkyl chain length of the carboxylate ligand. This trend was first noted in the discussion of the IR spectra where a higher number of methylene groups led to an increase in electron density at the Ru-NO fragment. The monometallic TPP derivatives appear to follow this trend as well; however, the minimal differences in $E^{\circ\prime}$ for the first oxidations and E_{pc} for the first reduction (~10 mV) are not quantitatively reliable enough to confidently state that a clear trend is present. In general, the redox behavior pattern does not differ between the porphyrin derivatives, and the discussion herein will focus on the T(*p*-OMe)PP analogues. While the ester compounds display a single fully reversible (i_{pc}/i_{pa} = 1.0) first oxidation at 200 mV/s, the dimetallic compounds seem to undergo a more complex oxidation mechanism. No distinguishable trend corresponding to the change in carboxylate chain length was detected for the second oxidations of the monometallic ester or dimetallic complexes, yet the features occur at E_{pa} in a similar region to others containing the same porphyrin macrocycle (i.e., TPP = +1.24-1.25 V; T(*p*-OMe)PP = +1.07-1.09 V).

Table 4.4 Formal and peak potentials for the oxidations and reductions of the various symmetric dicarboxylate bridged ruthenium nitrosyl porphyrin compounds and the monoester derivatives.[a]

	1st Ox. $E^{\circ\prime}$ (V)	2nd Ox. E_{pa}, E_{pc} (V)	1st Red. E_{pc} (V)
$PRuC_2OMe$	+0.67	+1.25, +1.21	-1.60
$PRuC_4OMe$	+0.66	+1.24, +1.20	-1.61
$PRuC_6OMe$	+0.65	+1.25, +1.20	-1.62
$TRuC_2OMe$	+0.57	+1.07, +0.97	-1.53
$TRuC_4OMe$	+0.56	+1.07, +0.99	-1.59
$TRuC_6OMe$	+0.53	+1.09, +0.98	-1.55
$TRuC_2RuT$	+0.53, +0.65	+1.08, +0.99	-1.52
$TRuC_4ORuT$	+0.58	+1.08, +0.98	-1.65
$TRuC_6ORuT$	+0.57	+1.09, +0.99	-1.61

[a]Experimental conditions: 1.0 mM analyte in CH_2Cl_2 containing 0.1 M NBu_4PF_6. Formal and peak potentials were measured at 200 mV/s with a Pt working electrode and referenced to $Fc^{0/+}$ set at 0.00 V.

$TRuC_2OMe$ and $TRuC_2RuT$

Figure 4.11 shows a comparison of the voltammograms for the monometallic ester and dimetallic compounds possessing the shortest alkyl chains, $TRuC_2OMe$ (top) and $TRuC_2RuT$ (bottom). The full voltammogram of the ester complex (Figure 4.11b) at a scan rate of 200 mV/s (solid line) displays an oxidation feature at E_{pa} = +0.61 V (vs $Fc^{0/+}$) followed by a second oxidation near the edge of the solvent window at E_{pa} = +1.07 V with a corresponding return wave at E_{pc} = +0.97 V. Two additional cathodic features are present, the first at +0.54 V that increases in current with a scan rate of 800 mV/s (dashed line) and the second at +0.73 V that decreases relative to the previous feature. Altering the switching potential (E_{sw}) to isolate the first oxidation (Figure 4.11a) demonstrates complete reversibility with a formal potential ($E^{\circ\prime}$) of +0.57 V, which matches closely to the first oxidations of the related (T(*p*-OMe)PP)Ru(NO)(OC(=O)R) complexes with published values in the range of $E^{\circ\prime}$ = +0.53-0.62 V that detail a porphyrin-centered first oxidation (Eq. 4.1) to yield the radical π-cation $[(T^{\bullet})RuC_2OMe]^+$ complex.[1,2]

$$TRuC_nOMe \rightleftharpoons [(T^{\bullet})RuC_nOMe]^{+} + e^{-} \quad \textbf{(4.1)}$$

Following the second oxidation, an increase in the current response of the aforementioned cathodic wave at +0.54 V associated with the first oxidation (accompanied by the new return wave at E_{pc} = +0.73 V) upon increasing the scan rate from 200 mV/s to 800 mV/s suggests a chemical step has taken place, likely slow loss of the carboxylate ligand (Eq. 4.2a). Increasing the scan rate for the full potential range outpaces loss of the carboxylate ligand allowing more of the initial $TRuC_2OMe$ complex to be reformed. This broad second oxidation feature could be the result of a complex mechanism consisting of multiple redox events but can only be confirmed through spectroelectrochemistry (see later). However, the presence of three distinct cathodic features when scanning the oxidations imply redox events of separate species (Eq. 4.2b and 4.3) including the first oxidation product.

$$[(T^{\bullet})RuC_nOMe]^{+} \longrightarrow [(por)Ru(NO)]^{+} + {}^{\ominus}C_nOMe \quad \textbf{(4.2a)}$$

$$[(T^{\bullet})RuC_nOMe]^{+} \longrightarrow [(T^{\bullet})RuC_nOMe]^{2+} + e^{-} \quad \textbf{(4.2b)}$$

$$[(por)Ru(NO)]^{+} \longrightarrow [(por)Ru(NO)]^{2+} + e^{-} \quad \textbf{(4.3)}$$

Switching to negative potentials and isolating the single reduction (Figure 4.11c) reveals a somewhat reversible cathodic feature at E_{pc} = -1.53 V, with an anodic return wave at E_{pa} = -1.16 V, and similarly appears to undergo a more complex mechanism (Eq. 4.4) than the well-behaved electron transfer observed in the first oxidation. Spectroelectrochemical experiments are required in order to assign the initial site of reduction. No significant change was observed in the reduction for the scan rate range used (50-1600 mV/s).

$$TRuC_nOMe + e^{-} \longrightarrow [TRuC_nOMe]^{-} \quad \textbf{(4.4)}$$

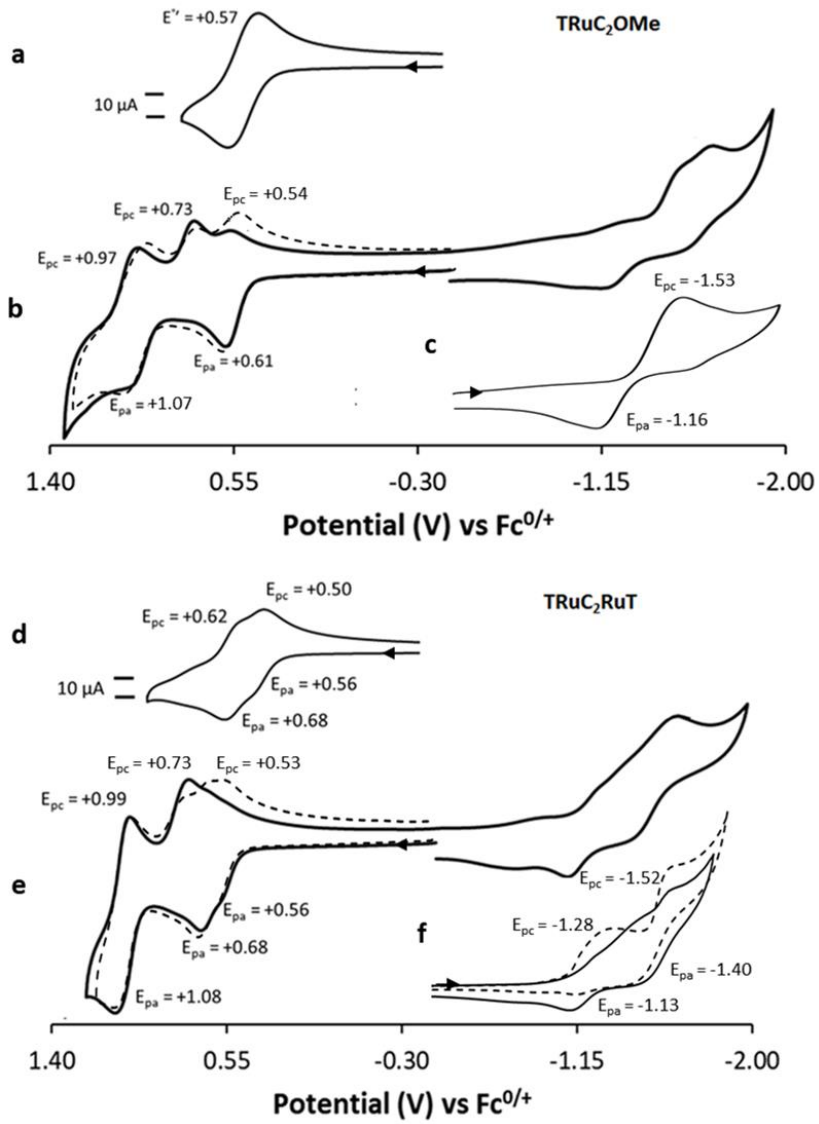

Figure 4.11 Cyclic voltammograms of 1.0 mM (a-c) $TRuC_2OMe$ and (d-f) $TRuC_2RuT$ containing 0.1 M NBu_4PF_6 showing the (a,d) first oxidations, (b,e) full voltammograms at a scan rate of 200 mV/s (solid line) and 800 mV/s (dashed line) and (c,f) first reductions at a scan rate of 50 mV/s (dashed line) and 200 mV/s (solid line), respectively.

The first oxidation of the $TRuC_2RuT$ compound (Figure 4.11d) displays a set of sequential features at $E^{\circ\prime}$ = +0.53 V and +0.65 V that exhibit electrochemical reversibility. This change in redox behavior from the monometallic to dimetallic suggests the short carboxylate chain length allows for minor electronic communication between the two redox active sites resulting in two sequential 1-electron oxidations (i.e., an EE-mechanism). Upon comparison of

the first oxidations between the monometallic and dimetallic species (at the same concentration) a current response ratio of ~1:1 was observed for the single feature in the ester complex voltammogram (4.11a) to each individual feature in the symmetric complex (4.11d). Measuring peak potential differences (ΔE_p) for the first oxidations of the ester and dimetallic compounds revealed a separation of 70 mV and 63/65 mV (for each dimetallic oxidation feature), respectively, with the ΔE_p values measured against the internal standard Fc = 59 mV. A follow-up oxidation for $TRuC_2RuT$, akin to that observed in $TRuC_2OMe$, takes place at E_{pa} = +1.08 V with a corresponding cathodic return wave of E_{pc} = +0.99 V (Figure 4.11e). Again, the cathodic feature at +0.73 V was present at a 200 mV/s scan rate (solid line) and begins to diminish when increasing to 800 mV/s (dashed line) along with the appearance of an additional return wave at +0.53 V, comparable to that seen in $TRuC_2OMe$. Similar to the ester complex a single feature is observed when switching to negative potentials with a E_{pc} = -1.52 V and corresponding anodic return waves at E_{pa} = -1.13 V and -1.40 V at 200 mV/s (Figure 4.11f, solid line). This cathodic feature demonstrates a current response similar in magnitude to that observed for the second oxidation with a ratio of ~5:6. At the slowest scan rate (50 mV/s) an additional cathodic feature was present in the dimetallic compound at E_{pc} = -1.28 V (Figure 4.11f, dashed line), which may suggest two sequential 1-electron reductions; however, CH_2Cl_2 is known to be unstable under cathodic conditions and may contribute to additional chemistry at the electrode surface.[41] A more detailed description of the first oxidation for the dimetallic compounds in comparison to the monometallic ester derivatives can be seen in Figure 4.14.

$TRuC_4OMe$ and $TRuC_4RuT$

The redox behavior for the compounds containing the intermediate carboxylate chain length ($TRuC_4OMe$ and $TRuC_4RuT$) is shown in Figure 4.12 with the monometallic ester

complex not differing significantly from that of the succinate derivative (Figure 4.11). At a slightly less positive potential than $TRuC_2OMe$, the first oxidation occurs at $E^{\circ\prime}$ = +0.56 V, as observed in Figure 4.12a. This is in line with the slight increase in electron donation from the longer chain carboxylate for the previously proposed porphyrin-centered oxidation to form $[(T^{\bullet})RuC_4OMe]^{+}$. The second oxidation (Figure 4.12b) that takes place out near the edge of the solvent window at E_{pa} = +1.07 V is followed up by the appearance of two return waves at E_{pc} = +0.73 V and +0.99 V at 200 mV/s (solid line). Additionally, a cathodic feature at E_{pa} = +0.53 V (return wave associated with the first oxidation) appears once the scan rate is increased to 800 mV/s (dashed line), as was observed in $TRuC_2OMe$. These results are in good agreement with the generation of the previously mentioned $[(por)Ru(NO)]^{+/2+}$ products as well as the unstable $[TRuC_4OMe]^{2+}$ intermediate. Switching focus to the reductions of this complex in Figure 4.12c, a somewhat reversible cathodic feature arises at E_{pc} = -1.59 V with a corresponding anodic return wave at E_{pa} = -1.18 V, resulting in a $[TRuC_4OMe]^{-}$ reduction product that is generally similar to what was seen for the succinate ester complex.

Initial examination of the $TRuC_4RuT$ voltammogram (bottom of Figure 4.12) revealed comparable redox features to those of the monometallic ester compound (top of Figure 4.12). The single broad feature for the reversible first oxidation features are found at $E^{\circ\prime}$ = +0.58 V with a ΔE_p = 102 mV, which is significantly larger than that of $TRuC_4OMe$ (ΔE_p = 62 mV) measured against Fc = 59 mV. Comparison of the first oxidations from the dimetallic species to the monometallic reveals a considerable increase in the current response with a ratio of ~5:3, a more detailed explanation for the redox behavior including proposed products are discussed later in Figure 4.14. These results are consistent with two sequential 1-electron oxidations, like that observed in $TRuC_2RuT$, but demonstrate near indistinguishable $E^{\circ\prime}$ for the individual features

and is consistent with sequential electron transfer mechanisms described by Bard and Faulkner.[38] It is expected for reversible processes that a concerted 2-electron oxidation would result in a decrease of ΔE_p to about half the value (~30 mV) of a 1-electron oxidation and a sharp increase in the current response (2:1) by the Nernst and Randles-Sevcik equations, respectively.[39] No detectable difference in the features for the first oxidation behavior upon alteration to the scan rate (50-1600 mV/s) were observed. A second oxidation located at E_{pa} = +1.08 V bears a strong resemblance to the $TRuC_2RuT$ derivative with the familiar return waves at E_{pc} = +0.73 V and +0.98 V at a scan rate of 200 mV/s (solid line). However, increasing the scan rate to 800 mV/s (dashed line) displays a minor feature at E_{pc} = +0.52 V that corresponds to the return peak of the first oxidation. The reduction was investigated and displayed a large somewhat reversible feature at E_{pc} = -1.65 V (E_{pa} = -1.12 V and -1.47 V), also similar to the dimetallic succinate complex but at significantly more negative potentials (ΔE_{pc} = -130 mV). Again, upon changing the scan rate from 200 mV/s (Figure 4.12f, solid line) to 50 mV/s (Figure 4.12f, dashed line) led to an additional cathodic feature being present at E_{pc} = -1.40 V.

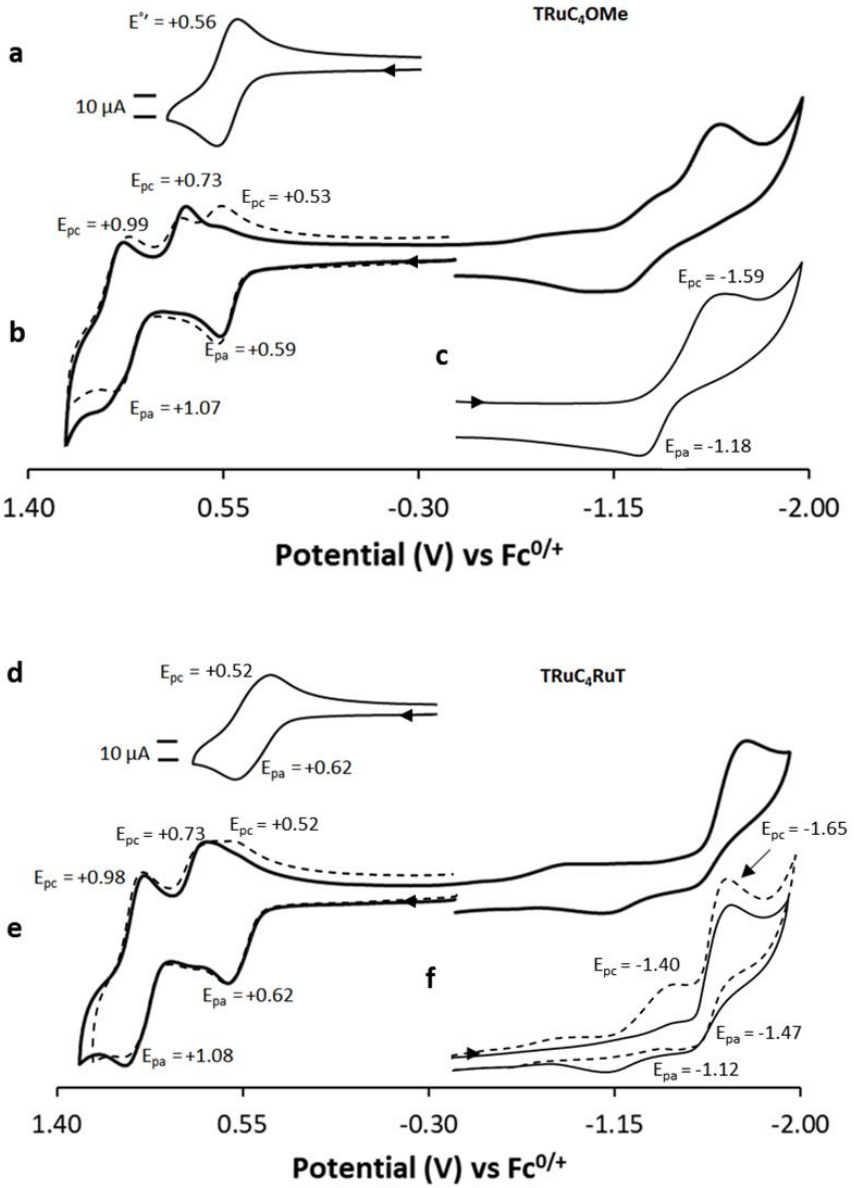

Figure 4.12 Cyclic voltammograms of 1.0 mM (a-c) $TRuC_4OMe$ and 1.1 mM (d-f) $TRuC_4RuT$ containing 0.1 M NBu_4PF_6 showing the (a,d) first oxidations, (b,e) full voltammograms at a scan rate of 200 mV/s (solid line) and 800 mV/s (dashed line) and (c,f) first reductions at a scan rate of 50 mV/s (dashed line) and 200 mV/s (solid line), respectively.

<u>$TRuC_6OMe$ and $TRuC_6RuT$</u>

The voltammograms for the monometallic and dimetallic compounds containing the longest carboxylate alkyl chains ($TRuC_6OMe$ and $TRuC_6RuT$) are illustrated in Figure 4.13. Results for $TRuC_6OMe$ demonstrate similar redox behavior to the $TRuC_2OMe$ and $TRuC_4OMe$

complexes, as observed in Figures 4.13a-c. The first oxidation takes place at the lowest potential of $E^{\circ\prime}$ = +0.53 V (Figure 4.13a) forming $[(T^{\bullet})RuC_6OMe]^+$ and in good agreement with the longest carboxylate chain being a slightly better donor from the cumulative electron density. The second oxidation occurs at E_{pa} = +1.09 V and subsequently leads to the appearance of two familiar cathodic return waves at E_{pc} = +0.73 V and +0.98 V in Figure 4.13b at 200 mV/s (solid line) and the additional feature at E_{pc} = +0.50 V at a scan rate of 800 mV/s (dashed line). As observed in the shorter carboxylate complexes, the second oxidation is expected to yield $[(por)Ru(NO)]^{+/2+}$ and $[TRuC_6OMe]^{2+}$ as its products. Scanning across the reductions results in a Faradaic response at E_{pc} = -1.55 V generating the $[TRuC_6OMe]^-$ complex, as observed in Figure 4.13c.

Probing the redox behavior of $TRuC_6RuT$ did not yield substantially different results from the $TRuC_4RuT$ compound discussed previously. The voltammogram displayed broad first oxidation features at $E^{\circ\prime}$ = +0.57 V and a ΔE_p = 95 mV that is markedly larger than the value determined for the ester complex (ΔE_p = 60 mV) from a comparison to Fc = 59 mV. Similar to the $TRuC_4RuT$ compound, the current response for the dimetallic complex is significantly larger than the monometallic ester derivative with a ~15:8 ratio. Again, likely the result of a poor communication between redox sites from the increased length of the bridging linker. A second oxidation occurs at E_{pa} = +1.09 V and is comparable to the features seen for the $TRuC_2RuT$ and $TRuC_4RuT$ derivatives with the corresponding cathodic return waves at E_{pc} = +0.73 and +0.99 V at 200 mV/s (solid line) and the reappearance of the feature at E_{pc} = +0.52 V after increasing the scan rate to 800 mV/s (dashed line). The cathodic behavior was investigated and displayed a large somewhat reversible feature at E_{pc} = -1.61 V (E_{pa} = -1.13 V and -1.38 V) that yielded an additional feature at E_{pc} = -1.41 V when decreasing the scan rate to 50 mV/s (Figure 4.13f,

dashed line). Specifics of the redox mechanism for the TRuC$_6$RuT complex, in comparison to TRuC$_6$OMe and the other derivatives, are detailed later in Figure 4.14.

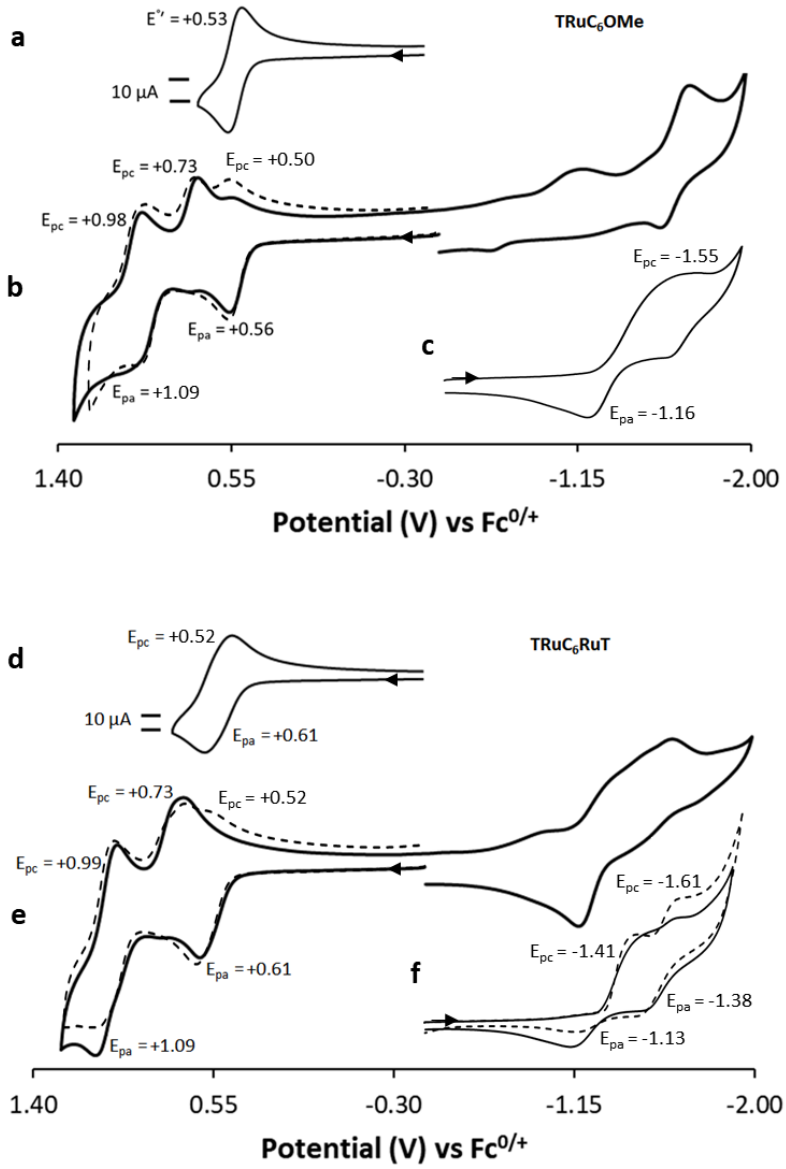

Figure 4.13 Cyclic voltammograms of 0.9 mM (a-c) TRuC$_6$OMe and 1.1 mM (d-f) TRuC$_6$RuT containing 0.1 M NBu_4PF_6 showing the (a,d) first oxidations, (b,e) full voltammograms at a scan rate of 200 mV/s (solid line) and 800 mV/s (dashed line) and (c,f) first reductions at a scan rate of 50 mV/s (dashed line) and 200 mV/s (solid line), respectively.

To shed light on the electron transfer mechanisms of the dimetallic complexes and their associated monometallic ester derivatives discussed earlier, an overlay of the first oxidations for

each of the $TRuC_nOMe$ and $TRuC_nRuT$ (n = 2, 4, 6) pairs are displayed in Figure 4.14. By comparison, the first oxidation of $TRuC_2OMe$ (Figure 4.14a, dashed line) exhibits a reversible 1-electron oxidation to form $[(T^{\bullet})RuC_2OMe]^+$ while the $TRuC_2RuT$ compound (Figure 4.14a, solid line) contains two features similar in appearance ~120 mV apart, and is in line with two sequential 1-electron oxidations that leads to a mixed valence state $[(T^{\bullet})RuC_2RuT]^+ \leftrightarrow [TRuC_2Ru(T^{\bullet})]^+$ being generated on its way to the final $[(T^{\bullet})RuC_2Ru(T^{\bullet})]^{2+}$ product. This proposed mixed valency has been observed in other bridged species, such as various forms of bi- and poly-ferrocenes, where the mono-cation is stabilized by low energy transitions (e.g., metal-metal interactions or conjugated systems) and shifts the redox potential of the subsequent oxidation to slightly more positive potentials.[8-13] The presence of two distinct features and a mixed valence state supports the notion of electronic communication between the metalloporphyrin components, given the proximity of the macrocycles and the expected flexibility of the alkyl chain present in the bridging carboxylate. Similar to the $TRuC_2OMe$ compound, the $TRuC_4OMe$ (Figure 4.14b, dashed line) and $TRuC_6OMe$ (Figure 4.14c, dashed line) derivatives bearing longer branched axial carboxylates show simpler first oxidations. When the alky chain length is extended in the dimetallic complexes, like in $TRuC_4RuT$ (Figure 4.14b, solid line) and $TRuC_6RuT$ (Figure 4.14c, solid line), only a single oxidation feature is observed with larger faradaic currents compared to the ester derivatives (~5:3 and ~15:8, respectively). These singular large features correspond to two sequential 1-electron oxidations likely generating mixed valence species as well enroute to $[(T^{\bullet})RuC_4Ru(T^{\bullet})]^{2+}$ and $[(T^{\bullet})RuC_6Ru(T^{\bullet})]^{2+}$, as demonstrated by the large ΔE_p and current response discussed earlier (102 and 95 mV, respectively) due to poor electronic communication. The decreasing peak potential difference and simultaneous increase of the current density ratio suggests that a substantially longer

bridging carboxylate may be required for the metalloporphyrin redox active sites to behave as truly isolated systems yielding a concerted multi-electron transfer mechanism.

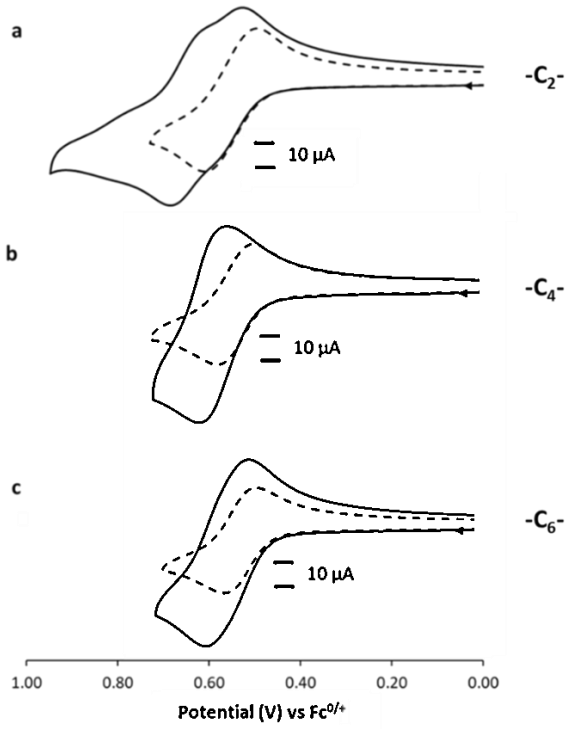

Figure 4.14 Cyclic voltammograms of ~1.0 mM $TRuC_nRuT$ (solid line) and $TRuC_nOMe$ (dashed line) (a) n = 2, (b) n = 4 and (c) n = 6 containing 0.1 M NBu_4PF_6 showing the first oxidations at a scan rate of 200 mV/s.

Semi-integral (Figures 4.15, left) and semi-derivative plots (Figures 4.15, right) were generated for the dimetallic species to supplement the overlayed voltammograms and definitively distinguish between two sequential 1-electron oxidations and potentially concerted 2-electron oxidation mechanisms. Semi-integration is a mathematical approach used for analyzing CV data and yields a sigmoidal shaped curve whose height corresponds to the number of electrons transferred in a given redox event.[28] The semi-integrals for the $TRuC_nRuT$ (n = 2, 4, 6) complexes display heights equivalent to two total electrons being passed during these first oxidation features. Similarly, semi-differentiation is another common data processing technique

where the square root of the y-axis value at the associated E_p also corresponds to the number of electrons transferred. As seen in the semi-derivative plots, the vertical scale of these dimetallic compounds all fall in the range of 1.20-1.34 and suggests that the mechanism is far more likely to undergo two sequential 1-electron oxidations, since the y-axis values are not large enough to indicate a concerted 2-electron oxidation. In a reversible process the half-wave potential separation ($\Delta E_{1/2}$) for the semi-derivative of a redox feature is expected to be 90.7 mV/n (n = number of electrons).[29,30] The resulting $\Delta E_{1/2}$ values for $TRuC_2RuT$, $TRuC_4RuT$ and $TRuC_6RuT$ were found to be 192, 147 and 135 mV (from a comparison to Fc = 91 mV), respectively, which are significantly larger than the expected ~45 mV for a concerted process and support the proposed EE mechanism (two sequential 1-electron oxidations) described previously.

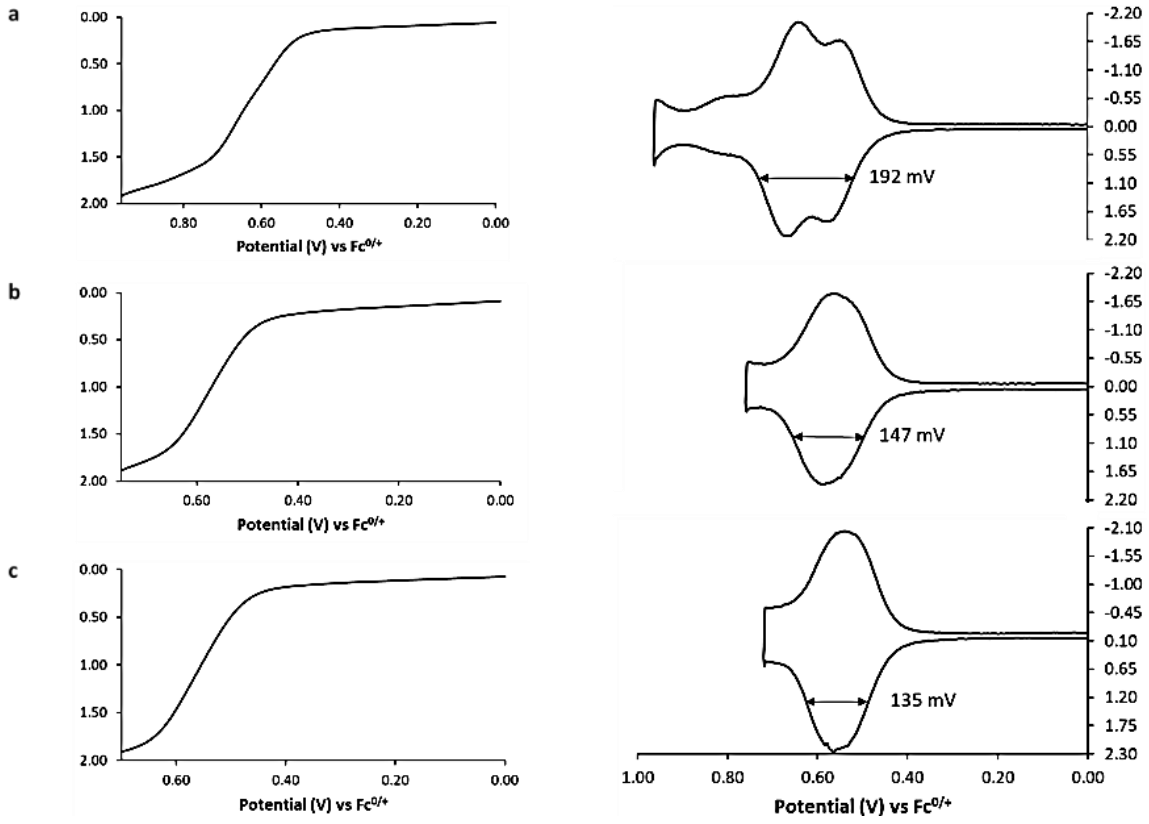

Figure 4.15 Semi-integral (left) and semi-derivative (right) plots of ~1.0 mM $TRuC_nRuT$ (a) n = 2, (b) n = 4 and (c) n = 6 containing 0.1 M NBu_4PF_6 showing the first oxidations at a scan rate of 200 mV/s.

4.3.3. IR spectroelectrochemistry in CH_2Cl_2

Reflectance IR spectroelectrochemistry (IR-SEC) was utilized to obtain structural information relating to the redox processes observed in the electrochemical studies discussed previously for the various $TRuC_nOMe$ and $TRuC_nRuT$ complexes (n = 2, 4, 6). The IR-SEC results for these compounds in CH_2Cl_2 containing 0.1 M NBu_4PF_6, displaying the products generated at the potentials which correspond to the first and second oxidations as well as the first reduction CV feature, are shown in Figures 4.16-18. Note that the first oxidation feature for the $TRuC_nRuT$ complexes (n = 2, 4, 6) are comprised of two sequential 1-electron oxidations, as discussed above.

In the difference IR spectrum of the first oxidation feature for $TRuC_2OMe$ (Figure 4.16a) a loss of the initial ν_{NO} band at 1852 cm^{-1} and appearance of a new ν_{NO} band at 1873 cm^{-1} ($\Delta\nu_{NO}$ = +21 cm^{-1}) were detected after the analyte was held at a potential of +0.65 V (just past the first oxidation CV feature). Low intensity bands occur at lower frequencies associated with the $\nu_{C=O}$ of the carboxylate ligand. Oxidation at this potential results in shifts of these bands from the starting 1645 cm^{-1} to 1662 cm^{-1} and is accompanied by a peak enhancement at 1600 cm^{-1}. These alterations to the observed bands match closely to previously reported values of the related (T(*p*-OMe)PP)Ru(NO)(OC(=O)OR) complexes (ν_{NO} = 1865-1886 cm^{-1}), and correspond to porphyrin-centered oxidations, thereby confirming formation of the $[(T^{\bullet})RuC_2OMe]^+$ product (Eq. 4.1).[1,2] Upon increasing the applied potential to +1.10 V (capturing the second oxidation feature) consumption of the starting ν_{NO} at 1852 cm^{-1} occurs with concomitant appearance of the ν_{NO} at 1881 cm^{-1} with lower intensity bands at 1900 cm^{-1} and 1918 cm^{-1}. The two nitrosyl bands in Figure 4.16b at 1881 cm^{-1} and 1900 cm^{-1} match closely to published values of the related $[(TPP^{\bullet})Ru(NO)(H_2O)]^{+/2+}$ complexes.[40] A similar peak enhancement with increased intensity and

loss of the $\nu_{C=O}$ band observed in the first oxidation took place during the second oxidation, along with a new broad band at 1746 cm^{-1}. Loss of the $\nu_{C=O}$ at 1645 cm^{-1} associated with the coordinated carboxylate and appearance of this broad $\nu_{C=O}$ band in the region of the free ester (1740 cm^{-1}) is consistent with slow loss of the axial ligand. Thus, the bands at 1881 cm^{-1} and 1900 cm^{-1} have been tentatively assigned to the likely solvated $[(T(p\text{-}OMe)PP^{\bullet})Ru(NO)]^{+}$ (Eq. 4.2a) and $[(T(p\text{-}OMe)PP^{\bullet})Ru(NO)]^{2+}$ (Eq. 4.3) species, respectively, while the band at 1918 cm^{-1} is believed to be the unstable $[(T^{\bullet})RuC_2OMe]^{2+}$ intermediate (Eq. 4.2b).

Extending these measurements to the first reduction (Figure 4.16c) by maintaining a potential of -1.55 V results in a shift of the ν_{NO} from 1852 cm^{-1} to 1824 cm^{-1} ($\Delta\nu_{NO}$ = -28 cm^{-1}). This is accompanied with a change of the $\nu_{C=O}$ at 1645 cm^{-1} to two new bands at 1681 cm^{-1} and 1723 cm^{-1}, and appearance of a new band at 1586 cm^{-1}. This small shift in ν_{NO} and possible peak enhancement at 1586 cm^{-1} suggests a porphyrin centered reduction to yield a $[TRuC_2OMe]^{-}$ complex (Eq. 4.4); however, this enhancement falls in the same region as published values for a reduction at the Ru-NO moiety (ν_{NO} = ~1575 cm^{-1}) and a ^{15}N-labelled experiment was performed to clarify (vide infra).[41-43]

Analysis of the IR-SEC results for $TRuC_2RuT$ (Figure 4.16, right) display qualitatively similar behavior to that of $TRuC_2OMe$. The first oxidation following an applied potential of +0.70 V (Figure 4.16d) yielded a shift of the ν_{NO} band at 1845 cm^{-1} to 1873 cm^{-1} ($\Delta\nu_{NO}$ = +28 cm^{-1}) along with a similar low intensity band shift of $\nu_{C=O}$ from 1641 cm^{-1} to 1660 cm^{-1} and a peak enhancement at 1600 cm^{-1}, consistent with a porphyrin-centered first oxidation. An attempt to capture the mixed valence state and final dicationic product separately was made by applying a potential range associated with the foot of each wave but no detectable change in ν_{NO} was observed. Since the $E^{\circ\prime}$ for the sequential oxidation features differ by only ~120 mV and the

applied potentials in these spectroelectrochemical experiments are held for a 1 m period, it indicates that once the two sequential 1-electron transfers take place to form $[(T^{\bullet})RuC_2Ru(T^{\bullet})]^{2+}$ at the electrode surface, comproportionation with starting material from the bulk solution results in an increased amount of $[(T^{\bullet})RuC_2Ru(T)]^{+}$. This conclusion is supported by the band at 1873 cm^{-1} in the dimetallic complex that matches the first oxidation product for $TRuC_2OMe$. When the potential is increased to +1.15 V (sufficiently past the second oxidation feature) two new bands appear at 1877 cm^{-1} and 1894 cm^{-1} with a shoulder at 1918 cm^{-1} (Figure 4.16e). A slight shift of ν_{NO} from 1873 cm^{-1} (first oxidation) to 1877 cm^{-1} (second oxidation) may imply that the dicationic product is present in higher concentrations away from the electrode under these conditions. However, it is likely that the expected $[(T(p\text{-OMe})PP)Ru(NO)]^{+}$ species ($TRuC_2OMe$: ν_{NO} = 1881 cm^{-1}) enroute to $[(T(p\text{-OMe})PP)Ru(NO)]^{2+}$ is overlapped by neighboring bands of other anodic products generated at this potential. The bands at 1894 cm^{-1} and 1918 cm^{-1}, like those of the ester derivative, correspond to the formation of $[(T(p\text{-OMe})PP)Ru(NO)]^{2+}$ and the tentatively assigned $[TRuC_2RuT]^{4+}$ complex, respectively. Loss of the low intensity $\nu_{C=O}$ band at 1641 cm^{-1} is in line with slow dissociation of the coordinated carboxylate ligand but it is unclear whether the bridging dicarboxylate dissociates from one coordination site at a time or simultaneously. A similar peak enhancement observed in the first oxidation is present during the second oxidation at 1596 cm^{-1}. The electrochemically generated products formed at an applied potential of -1.65 V display a new ν_{NO} band at 1824 cm^{-1} that is accompanied with the appearance of a band at 1570 cm^{-1} (Figure 4.16f). This behavior is similar to that observed in the monometallic ester derivative, for which I have assigned as a porphyrin-centered reduction.

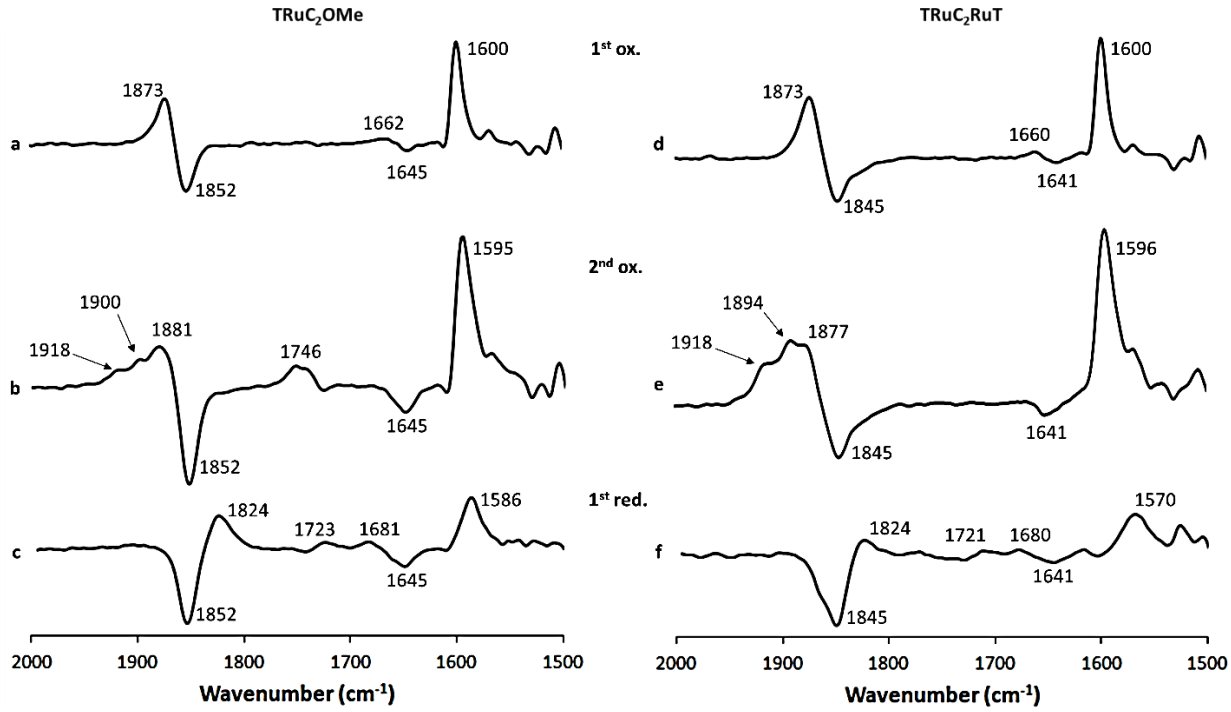

Figure 4.16 Difference IR spectra showing the products from the (a,d) first oxidation, (b,e) second oxidation and (c,f) first reduction features of (a-c) $TRuC_2OMe$ and (d-f) $TRuC_2RuT$ in CH_2Cl_2 containing 0.1 M NBu_4PF_6, with the potential held at (a) +0.65, (b) +1.10 and (c) -1.55 V; (d) +0.70 V, (e) +1.15 V and (f) -1.65 V vs the $Fc^{0/+}$ couple.

The IR-SEC results obtained for $TRuC_4OMe$ and $TRuC_4RuT$ were not unlike those for the succinate species mentioned above. Figure 4.17a shows the difference IR spectrum for the product formed during the first oxidation of $TRuC_4OMe$, which displayed the consumption of the initial ν_{NO} at 1851 cm^{-1} and appearance of the new ν_{NO} at 1872 cm^{-1} ($\Delta\nu_{NO}$ = +21 cm^{-1}) after the analyte was held at a potential of +0.65 V. The low intensity bands assigned to the $\nu_{C=O}$ of the carboxylate ligand shift from 1645 cm^{-1} to 1662 cm^{-1}, while a simultaneous peak enhancement at 1599 cm^{-1} takes place. Similar to the succinate complex, these shifts has been assigned to a porphyrin-centered first oxidation resulting in the formation of $[(T^{\bullet})RuC_4OMe]^+$. Increasing the potential to +1.10 V, in Figure 4.17b, leads to the loss of the initial ν_{NO} at 1851 cm^{-1} and occurs with concomitant appearance of ν_{NO} = 1881 cm^{-1} with added low intensity

bands at 1899 cm^{-1} and 1918 cm^{-1}. Given the similarity of these bands to the $TRuC_2OMe$ derivatives, the products formed at the second oxidation are assigned to $[(T(p\text{-}OMe^{\bullet})PP)Ru(NO)]^{+/2+}$ and $[(T^{\bullet})RuC_4OMe]^{2+}$, respectively. The peak enhancement and low intensity $\nu_{C=O}$ observed at the first oxidation are present during the second oxidation with increased intensity, along with a new small band at 1746 cm^{-1}. Holding the potential at -1.65 V to capture the electrochemically generated reduction product (Figure 4.17c) resulted in a shift of the ν_{NO} from 1851 cm^{-1} to 1823 cm^{-1} ($\Delta\nu_{NO}$ = -28 cm^{-1}), loss of the $\nu_{C=O}$, and appearance of a new band at 1576 cm^{-1}, changes which have been tentatively assigned to formation of $[TRuC_4OMe]^{-}$.

Repeating this study for the $TRuC_4RuT$ derivative resulted in comparable redox behavior to the previously discussed dimetallic succinate derivative. Specifically, oxidation at a potential just past the two sequential 1-electron transfer (+0.65 V) yields a shift of the ν_{NO} band from 1847 cm^{-1} to 1872 cm^{-1} ($\Delta\nu_{NO}$ = +24 cm^{-1}), along with the low intensity band shift of $\nu_{C=O}$ from 1638 cm^{-1} to 1659 cm^{-1} and peak enhancement at 1598 cm^{-1} (Figure 4.17d). Similar to the $TRuC_2RuT$ compound, two sequential 1-electron transfers and subsequent comproportionation with $TRuC_4RuT$ from the bulk solution results in the formation of $[(T^{\bullet})RuC_4Ru(T)]^{+}$. Maintaining a potential of +1.15 V leads to the production of a new ν_{NO} band at 1877 cm^{-1} with low intensity shoulders around 1897 cm^{-1} and 1917 cm^{-1} (Figure 4.17e). A loss of the low intensity $\nu_{C=O}$ at 1638 cm^{-1} takes place along with a slight shift to the previously observed peak enhancement to 1595 cm^{-1}. Oxidation at this higher potential likely results in the formation of the $[(T(p\text{-}OMe)PP)Ru(NO)]^{2+}$ product (ν_{NO} = 1897 cm^{-1}) and the $[(T^{\bullet})RuC_4Ru(T^{\bullet})]^{2+}$ (ν_{NO} = 1877 cm^{-1}) and $[TRuC_4RuT]^{4+}$ (ν_{NO} = 1917 cm^{-1}) complexes. Probing the reductions after the potential is held at -1.70 V resulted in a new ν_{NO} band at 1824 cm^{-1} accompanied by the appearance of a band at 1572 cm^{-1} (Figure 4.17f) that is expected to result from porphyrin-centered reduction.

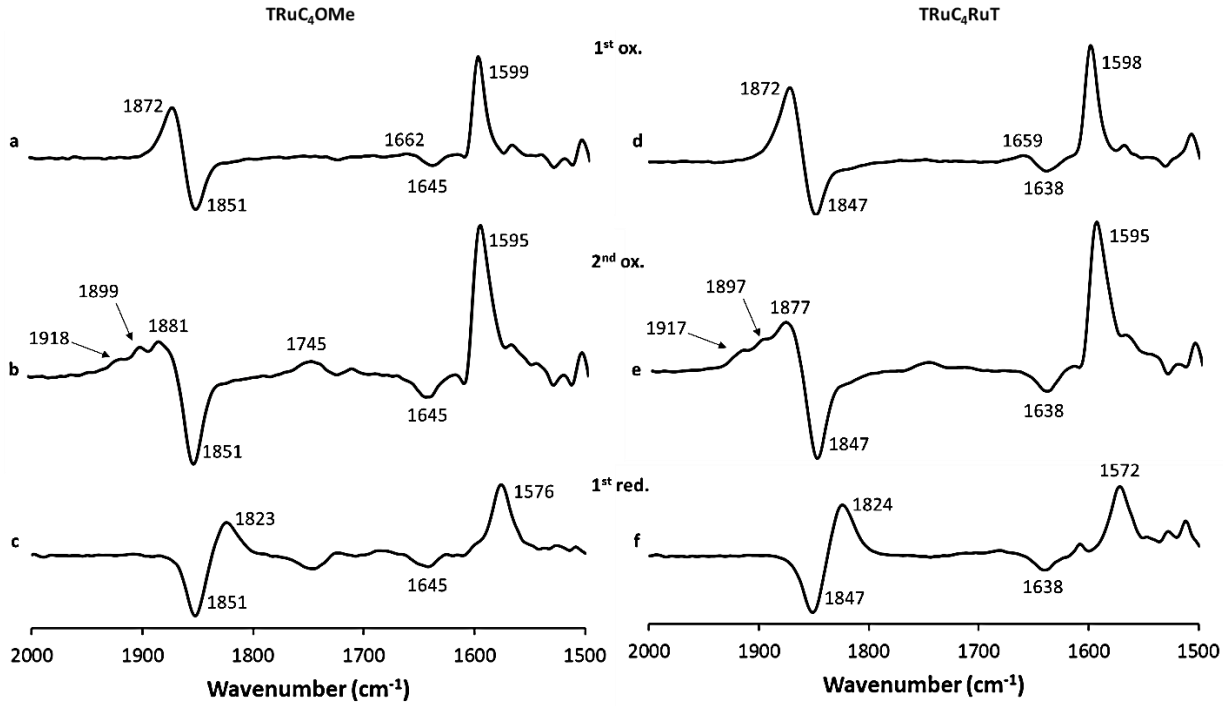

Figure 4.17 Difference IR spectra showing the products from the (a,d) first oxidation, (b,e) second oxidation and (c,f) first reduction features of (a-c) $TRuC_4OMe$ and (d-f) $TRuC_4RuT$ in CH_2Cl_2 containing 0.1 M NBu_4PF_6, with the potential held at (a) +0.65, (b) +1.10 and (c) -1.65 V; (d) +0.65 V, (e) +1.15 V and (f) -1.70 V vs the $Fc^{0/+}$ couple.

Figure 4.18 details the IR-SEC results of $TRuC_6OMe$ and $TRuC_6RuT$, which closely resemble that of the succinate and adipate complexes discussed earlier. A difference IR spectrum for the first oxidation of $TRuC_6OMe$ (Figure 4.18a) shows the consumption of the starting ν_{NO} at 1850 cm^{-1} and the formation of a new ν_{NO} band at 1872 cm^{-1} ($\Delta\nu_{NO}$ = +22 cm^{-1}) following an applied potential of +0.60 V. The low intensity $\nu_{C=O}$ of the carboxylate ligand present at 1642 cm^{-1} shifts to 1662 cm^{-1} along with an enhancement at 1598 cm^{-1}, which is in good agreement with the succinate and adipate analogues to yield $[(T^{\bullet})RuC_6OMe]^+$. Figure 4.18b demonstrates the loss of the initial ν_{NO} at 1850 cm^{-1} with concomitant appearance of the ν_{NO} at 1876 cm^{-1} upon raising the potential to +1.10 V as well as low intensity bands at 1898 cm^{-1} and 1920 cm^{-1}. The peak enhancement and loss of $\nu_{C=O}$ observed in the first oxidation take place during the second

oxidation with a new weak band at 1745 cm^{-1}. This result matches closely with what was observed in the second oxidation products formed for the $TRuC_2OMe$ and $TRuC_4OMe$ compounds, namely, the formation of $[(T(p\text{-}OMe)PP)Ru(NO)]^{+/2+}$ and $[TRuC_6OMe]^{2+}$. Holding the potential at -1.75 V (capturing the first reduction) yields a ν_{NO} shift from 1850 cm^{-1} to 1823 cm^{-1} ($\Delta\nu_{NO}$ = -27 cm^{-1}), accompanied by a new band at 1573 cm^{-1} and the consumption of $\nu_{C=O}$ at 1642 cm^{-1} (Figure 4.18c), corresponding to the $[TRuC_6OMe]^-$ complex.

The spectrochemical results for $TRuC_6RuT$ in Figure 4.18d illustrate the electrochemically generated products during the first oxidation after an applied potential of +0.65 V., and do not differ significantly from what was observed for the $TRuC_2RuT$ and $TRuC_4RuT$ derivatives. Namely, a change in the ν_{NO} band from 1849 cm^{-1} to 1871 cm^{-1} ($\Delta\nu_{NO}$ = +22 cm^{-1}), accompanied by a shift of the low intensity $\nu_{C=O}$ from 1642 cm^{-1} to 1660 cm^{-1} and peak enhancement at 1598 cm^{-1}. After the potential is increased to +1.15 V a new band at 1875 cm^{-1} with low intensity bands around 1896 cm^{-1} and 1914 cm^{-1} are observed (Figure 4.18e). These results match those observed for the symmetric succinate and adipate analogues. In addition to these new bands, the loss of the low intensity $\nu_{C=O}$ at 1642 cm^{-1} takes place, as well as a slight shift to the previous peak enhancement to 1595 cm^{-1}. Maintaining an applied at -1.65 V resulted in a shift of the ν_{NO} from 1849 cm^{-1} to 1823 cm^{-1} along with a new band at 1572 cm^{-1} (Figure 4.18f), which also support a porphyrin-centered reduction.

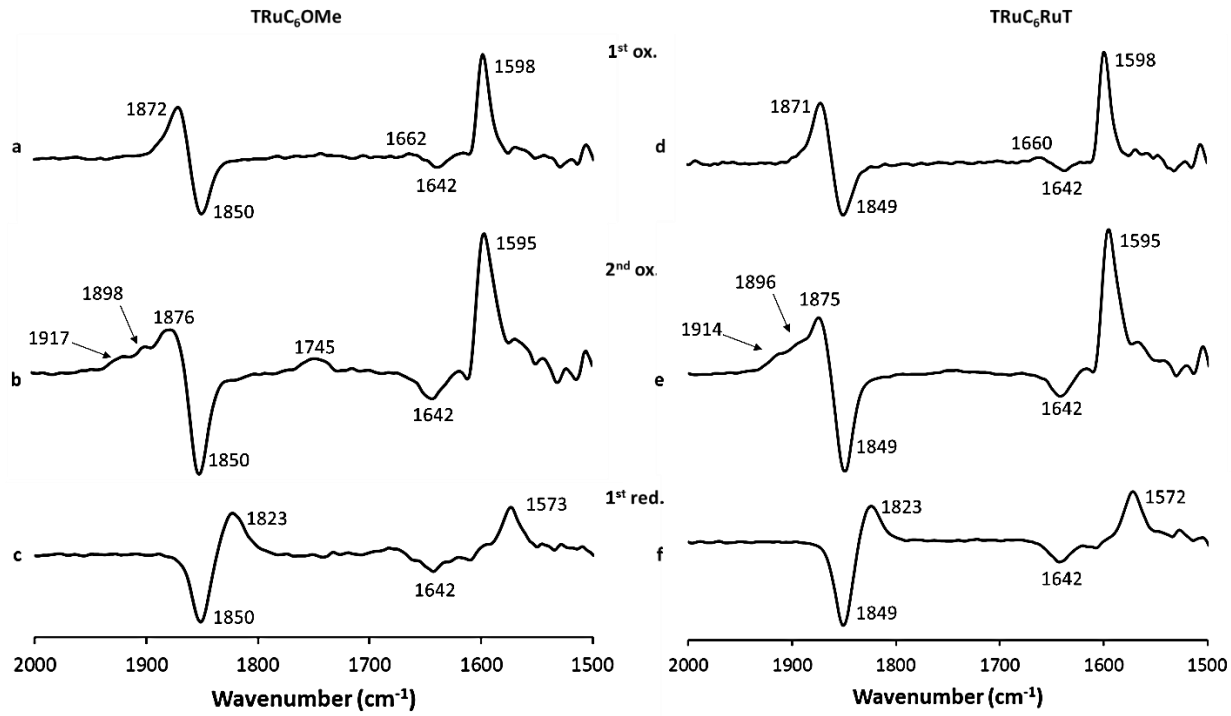

Figure 4.18 Difference IR spectra showing the products from the (a,d) first oxidation, (b,e) second oxidation and (c,f) first reduction features of (a-c) $TRuC_6OMe$ and (d-f) $TRuC_6RuT$ in CH_2Cl_2 containing 0.1 M NBu_4PF_6, with the potential held at (a) +0.60, (b) +1.10 and (c) -1.75 V; (d) +0.65 V, (e) +1.15 V and (f) -1.65 V vs the $Fc^{0/+}$ couple.

Table 4.5 IR nitrosyl stretching frequencies for the neutral precursors and the electrochemically generated oxidation and reduction products of the monometallic ester and dimetallic complexes.[a]

	Neutral	**1st ox[b]**	**2nd ox[b]**	**1st red[b]**
$PRuC_2OMe$	1854	1875	1882, 1900, 1922	1824
$PRuC_4OMe$	1852	1875	1884, 1903, 1922	1824
$PRuC_6OMe$	1853	1874	1883, 1902, 1920	1825
$TRuC_2OMe$	1852	1873	1881, 1900, 1918	1824
$TRuC_4OMe$	1851	1872	1881, 1899, 1918	1823
$TRuC_6OMe$	1850	1872	1876, 1898, 1917	1823
$TRuC_2RuT$	1845	1873	1877, 1894, 1918	1824
$TRuC_4RuT$	1847	1872	1877, 1897, 1917	1824
$TRuC_6RuT$	1849	1871	1875, 1896, 1914	1823

[a] Experimental conditions: 1.0 mM analyte in CH_2Cl_2 containing 0.1 M NBu_4PF_6 with a Pt working electrode.

[b] 1st ox. indicates IR bands observed when electrode potential set ~100 mV positive of the $E^{\circ\prime}$ for the two sequential 1-electron features in the CV, 2nd ox. Recorded ~50 mV positive of the E_{pa} for the second ox. feature in the CV, and 1st red. recorded ~50 mV negative of the E_{pc} for the 1st red. feature in the CV.

Investigation into the reductions for these complexes led to the necessity of a control experiment to determine the initial site of electron transfer during the cathodic process. In order to rule out the possibility of multiple reduction sites, an ^{15}NO-labelled analogue of TRuC$_2$OMe was prepared and the IR spectroelectrochemical experiment was repeated. The resulting difference spectra of the reduction product formed can be seen in Figure 4.19 when an applied potential of -1.60 V was held. A loss of the initial ν_{NO} at 1815 cm^{-1} was detected with the simultaneous appearance of a new ν_{NO} band at 1787 cm^{-1} ($\Delta\nu_{NO}$ = -28 cm^{-1}). At significantly lower frequencies a new band can be seen (1585 cm^{-1}) that is near the region where the peak enhancements corresponding to the tetraaryl porphyrin macrocycle were observed (1590-1600 cm^{-1}) in the oxidations. The observation of a relatively unshifted band at 1586 cm^{-1} (Figure 4.16c) confirms it does not arise from a vibration that involves the Ru-^{15}NO fragment. This minimal shift to ν_{NO} and accompanied band enhancement associated with the porphyrin macrocycle implies a porphyrin-centered reduction on the timescale of the spectroelectrochemical experiments. Additionally, the $\nu_{C=O}$ bands associated with the carboxylate ligand appear to shift slightly from 1649 cm^{-1} to 1681 cm^{-1} and 1723 cm^{-1} once the potential is applied, as was observed in the unlabeled carboxylate complexes.

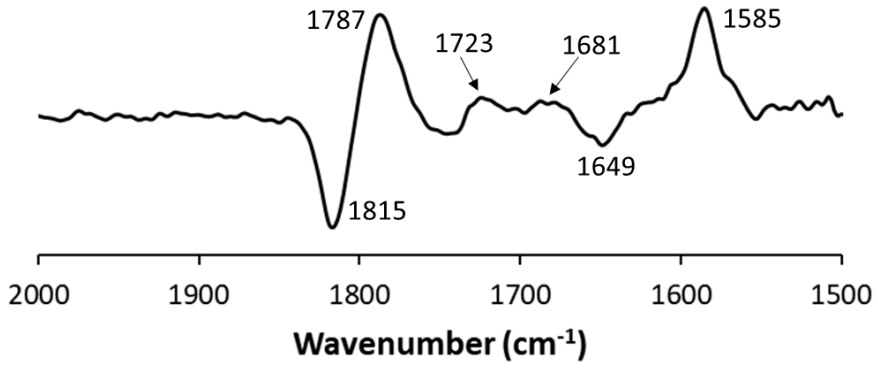

Figure 4.19 Difference IR spectra showing the products from the first reduction of the ^{15}NO-labeled analogue of TRuC$_2$OMe in CH_2Cl_2 containing 0.1 M NBu_4PF_6, with the potential held at -1.60 V vs the $Fc^{0/+}$ couple.

4.3.4. Computational consideration

As a complementary study to the redox behavior observed during the electrochemical and spectroelectrochemical experiments, DFT calculations were employed using a (porphine)Ru(NO)(OC(=O)$(CH_2)_2$C(=O)OMe) complex in the ground state; a simplified analogue of $TRuC_2OMe$. Comparing the experimentally obtained structural data from compounds $PRuC_2OH$ and $TRuC_2OMe$ to the optimized geometry of the porphine complex (< 3% error) is listed in Table 4.6, including a vibrational frequency analysis. These preliminary calculations were employed using the ωB97XD functional and DGDZVP basis set in the gas phase. From the optimized geometry of this complex, electron density maps of the frontier molecular orbitals were calculated. As seen in Figure 4.20a the sole contribution of electron density in the HOMO of (porphine)Ru(NO)(OC(=O)$(CH_2)_2$C(=O)OMe) is attributed to the porphyrin macrocycle, while in the LUMO the concentration is split between the Ru-NO and porphyrin fragments (Figure 4.20b). These computational results support the proposed porphyrin-centered first oxidation and reduction.

Table 4.6 Experimental structure and spectroscopic values vs calculated parameters of the (porphine)Ru(NO)(OC(=O)$(CH_2)_2$C(=O)OMe) optimized geometries using the ωB97XD functional and DGDZVP basis set.

	Ru-N(O) (Å)	**∠RuNO (°)**	**Ru-O(C) (Å)**	**ν_{NO} (cm^{-1})**	**$\nu_{C=O}$ (cm^{-1})**
$PRuC_2OH$	1.7401(19)	173.89(18)	2.0131(15)	1850	1640, 1712
$TRuC_2OMe$	1.716(5)	179.2(5)	2.002(4)	1840	1657, 1735
Calculated	1.752	177.668	2.028	1847.94[a]	1619.40, 1680.16[a]

[a] 0.91 scaling factor

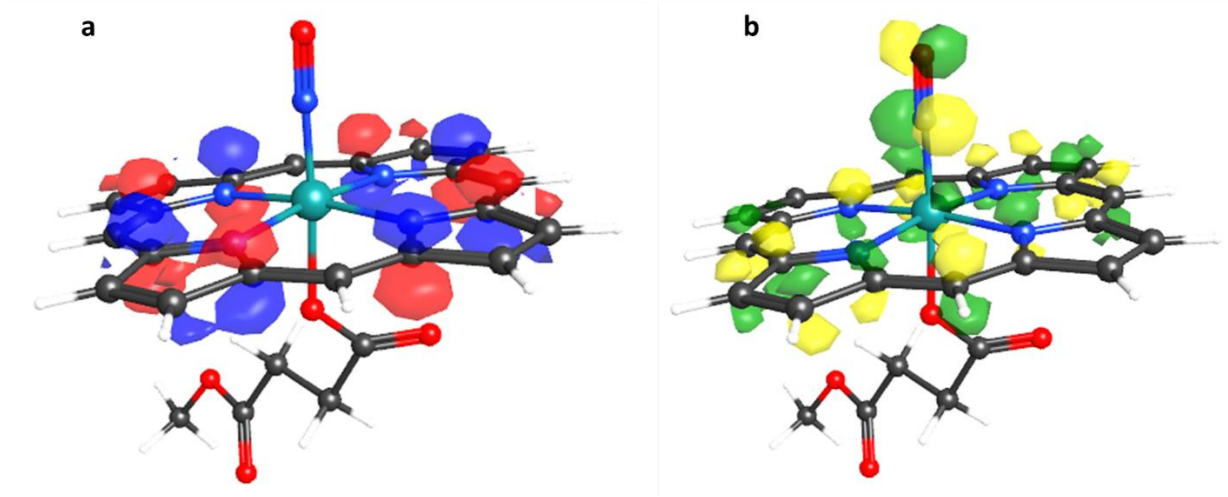

Figure 4.20 Calculated frontier molecular orbitals (a: HOMO; b: LUMO) from the optimized geometries of the (porphine)Ru(NO)(OC(=O)$(CH_2)_2$C(=O)OMe) complex.

4.3.5. Chemical oxidation: IR spectroscopy of (T(*p*-OMe)PP)Ru(NO)(FPF_5)

In an effort to further elucidate the proposed mechanism of the first oxidation as explored by cyclic voltammetry, IR spectroelectrochemistry and preliminary DFT results, a chemical oxidation was performed on the dimetallic compound TRuC$_2$RuT using $AgPF_6$ (~1 equiv. per Ru) as the oxidant in CH_2Cl_2. Choice of oxidizing agent was made based on published redox potential values for chemical reagents in similar solvent and supporting electrolyte systems used in the electrochemical experiments that closely match those of the dimetallic compound.[44] The comparison of IR spectra before and after chemical oxidation (Figure 4.21) reveals the disappearance of the $\nu_{C=O}$ band previously at 1661 cm^{-1}, along with a ν_{NO} shift from 1831 cm^{-1} for the initial dimetallic complex to 1870 cm^{-1} ($\Delta\nu_{NO}$ = +39 cm^{-1}). Additional bands were observed at 730 cm^{-1} and 867 cm^{-1} that match closely to a weakly coordinated $^{-}FPF_5$ ligand to form the (T(*p*-OMe)PP)Ru(NO)(FPF_5) product obtained in 78% yield (per Ru).[45,46] This result, in conjunction with the electrochemical and computational works, suggest the proposed

porphyrin-centered first oxidation ultimately leads to dissociation of the bridging dicarboxylate ligand (on a timescale exceeding that of the spectroelectrochemical experiments).

Figure 4.21 Truncated IR spectra of the compound $TRuC_2RuT$ (a) before and (b) after chemical oxidation with a slight excess of $AgPF_6$ (~1 equiv. per Ru), highlighting the ν_{PF} signals at 730 cm^{-1} and 867 cm^{-1}.

4.3.6. Chemical reduction: IR and ^{1}H NMR spectroscopy of product mixture

Similar to the utilization of chemical oxidation, a chemical reduction of the $TRuC_2RuT$ complex using Cp^*_2Co as the reductant (chosen from reported chemical redox agents in similar systems)[43] was also performed to substantiate the mechanism proposed from results obtained during the cathodic investigation of this compound. Figure 4.22 details a comparison of the IR spectra before the chemical reduction and following isolation of the product. Again, the $\nu_{C=O}$ band at 1661 cm^{-1} associated with the bridging dicarboxylate ligand disappears in the product obtained in ~50% yield. However, a small additional feature appears around 1726 cm^{-1} that is in the approximate region of an uncoordinated carboxylate.[46] A shift of the ν_{NO} from 1831 cm^{-1} to a slightly lower frequency at 1815 cm^{-1} ($\Delta\nu_{NO}$ = -16 cm^{-1}) is detected as well and matches

published values for (por)Ru(NO)(OH) complexes.[47-49] Coordination of hydroxide is likely the result of being exposed to adventitious air during attempts to crystallize the product following reduction.

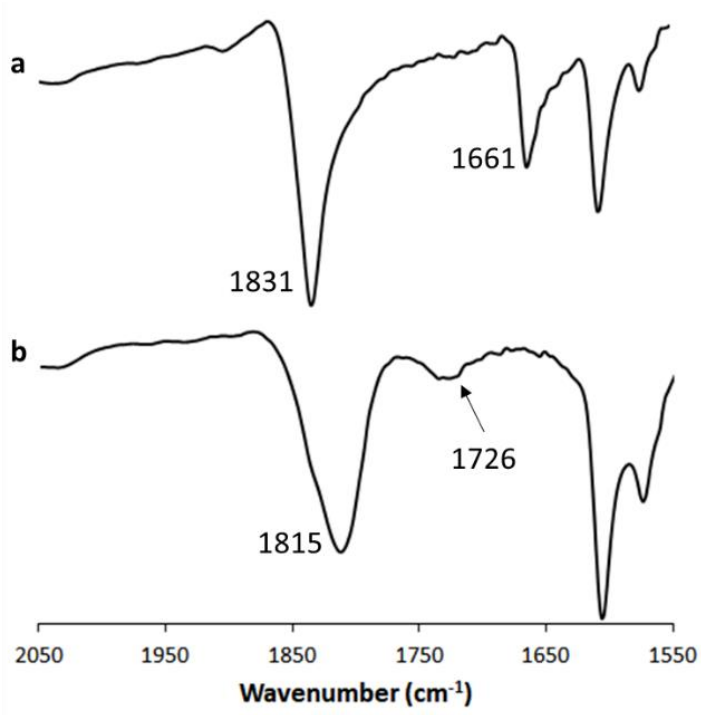

Figure 4.22 IR spectra of compound $TRuC_2RuT$ (a) before and (b) after chemical reduction with Cp^*_2Co, highlighting the $\nu_{C=O}$ bands at 1661 cm^{-1} and 1726 cm^{-1}.

The ^1H NMR spectrum of the isolated reduction product (Figure 4.23) shows the loss of the characteristic signal for the alkyl chain between the bridging dicarboxylate ligand, previously observed to be a singlet at δ -3.86 ppm. Peaks corresponding to the pyrrole- and tetraaryl-H's of the T(*p*-OMe)PP macrocycle in a region consistent with both the nitrosyl hydroxo precursor prepared in this work and literature values for other porphyrin derivatives.[47-49] Specifically, a noticeable shift of the pyrrole-H peak from δ 8.69 ppm to 8.98 ppm (Δδ = +0.29 ppm) and rearrangement of the doublet of doublets that arose from the restricted rotation of the tetraaryl-H's in the initial dimetallic complex. A new signal was detected in the reduction product at δ

2.54 ppm, in good agreement with the known chemical shift for free succinic acid,[46] and an integration ratio of 1:6 vs the -OMe of the porphyrin. The additional δ 1.79 ppm peak matches published pentamethyl-H values of the spent reductant Cp^*_2Co,[50] however, since this reagent was added in excess it is likely various cobaltocenium salts form, including the $[Cp^*_2Co]_2[OC(=O)(CH_2)_2C(=O)O']$ complex. Similar to what was observed in the chemical oxidation, dissociation of the bridging dicarboxylate takes place following an initial porphyrin-centered reduction.

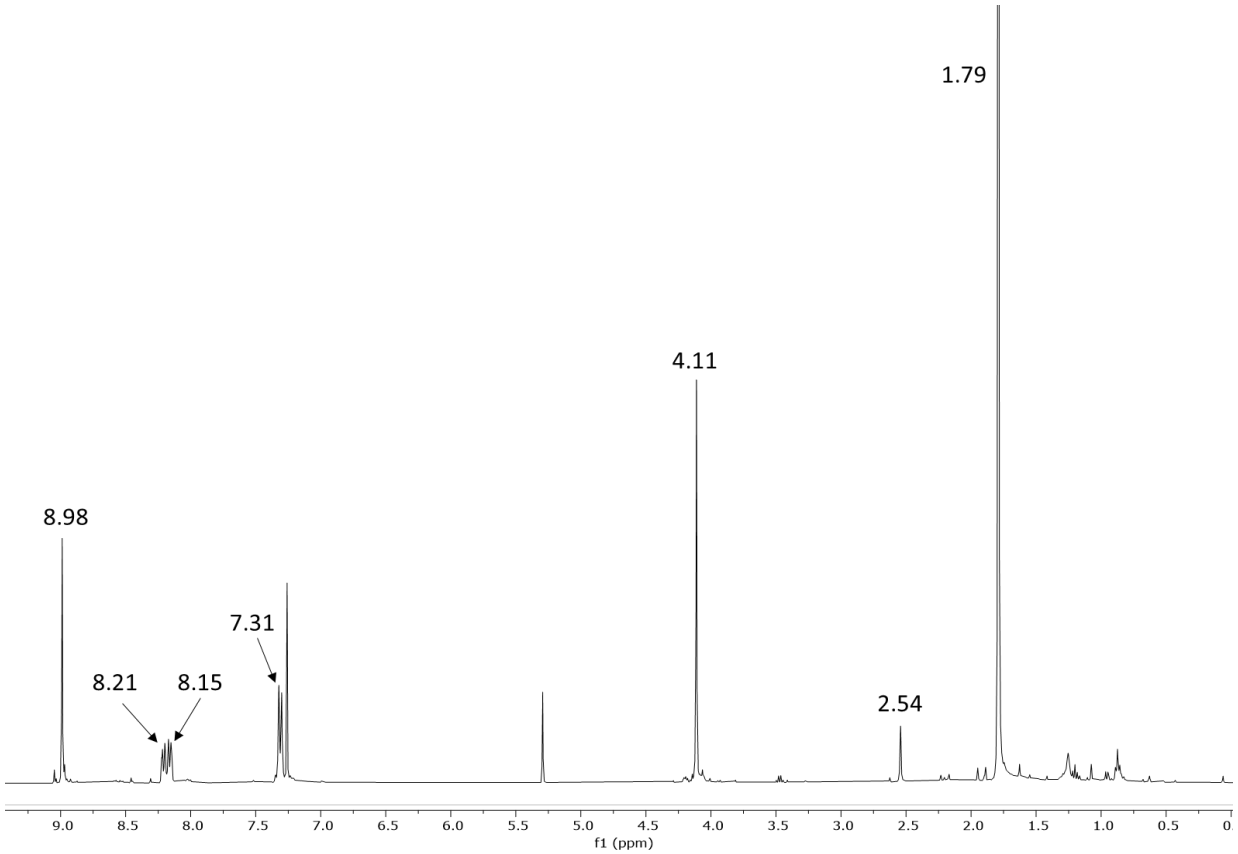

Figure 4.23 ^{1}H NMR spectrum of compound $TRuC_2RuT$ in $CDCl_3$ after chemical reduction with Cp^*_2Co.

4.4. Summary and Conclusions

In summary, a synthetic approach to the monometallic carboxylate complexes of ruthenium nitrosyl porphyrins and their respective symmetric dimetallic derivatives, along with the spectroscopic properties and redox behavior is reported. The IR spectra of the monometallic compounds has shown that with an increasing chain length of the axial carboxylate ligand resulted in a shift of the ν_{NO} to lower frequencies. This shift is due to the cumulative electron density present of the longer alkyl chains that increase the donor ability of the carboxylate ligand to the Ru-NO moiety. However, the opposing trend is observed for the dimetallic systems owed to weak electronic communication between the porphyrin macrocycles that begins to diminish as the bridging alkyl chain length increases. ^{1}H NMR spectral data revealed that the target compounds demonstrate a simple AB splitting pattern, with the exception of the monometallic succinic acid derivatives (AA′BB′), for the methylene protons in the carboxylate alkyl chain, as confirmed by simulated spectra. A similar complex spin system leading to unique splitting patterns was observed for the restricted rotation of tetraaryl substituents present in the T(*p*-OMe)PP macrocycle between the monometallic acid/ester and dimetallic complexes. Additionally, an enhanced ring effect is present in the dimetallic species that results in noticeable upfield shifts to the pyrrole-H signals and downfield shifts to the -CH_2- signals, which lessens as the distance between the metalloporphyrins increases. In the case of the insoluble PRuC_nRuP compounds, elemental analysis in conjunction with IR data aided in characterization. Attempts to isolate a spectroscopically pure sample of the symmetric TRuC_0RuT compound proved unsuccessful but did result in the apparent splitting of oxalic acid to generate (T(*p*-OMe)PP)Ru(CO), which is the first example of the conversion from a dicarboxylic acid to form a metal carbonyl. Similarly, any efforts to separate the unsymmetric mixed porphyrin TRuC_2RuE

and heterobimetallic $TRuC_2OsT$ complexes from their respective reaction mixtures led to decomposition. However, tracking the reaction progress of the unsymmetric species via ^1H NMR spectroscopy suggests the desired compounds were formed.

The redox behavior of the monometallic and dimetallic compounds exhibited an expected trend for the more electron donating components in these studies (e.g., T(*p*-OMe)PP > TPP and $C_6 > C_2$), which yield slightly lower oxidation (E_{pa}) and higher reduction (E_{pc}) potentials. These complexes appear to undergo very similar redox mechanisms and begin with a 1-electron porphyrin-centered first oxidation. In the dimetallic derivatives this first oxidation exhibits two sequential 1-electron transfers that forms a mixed valence state $[(T^{\bullet})RuC_nRuT]^+ \leftrightarrow [TRuC_nRu(T^{\bullet})]^+$ enroute to $[(T^{\bullet})RuC_nRuT(T^{\bullet})]^{2+}$, as demonstrated by the large peak potential differences and current response. DFT calculations for the frontier molecular orbitals of the (porphine)Ru(NO)(OC(=O)$(CH_2)_2$C(=O)OMe) complex support this notion of a porphyrin-centered electrochemical step. A chemical oxidation of the $TRuC_2RuT$ compound with $AgPF_6$ resulted in slow loss of the carboxylate ligand to yield a (T(*p*-OMe)PP)Ru(NO)(FPF_5) product. Following a slightly more complex second oxidation the proposed $[(por)Ru(NO)]^{+/2+}$ and $[TRuC_nOMe]^{2+}$ (dimetallic: $[TRuC_nRuT]^{4+}$) were suggested by IR spectroelectrochemistry. Probing the cathodic behavior, in particular the utilization of an ^{15}NO-labelled analogue, resulted in the confirmation of a porphyrin-centered reduction, as supported by the DFT results. Similar to the chemical oxidation, a chemical reduction of $TRuC_2RuT$ using Cp^*_2Co yielded slow dissociation of the carboxylate ligand to form the nitrosyl hydroxo complex upon exposure to adventitious air. This study offers insight into the effect that the bridging length of the dimetallic heme models complexes has on the redox behavior in comparison to the monometallic analogues.

4.5. References

1. Awasabisah, D.; Xu, N.; Sharmah Gutman, K. P.; Powell, D. R.; Shaw, M. J.; Richter-Addo, G. B. *Eur. J. Inorg.* **2016**, *19*, 509-518.

2. Awasabisah, D.; Xu, N.; Sharmah Gautam, K. P.; Powell, D. R.; Shaw, M. J.; Richter-Addo, G. B. *Dalton Trans*. **2013**, *42*, 8537-8540.

3. Reid, T. J.; Murthy, M. R. N.; Sicignano, A.; Tanaka, N.; Musick, W. D. L.; Rossmann, M. G. *Proc. Natl. Acad. Sci*. **1981**, *78*, 4767-4771.

4. Ko, T. P.; Day, J.; Malkin, A. J.; McPherson, A. *Acta Cryst*. **1999**, *D55*, 1383–1394.

5. G. C. Brown, *Eur. J. Biochem.* **1995**, *232*, 188-191.

6. Lee, J.; Yi, G.-B.; Khan, M. A.; Richter-Addo, G. B. *Inorg. Chem*. **1999**, *38*, 4578-4584.

7. Cheng, L.; Chen, L.; Chung, H.-S.; Khan, M. A.; Richter-Addo, G. B. *Organometallics.* **1998**, *17*, 3853-3864.

8. Muraoka, H.; Watanabe, Y.; Takahashi, A.; Kamoto, H.; Ogawa, S. *Heteroatom Chem.* **2014**, *25*, 473-481.

9. Morrison, W. H.; Krogsrug, S.; Hendrickson, D. N. *Inorg. Chem.* **1973**, *12*, 1998-2003.

10. Nishihara, H. *Adv. Inorg. Chem.* **2002**, *53*, 41-86.

11. Brown, G. B.; Meyer, T. J.; Cowan, D. O.; Levanda, C.; Kaufman, F.; Roling, P. V.; Rausch, M. D. *Inorg. Chem.*, **1975**, *14*, 506-512.

12. Levanda, C.; Bechgaard, K.; Cowan, D. O. *J. Org. Chem*. **1976**, *41*, 2700-2704.

13. Kadish, K. M.; Xu, Q. Y. *Inorg. Chem.* **1987**, *26*, 2566-2568.

14. Chen, W.-Z.; Protasiewicz, J. D.; Davis, S. A.; Updegraff, J. B.; Ma, L.-Q.; Fanwick, P. E.; Ren, T. *Inorg. Chem*. **2007**, *46*, 3775-3782.

15. Steed, J. W.; Tocher, D. A. *Polyhedron*. **1992**, *11*, 1849-1854.

16. Sbrana, G.; Braca, G.; Giannetti, E. *J.C.S. Dalton Trans*. **1976**, 1847-1852.

17. Lin, Y. H.; Duclaux, L.; Gonzàlez de Rivera, F.; Thompson, A. L.; Wilton-Ely, J. *Eur. J. Inorg. Chem.* **2014**, 2065–2072.

18. Armstrong, J. E.; Robinson, W. R.; Walton, R. A. *Inorg. Chem*. **1983**, *22*, 1301-1306.

19. Kopel, P.; Sindelar, Z.; Klicka, R. *Transition Met. Chem*. **1998**, *23*, 139-142.

20. Smekal, Z.; Brezina, F.; Sindelar, Z.; Klicka, R. *Polyhedron.* **1996**, *15*, 971-974.

21. Thomas, V. P.; Benedix, M.; Hennig, H. *Z. Anorg. Allg. Chem*. **1980**, *468*, 213-220.

22. Rummelt, S. M.; Zhong, H.; Korobkov, I.; Chirik, P. J. *J. Am. Chem. Soc*. **2018**, *140*, 11589-11593.

23. Chu, Q.; Zhang, M.; Ding, C. *Asian J. Chem.* **2010**, *22*, 893-901.

24. Connelly, N. G.; Draggett, P. T.; Green, M.; Kuc, T. A. *J.C.S. Dalton Trans.* **1977**, *1*, 70-73.

25. Miranda, K. M.; Bu, X.; Lorkovic´, I.; Ford, P .C. *Inorg. Chem.* **1997,** *36*, 4838-4848.

26. Lorkovic, I. M.; Ford, P. C. *Inorg. Chem.* **1999,** *38*, 1467-1473.

27. Slebodnick, C.; Seok, W. K.; Kim, K. M.; Ibers, J. A. *Inorg. Chim. Acta.* **1996**, *243*, 57-65.

28. Imbeaux, J. C.; Saveant, J. M. *J. Electroanal. Chem. Interf. Electrochem.* **1973**, *44*, 169-187.

29. Dalrymple-Alford, P.; Goto, M.; Oldham, K. B. *J. Electroanal. Chem*. **1977**, *85*, 1-15.

30. Rahman, M. H.; Atifi, A.; Rosenthal, J.; Ryan, M. D. *Inorg. Chem.* **2021**, *60*, 10631-10641.

31. Frisch, M. J.; Trucks, G. W.; Schlegel, H. B.; Scuseria, G. E.; Robb, M. A.; Cheeseman, J. R.; Scalmani, G.; Barone, V.; Mennucci, B.; Petersson, G. A.; Nakatsuji, H.; Caricato, M.; Li, X.; Hratchian, H. P.; Izmaylov, A. F.; Bloino, J.; Zheng, G.; Sonnenberg, J. L.; Hada, M.; Ehara, M.; Toyota, K.; Fukuda, R.; Hasegawa, J.; Ishida, M.; Nakajima, T.; Honda, Y.; Kitao, O.; Nakai, H.; Vreven, T.; Montgomery Jr., J. A.; Peralta, J. E.; Ogliaro, F.; Bearpark, M. J.; Heyd, J.; Brothers, E. N.; Kudin, K. N.; Staroverov, V. N.; Kobayashi, R.; Normand, J.; Raghavachari, K.; Rendell, A. P.; Burant, J. C.; Iyengar, S. S.; Tomasi, J.; Cossi, M.; Rega, N.; Millam, N. J.; Klene, M.; Knox, J. E.; Cross, J. B.; Bakken, V.; Adamo, C.; Jaramillo, J.; Gomperts, R.; Stratmann, R. E.; Yazyev, O.; Austin, A. J.; Cammi, R.; Pomelli, C.; Ochterski, J. W.; Martin, R. L.; Morokuma, K.; Zakrzewski, V. G.; Voth, G. A.; Salvador, P.; Dannenberg, J. J.; Dapprich, S.; Daniels, A. D.; Farkas, Ö.; Foresman, J. B.; Ortiz, J. V.; Cioslowski, J.; Fox, D. J.; Gaussian, Inc.: Wallingford, CT, USA, 2009.

32. Bruno, G.; Schiavo, S. L.; Piraino, P.; Faraone, F. *Organometallics*. **1985**, *4*, 1098-1100.

33. Bauer, H.; Nagel, U.; Beck, W. *J. Organomet. Chem*. **1985**, *290*, 219-229.

34. Benvenuto, M. A.; Sabat, M.; Grimes, R. N. *Inorg. Chem*. **1992**, *31*, 3904-3909.

35. Dean, J. A. *Handbook of Organic Chemistry*. McGraw-Hill Book Co., 1987; New York, NY, pp 8-50.

36. Eaton, S. S. and Eaton, G. R. *J. Am. Chem. Soc.* **1977**, *99*, 6594-6599.

37. Eaton, S. S. and Eaton, G. R. *J. Am. Chem. Soc.* **1974**, *97*, 3660-3666.

38. Bard, A. J.; Faulkner, L. R. *Electrochemical Methods: Fundamentals and Applications*, 2nd ed.; John Wiley and Sons, 1980; New York, NY, pp 475-507.

39. Elgrishi, N.; Rountree, K. J.; McCarthy, B. D.; Rountree, E. S.; Eisenhart, T. T.; Dempsey, J. L. *J. Chem. Educ.* **2018**, *95*, 197-206.

40. Kadish, K. M.; Adamian, V. A.; Van Caemelbecke, E.; Tan, Z.; Tagliatesta, P.; Bianco, P.; Boschi, T.; Yi, G.-B.; Khan, M. A.; Richter-Addo, G. B. *Inorg. Chem.* **1996,** *35*, 1343-1348.

41. Singh, P.; Kumar Das, A.; Sarkar, B.; Niemeyer, M.; Roncaroli, F.; Olabe, J. A.; Fiedler, J.; Zalis, S.; Kaim, W. *Inorg. Chem.* **2008**, *47*, 7106-7113.

42. Zink, J. R.; Abucayon, E. G.; Ramuglia, A. R.; Fadamin, A.; Eilers, J. E.; Richter-Addo, G. B.; Shaw, M. J. *ChemElectroChem*. **2018**, *5*, 861-871.

43. El-Attar, M. A.; Xu, N.; Awasabisah, D.; Powell, D. R.; Richter-Addo, G. B. *Polyhedron*. **2012**, *40*, 105-109.

44. Connelly, N. G.; Geiger, W. E. *Chem. Rev.* **1996**, *96*, 877-910.

45. Bruno, G.; Schiavo, S. L.; Piraino, P.; Faraone, F. *Organometallics*. **1985**, *4*, 1098-1100.

46. Bauer, H.; Nagel, U.; Beck, W. *J. Organomet. Chem*. **1985**, *290*, 219-229.

47. Singh, S.; Verma, M.; Singh, K. N. *Synth. Comm.* **2004**, *34*, 4471-4475.

48. Bohle, D. S.; Hung, C.-H.; Smith, B. D. *Inorg. Chem.* **1998**, *37*, 5798-5806.

49. Lorkovic, I. M.; Ford, P. C. *Inorg. Chem.* **1999**, *38*, 1467-1473.

50. Benvenuto, M. A.; Sabat, M.; Grimes, R. N. *Inorg. Chem*. **1992**, *31*, 3904-3909.